Application of the Cross-hole Technique For Analysis of Shear Waves in Fractured Limestone Reservoirs

by

Brian J. Baptie

B.Sc.(Hons.) Geophysics 1988
University of Edinburgh

Thesis submitted for the degree of Doctor of Philosophy
Department of Geology and Geophysics
University of Edinburgh
1996

ABSTRACT

In this study, I use the cross-hole method to examine the relationship between fractures in limestone reservoirs, where the presence of fractures has been determined by *a priori* information, and the shear-wave anisotropy of the rockmass. I process and interpret multicomponent seismic data from two producing areas: the East Fitts field Oklahoma, where a multi-azimuthal cross-hole survey is used to image the Hunton and Viola reservoir formations at depths of 3000-4000 feet; and the Iatan East Howard field, Texas, where two cross-hole azimuths are used to image the Clearfork reservoir formation at a similar depth. I apply a numerical method to measure the shear-wave splitting parameters, $qS1$ polarization and time delay between $qS1$ and $qS2$ arrivals, and best-fit parameters for reservoir crack strike and crack density are determined by forward modelling. The observed $qS1$ polarizations at three azimuths from the East Fitts site can be related to propagation through two thin layers, representing the Hunton and Viola reservoir zones, each containing distributions of micro-cracks with a best-fit strike of N35°E. The observed time delays between $qS1$ and $qS2$ arrivals can also be modelled by lower crack densities distributed throughout the layered model. Polarization measurements at one cross-hole azimuth from the Iatan site agree with the *a priori* reservoir fracture direction of N60°E-N85°E. Results from the second azimuth fall within the expected zone of behaviour for cracks striking ±12.5° of N170°E. A measured $qS1$ polarization direction of N170°E from near-offset VSP data at the Iatan site also disagrees with the known reservoir fracture direction. The Iatan measurements are incompatible with hexagonal anisotropic symmetry with a horizontal axis of symmetry. No improvements in the resolution of the anisotropic parameters of fractured rocks and reservoirs was achieved by using the cross-hole method although propagation through the near-surface is avoided. Acceptable model solutions have been found for the observations, however, the problems of non-uniqueness are inherent in the forward modelling approach.

ACKNOWLEDGEMENTS

CONTENTS

CHAPTER 1 - INTRODUCTION

1.1 Previous developments

Many hydrocarbon reservoirs contain distributions of natural fracture systems which have an important effect on fluid flow within the reservoir. This has important consequences for the storage and extraction of hydrocarbons, in terms of providing primary or secondary reservoir porosity and permeability. The relationship between such fracture systems and seismic response remains unresolved, and to a large extent dependent on the scale of observation. For instance, reservoir heterogeneities imaged by well log data may appear very different from those in surface reflection data.

It has been proposed that distributions of micro-cracks or fractures, aligned by stress or geological history, can give rise to effective seismic anisotropy (Crampin *et al.* 1984). A major consequence of body wave propagation in anisotropic media is that two shear waves exist for each direction of propagation, each (in general) with different velocities and polarizations (Love 1944). This phenomenon is widely known as *shear wave splitting*.

Multicomponent seismic data, from reflection surveys and vertical seismic profiles (VSP's), are now being increasingly used to relate shear-wave properties to the directions of in-situ stresses and the orientation of micro-cracks, smaller than the seismic wavelength, within the rockmass. Mueller (1991) uses the differential amplitudes of split shear-waves, in reflection surveys, to detect fractured zones in the Austin Chalk, Texas. These fracture zones were later confirmed by horizontal drilling. The correlation of polarizations with fracture orientation was also shown by Martin and Davis (1987). Li *et al.* (1993) show that there may be a relationship linking the time delay between the two split shear waves and hydrocarbon production rates in the Dimmit field, Texas. The amount of hydrocarbon production has also been correlated to the percentage of differential shear wave velocity anisotropy, in the Silo field, Wyoming, by Davis and Lewis (1990) and in the Romashkino field, Russia, by Cliet *et al.* (1991). The particle motions of synthetic seismograms generated by propagation

through theoretical models of a cracked rockmass have been found to closely match the observed particle motions from VSP data (Bush 1990).

However, the near-surface has been shown, on a great many occasions, to be highly anisotropic (*e.g.* Campden 1990; Kramer 1991; Yardley 1994). This can severely degrade the quality of multicomponent seismic data and have can prevent accurate measurement of seismic anisotropy from surface sources and result in errors in estimated shear-wave splitting parameters. Although layer stripping and other near surface corrections can be made, these methods are often unstable, particularly in the presence of noise.

Analysis of shear wave anisotropy in a cross-borehole environment, has, until now, been rarely considered. Cross-hole surveys are seldom used as an exploration tool as two wells are necessary for sources and receivers, respectively. Instead, such surveys are often used to monitor changes in producing reservoirs, typically during improved oil recovery operations. Another major use of cross-hole data has been for the tomographic inversion of compressional waveforms. These methods have generally used *P*-waves rather than shear waves. In his Ph.D. thesis, Liu (1989), considered some of the theoretical aspects of shear wave splitting in a cross-hole environment. He concludes from synthetic modelling studies that shear wave splitting should be observable in cross-hole surveys, however, it is more difficult to extract diagnostic information on the seismic anisotropy than from vertical seismic profiles. Liu *et al.* (1991) have investigated the relationship between natural fractures and shear wave propagation in a cross-hole survey at the Conoco Borehole Test Facility, Oklahoma. However, this only considered a near surface area, above a depth of 40m.

1.2 Body Wave Propagation in Anisotropic Media

My treatment of the mathematical formulations is brief as the general theory of wave motion in anisotropic materials is well known, Love (1944) and reviewed by Crampin (1984). Any material whose physical properties have directional dependence can be called anisotropic. The elastic behaviour of such materials may be described

by effective elastic constants in one of a range of anisotropic symmetry systems.

1.2.1 Stress-strain relationship

Hookes Law linearly relates stress and strain by the elastic tensor. The three dimensional generalization of Hookes law is

$$\sigma_{ij} = c_{ijkl} \, u_{k,l} \tag{1.1}$$

where, σ_{ij} is the second order stress tensor, $u_{k,l} = \partial u_k/\partial x_l$ the strain tensor and c_{ijkl} is the fourth order tensor of elastic constants. All suffixes take the values of 1, 2 and 3 unless otherwise stated. The elastic tensor, c_{ijkl} has the following symmetry relationships:

$$c_{ijkl} = c_{ijlk} = c_{jikl} = c_{klji} \tag{1.2}$$

This reduces the number of independent elastic constants to 21, the minimum required to describe stress-strain relations for the most general case of anisotropy.

The number of elastic constants can be further reduced by the anisotropic symmetry of the medium. Uniform, homogeneous elastic solids may be divided into eight anisotropic symmetry systems (Crampin and Kirkwood 1981), which describe all possible cases of elastic symmetry. In the lowest order of symmetry, triclinic, wave propagation is described by 21 elastic constants. The number and pattern of elastic constants is unique for each symmetry system. Increasing the order of symmetry reduces the number of independent elastic constants required to describe the three dimensional wave behaviour. In the limiting case of isotropic solids only two independent elastic constants are required.

Anisotropic symmetries are based on the geometric nature of the variations in physical properties, within a particular medium. A symmetry system is classified by the number of planes of mirror symmetry. The number and orientation of the symmetry planes being characteristic of the system. Most cases of exploration interest consider between 5 and 9 elastic constants. These describe the hexagonal and

orthorhombic symmetry systems. The other anisotropic symmetries are cubic, trigonal, tetragonal, and monoclinic, described by three, six, six and thirteen elastic constants, respectively.

Causes for such anisotropic symmetries may be related to the crystal lattice of a mineral, e.g. olivine displays orthorhombic symmetry, or the alignment of minerals or inclusions, within the rockmass. Information on anisotropic symmetry systems may be found in much of the literature on crystallography, for example: Musgrave (1970).

1.2.2 Body wave propagation at phase velocity

The elastodynamic equations of motion in a purely elastic anisotropic medium are

$$\rho \frac{\partial^2 u_i}{\partial t^2} = c_{ijkl} \frac{\partial^2 u_k}{\partial x_l \partial x_j} \tag{1.3}$$

where ρ is the density, u_i is the component of displacement in the ith direction. The velocities of plane body waves are given by substitution of the expression for plane waves into the equations of motion (1.3). Following Musgrave (1970), assuming harmonic plane-wave displacement,

$$u_k = a_k e^{i\omega(s_r x_r - t)} \tag{1.4}$$

where a_k is the amplitude of motion in the kth direction, specifying the polarization, ω, is the angular frequency, and s_r is the slowness vector. The slowness vector gives the direction of the wavefront normal and can be given as

$$s_r = v^{-1} n_r \tag{1.5}$$

where v is the phase velocity and n_r is the wavefront normal vector. Substituting (1.4) and (1.5) into (1.3) gives

$$(c_{ijkl} n_j n_l - \rho v^2 \delta_{ij}) a_k = 0 \tag{1.6}$$

Introducing, the Kelvin-Christoffel stiffnesses, given by Musgrave (1970) as,

$$\Gamma_{ij} = c_{ijkl} n_j n_l \qquad (1.7)$$

equation (1.7) may be rewritten as

$$(\Gamma - \rho v^2 I)a = 0 \qquad (1.8)$$

where I is the 3×3 identity matrix and a is the amplitude vector of the displacements. This may now be considered as a linear eigenvalue problem. Due to the symmetry relationship (1.2), Γ is a symmetric matrix, therefore, the eigen value problem (1.8) has three real positive roots for ρv^2 with orthogonal eigenvectors a, each eigenvalue and associated eigenvector corresponding to the velocity and polarization of a body-wave.

Thus, in an anisotropic medium, there are three waves in each direction of phase propagation, with directionally dependent velocities and mutually orthogonal polarizations. These waves correspond to a quasi P-wave, qP, with approximately longitudinal particle motion, and two quasi shear waves, $qS1$ and $qS2$, with approximately transverse particle motions. The variation of the body wave velocities can be described by velocity surfaces or sheets. Figure 1.1 shows the variation between the three body wave velocity sheets in three orthogonal planes, for an azimuthally anisotropic material.

The major consequence of this is that, a shear wave entering an anisotropic medium splits into two components with different velocities and orthogonal polarizations, appropriate for the particular raypath through the anisotropic symmetry system. The two quasi shear waves separate with time giving rise to a time delay, which, along with the polarizations, is preserved on subsequent propagation through isotropic media. Shear wave polarization directions and the time delay between the split shear waves constrain the orientation of the principal axes of strain and the degree of anisotropy for the medium.

This phenomenon is known as *shear wave splitting* or *shear-wave birefringence*, due to the similarity to the birefringence of light in optics.
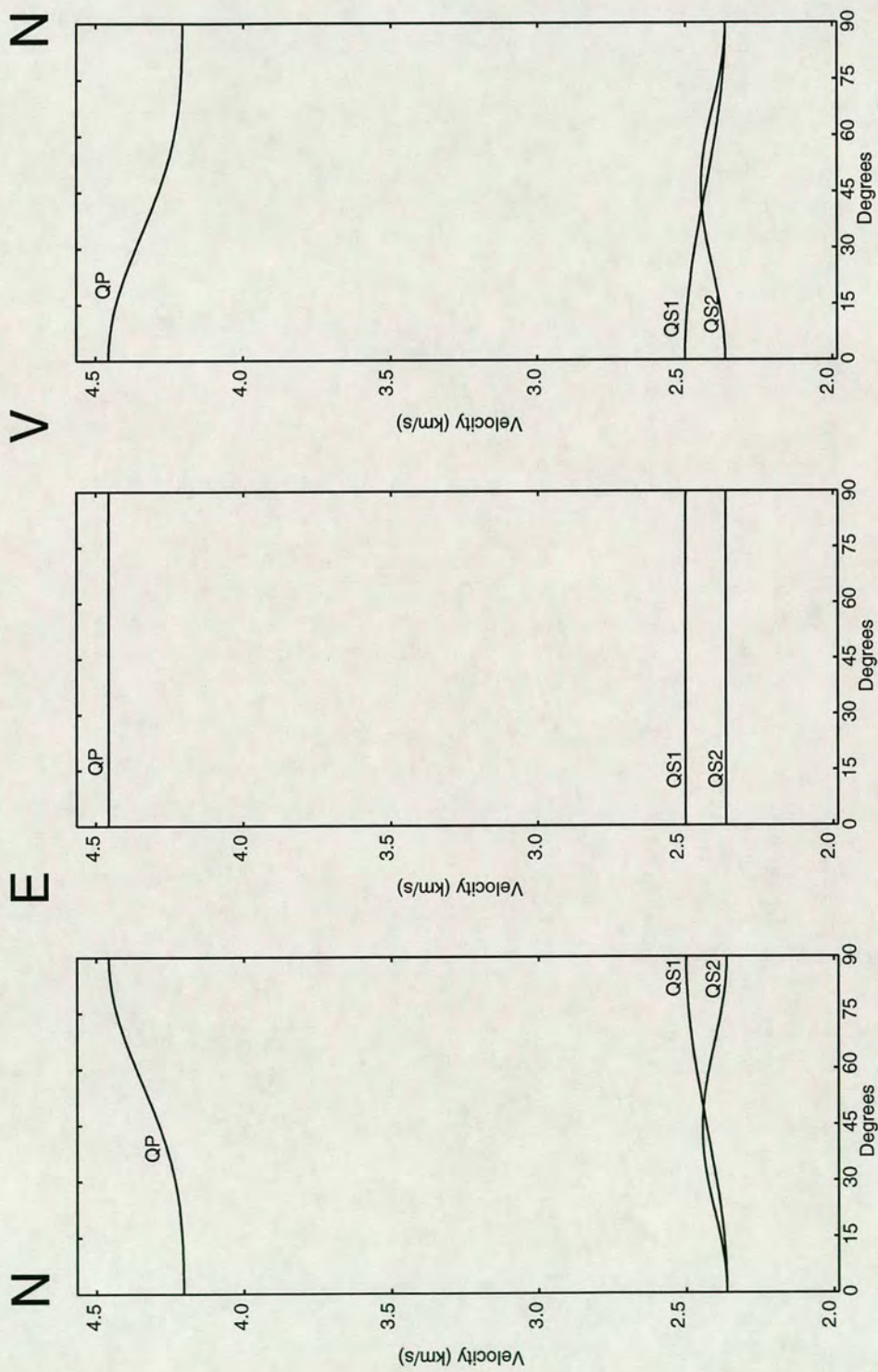
Figure 1.1. Velocity variations typical of azimuthal anisotropy in three mutually orthogonal planes: (N)orth-(E)ast; (E)ast-(V)ertical; and (V)ertical-(N)orth. Here, azimuthal anisotropy is modelled by distributions of liquid-filled vertical microcracks striking east-west.

1.2.3 Body wave propagation at group velocity

The vector nature of phase velocity in anisotropic media requires that the wavenumber, κ, the number of wavelengths in a unit distance, is also a vector. Thus the expression for group velocity in isotropic media, $\partial\omega/\partial\kappa$, where ω is the angular frequency, must be rewritten as

$$V = (\frac{\partial\omega}{\partial\kappa_1}, \frac{\partial\omega}{\partial\kappa_2}, \frac{\partial\omega}{\partial\kappa_3}) \qquad (1.9)$$

Energy transport of seismic waves in anisotropic media is not normal to the plane of constant phase (Figure 1.2), except in the case of propagation in the direction of an anisotropic symmetry plane. Travel times measured from field observations are measured along seismic rays propagating at group velocity seldom allowing phase velocity to be determined. The deviation of the group velocity from the phase velocity direction, has a negligible effect on body wave propagation in weakly anisotropic media. However, in more strongly anisotropic materials, the deviation may cause effects such as cusps in the shear-wave velocity surface (Levin 1979).

The surface traced out by the energy radiated from a point source is known as the wave surface. An expression of the wave surface may be obtained by considering the envelope of wavefronts, radiating from a point source in a given time.

1.3 Effective Anisotropy

An inhomogeneous medium containing heterogeneities such as cracks fractures or layers, can be represented by an equivalent medium which is anisotropic to seismic wave propagation. The parameters of the equivalent medium represent a weighted average of the parameters of the constituent parts of the medium. Effective anisotropy is strongly dependent on the scale of observation, the wavelength of the seismic wave. For example heterogeneities within a rockmass, such as a sequence of fine layers, may result in an equivalent homogeneous medium at longer wavelengths such as those used in surface to surface or surface to borehole seismic exploration. However, at shorter

$\cos \Delta = v/V$
$v = AB/\delta t$ *(phase)*
$V = AC/\delta t$ *(group)*
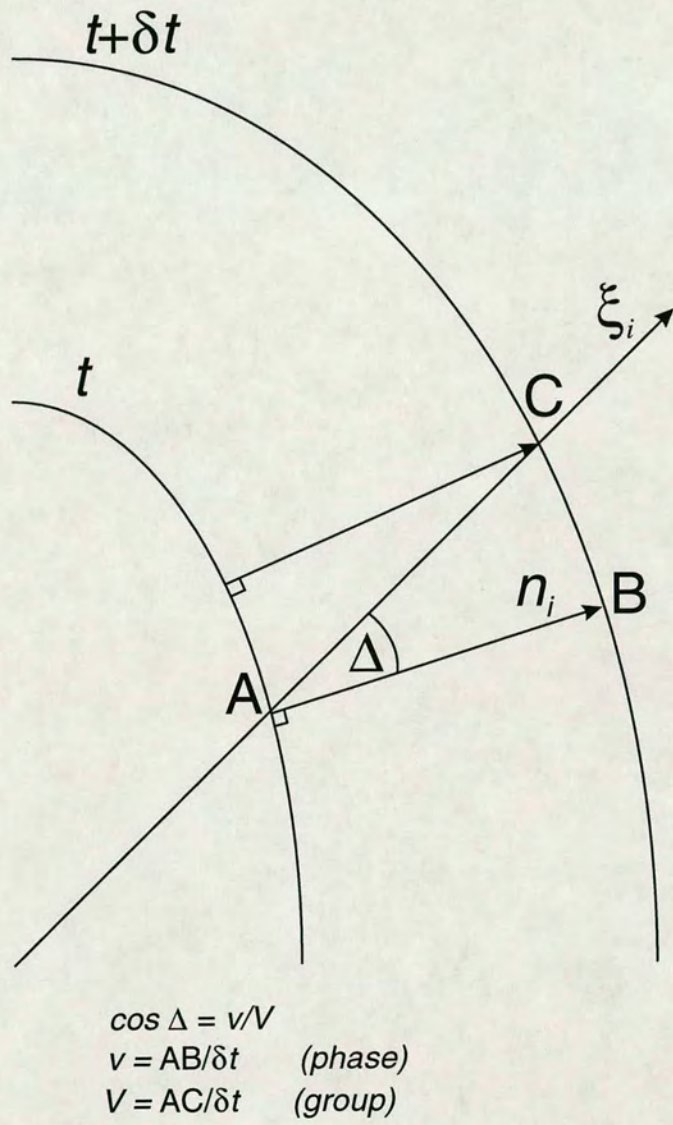
Figure 1.2. Schematic representation of a wavefront in an anisotropic medium at times t and $t+\delta t$, showing phase and group velocities v and V and their respective unit vectors, n_i and ξ_i seperated by the angle Δ.

wavelengths, such a continuous velocity log, the separate layers may be imaged as individual scatters of seismic energy. The alignment of the micro-structure in certain preferred directions may result in an average response on a macroscopic scale which is anisotropic.

1.3.1 *Periodic thin layer anisotropy.*

Postma (1955) and Backus (1962) demonstrate that the long wavelength limit of a periodic sequence of isotropic layers is equivalent to a homogeneous elastic solid with hexagonal anisotropic symmetry. The elastic constants are dependent on the ratio of thicknesses of the two layer and their relative physical properties. This is valid for layer thicknesses of up to half the seismic wavelength. For horizontal layering, this results in transverse isotropy with a vertical axis of symmetry. An example of this would be a clastic sequence consisting of alternating sandstones and shales.

Seismic wave propagation in PTL materials has been extensively studied. Krey and Helbig (1956), Levin (1979) and Helbig (1984), all consider seismic wave propagation in transversely isotropic (T.I.) media, in some detail. Five elastic constants and density are required to describe the elastic behaviour of a T.I. medium. Levin, derives expressions for *P*, *SV* and *SH* velocities in terms of the elastic parameters and the propagation angle from vertical. The three wave surfaces for a T.I medium are shown in Figure 1.3.

1.3.2 *Crack induced anisotropy.*

Cracks, micro-cracks, pore spaces or other inclusions are all examples of heterogeneities within a rockmass which, subject to stress-induced alignment, may cause effective seismic anisotropy. This gives rise to hexagonal anisotropic symmetry. If the cracks are vertical then the axis of symmetry is horizontal . Such a cracked rock will display the type of azimuthal variation in seismic properties, which have been observed in many areas of the subsurface.
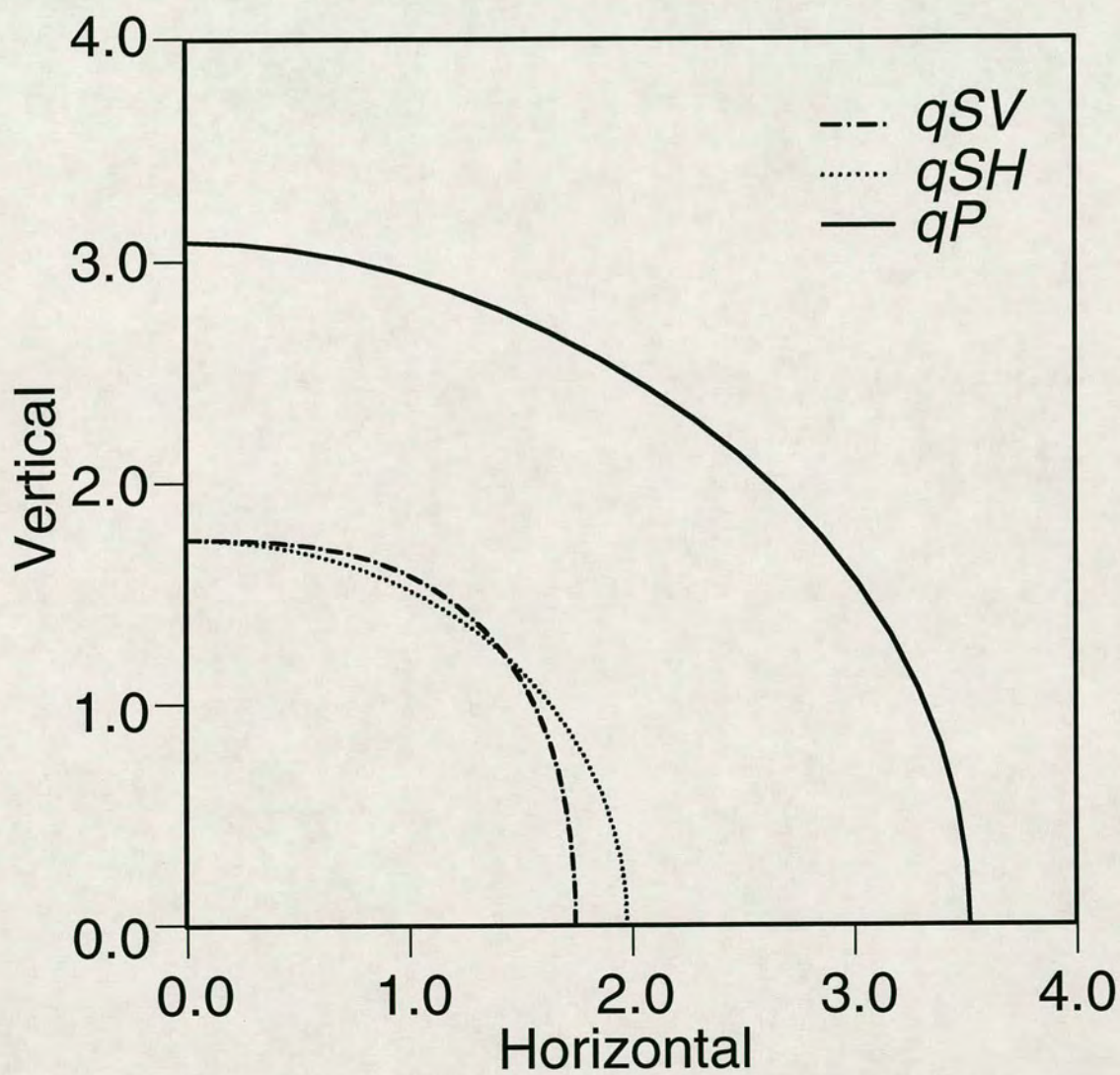
Figure 1.3. Wave surfaces for *qP, qSH* and *qSV* waves for a transversely isotropic material. Velocities are in km/s.

Crampin *et al.* (1984) suggest that stress-aligned, fluid-filled cracks, or micro-cracks, commonly occur in the upper crust. This hypothesis, known as *Extensive Dilatancy Anisotropy*, or *EDA*, was originally introduced to explain observations of shear-wave splitting in the vicinity of local earthquakes (Booth *et al.* 1985). Horizontal polarization directions of shear waves were found to be parallel or sub-parallel to the maximum compressive stress. The observed polarization directions proved to be consistent for a cone of solid angle directions within ±45° of the vertical. Hexagonal anisotropic symmetry, due to vertical, stress-aligned inclusions provides the mechanism to explain the observations.

Whether EDA is indeed the physical mechanism explaining such observations, is difficult to ascertain as drilling and coring would disrupt the local stress field, thus distorting the cracks. Crampin (1993) in "Arguments for EDA" presents a detailed description of evidence for and against the EDA hypothesis.

1.4 Modelling fractured or cracked rocks

Due to the complex nature of real earth structures, we generally consider some averaged characteristic of the real medium to calculate a geophysical model. Equivalent homogeneous media can be used to represent the effective characteristics of heterogeneous micro-structure within the earth. This allows the representation of micro-fracture systems by effective or equivalent media which have the same elastic properties as the heterogeneous fractured material. There are several models which can be used to calculate effective elastic constants of fractured rock. One class of model considered here are the isolated inclusion models. As the name suggests, these models consist of isolated inclusions within a homogeneous matrix. The inclusions may be empty, or consist of material with different properties from the matrix. In general, the inclusion may take any shape, but most models are based on the work of Eshelby (1957) who developed solutions for a homogeneous ellipsoid, set in an unbounded homogeneous material,and deformed by an arbitrary static stress field.

Garbin and Knopoff (1975) calculate the static elastic moduli of a solid with

dilute concentrations of aligned circular cracks. Hudson (1980 and 1981) calculates effective elastic constants of media containing aligned circular cracks based on the scattering of elastic waves at the cracks. The cracks are assumed to be small with respect to wavelength of observation. It is also assumed that the concentration of the cracks is low and that the aspect ratio of the cracks γ ($\gamma = b/a$, where b is the width and a is the diameter of the cracks) is small. In addition, connectivity between the cracks is not considered. The Hudson model accounts for both first and second order perturbations due to scattering from the cracks and crack interactions. The results can be written so that the real parts of the elastic tensor model velocity variation and the imaginary parts model attenuation.

Nishizawa (1982) uses a static approach to calculate the effective elastic constants for media containing aligned elliptical inclusions, which are small with respect to wavelength. The ellipsoids have two equal semi-axes of length a and a third axis of length b, which may take any value, allowing the cracks to assume any aspect ratio. Nishizawa's method uses a numerical algorithm to calculate the effective elastic constants, whereby large concentrations of cracks may be achieved by an iterative procedure.

In a numerical study, Douma (1988), shows that both Nishizawa's and Hudson's models give similar results for a wide range of aspect ratios. Significant differences were found to exist only for large aspect ratios ($\gamma > 0.3$) and crack densities ($\varepsilon > 0.05$).

More recently, Zatsepin and Crampin (1995) develop theoretical equations of state to model the response of a fluid saturated stress-sensitive rockmass to changes in *in situ* conditions. The application of differential horizontal stress on the rockmass results in the partial alignment of intergranular pore space and micro-cracks and resulting azimuthal anisotropy.

1.5 Forward Modelling in anisotropic media

Forward modelling has been commonly applied to generate synthetic

13

traveltimes and amplitudes for comparison with actual data. This has proved useful in improving understanding of wave propagation in anisotropic media. However such methods can be extremely CPU intensive given the complex mathematics involved, so some intuitive first approximation model, based upon the modeller's experience of dealing with such data, is usually required. There are two principal techniques for computing synthetic seismograms in anisotropic media: the ray method and the reflectivity method.

Ray tracing methods (Cerveny and Firbus 1984) can be applied to the study of laterally inhomogeneous anisotropic media and areas of complicated geology. Such methods may only be applied if both wave and medium parameters vary slowly within a wavelength. Also, ray methods require modification in the vicinity of caustics such as shear wave singularities (Chapman and Shearer, 1989).

The reflectivity method was developed by Fuchs and Müller (1971) to calculate synthetic seismograms in horizontally stratified isotropic media. This was extended to include anisotropic media by Booth and Crampin (1983) and is probably a more exact method of modelling wave propagation in plane layered anisotropic media. The reflectivity method is a full wave modelling technique, so, interface, channel, surface and other non-geometrical inhomogeneous waves may be generated in addition to body waves. For this reason the anisotropic reflectivity method is to be preferred for modelling simple geological structures, which are horizontally stratified.

In this thesis I make use of the anisotropic modelling package, ANISEIS (Taylor 1990), to calculate synthetic seismograms using the reflectivity method. ANISEIS calculates the synthetic seismograms for point sources in horizontal, plane layered anisotropic media by integration of plane waves along summation paths over slowness in the vertical plane and azimuth in the horizontal plane. Sources and geophones can be placed anywhere within the model, allowing various recording geometries to be simulated.

1.6 The aims of this study

My aim, is to investigate the behaviour of seismic shear waves, propagating through known fractured reservoirs and compare this with elastic wave behaviour in equivalent anisotropic media, to determine the presence of seismic anisotropy in the rockmass. Examination of cross-hole data should allow the study of shear wave behaviour at depth without degradation in data quality due to the sometimes severe interactions of shear waves with the free surface (Booth and Crampin 1985). Also, the detrimental effects of near-surface anisotropy are by-passed. The comparatively short length of raypath allows shear waves to be studied at higher frequencies and shorter wavelengths than in vertical seismic profiles. A forward modelling approach is used to calculate shear-wave splitting parameters, both by generation synthetic seismograms for anisotropic models and directly from the elastic constants of cracked media, which are then compared with the properties of the observed wavefield.

1.7 Outline of work in this thesis

In Chapter 2, I use Plate Carée projections to display polarizations and time delays of shear waves propagating in anisotropic media of different symmetry systems. Body wave properties are calculated in media with orthorhombic anisotropic symmetry by extending the method used by McGonigle and Crampin (1981) to calculate body wave velocity and polarization from the effective elastic constants, for each direction of propagation. This work has been published by Baptie, Crampin and Liu (1993). The modelling demonstrates the probable sensitivity of the parameters of shear-wave splitting to variations in the types and relative amounts of anisotropy.

Chapter 3 considers the processing and interpretation of a cross-hole data-set from the East Fitts field, Oklahoma. Shear-waves propagating between source and receiver boreholes at three separate azimuths display shear-wave splitting, while anomalous transversely polarized shear energy is reflected from the reservoir zone. A numerical method is used to measure the anisotropic parameters, $qS1$ polarization and

time delay between *qS1* and *qS2* arrivals at the three different azimuths. Observations are compared with the calculated splitting parameters for a number of models with different crack orientations and crack densities. Crack orientation is constant with depth. A best-fit model for the crack parameters is defined statistically and synthetic seismograms are generated for these parameters.

In Chapter 4, I examine cross-hole and VSP data from the Upper Clearfork group, a fractured dolomite reservoir at the Iatan field in West Texas. Fracture orientation obtained from core measurements and injection water breakthrough during waterflood operations agrees with the strong regional trend in this area. Principal shear wave polarization directions measured in VSP data do not agree with the expected trend. I use forward modelling to find a best-fit model for the observed shear-wave splitting measurements. Cross-hole data within the reservoir zone also show evidence of splitting. However, estimates of *qS1* polarization at two different azimuths give conflicting results. Anisotropic modelling suggest that the results at one azimuth agree with the VSP observations, while results at the other azimuth agree with the *a priori* estimates of fracture orientation. Preliminary results were presented by Baptie and Crampin (1994).

Chapter 5 contains the conclusions to this thesis. I discuss how measurements of shear-wave anisotropy observed in the above case studies relate to known fracture orientation and distribution. An appraisal of the use of cross-hole seismic data for evaluating seismic anisotropy is made and the implications for fracture detection in hydrocarbon reservoirs are further considered. Finally, I make a number of suggestions for the directions of future work in this field.

CHAPTER 2 - DISPLAYING SHEAR-WAVE SPLITTING IN CROSS-HOLE SURVEYS

2.1 Introduction

The dip of raypaths in cross-hole surveys and other subsurface seismic experiments is usually significantly different from the near vertical raypaths in reflection surveys and vertical seismic profiles. Shear-wave energy is contained in the plane normal to the raypath, so analysis of the horizontal plane particle motion is no longer appropriate for high incidence. Similarly, polar projections of the horizontal plane are no longer the most appropriate means of displaying the parameters of shear-wave splitting.

Liu *et al.* (1989) show how shear-wave polarizations and time delays between the fast and slow shear-wave arrivals may be displayed on Plate Carée projections. These are equal-area cylindrical projections which show a full range of raypaths, covering 360° of azimuth, and dips from +90° for downward propagation, to -90° for upward propagation. The polarizations of shear waves in both the horizontal plane (radial-transverse) and the normal plane (vertical-transverse) are considered.

Bush and Crampin (1987) use point singularities to infer a combination of azimuthal anisotropy, and transverse isotropy with a vertical axis of symmetry, in the Paris Basin. The combination of these two types of hexagonal anisotropic symmetry, leads to orthorhombic symmetry with three mutually perpendicular symmetry planes. Wild and Crampin (1991) show that such combinations have many directions of point singularities, where rays of shear waves have anomalous particle motion. The directions of these singularities are dependent on the types and relative amounts of anisotropy in the rockmass.

In this chapter, I use Plate Carée projections to demonstrate the likely sensitivity of shear-wave behaviour to small variations in the anisotropic rock properties. Shear-wave behaviour is displayed on Plate Carée projections for a number of materials which have combinations of EDA and PTL anisotropy (Baptie, Crampin

and Liu, 1993). The three-dimensional shear wave behaviour is shown to be sensitive to relative amounts and strengths of the two types of anisotropy. Secondly, I show how the spatial distributions of the polarizations and time delays can be used for interpreting multi-component cross-hole data. Finally, I comment on how lack of uniqueness effects these results.

2.2 Equal Area Projections

The behaviour of shear waves in an anisotropic medium is dependent on the propagation direction. Thus, polarizations and time delays vary with the incidence and azimuth angles of the propagation direction. Equal-area polar projections provide a means of mapping three-dimensional shear-wave behaviour on a spherical surface to a two-dimensional surface. For downwards propagation, the polar projection is constructed for a hemisphere of directions about the source. Quasi-shear wave polarizations and the time delays between fast and slow split shear waves, referred to as $qS1$ and $qS2$ throughout, for each azimuth and incidence angle are mapped on to a plane surface. This gives 360° of azimuthal coverage, and angles of incidence from +90° for downwards propagation to 0° for horizontal propagation.

The pattern of polarizations and delays for shear waves propagating through a medium containing thin, parallel, liquid filled microcracks, aligned vertically and striking east-west is shown in Figure 2.1. Polarizations are plotted in the horizontal (radial-transverse) plane (Figure 2.1a). While time delays are contoured in milliseconds for a normalized path length of 1km (Figure 2.1b). The $qS1$ polarizations are parallel to the crack strike for a broad band of directions across the centre of the projection. Observations of the $qS1$ polarization direction along near vertical raypaths, will therefore give an estimation of crack strike. Time delays are also at a maximum for the vertical direction.

Figure 2.2 shows how an equal-area polar projection is constructed for an azimuthal cross-section. The points where each raypath intersects with a sphere about the source, are projected on to the horizontal plane. Radial distance in the horizontal

(b)

Group delays in milliseconds, normalized over 1km.

(a)

Horizontal qS1 Polarizations
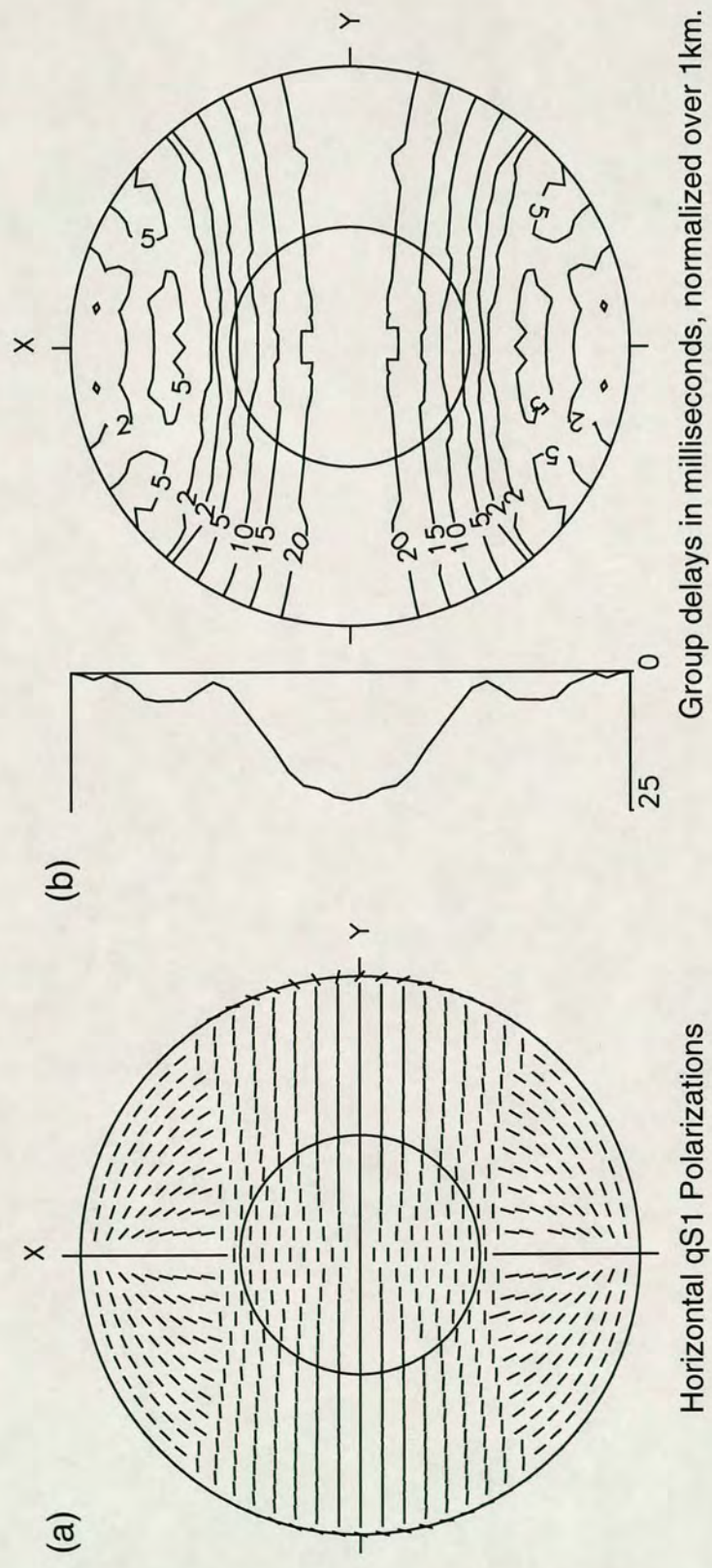
Figure 2.1. Polar equal area projection over a hemisphere of directions fo the behaviour of split shear-waves propagating at group velocity through a medium containing EDA cracks, striking east-west, with a crack density of $\epsilon = 0.05$ and aspect ratio $\gamma = 0.05$.
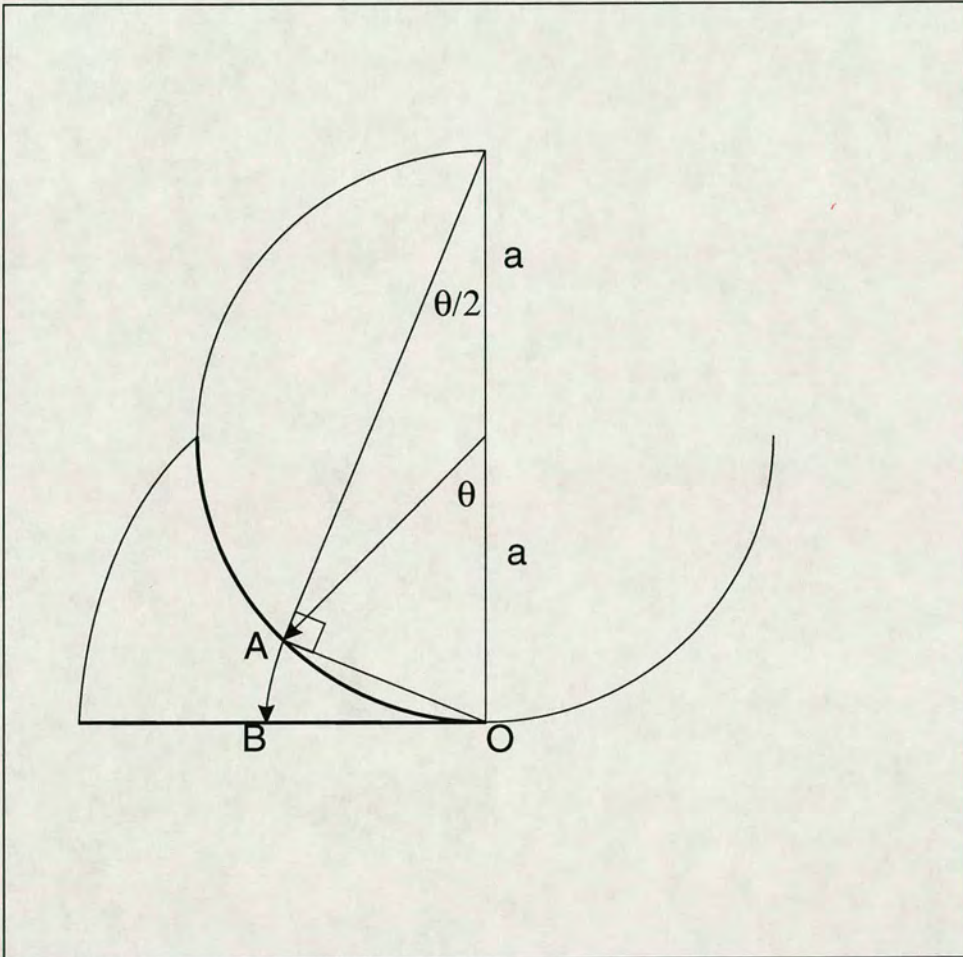
Figure 2.2. Geometry of an equal area polar projection. A raypath through direction A on the sphere, maps to point B in the horizontal plane. Distance **OA** = **OB** = 2a*sin(θ/2). Areas are preserved so that a proportional area on the sphere is equivalent to a proportional area in the horizontal plane.

is given by the relationship, $r = 2a*\sin\theta/2$, where θ is the angle of incidence of the raypath and a is the radius of the sphere. Each direction is represented by an equal area of the circle of projection. From this, it is clear that horizontal directions of propagation, which lie at the edges of the plot, will be severely elongated and distorted.

Cross-hole datasets are likely to include raypaths closer to horizontal than vertical directions. Along these directions, shear wave energy will lie mainly in the normal (vertical-transverse) plane. Another disadvantage of equal-area polar plots about the vertical, for these types of geometries is that they do not lend themselves to depicting anything except horizontal shear-wave polarizations. The Plate Carée projections discussed in this chapter offer an alternative means of display for shear-wave properties at such angles of incidence.

2.3 Formulations for EDA- and PTL- Anisotropy

Before displaying the variation of polarization and delays on Plate Carée projections the elastic constants for a number of theoretical anisotropic materials must first be calculated. The solution to the Christoffel equation (1.8) is used to derive the body wave velocities and polarizations, using the elastic constants for each material.

2.3.1 Calculating Elastic Constants for PTL Materials

The five independent elastic constants of a PTL solid may be derived from the elastic properties and the ratio of thicknesses of repeated sequences of isotropic layers by the formulations of Postma (1955). These are valid for layer thicknesses less than about half a seismic wavelength. The resultant structure has hexagonal anisotropic symmetry, with the axis of symmetry normal to the layering, assumed here to be vertical. Varying amounts of PTL anisotropy may be expressed as the percentage of differential shear-wave velocity anisotropy: the percentage velocity difference between the fast and slow shear-wave arrivals. Strictly speaking, in this case, this is the

velocity difference between the *SH* and *SV* wave types at horizontal incidence. At vertical incidence, this anisotropy has azimuthal isotropy and there is no shear-wave splitting.

The velocity variation of the three PTL materials used is displayed in Figure 2.3, for a quadrant of directions from vertical (0°) to horizontal (90°) in a symmetry plane through the axis of symmetry. This shows the $\sin 4\theta$ periodicity in this section of the *SV* velocity surface. and the $\sin 2\theta$ periodicity in the *SH* velocity surface. Elastic constants for the PTL materials used here are calculated after the procedure of Bush (1990). This uses an empirical relationship between the elastic properties of individual isotropic layers and those of a long wavelength equivalent transversely isotropic medium. This relationship is given by Bush (1990) as,

$$[\frac{\alpha_1 - \alpha_2}{\bar{\alpha}}]^2 A \simeq \Phi_p \qquad (2.1)$$

where α_1 and α_2 are the *P*-wave velocities of the two isotropic periodic thin layers, Φ_p is the differential *P*-wave velocity anisotropy, *A* is a constant and α' is the *P*-wave velocity of the unlaminated isotropic medium, which may be written as,

$$\alpha' = [\frac{1}{2}\alpha_1^2 + \frac{1}{2}\alpha_2^2] \qquad (2.2)$$

The above relationships 2.1 and 2.2 can be rewritten to give expressions for α_1 and α_2

$$\alpha_1 \simeq \frac{\alpha'}{2}[(4 - \frac{\Phi_p}{A})^{\frac{1}{2}} + (\frac{\Phi_p}{A})^{\frac{1}{2}}] \qquad (2.3)$$

$$\alpha_2 \simeq \frac{\alpha'}{2}[(4 - \frac{\Phi_p}{A})^{\frac{1}{2}} - (\frac{\Phi_p}{A})^{\frac{1}{2}}] \qquad (2.4)$$

For a given Φ_p and α' an iterative procedure is used to determine the values of α_1 and α_2 which best fit the desired Φ_p. The constant *A* is initially calculated using Postma's (1955) formulae for a range of values of α_1 and α_2. Then, for the desired Φ_p, the
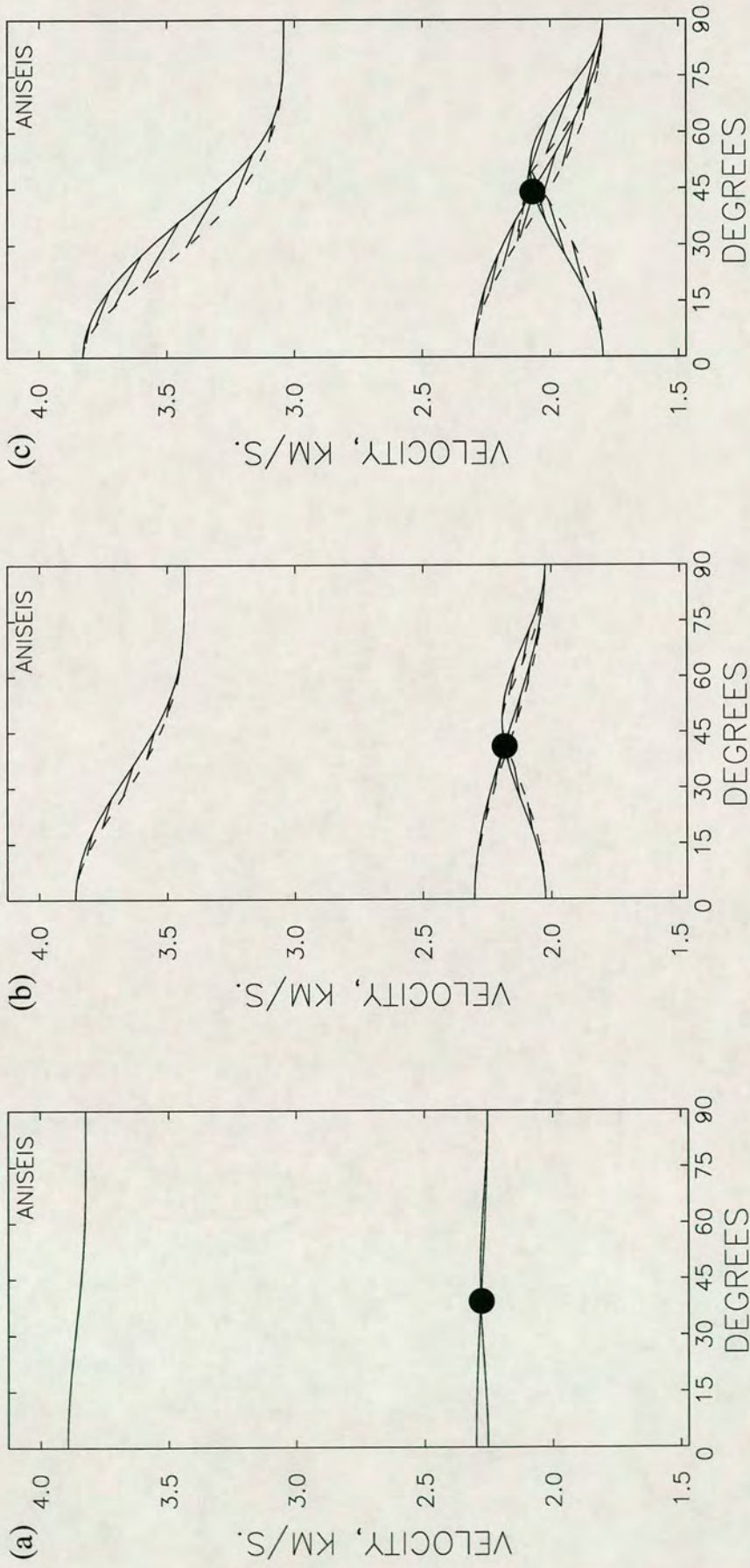
Figure 2.3. Phase (solid line) and group (dashed line) velocity variations, in the horizontally laminated PTL materials of Table 2.1, for a quadrant of directions from horizontal to vertical (0-90). The three PTL materials have differential shear-wave velocity anisotropies of: (a) 2%; (b) 12%; and (c) 22%. The line singularities where the two shear-wave velocity sheets intersect are marked by black dots.

velocities α_1 and α_2 are calculated using equations 2.3 and 2.4 and the value of A calculated above. Postma's formulae are then applied to calculate a new value of Φ_p for these velocities. The difference between the desired and calculated values of Φ_p is then minimized using a Newton-Raphson iteration. Shear wave velocities are calculated in a similar manner. For layers of equal thickness, the maximum shear-wave velocity in the PTL medium is the same as the shear-wave velocity in the isotropic medium, from which the PTL material defined. This allows the percentage anisotropy to be increased while holding the horizontal $qS1$ velocity constant. The elastic constants for the three PTL materials used are given in Table 2.1. These were calculated using isotropic velocities of α=3.9km/s and β=2.3km/s and percentage shear-wave anisotropies if 2%, 12% and 22%. The resulting horizontal SH-velocity in each of the PTL media is constant at 2.3km/s.

2.3.2 Elastic Constants for EDA Materials

Azimuthal anisotropy may be modelled by distributions of stress aligned, fluid-filled microcracks and orientated pore spaces (Crampin 1984b). The elastic constants for equivalent anisotropic cracked media may be calculated using the formulations of Hudson (1980, 1981) for the scattering of seismic waves by distributions of aligned cracks. Given an isotropic material, described by a density, ρ, and P- and S-wave velocities, a crack set is defined for a given frequency of seismic wave by, radius, a, crack density, ε, aspect ratio, γ, as well as the crack content (liquid-filled or gas-filled). Crack density and aspect ratio are defined as

$$\varepsilon = \frac{N\langle a^3 \rangle}{v} \tag{2.5}$$

and

$$\gamma = \frac{d}{a} \tag{2.6}$$

Table 2.1. Elastic constants of PTL-anisotropy, in 10^9 Pa. Density = 2.6g/cm^3.

	Percentage anisotropy	$c_{1111}=c_{2222}$	c_{3333}	c_{1122}	$c_{3311}=c_{2233}$	$c_{2323}=c_{1313}$
PTL1	2%	39.401	37.980	11.893	11.561	13.209
PTL2	12%	38.719	30.624	11.211	9.322	10.651
PTL3	22%	38.111	24.060	10.603	7.324	8.368

where N is the number of cracks of radius a and half thickness d in volume v. The aspect ratio relates to the "fatness" of the cracks: how flat they are. Crack dimensions are assumed to be small with respect to seismic wavelength, and the approximations are thought to be valid for $\varepsilon < 0.1$ (Crampin 1984b) and $\gamma < 0.3$, (Douma and Crampin 1990). Here, I have used crack densities of $\varepsilon = 0.01$ and $\varepsilon = 0.05$, and aspect ratios of $\gamma = 0.001$ and $\gamma = 0.05$, these values being well within the above limits.

Incorporating the EDA cracks in anisotropic materials requires using the extension to the Hudson (1986) formulations, which describes the scattering caused by distributions of cracks in weakly anisotropic materials. This enables cracks to be inserted into the PTL materials described above giving a new material with orthorhombic anisotropic symmetry.

2.3.3 Calculation of Polarizations and Delays

The elastic constants for each combination are used to calculate polarizations and delays. The Fortran program of McGonigle and Crampin (1982) was modified so polarizations and delays could be calculated for orthorhombic symmetry systems (previously it was only valid for hexagonal order symmetries). The Christoffel equation, (1.8), is solved as a linear eigenvalue problem to obtain the three body wave phase velocities and their polarizations. The three eigenvalues and their corresponding eigenvectors give the three body-wave velocities and polarizations, respectively. Since the group velocity direction is not, in general, the same as the phase velocity direction, I use a simplified form of the generalized expression for the group vector at any point on the wave surface given by Musgrave (1970), to calculate the magnitude and direction of the group vector. For orthorhombic, and higher order symmetries, the wavefront equation can be written as,

$$V_j = \frac{a_j^2(\rho v^2 - \Gamma_{jj})}{\rho v n_j} + \frac{n_j}{\rho v} \sum_{k=1}^{3} a_k^2 S_{jk} \quad , j = 1,3 \qquad (2.7)$$

where, S is given by the matrix composed of the diagonal elements of the elastic tensor, and

V is the group velocity vector

a is the displacement vector

ρ is the density

v is phase velocity

n are the direction cosines

Γ_{jj} are the Kelvin Christoffel stiffnesses.

$$S_{ij} = \begin{matrix} c_{11} & c_{66} & c_{55} \\ c_{66} & c_{22} & c_{44} \\ c_{55} & c_{44} & c_{33} \end{matrix} \qquad (2.8)$$

In the case of orthorhombic symmetry the six independent Kelvin-Christoffel stiffnesses are given as:

$$\begin{aligned}
\Gamma_{11} &= n_1^2 C_{11} + n_2^2 C_{66} + n_3^2 C_{55} \\
\Gamma_{22} &= n_1^2 C_{66} + n_2^2 C_{22} + n_3^2 C_{44} \\
\Gamma_{33} &= n_1^2 C_{55} + n_2^2 C_{44} + n_3^2 C_{33} \\
\Gamma_{23} &= n_2 n_3 (C_{23} + C_{44}) \\
\Gamma_{31} &= n_3 n_1 (C_{31} + C_{55}) \\
\Gamma_{12} &= n_1 n_2 (C_{12} + C_{66})
\end{aligned} \qquad (2.9)$$

Equation 2.7 above is solved for a regular grid of phase directions to cover the entire Plate Carée projection. The group velocity direction cosines are generally close to the direction of phase propagation for weak anisotropy, however, for stronger anisotropic materials the deviation increases. A search is implemented over the grid of group velocities and polarizations to find the direction cosines which give the

closest match to the required directions on the regular grid. Values of group velocity and polarization for those directions are assigned to be output.

Time delays between the *qS1* and *qS2* arrivals are calculated by normalization over an appropriate distance. The displacement vectors output by the above procedure are then used to calculate polarization by projection into either the horizontal or normal planes. The polarizations are also normalized to give an idea of the amplitude of the shear wave in that particular plane. A grid spacing of 4.5° is used for the calculation of time delays and a 10° spacing for polarizations. This may lead to some distortion as suggested above, but this is difficult to avoid by calculation of theoretical behaviour by this method.

2.4 Shear Wave Singularities

Phase velocity surfaces in anisotropic media, are analytically continuous and must touch in at least two directions (usually many more) called shear wave singularities (Crampin and Yedlin, 1981). There are three distinct types of singularity: line, kiss, and point singularity. Sections of phase velocity surfaces near point singularities, the commonest type of singularity, usually display high curvature, so that shear wave polarizations may vary rapidly for small differences in raypath direction. Shear waves propagating at group velocity near point singularities show much more irregular behaviour than those propagating at phase velocities and significant differences in the patterns of polarizations and time delays can occur. The multiplicity of group velocity surfaces make time delays multi-functional. Also, anomalies in polarizations and amplitudes occur, as well as various cuspoidal features.

2.5 Shear-wave splitting in Plate Carée Projection

The behaviour of shear-wave splitting in Plate Carée projection is demonstrated in Figure 2.4, 2.5 and 2.6 for PTL, EDA and Orthorhombic anisotropies. Each plot describes a full range of raypaths, covering 360° of azimuth, and dips from +90° for

Figure 2.4. Plate Carée equal area cylindrical projections of the *qS1* polarizations and time delays between *qS1* and *qS2* arrivals of split shear-waves propagating along rays at group velocities through PTL anisotropy with 12% differential shear-wave velocity anisotropy. The four sections of the figure are: (a), *qS1* polarizations projected on to the horizontal (R)adial-(T)ransverse plane; (b), *qS1* polarizations projected on to the normal (V)ertical-(T)ransverse plane; (c), contours of the time delays between the two split shear-waves in ms normalized over 1km; and (d), north-south sections of the contoured time delays at the indicated azimuths. The polarizations show projections of a fixed lenght vector on to the appropriate R-T and V-T planes. Arrows indicate directions of line singularities and solid circles indicate directions of Kiss singularities.
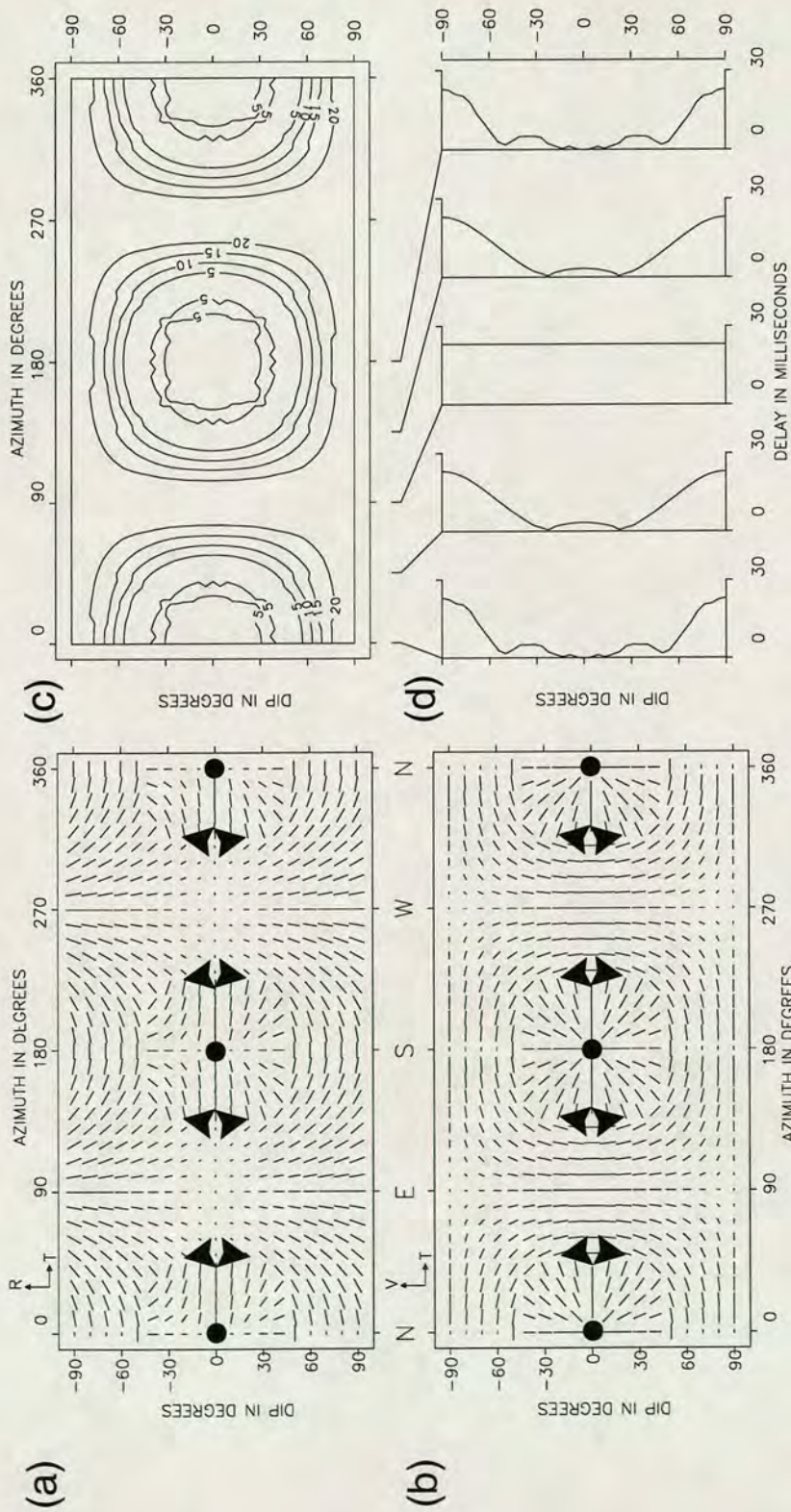
Figure 2.5. Plate Carée equal area cylindrical projections of the *qS1* polarizations and time delays between *qS1* and *qS2* arrivals of split shear-waves propagating along rays at group velocities through EDA anisotropy of parallel vertical cracks striking East-West, parallel to the transverse direction, with a crack density of ε=0.05 and aspect ratio γ=0.05. The four sections of the figure are: (a), *qS1* polarizations projected on to the horizontal (R)adial-(T)ransverse plane; (b), *qS1* polarizations projected on to the normal (V)ertical-(T)ransverse plane; (c), *qS1* polarizations projected on to the two split shear-waves in ms normalized over 1km; and (d), north-south sections of the contoured time delays at the indicated azimuths. The polarizations show projections of a fixed lenght vector on to the appropriate R-T and V-T planes. Arrows indicate directions of line singularities and solid circles indicate directions of Kiss
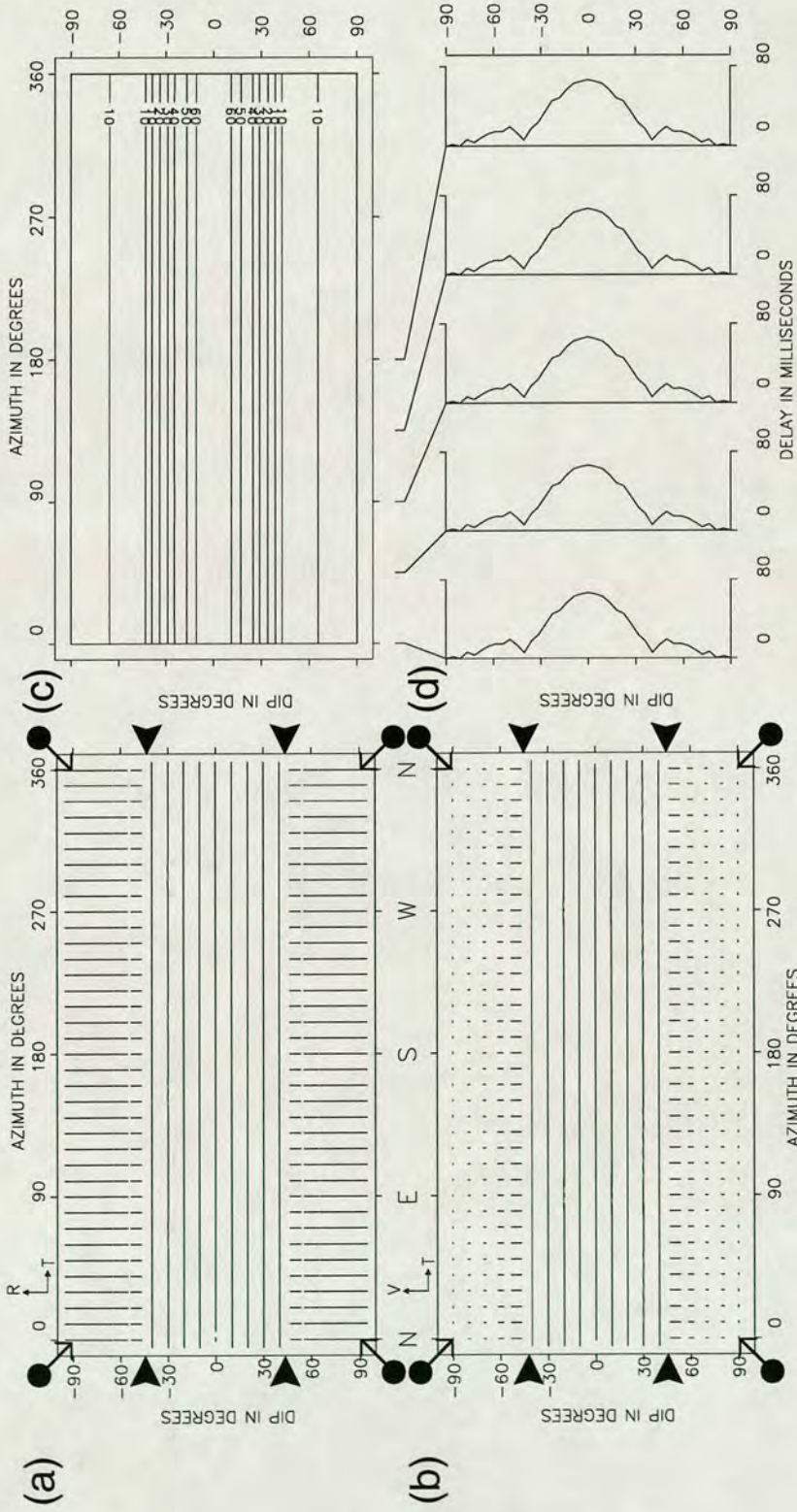
29

Figure 2.6. Plate Carée equal area cylindrical projections of the *qS1* polarizations and time delays between *qS1* and *qS2* arrivals of split shear-waves propagating along rays at group velocities through the orthorhombic anisotropy resulting from the combination of the PTL material in Figure 2.4 with the cracks in Figure 2.5. The four sections of the figure are: (a), *qS1* polarizations projected on to the horizontal (R)adial-(T)ransverse plane; (b), *qS1* polarizations projected on to the normal (V)ertical-(T)ransverse plane; (c), *qS1* polarizations projected on to the normal (V)ertical-(T)ransverse plane; (c), *qS1* polarizations projected on to the normal (V)ertical-(T)ransverse plane; and (d), north-south sections of the contours of the time delays between the two split shear-waves in ms normalized over 1km; and (d), north-south sections of the contoured time delays at the indicated azimuths. The polarizations show projections of a fixed lenght vector on to the appropriate R-T and V-T planes. Arrows indicate directions of line singularities and solid circles indicate directions of Kiss singularities.
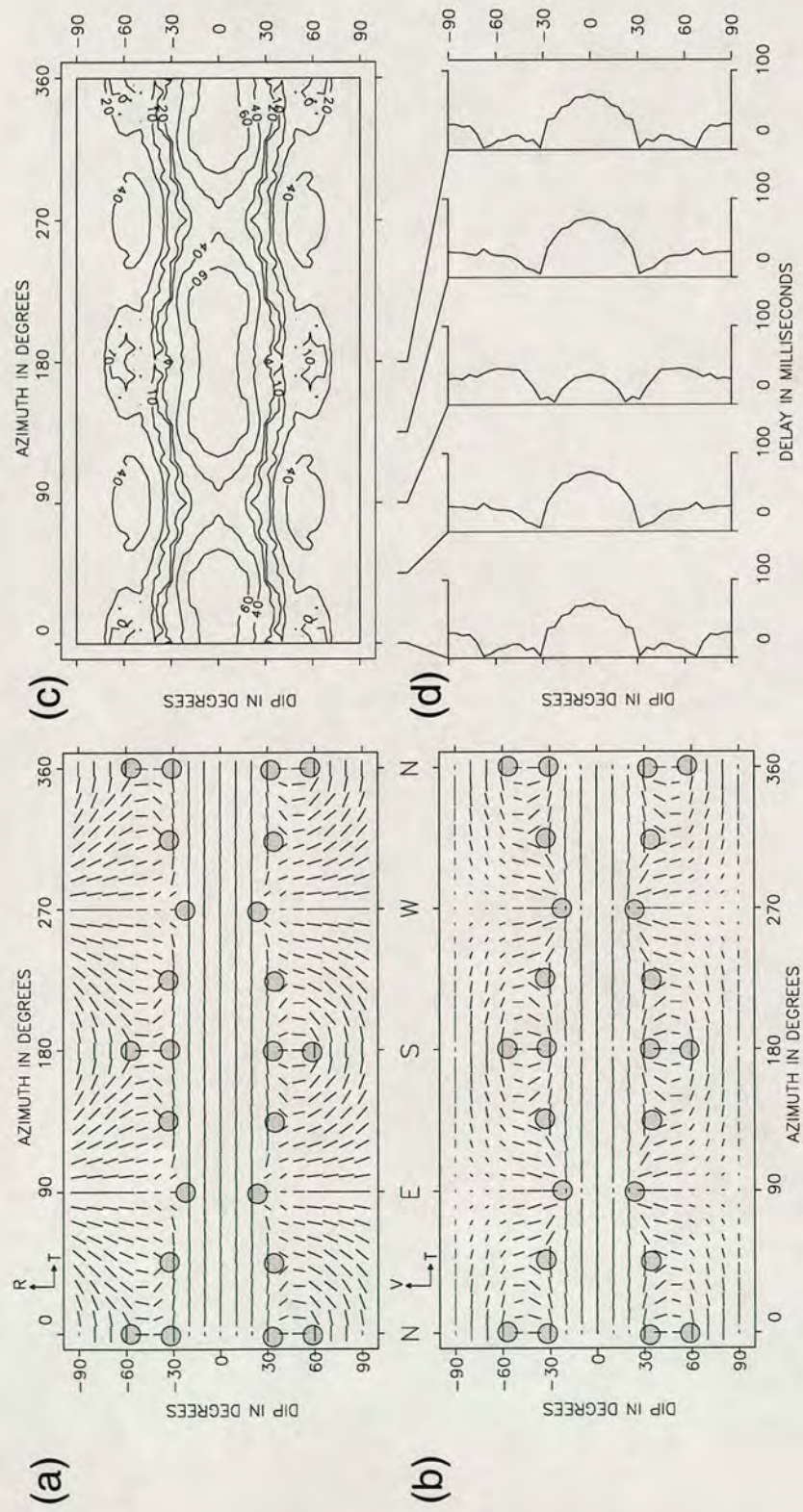
downward propagation, to -90° for upwards propagation. This represents the polarizations of shear waves radiating from a point source, as measured by horizontal instruments (R-T plane) and vertical-transverse instruments (V-T plane), on the walls of a cylinder enclosing the source. The cylinder has then been opened out to give a conventional cartesian (Plate Carée) map projection.

Figure 2.4 demonstrates shear wave behaviour in a purely PTL material, PLT2 of Table 2.1, defined here as having 12% differential shear wave velocity anisotropy. Figure 2.5 shows the pattern of polarizations and delays for shear waves propagating through parallel, vertical, water-filled EDA cracks, striking east-west, with a crack density of $\varepsilon = 0.05$ and aspect ratio $\gamma=0.05$. This represents 5% differential shear wave velocity anisotropy. The cracks are inserted in a background isotropic matrix defined by $V_p = 2.5$ km/s, $V_s = 2.02$ km/s and $\rho = 2.2$ g/cm^2. The effect of inserting the EDA cracks of Figure 2.5 into a matrix with the PTL anisotropy of Figure 2.4, leading to orthorhombic anisotropic symmetry is shown in Figure 2.6.

2.5.1 PTL Anisotropy

The purely PTL-anisotropy in Figure 2.4 shows a distinctive band of transverse polarizations of the leading split shear wave, for directions of propagation between about ±40° of the horizontal, indicating that the *SH*-wave is the first arrival. Outside this band, shear waves are polarized in the sagittal plane, representing *qSV*-motion. The 90° change in polarization marks the direction of a line singularity (indicated by arrowheads), characteristic of hexagonal anisotropic symmetry (Crampin 1989), where the *SH*- and *qSV*- velocity sheets intersect. There are also kiss singularities (indicated by solid circles) in the directions of the symmetry axes - the North and South poles of Figure 2.4. Time delays are largest for horizontal propagation where the difference between *SH*- and *qSV*- velocities is at a maximum.

2.5.2 EDA Anisotropy

The projection of purely EDA-anisotropy in Figure 2.5 also shows distinctive patterns of behaviour. There is a band of nearly parallel polarizations for azimuths close to the crack strike in both the R-T and V-T projections. Time delays are at a maximum in these directions. The cracked medium also exhibits hexagonal anisotropic symmetry but with a horizontal axis of symmetry as opposed to vertical. Thus, line singularities are also present, but with an orthogonal orientation to those for PTL-anisotropy. Two kiss singularities are marked with dots. The patterns of polarizations and delays, produced by EDA-anisotropy in Plate Carée projections, lack any strongly diagnostic features such as seen in polar projections, where the shear-wave polarizations along one near vertical raypath can demonstrate the strike of the EDA-cracks. This means that observations from a large number of directions of dip and azimuth, are required to identify the characteristics of EDA in cross-hole surveys (Liu et al, 1989).

2.5.3 Orthorhombic Anisotropy

The combined PTL- and EDA- anisotropies in Figure 2.6 yield patterns of polarizations and delays displaying orthorhombic anisotropic symmetry. The line singularities of Figures 2.4 and 2.5 have been "pulled apart" and point singularities have appeared at places along the remnants of the old line singularities (Crampin 1989). These point singularities, in directions approximately indicated by shaded circles, mark places, where the phase velocity surfaces of the fast and slow split shear waves, touch at the vertices of convex and concave cones. The polarizations and time delays along seismic rays propagating at the group velocity may be much more complicated, with complex cuspoidal lids, fins and ridges on the surface of the group-velocity surfaces (Crampin 1991). The point singularity in the phase- velocity sheet transforms to an ellipse in the group-velocity sheet. These features are irregular in outline and frequently do not have well defined centres. Consequently, the positions

of the circles on the Plate Carée projections, merely indicate the approximate centre of the anomaly.

2.6 Combinations of EDA and PTL in Plate Carée Projections

The pattern of shear-wave behaviour for a range of directions in rocks with combinations of EDA and PTL varies significantly with the relative amounts of PTL anisotropy, and crack densities, and aspect ratios of the distributions of parallel vertical cracks. Figures 2.7, 2.8 and 2.9 show Plate Carée projections of delays and polarizations produced by EDA cracks introduced into three different PTL solids. The PTL materials, PTL1, PTL2 and PTL3, have anisotropies with differential shear wave velocities of 2%, 12% and 22%, respectively. The elastic constants are as given in Table 2.1. The EDA cracks are specified by crack densities of $\varepsilon = 0.01$ and 0.05 (giving differential shear-wave velocity anisotropies of approximately 1% and 5%) and aspect ratios of $\gamma = 0.001$ and 0.05. These crack densities are in accordance with values commonly observed in exploration seismology. Each diagram is similar in format and notation to Figure 2.4. Note that there is inversion symmetry about a point source for all anisotropic variations in uniform homogeneous solids.

The directions of point singularities in these orthorhombic symmetries, are sensitive to changes in the relative parameters of the anisotropies. Their directions may be used as a benchmark to describe the differences between each projection.

2.6.1 Variations in PTL Anisotropy

Figure 2.7 shows the effects of variations in PTL anisotropy. Combinations of the three PTL solids, PTL1, PTL2 and PTL3, are shown pervaded by thin cracks with crack density $\varepsilon = 0.01$ and aspect ratio $\gamma = 0.001$. For the strong PTL anisotropy of 22% for PTL3 in figure 2.7(c), the broad band of transverse polarizations of pure PTL is still present, but the line singularities at the edge of the broad band have each been replaced by eight nearly co-planar point singularities. The kiss singularity, which
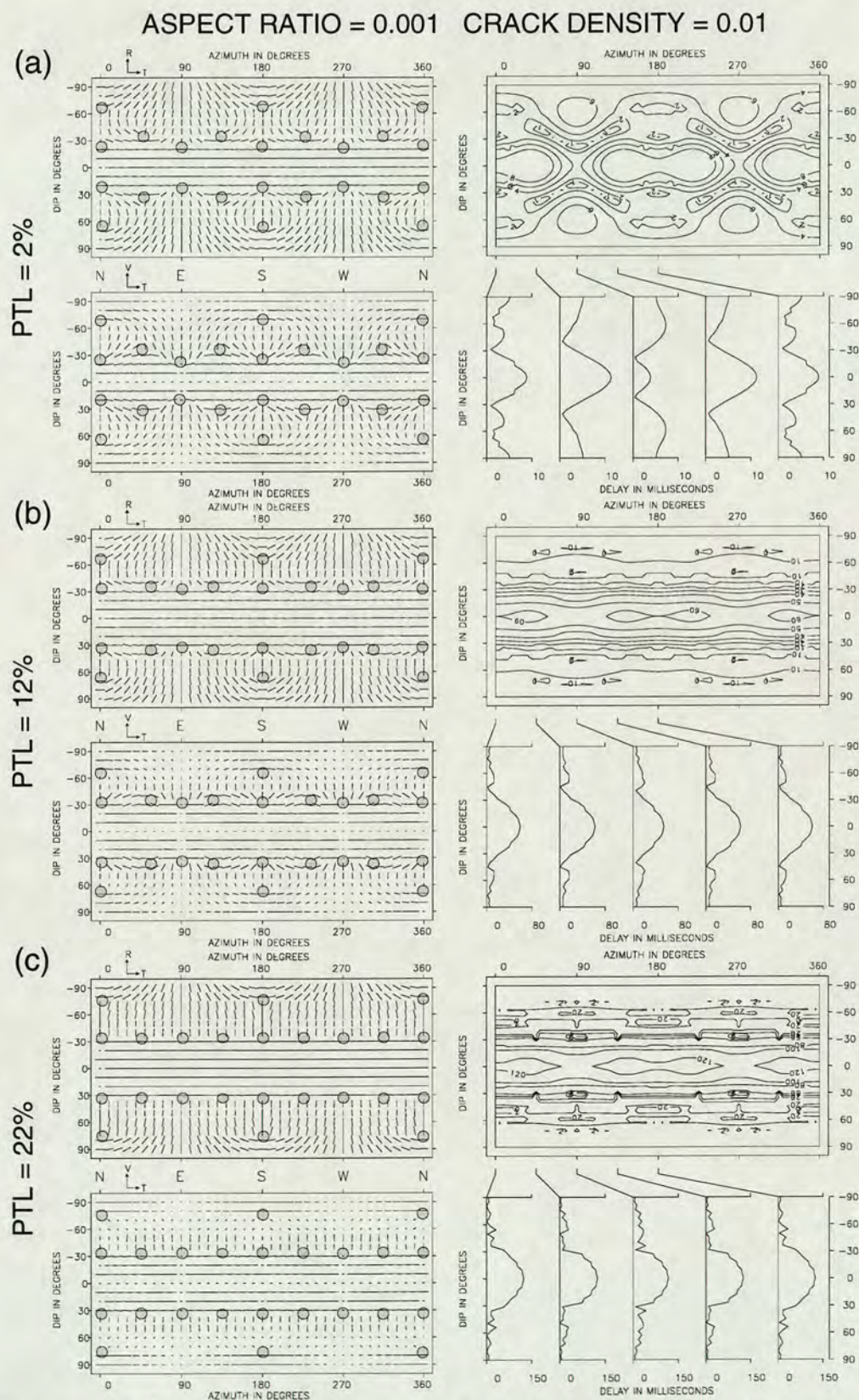
Figure 2.7. Plate Caree cylindrical projections of the polarizations and time delays of split shear-waves propagating along rays at group velocity through orthorhombic anisotropy, with an EDA crack distribution with crack density ε =0.01 and aspect ratio γ =0.001 in uncracked matrices with PTL anisotropy: (a) PTL1=2% differential shear-wave velocity anisotropy; (b) PTL2=12%; and (c) PTL3=22%. Format and notation as in Figure 2.4.

exists for vertical directions of propagation in pure PTL anisotropy, with hexagonal symmetry (Figure 2.4) has divided into two point singularities, which have moved towards the horizontal plane at azimuths of 0° and 180°, the 360° azimuth is a repeat of the 0° azimuth.

In contrast, Figure 2.7a (PTL1), where the PTL anisotropy is comparable to the crack anisotropy, the singularities which in Figure 2.7(c) are close to the directions of the line singularities of the pure PTL anisotropy (Figure 2.4), have now moved closer to the line singularity position in pure EDA (Figure 2.5). Again, the line singularity has been replaced by eight point singularities. The three dimensional distribution of the singularities corresponding to the projection shown in Figure 2.7(a) is approximately equivalent to the distribution shown in Figure 2.7(c), rotated by 90° about a horizontal E-W axis (azimuth 90°).

For the intermediate PTL anisotropy of 12%, PTL2 in Figure 2.7(b), the point singularities are dispersed in directions between the almost planar line singularities of PTL and EDA. The line singularities of these two types of anisotropy are perpendicular, because of the orthogonal symmetry axes. As the ratio of relative PTL and EDA changes, the point singularity, derived from the kiss singularity, moves towards the pull-apart remnant of the line singularity, and displaces a point singularity which moves towards the centre of the orthogonal pull-apart remnant line singularity.

The other effect of decreasing the amount of PTL, for a fixed crack anisotropy, is to decrease the time delays between the first and second split shear waves. For PTL3 (22%), the maximum delay is around 150ms, and for PTL2 (12%), the maximum delay is about half this value. While for PTL1 (2%), the maximum delay has decreased to about 10ms. Note that all time delays have been normalized over 1km.

2.6.2 Variations in EDA crack density.

Figures 2.7 and 2.8 show the same PTL anisotropies for two different crack densities, $\varepsilon=0.01$ and $\varepsilon= 0.05$, with a constant aspect ratio of $\gamma= 0.001$. It can be seen

ASPECT RATIO = 0.001   CRACK DENSITY = 0.05

Figure 2.8. Similar projections to Figure 2.7 for EDA crack distributions with crack density of ε =0.05 and aspect ratio of γ =0.001 in the same three PTL anisotropies. Format and notation as in Figure 2.4.
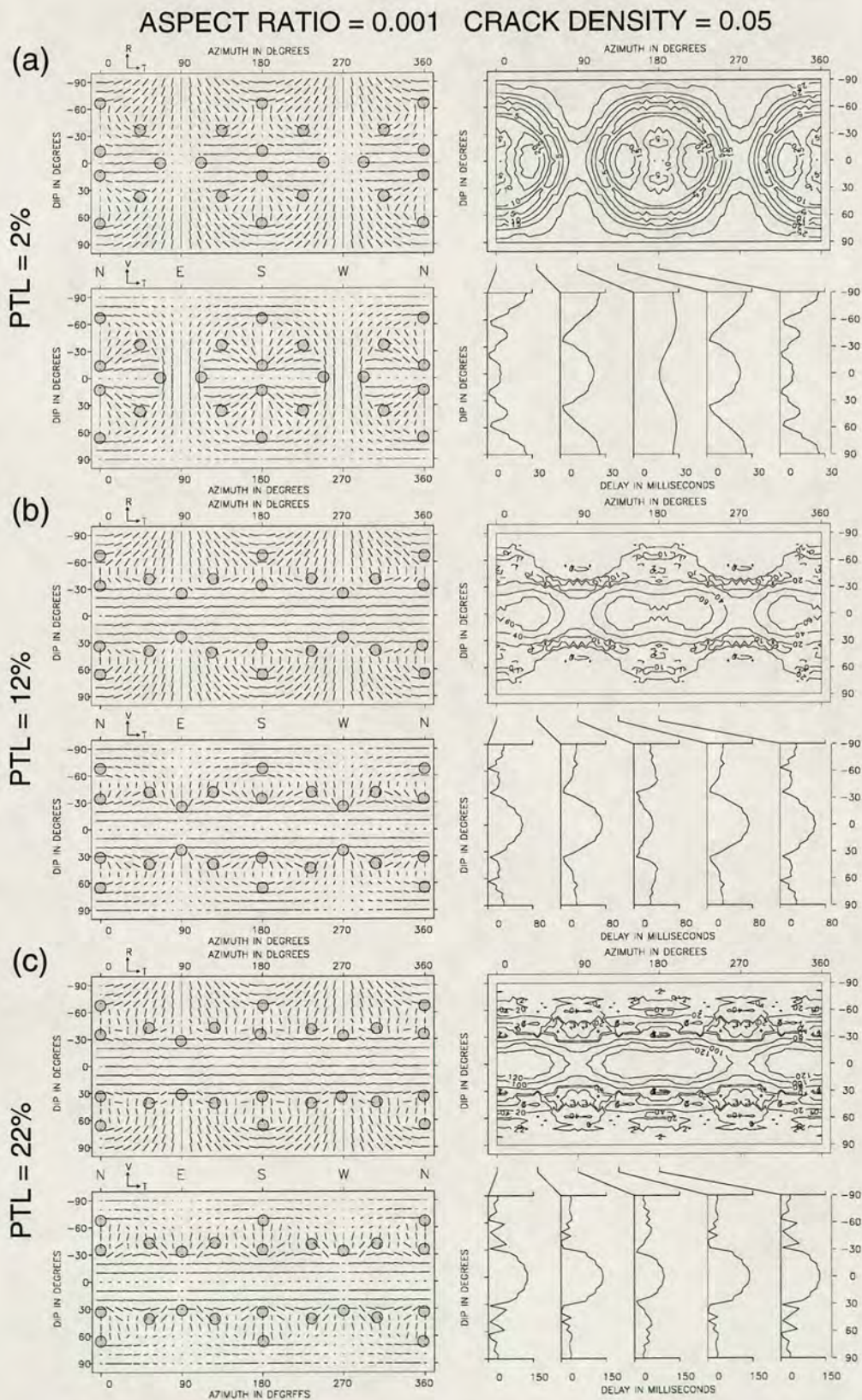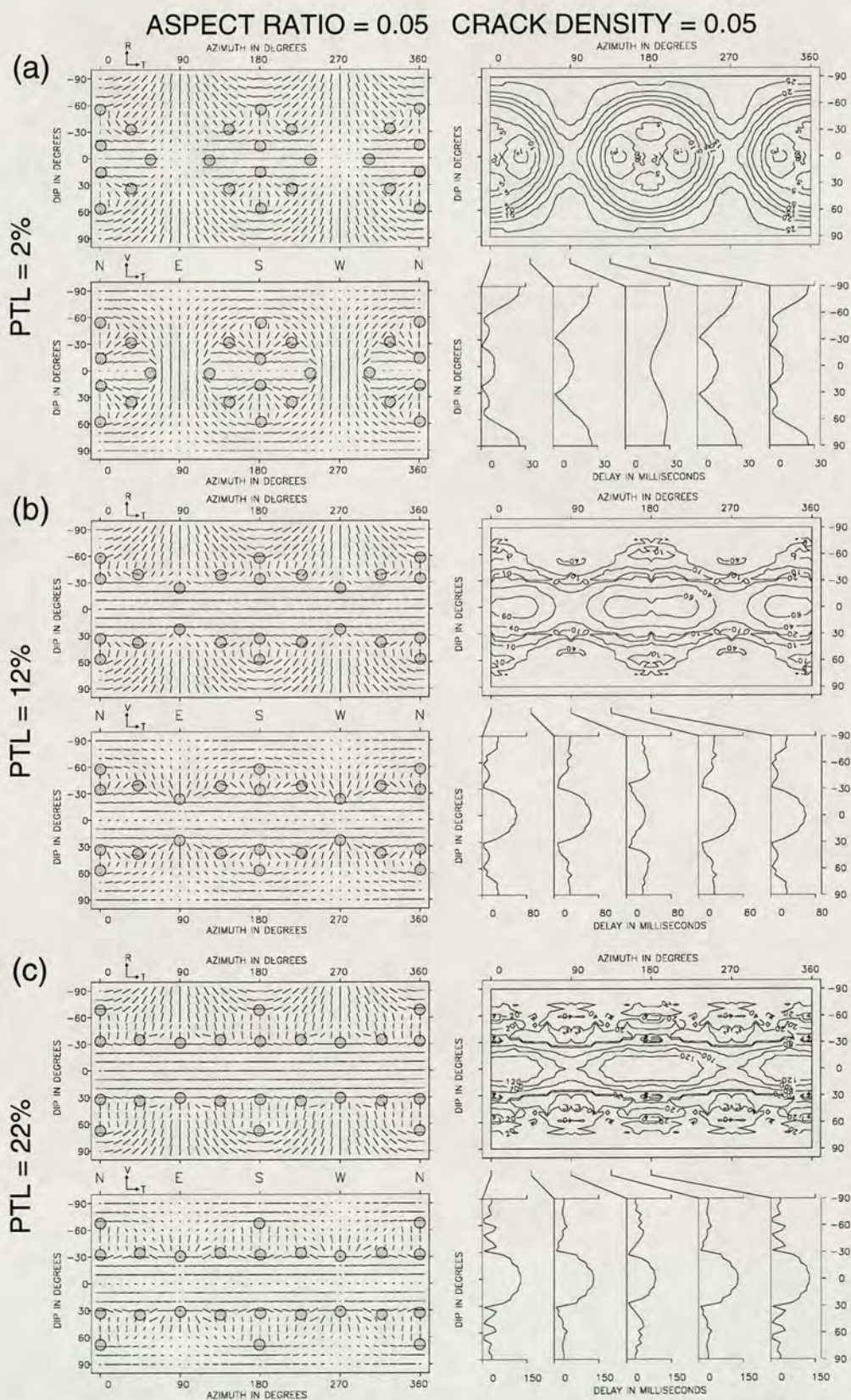
ASPECT RATIO = 0.05   CRACK DENSITY = 0.05

Figure 2.9. Similar projections to Figure 2.7 for EDA crack distributions with crack density $\varepsilon = 0.05$ and aspect ratio γ -0.05 in the same three PTL anisotropies. Format and notation as in Figure 2.4.

that increasing crack density, produces similar effects as reducing the percentage of PTL anisotropy, since the directions of the singularities are dependent on the ratio of EDA to PTL. The point singularities move away from directions centred around one symmetry axis to directions centred around the other symmetry axis. Examining Figures 2.7(a) and 2.8(a), we can see that as the crack anisotropy exceeds that due to PTL, this shift in symmetry axes becomes complete. With increasing crack density, the band of parallel polarizations parallel to the crack strike becomes much more pronounced. Delays increase with crack density increases in each of the three PTL anisotropies.

2.6.3 Variations in EDA crack aspect ratio.

The effect of varying aspect ratio can be seen by comparing Figures 2.8 and 2.9, which have the same PTL anisotropies, pervaded by cracks of the same crack density ($\varepsilon=0.05$), with two different aspect ratios, $\gamma = 0.001$ and $\gamma = 0.05$, respectively. Changing the crack aspect ratio makes comparatively little difference to the directions of the singularities for PTL anisotropies of 12% and 22%. However, the point singularities away from the equator, tend to cluster together with increasing aspect ratio at about 45° from the horizontal direction. This feature is most marked for the lowest PTL, 2%.

2.7 Discussion

Polarizations and time delays of split shear-waves have been calculated from the elastic constants of materials with varying combinations of two anisotropic symmetries. These parameters are displayed on Plate Carée projections for a full range of azimuths and incidence angles. Postma's equations were used to directly determine the elastic constants for a sequence of fine layers. Although other parameterization schemes could have been used, the intention here was to model the type of layered sequences found in sedimentary basins. In the Postma model the effective anisotropy

is a direct consequence of the layering, therefore this method is the most appropriate. Thomsen (1986) uses the parameters, δ, ε and γ to describe a transversely isotropic medium. The parameters are derived directly from the phase velocity equations for propagation in an anisotropic media. This method has the added advantage of validity for other types of TI media, but is less physically intuitive in this case.

Observations in cross-hole surveys are usually strictly confined to raypaths in a few vertical sections, within about $\pm45°$ of the horizontal. It is clear from examining any of Figures 7-9, that such raypaths in a limited number of vertical sections will probably not yield enough diagnostic information to identify PTL and EDA anisotropies and orientations. This is a different situation from polar projections of vertical motion, when a few nearly vertical rays of shear waves can lead to estimates of crack strike. Accurate resolution of the anisotropy is likely to require observations from a number of azimuths and dips to interpret the polarizations and delays in terms of rock structure. Plate Carée projections may be particularly useful for the interpretation of datasets where the angular coverage is large, as in the experiment described by Holmes et al. (1993), where the results have been plotted in cylindrical projection and interpreted using models similar to the ones used here.

The modelling demonstrates the probable sensitivity of the parameters of shear-wave splitting to variations in the type and relative amounts of anisotropy present in a rockmass. Polarizations of shear waves at the wide angles typical of cross-hole surveys through vertical or near vertical cracks are no longer parallel to the crack strike in media with orthorhombic symmetry. Small variations in crack properties are likely to be difficult to detect directly, as even large changes result in comparatively minor differences in shear-wave behaviour. This is particularly true for crack aspect ratio. This means that parameter space becomes non-unique as models with slightly different crack properties display remarkably similar behaviour. The implications for field data are that unimodal solutions may not exist for a particular set of observations. Instead, many possible solutions may exist for a particular set of results, which cannot be easily resolved, particularly where experimental errors are large.

However, the position of shear-wave singularities does appear to contain

important information on the types and relative amounts of anisotropy. The point singularities which occur in combinations of EDA and PTL anisotropy can have a significant effect on shear wave propagation. The shear wave polarizations change by 90° near point singularities and have anomalous time delays between the split shear-waves, and anomalous amplitudes. The directions of the point singularities for the models shown, are widely distributed over the range of azimuths and dips. In a cross-hole survey it is likely that the behaviour of the shear waves would show the effect of propagation near such point singularities. The accurate positioning of singularities from real data sets and comparisons with models are important as the directions (azimuths and angles of incidence) of singularities are critically dependent on the relationships of EDA and PTL anisotropy. These positions may provide a valuable directional correlation with the estimates of EDA and PTL anisotropy, which are usually derived from velocity information. This may enable complex field measurements of polarizations and delays to be interpreted in terms of a uniform anisotropic structure, rather than mistaking such features for geological discontinuities.

CHAPTER 3: EAST FITTS CROSS-HOLE SEISMIC MONITORING:
MODELLING THE WAVEFIELD IN ANISOTROPIC MEDIA.

3.1 Introduction

Transmitted and reflected components of the cross-hole wavefield from a fractured limestone reservoir, in mid-continental U.S., are shown to display the characteristic features of wave propagation in anisotropic media. Shear wave transmission through the reservoir results in shear-wave splitting, while reflected shear waves show anomalous transverse polarizations, attributed to anisotropic rock properties. The generation of synthetic seismograms for an isotropic model shows that propagation in homogeneous isotropic layered media cannot readily explain the observed wavefield properties.

The anisotropic parameters, $qS1$ polarization and time delay between $qS1$ and $qS2$ arrivals are measured numerically for three azimuths of the multi-azimuthal, cross-hole survey. These measurements are then compared with the shear-wave splitting parameters for different anisotropic models. Model parameters are calculated for direct shear waves by ray tracing through the layered anisotropic model to find the polarization and time delay for a particular incidence angle.Model parameters are calculated for reflected shear waves by generating synthetic seismograms for a particular choice of model parameters, then measuring polarization and time delay in the same way as for the observations.

The best-fit model for crack orientation and crack density is obtained by defining a merit function to give the misfit for a particular model. Synthetic seismograms are generated for the best-fit anisotropic model parameters. The best-fit crack orientation is interpreted in terms of a consistent reservoir fracture direction in the area of the survey and compared with observed stress directions. Precise delineation of the reservoir pay zone is estimated from well log and core information.

3.2 Reservoir Geology

The East Fitts field is situated in the Franks Graben area of the Arkoma basin, South Oklahoma (Figure 3.1). The Arkoma basin extends 400km west from the gulf coastal plain to the Arbuckle mountains in central Oklahoma, the width varying between 32-80km. The basin is bounded to the north by the Ozark Uplift and the North-East Oklahoma Platform, and to the south by the Ouachita fold belt.

3.2.1 Regional structure and depositional environment

From the early Cambrian to the early Pennsylvanian, the basin was part of a broad stable shelf along a passive continental margin, bounded by the Ouachita trough to the south (Sutherland 1988). During this time, patterns of deposition varied between carbonate environments and terrigenous clastics. Figure 3.2 shows a typical geologic section for the East Fitts area of the Arkoma basin. In the early Cambrian to the late Mississippian, a thick sequence of shallow water carbonates, including the McLish, Bromide, Viola and Hunton formations, was deposited on the shelf. These formations were alternate with deeper water black shales and cherts, such as the Woodford and Sylvan formations.

Continental convergence began in the middle Mississippian, resulting in the creation of a foreland basin with down-warping of the southern margin of the shelf along the Ouachita fold belt during the middle Atokan. Closure and rapid deposition resulted in the closing and filling of this foreland basin by the end of the middle Atokan. Deformation of the Arkoma basin culminated in the late Pennsylvanian with the thrusting of the Ouachita orogeny. East-west trending box shaped synclines and narrow anticlines are the dominant surface structures in the Arkoma basin. In the western part of the basin, thrust faults are exposed in the crests of many anticlines, these also strike east-west.

The structure of the Fitts field is a faulted anticline (Hyatt 1936). Figure 3.3 shows how accumulation to the south is controlled by the Fitts fault, which runs
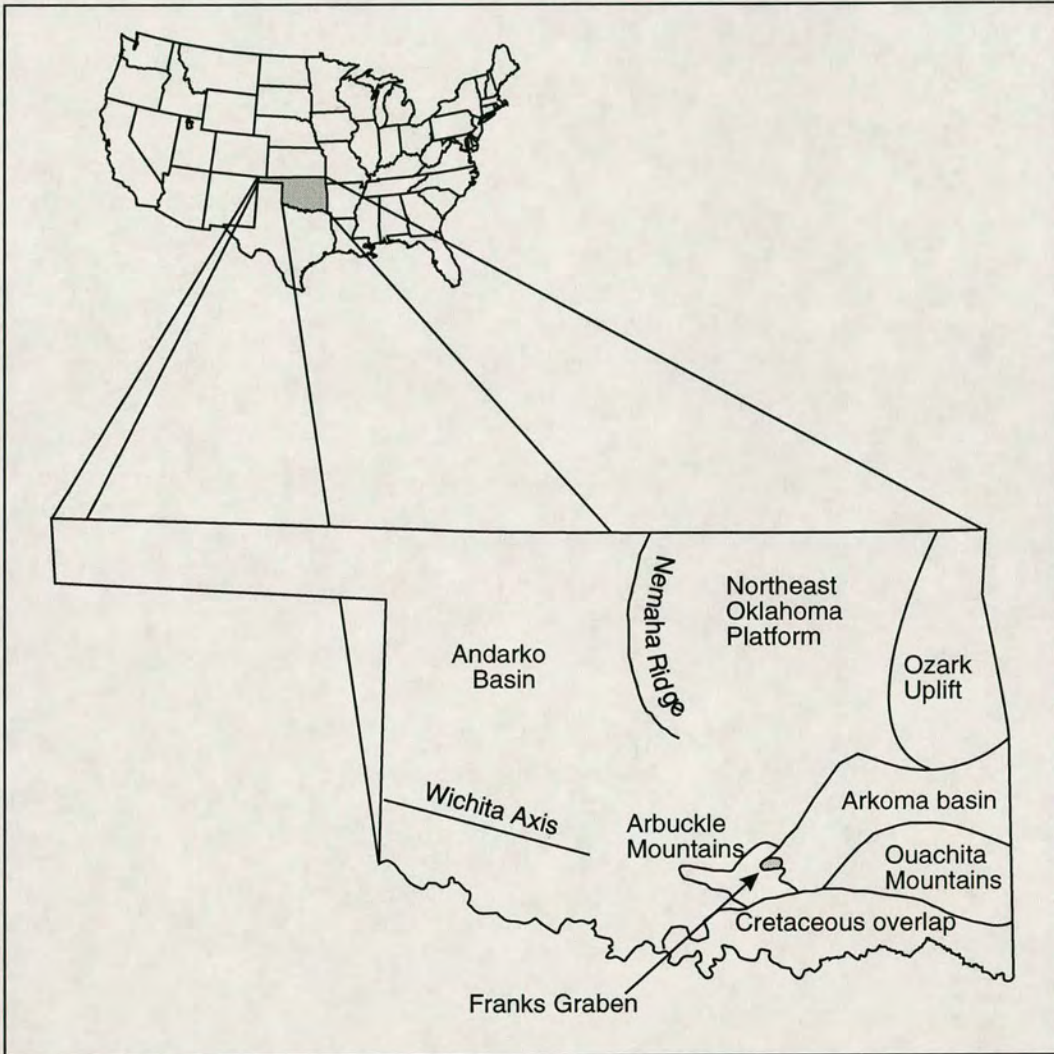
Figure 3.1. Regional tectonic features of Oklahoma State, U.S.A. (after Arbenz 1956). The Fitts field is situated in Franks Graben (marked by arrow), at the Western end of the Arkoma basin.
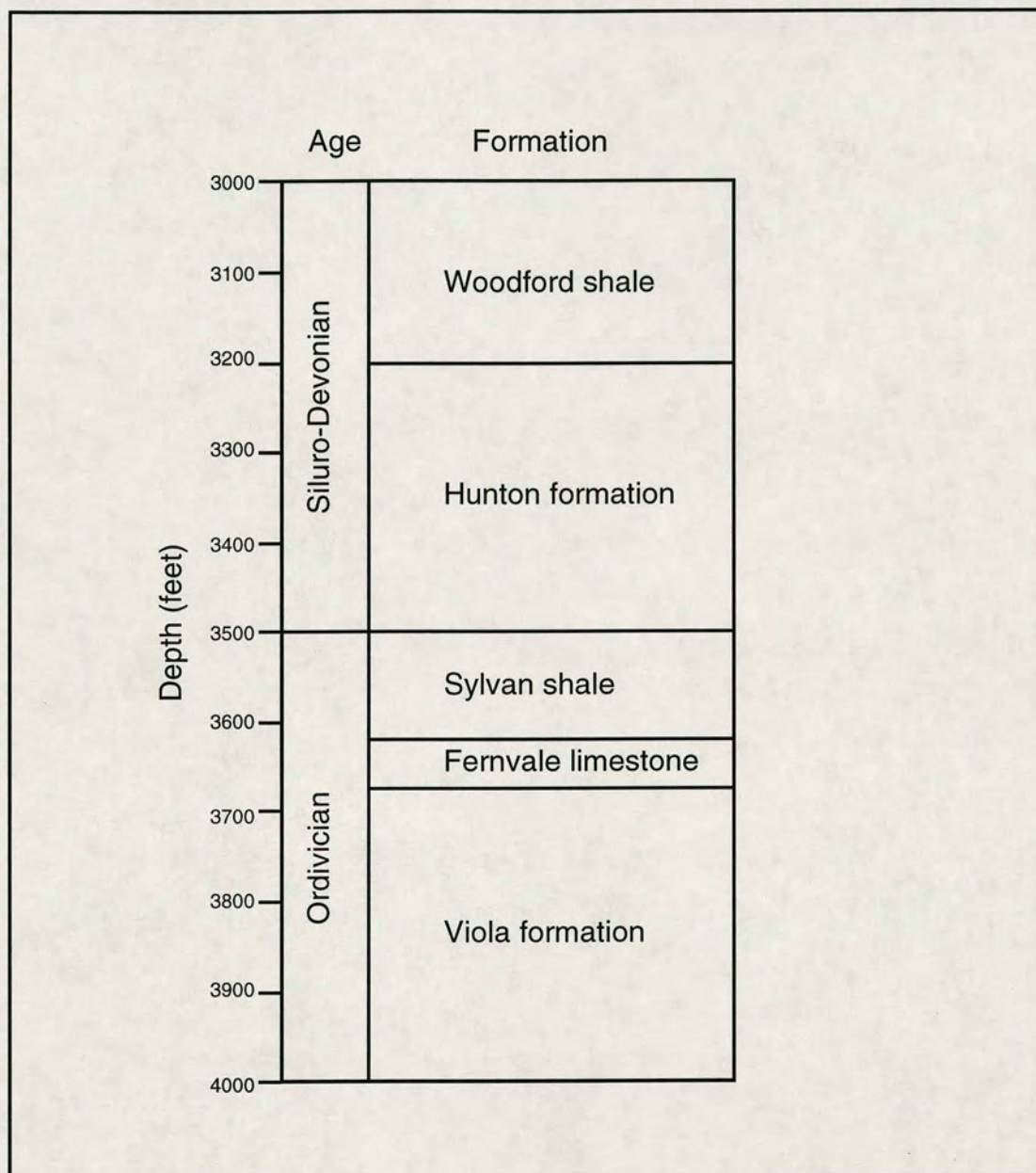
Figure 3.2. A typical geologic section of the East Fitts unit, showing the principal litho-stratigraphic boundaries (after Mairs 1966).
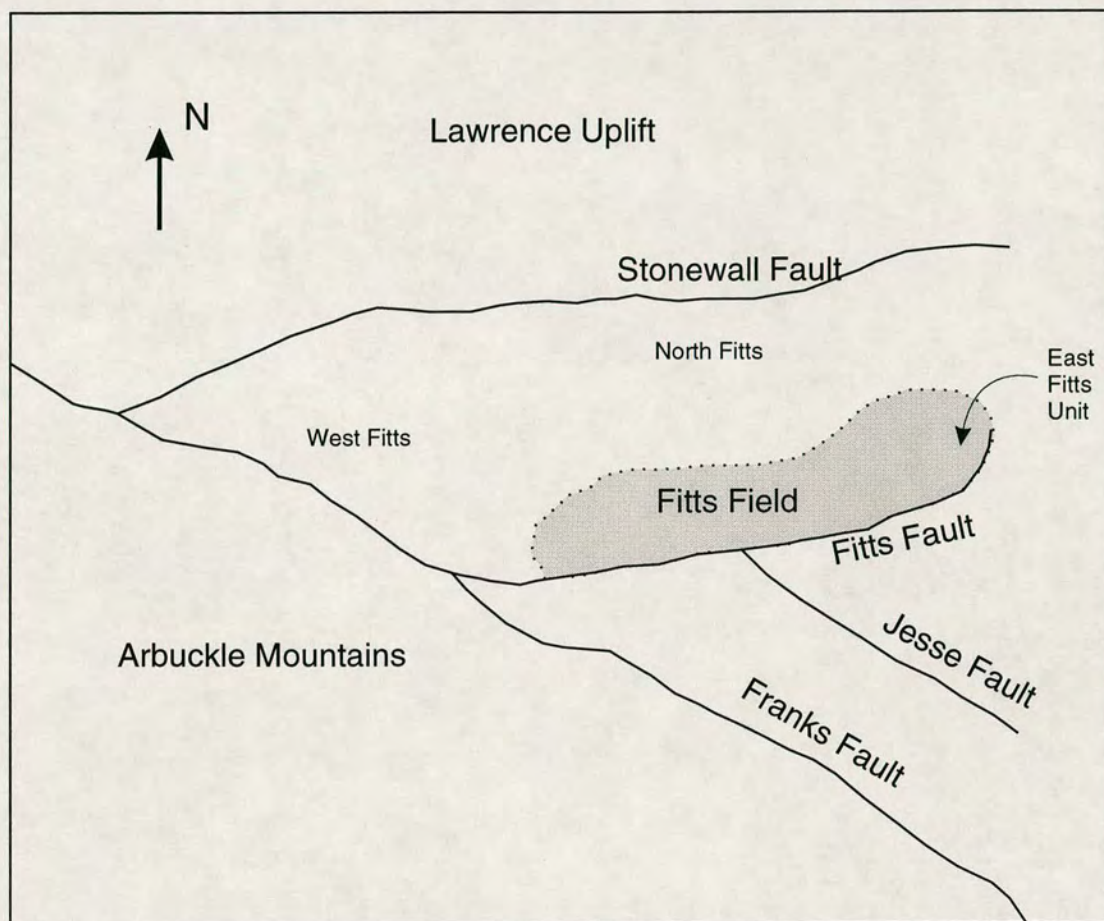
Figure 3.3. Major structural features around the Fitts Field. The field is limited to the South by the Fitts fault. Sediments dip southwards into this feature forming the hydrocarbon trap (after Hyatt 1936).

approximately east-west. Associated normal faults running perpendicular to the major fault zone can be seen in a schematic east-west cross-section in Figure 3.4. These faulted blocks descend to the east. The field is approximately 5 miles long, with a maximum width of 1.5 miles, and is located in the south-east part of Pontotoc county. Oil production dates back to the thirties and is from seven different horizons ranging in age from Ordovician to Pennsylvanian. The two principal reservoir zones covered by the cross-hole seismic are also shown in Figure 3.4.

3.2.2 Local reservoir geology

The cross-hole seismic focuses on the Viola and Hunton reservoirs between depths of 3000-4000 feet. The Viola limestone is a massive limestone with an average thickness of 300 feet and is primarily a finely crystalline or granular limestone. This is further divisible into four sub-zones on the basis of physical characteristics (Mairs 1966). Viola sub-zone 3 is the most productive zone and is characterized by thick massive beds with planar and irregular bedding planes. Figure 3.5 shows a depth contour map for the top of Viola sub-zone 3, over the East Fitts unit. The formation can be seen to dip gently from South to North with a dip of approximately 6° from horizontal. The wells marked show the locations of available logs and cores, and of the cross-hole seismic acquisition wells. Core analysis of the Viola gives an average porosity of 12.2% and permeability of 3.9md. The presence of small vertical fractures in Viola sub-zone 3 has also been noted from core analysis of well 9-41(M.Mathisen, Mobil Research and Development Corp.), but dimensions are not recorded. Figure 3.6 shows density-porosity and neutron porosity logs over the Viola formation from well 9-44. The density porosity log measures the back-scattering of gamma rays from the formation. This is dependent on the density of electrons, which is roughly proportional to the bulk density. Neutron porosity logs also measure the back-scattered gamma radiation from the emission of neutrons. The capture of neutrons by the surrounding atomic nuclei, results in the emission of a gamma ray. Viola sub-zone 3 is indicated by the shaded area. The difference between the neutron

47
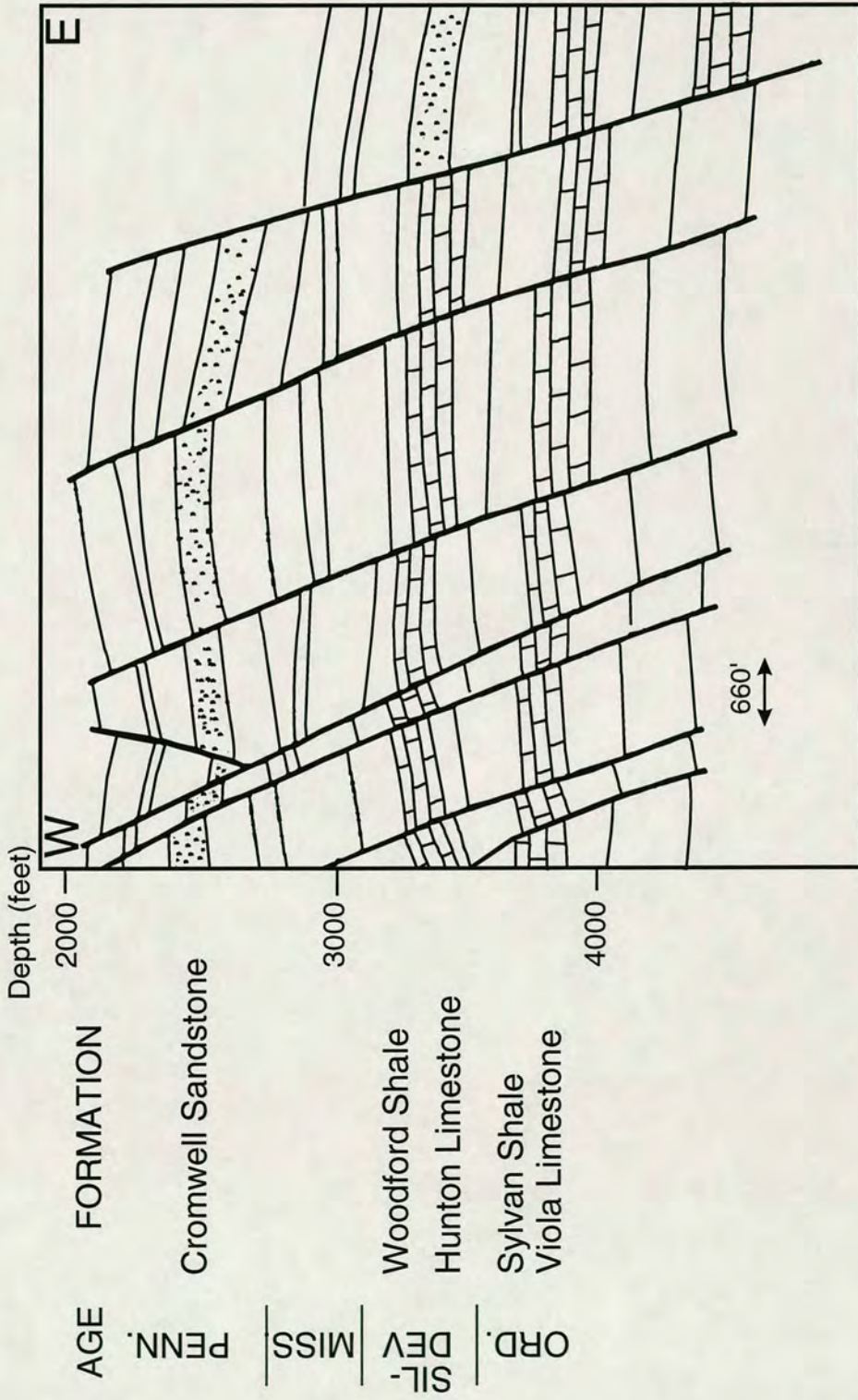
Figure 3.4. Schematic cross-section from west-east across the Fitts Field. The East Fitts Unit is situated approximately in the centre. The structure consists of a series of normal faulted blocks descending to the east. Some of the principal stratigraphic units are shown on the left (personal communication M. Mathison, Mobil Research and Development Corporation).
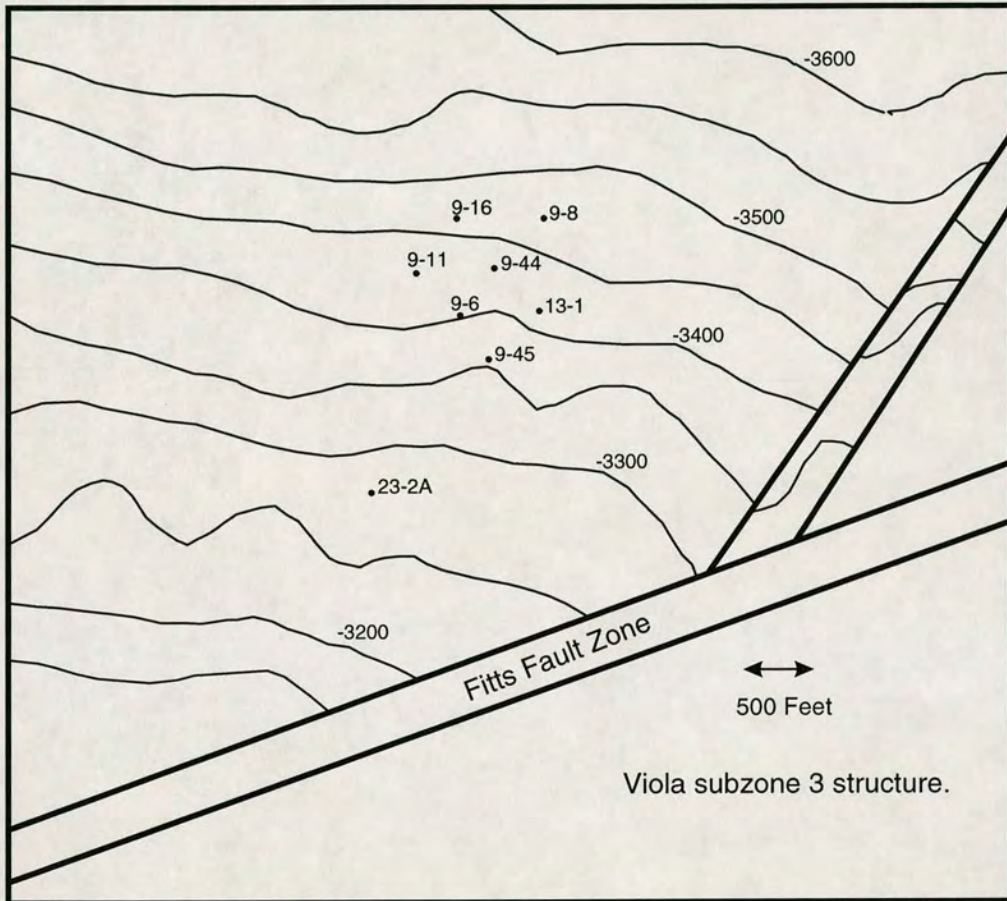
Figure 3.5. Contour depth map of Viola Subzone 3 of the East Fitts Unit of Fitts field. Depths are given in feet from sea level, which is equivalent to KB-700'. The Viola formation dips gently from North to South at about 6 degrees from horizontal (personal communication M. Mathison, Mobil Research and Development Corporation).
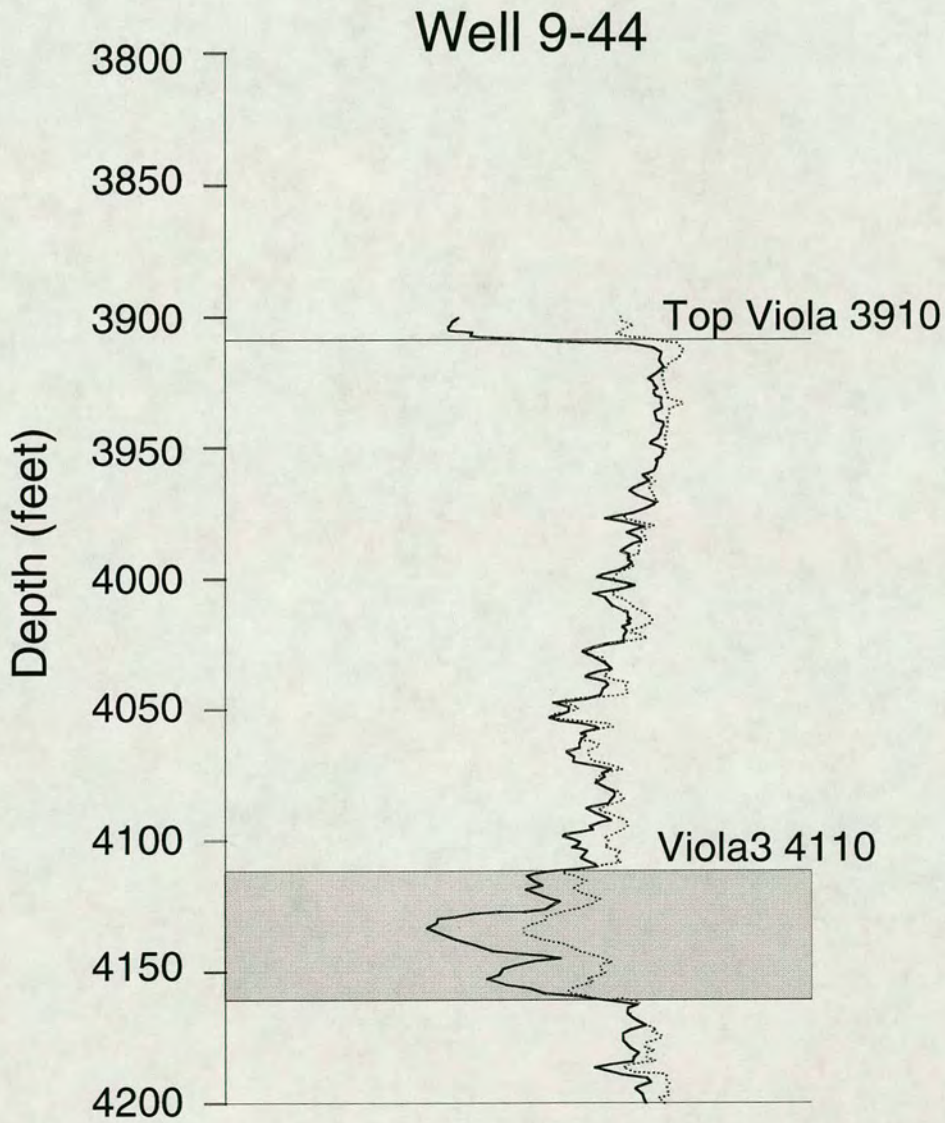
Figure 3.6. Neutron porosity (solid line) and density porosity (dashed line) logs over the Viola formation from well 9-44. The Viola3 reservoir zone is marked by shaded area. The difference between the neutron and density porosity logs in this region is indicative of the presence of pore fluids.

and density-porosity logs is indicative of the presence of pore fluids, as neutrons are more readily absorbed.

Overlying the Viola formation is the Sylvan shale. This is a finely textured shale of uniform character and an average thickness of 110 feet.

The Hunton limestone is divided into three members: the lower Chimneyhill member, with an average thickness of 40 feet; the middle, or Haragan member, with an average thickness of 200 feet; and the upper or Bois d'Arc member, with an average thickness of 60 feet. Oil production is obtained from both the Chimneyhill (oolitic limestones) and the Bois d'Arc (crystalline limestone).

The Woodford formation lies unconformably on the Hunton limestones and has an average thickness of 200 feet. The Woodford is essentially a dark brown-to-black impure shale, with occasional inter-beds of black chert.

Figure 3.7 shows a sonic log in the area of interest, from well 23-2a, slightly to the south of the cross-hole seismic. The three known reservoir zones are marked by the shaded areas. Large velocity contrasts exist at the Sylvan shale interfaces and also at the Viola sub-zone 3. Implications for seismic wave propagation are that strong reflections may be observed, along with significant ray bending.

3.2.3 Regional stress measurements

Oklahoma lies within the tectonically stable mid-continent stress province. Throughout this province a uniform NE-SW stress field exists, largely defined by examination of hydraulic fractures and earthquake focal mechanisms (Zoback and Zoback 1980). Dart (1987) measures horizontal crustal stresses in the Arkoma basin using well-bore breakouts. These are elongations in the cross-sectional shape of the well-bore, caused by the in-situ stress field. The azimuth of the long dimension of the hole is parallel to the direction of least horizontal stress. Regional maximum compressive stress directions (S_H max) in the Arkoma basin are found to have consistent north-east to east orientations. This agrees well with S_H max orientations of N65°E based on a hydrofracture survey.
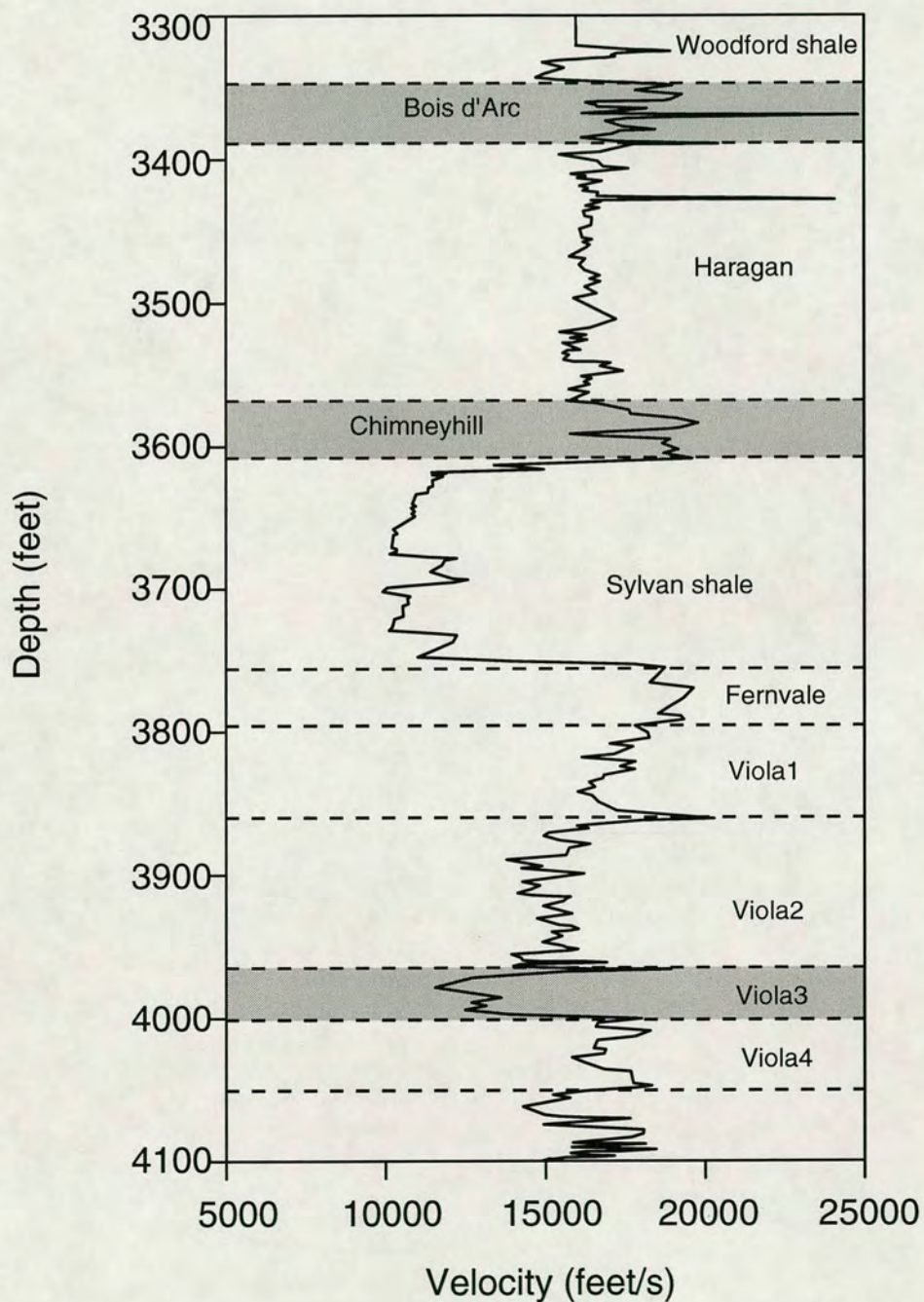
Figure 3.7. Sonic log from well 23-2A. The three subdivisions in the Hunton formation and the four subdivisions in the Viola formation are indicated. Hydrocarbon producing zones are marked by the shaded areas.

3.3 Acquisition geometry

Cross-hole data were recorded in 5 wells positioned at varying azimuths around a central source well, 9-44. Figure 3.8(a) shows a plan view of the spatial location of the well-heads as well as sources and geophone positions. The airgun source was positioned at depths 3100 feet, 3575 feet and 4150 feet. Forty geophone levels were recorded, between 2900 and 4200 feet, with an average spacing of 25 feet.

Gyrodata measurements every 50 feet allow calculation of the well deviations and precise location of source and geophone positions. The cross-sectional view in Figure 3.8(b), shows the maximum deviation of sources in well 9-44 and geophones in well 9-16 from the 9-44 well-head position. The maximum deviation is defined as the greatest distance from the well-head in the horizontal plane. All wells deviate from vertical by less than 10°. In general, the dip of the deviated wells is in the north-south plane, except for well 13-01, and the structural dip is to the north. Therefore the well axes remain approximately orthogonal to interfaces. In view of this, I conclude that a plane layer approximation should provide suitable accuracy for modelling the cross-hole wavefield. Oil production was ongoing in each of the wells at the time of acquisition.

An airgun is used to generate both *P*- and *S*-wave energy at each source position. The sources hang freely in the fluid column. This results in distinctive radiation patterns for both *P*- and *S*-waves.

3.4 Modelling the downhole source radiation pattern

Lee and Balch (1982) derive expressions for the far field displacement of an airgun source in an infinitely long fluid-filled borehole, embedded in an infinite elastic medium. Displacements for *P*- and *S*-waves are given in terms of a cylindrical coordinate system as
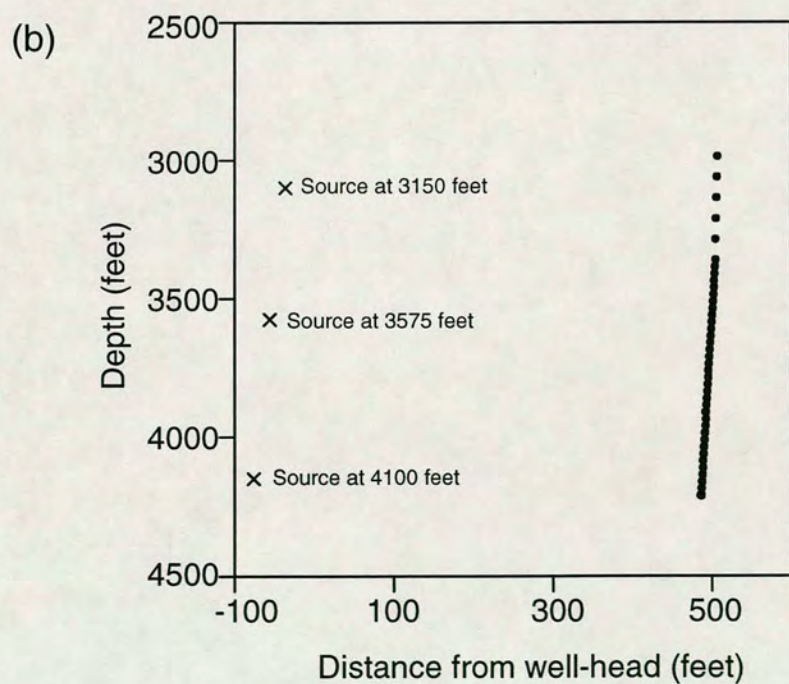
(a)

(b)
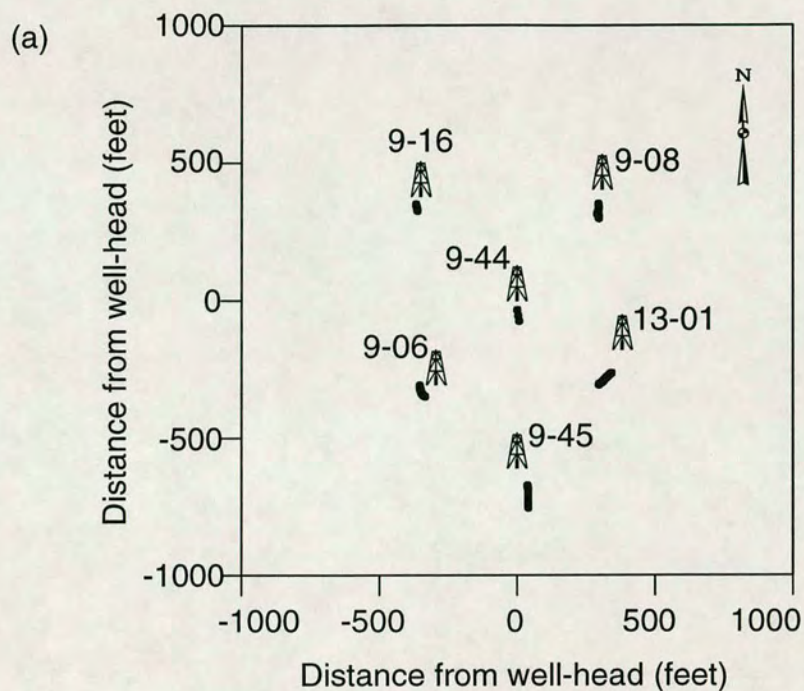
Figure 3.8. Spatial location of sources and geophones for Fitts cross-hole experiment.Plan view (a), maximum deviation section (b). All distances are relative to the well-head position the source well, 9-44.

$$U_R = \frac{EF_p(1 - 2\frac{\beta_2^2}{\alpha_2^2}\cos^2\varphi)}{\alpha_2 R} \tag{3.1}$$

and

$$U_\varphi = \frac{2EF_s\sin\varphi\cos\varphi}{\beta_2 R} \tag{3.2}$$

Where R is the distance from source to receiver, ϕ is the angle of propagation from vertical, α_2 and β_2 are the P- and S-wave velocities in the surrounding elastic solid. E is a scalar term which determines the amplitude of the displacement. F_p and F_s describe the effect of the borehole fluid on the radiation pattern. For an empty borehole, the radiation pattern is controlled only by the P- and S-wave velocities in the surrounding solid and $F_p=F_s=1$. When the borehole contains a fluid,

$$F_p = \frac{1}{\frac{\rho_1}{\rho_2} + \frac{\beta_2^2}{\alpha_1^2} + \frac{\beta_2^2}{\alpha_2^2}\cos^2\varphi} \tag{3.3}$$

and

$$F_s = \frac{1}{\frac{\rho_1}{\rho_2} + \frac{\beta_2^2}{\alpha_1^2} - \cos^2\phi} \tag{3.4}$$

where ρ is density.

I apply these expressions to calculate the radiation pattern for a volume displacement source acting on the axis of a fluid filled borehole. Compressional velocity in the fluid $\alpha_1=1.6$ km/s, and density $\rho_1=1.1$ g/cm^3. The velocities in the surrounding solid are $\alpha_2=3.5$ km/s, $\beta_2=2.021$ km/s and $\rho_2=2.2$ g/cm^3.

The resulting source radiation in Figure 3.9 shows that the maximum amplitude of the P-wave is perpendicular to the borehole axis, while maximum amplitudes of

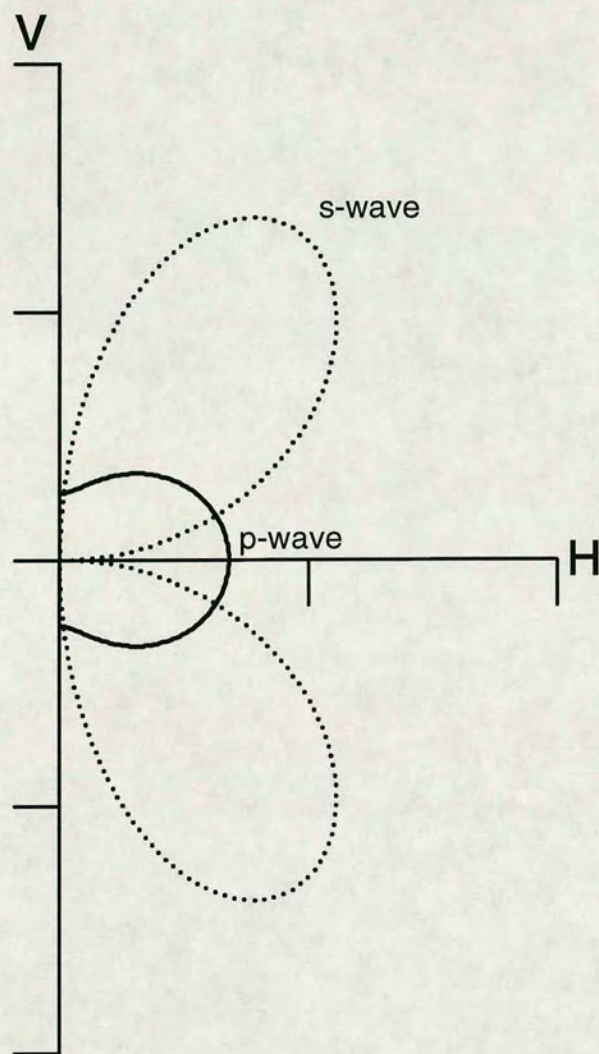Figure 3.9. Radiation pattern of a point volume displacement source acting on the axis of a fluid-filled borehole, in an homogeneous elastic medium with $\rho=2.2$, $\alpha=3.5$km/s and $\beta=2.021$km/s. Fluid parameters are $\rho=1.1$ and $\alpha=1.6$km/s.

SV-waves are at 56° from horizontal. The airgun sources used in the cross-hole experiment, hang freely within a fluid column and are expected to display a similar source radiation pattern.

The modelling package, ANISEIS, which I use to generate synthetic seismograms has two important limitations. Firstly, at the time of writing, the package does not support the above borehole radiation pattern. However, I have discussed this matter with D. Taylor, author of the package, and hopefully this limitation will soon be rectified. As an alternative, I apply a point source which generates a unit horizontal force in the *X*-direction. Such a point force is not a dipole source and is only strictly valid when positioned at a free surface, not embedded at depth. The resultant radiation pattern is similar to that of an airgun in a borehole, for *P*-waves but differences arise in the *S*-wave radiation pattern.

To quantify this source radiation pattern, I generate synthetic seismograms for an elastic halfspace, whose parameters are the same as those of the elastic material used above. Geophones are positioned on a circular arc about the point source. Amplitudes are measured for windowed *P*- and *S*-wave arrivals at each radial direction from the source position. The variation of normalized amplitudes with direction of propagation is shown in Figure 3.10. We can see that the *P*-wave radiation pattern is similar to the theoretical radiation pattern for a borehole source, with *P*-wave amplitudes at a maximum in the horizontal direction. However, *S*-wave amplitudes are greatest for vertical propagation. Consequently, amplitude variation between modelled and observed seismograms will arise due to source effects as well as propagation effects along the ray-path. Differences will naturally be greatest for near-vertical propagation.

The second limitation is that ANISEIS does not support the placing of a point source within an anisotropic layer. Where it is required that the source be in an anisotropic layer, a very thin isotropic layer is placed around the source. The properties of this layer are chosen to minimize high incidence reflections and inward reflections are suppressed.
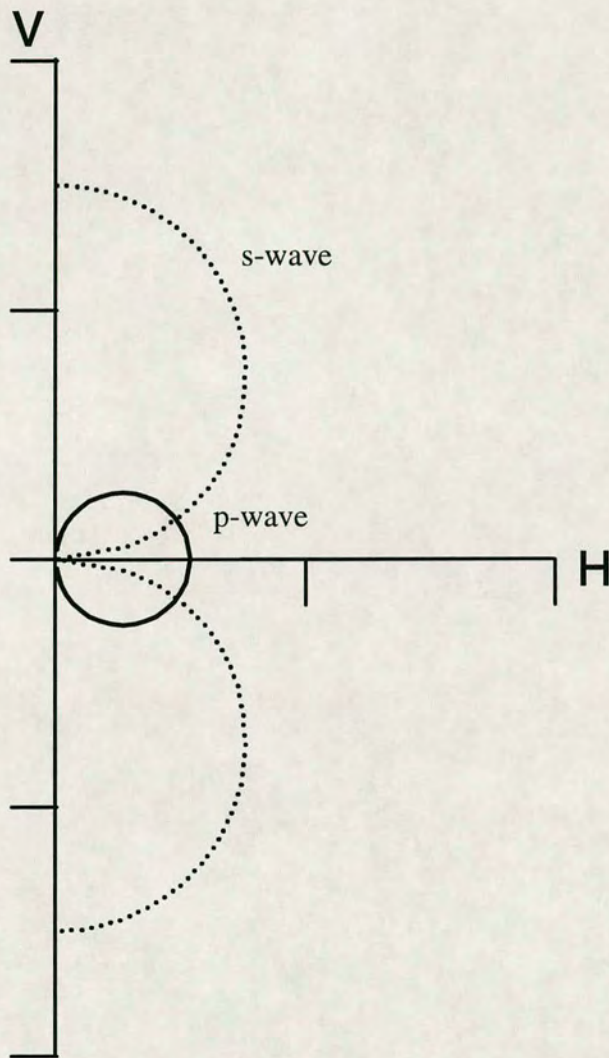
Figure 3.10. Source radiation pattern calculated for the horizontal point force in theANISEIS modelling package. The source is embedded in an elastic medium with $\rho=2.2$ g/cm^3, $\alpha=3.5$ km/s and $\beta=2.021$ km/s.

3.5 The cross-hole wavefield

Three-component common source gathers at three of the five azimuthal receiver wells are displayed in Figures 3.11, 3.12 and 3.13 for source depths of 3100 feet, 3575 feet and 4150 feet, respectively. Data from each well are indicated by: (a) 13-01; (b) 9-45; and (c) 9-16. The horizontal geophone components from wells 9-6 and 9-8 were badly contaminated by noise, to such an extent that no signal could be recovered on these components. As a result, data from these two wells had to be disregarded. Scaling is relative between individual geophone components but not between geophone depths. There is also relative scaling between the three azimuths shown in (a), (b) and (c). Arrivals on individual source gathers are consistent for each of the three azimuths. Figure 3.14 shows my interpretation of arrival types seen at well 9-16. Direct P- and S-waves are clearly observable from both the shallow and deep sources. Considerable reflected energy is also apparent from the intermediate source level. In addition, energy is distributed across all three geophone components.

3.5.1 Data processing

Data are rotated in the horizontal plane to align the geophone into in-line and cross-line directions using the polarization of initial P-wave motion. Polarization angles are calculated by eigen-analysis of the covariance matrix, constructed for a 10ms window about the initial P-wave arrival. As the geophone remains in the same position for each shot point, rotation angles for each source gather should be equivalent. I use a weighted average of the three source angles as the actual rotation angle. Higher weightings are assigned to horizontal raypaths, which contain most P-wave energy.

A zero phase band pass filter is designed to remove high frequency borehole tube waves from the data. Filter parameters are optimised by visual analysis of seismograms and amplitude spectra. The pass-band lies between 50-150Hz. Filter slopes are 12 dB/oct and 36 dB/oct for lower and upper frequency limits, respectively.

Figure 3.11. Multicomponent common sources gathers for a source depth of 3100 feet, from: (a) well 13-01; (b) well 9-45; (c) well 9-16.

Figure 3.12. Multicomponent common sources gathers for a source depth of 3575 feet, from: (a) well 13–01; (b) well 9-45; (c) well 9-16.
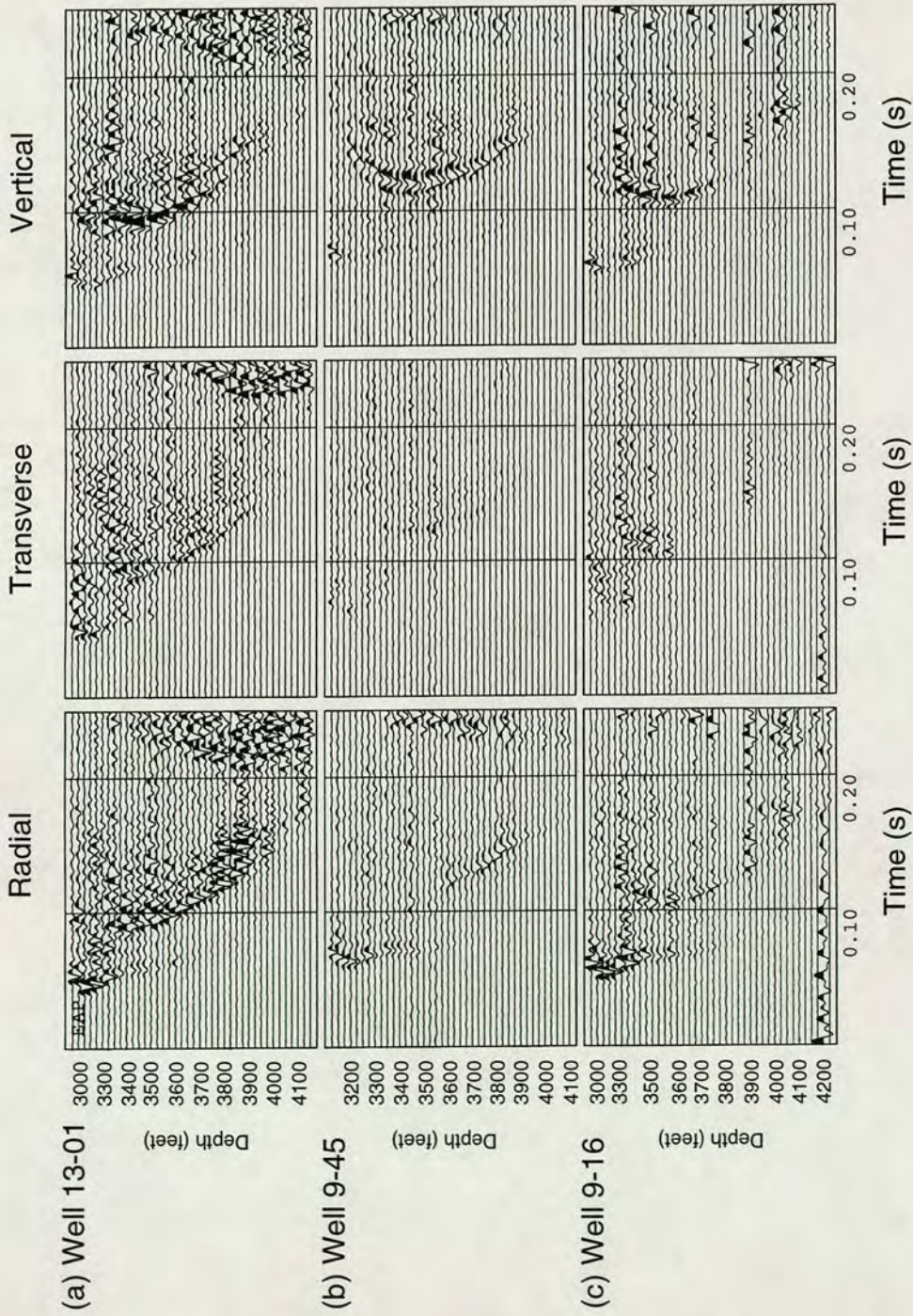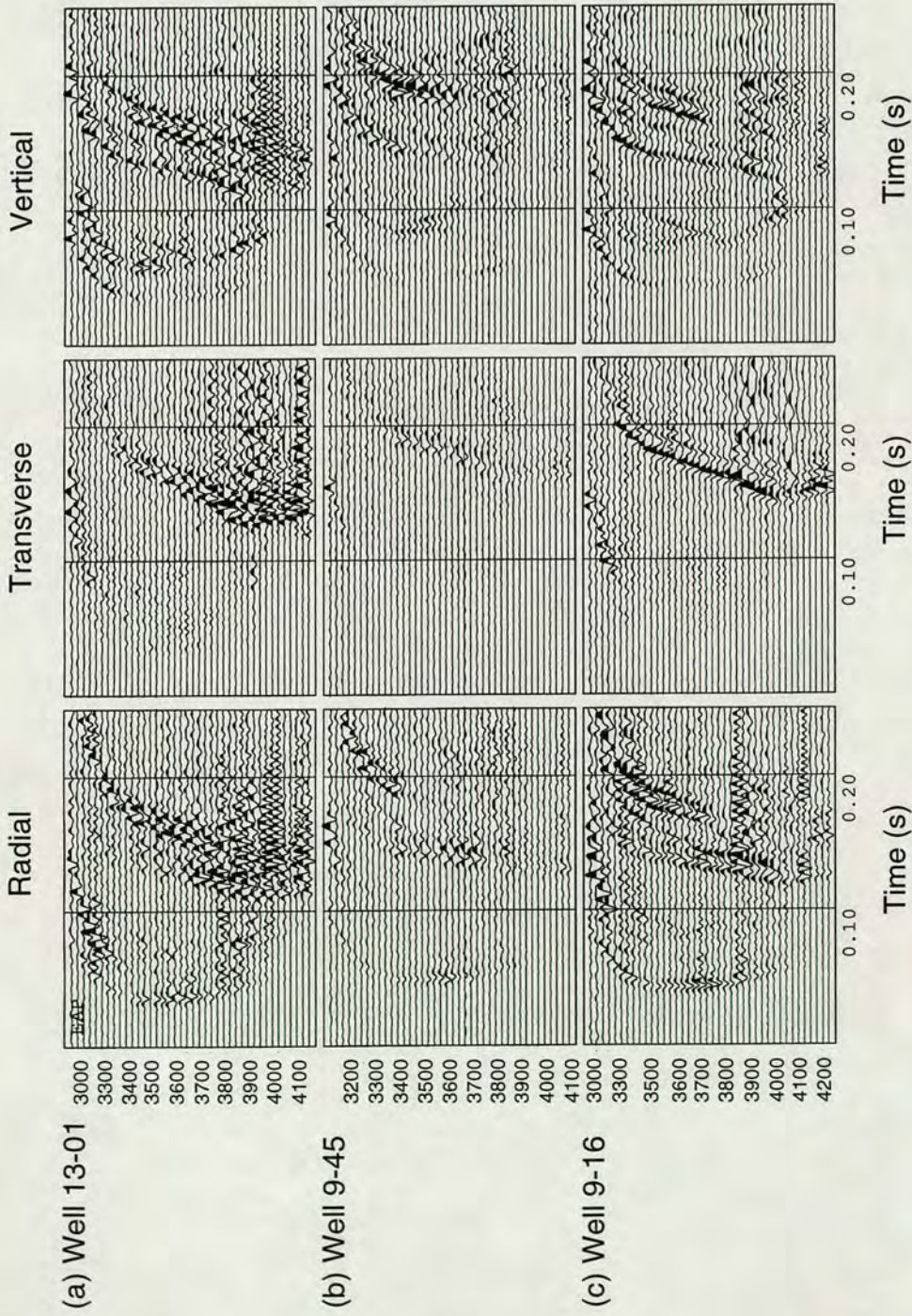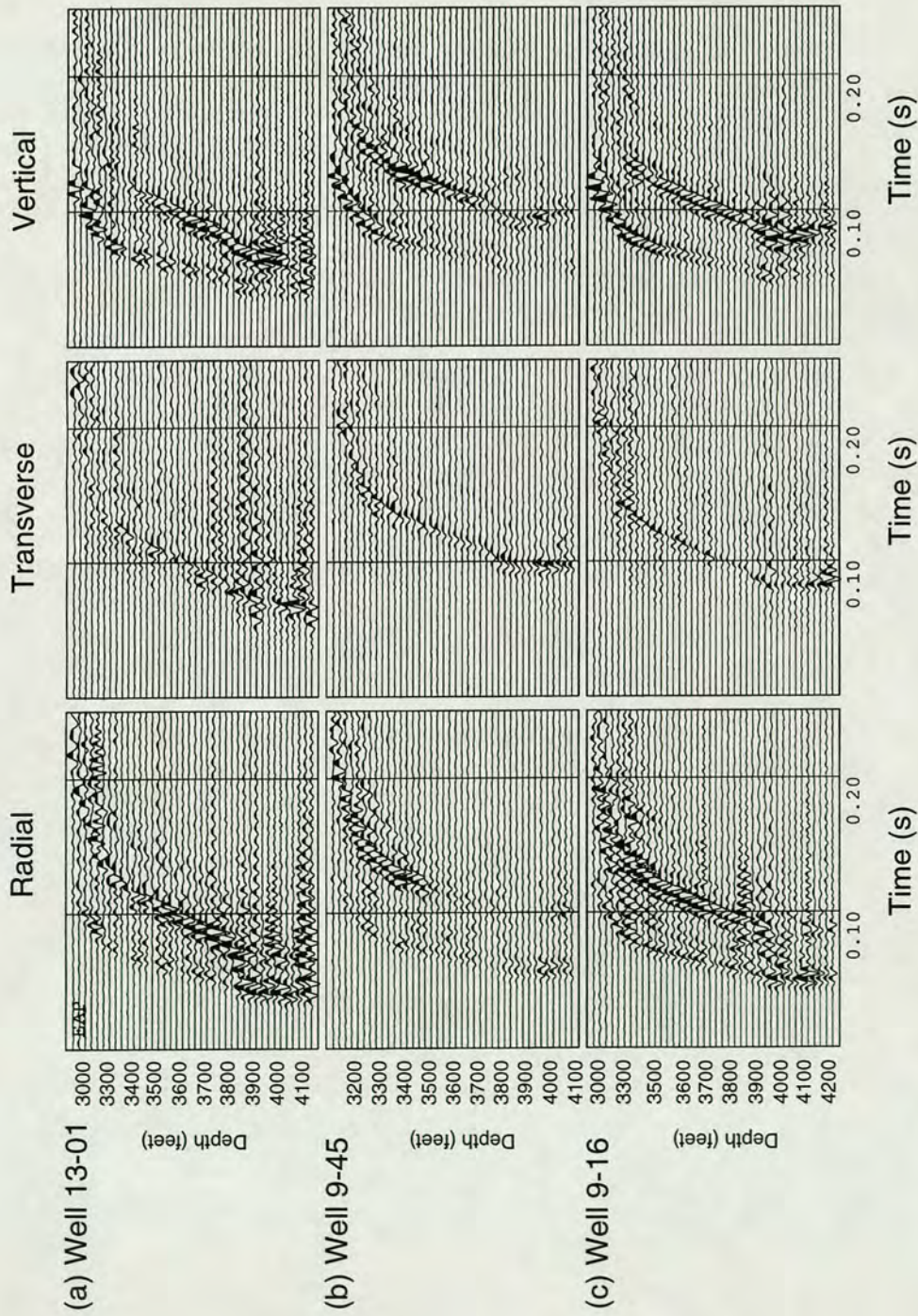
61

Figure 3.13. Multicomponent common sources gathers for a source depth of 4150 feet, from: (a) well 13-01; (b) well 9-45; (c) well 9-16.
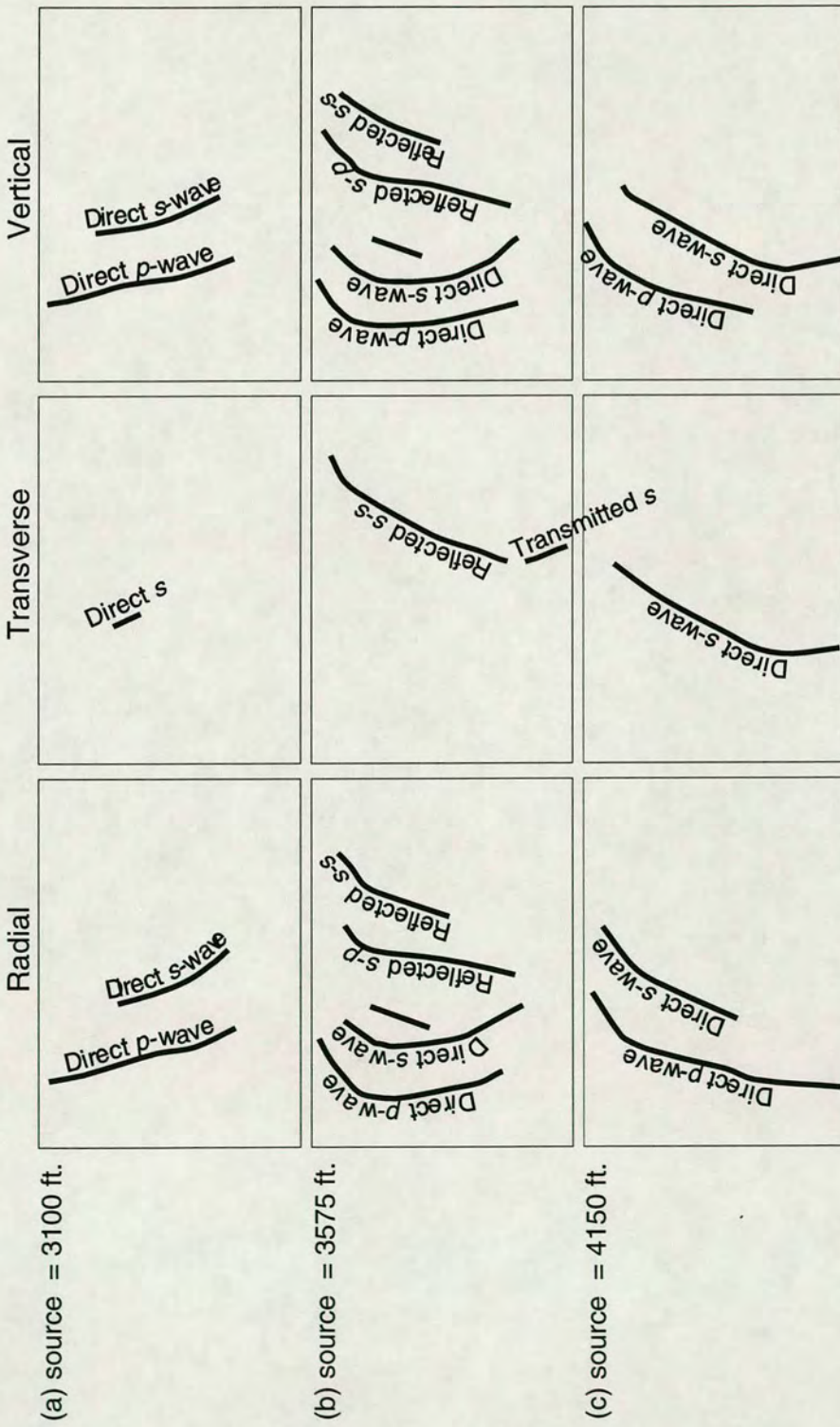
Figure 3.14. Initial interpretation of the cross-hole wavefield from well 9-16. Solid lines indicate the principal arrivals observed from each source gather at depths of: (a) 3100 feet; (b) 3575 feet; and (c) 4150 feet.

3.5.2 Initial interpretation of seismograms

Figure 3.11 shows multicomponent gathers from each of the three wells for a source depth of 3100 feet. Near horizontal raypaths are dominated by the radial *P*-wave energy. The direct shear-wave arrival is identified as the second higher amplitude direct arrival, between depths of 3400-4000 feet. Successful application of geophone rotation is confirmed by the minimization of *P*-wave energy on the transverse geophone component. Shear-wave energy is distributed predominantly on the vertical component, with decreasing proportions on the radial and transverse components. Downgoing shear waves from wells 13-01 and 9-45 exhibit a transverse component of motion below depths of 3400 feet, above this depth shear-wave particle motion seems restricted to the vertical and radial components. The anomalous transverse component of motion may suggest propagation through an effectively anisotropic medium. Shear waves from well 9-16 do not display a well defined transverse component of motion. One possibility for the lack of scattering in this direction may be that the azimuth of acquisition is close to an anisotropic symmetry plane, which results in no observable shear-wave splitting.

Three component common source gathers for source depth of 3575 feet are displayed in Figures 3.12. The gathers are dominated by upgoing reflected energy from an interface at around 4000-4100 feet. The first reflection is apparent only on the radial and vertical components and can be identified as an *S-P* reflection in the sagittal plane particle motions from well 9-16, in Figure 3.15(a). The second reflected arrival has a component of motion on all three geophone components. The particle motion plots, also from well 9-16, in Figure 3.15(b), suggest this is an *S-S* reflection. A possible explanation for such behaviour is reflection from an anisotropic layer. Keith and Crampin (1977) investigate the behaviour of waves incident at a plane boundary between isotropic and anisotropic media. Incident *SV* waves are found to generate both quasi-*SV* and quasi-*SH* waves on reflection from the anisotropic medium, whose relative magnitudes are dependent on incidence angle and properties of the anisotropic medium. Below this interface, transmitted shear waves also have a strong transverse
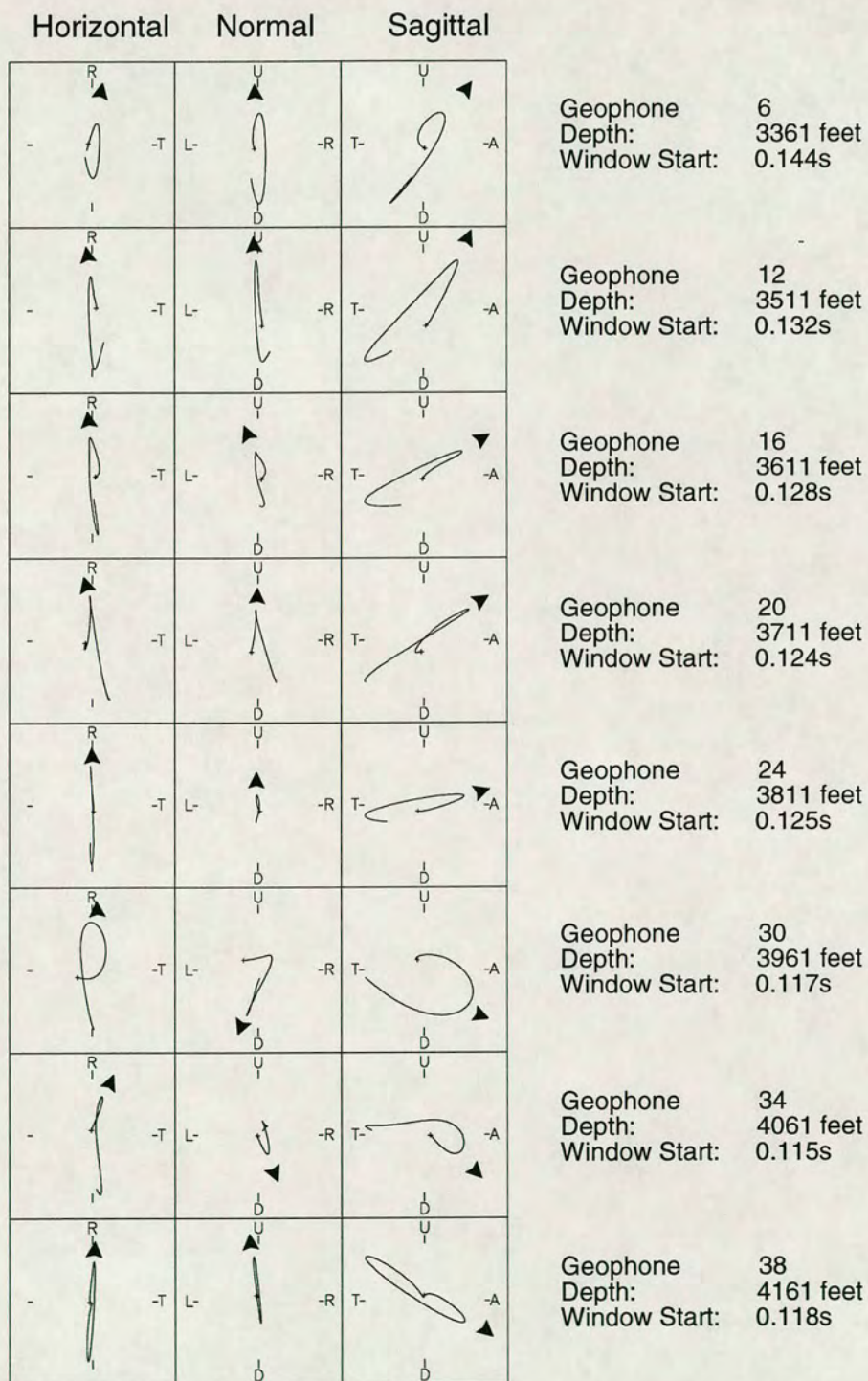
Figure 3.15(a). Windowed particle motion diagrams for the *S-P* reflection from the Viola subzone 3 reservoir, from the source at 3575 feet to well 9-16.
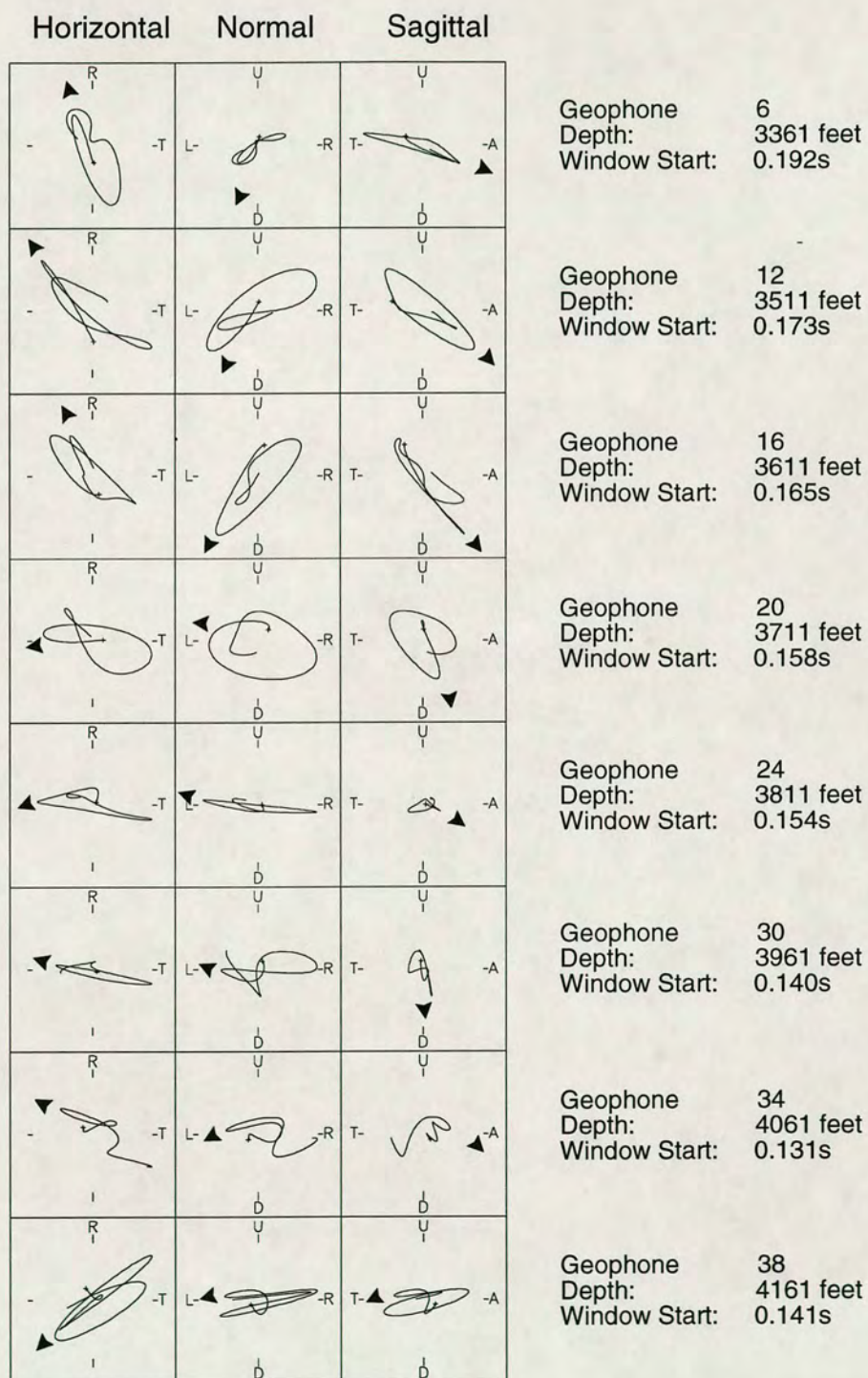
Figure 3.15(b). Windowed particle motion diagrams for shear waves reflected from the Viola subzone 3 reservoir, from the source at 3575 feet to well 9-16.

component of motion. Upgoing reflections can also be seen at the interface between the Sylvan shale and the overlying Hunton formation at a depth of around 3850 feet.

Figure 3.13 shows the common source gathers for the deepest source. A source depth of 4150 feet, means that the source is located within Viola sub-zone 3, the fractured hydrocarbon unit. Up-going shear waves have a component of motion on all three geophone components, which is consistent with wave propagation through anisotropic rocks.

3.5.3 Automatic measurement of polarization and time delay

I apply the automatic estimation method, *Direct Time Series Fitting* or *DTS*, (Campden 1990) to calculate *qS1* polarization angles and time delays between *qS1* and *qS2* arrivals. This method is essentially a global search technique. The geophone components are rotated in 1° increments and the cross-components are multiplied with the theoretical *qS1* and *qS2* amplitudes. The products are subtracted. The minimum in this function gives the optimum rotation angle and time-delay. The split shear waves are assumed to be orthogonal so that the source vector can be divided into two linearly independent components.

Conventionally, in VSP and reflection surveys, the horizontal plane has been used to measure anisotropic parameters. This gives a fixed reference frame in which shear-wave polarization estimates may be displayed and compared. Given the nature of the cross-hole acquisition, shear-wave energy is no longer concentrated in the horizontal plane. Also, the horizontal plane projections of the two split shear waves are not necessarily orthogonal, even for propagation in a purely hexagonal anisotropic symmetry system. As an alternative to the horizontal plane, I apply measurement in a dynamic plane, normal to the raypath. The three-component geophones are rotated about a transverse axis of rotation in the sagittal plane. I use calculated *P*-wave incidence angles to rotate each geophone, so that the *P*-wave arrivals are maximised on the radial component. I maximise the *P*-wave energy on the radial component rather than *S*-wave energy on the vertical component, because the *P*-wave particle

motions show greater linearity and smoother variation with depth, particularly for near horizontal raypaths. The disadvantage of this, is the assumption that both P- and S-waves follow the same raypaths. Allowing that this is not necessarily the case for varying V_P / V_S ratios, shear-wave energy will not be maximised within the dynamic plane normal to the P-wave raypath. Estimates of the $qS1$ polarization direction in the dynamic coordinate system, are then projected back into the horizontal plane, so that all measurements at individual geophones are with respect to a fixed coordinate system.

The resulting polarization and time delay measurements given by DTS are displayed in Figures 3.16 and 3.17 as a function of geophone depth, along with estimated experimental errors. The experimental errors are based on quality of the shear-wave arrivals and confidence in the geophone rotation. In general, I have assigned errors of $\pm 10°$ for polarization measurements and ± 1ms in time delay measurements.

Figures 3.16 and 3.17 (a), (b) and (c) show DTS measurements given by shear waves from the shallowest source. Measured polarizations from well 13-01 show a marked variation with depth, while those from wells 9-45 and 9-16 are more stable with depth. The measured time delays are small in magnitude as expected for propagation along short path lengths.

Figures 3.16 and 3.17 (d), (e) and (f) show similar DTS measurements of polarization angle and time delay for reflected shear waves from the 3575 foot source. Polarization estimates for each of the three azimuths are distributed closely around N50°E, N45°E and N25°E.

Finally, I consider the deepest source at a depth of 4150 feet. In this case the source is positioned within the Viola limestone reservoir zone. DTS measurements of polarization angle from North are displayed in Figure 3.16 (g), (h) and (i). Polarizations from wells 13-01, 9-45 and 9-16 are distributed about N41°E, N56°E and N34°E. Measured time delays, Figure 3.17 (g), (h) and (i), also have clearly defined trends. Time delays from well 9-45 appear to decrease slightly with depth, from around 7ms at 3350 feet to just under 5ms. Delays from wells 13-01 and 9-16 increase
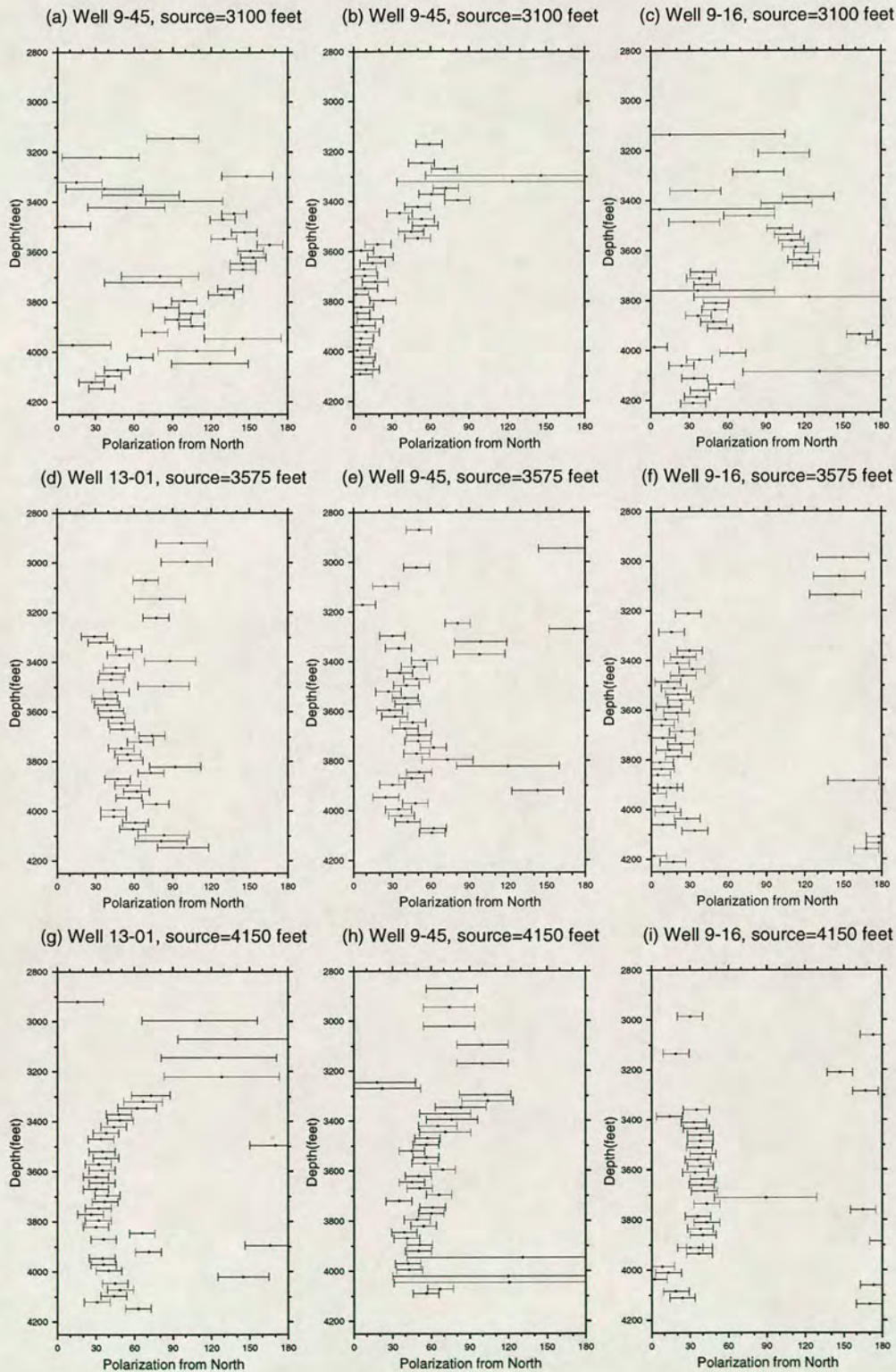
68

Figure 3.16. Horizontal plane *qS1* polarizations measured using *DTS* at each well azimuth, 13-01, 9-45 and 9-16; and source depths 3100, 4150 and 3575 feet.
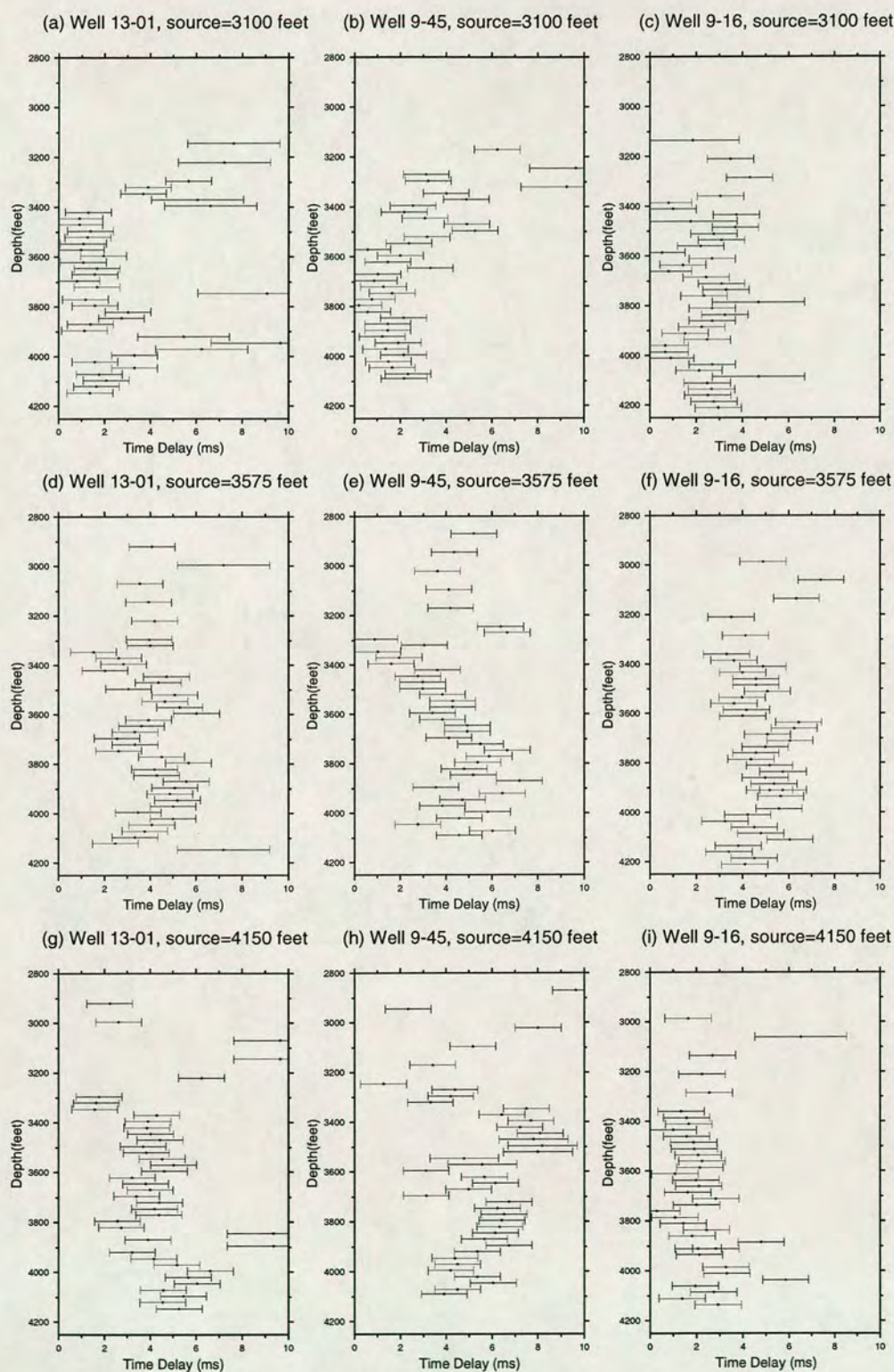
Figure 3.17. Time delays between *qS1* and *qS2* arrivals, measured using *DTS*, for each well azimuth, 13-01, 9-45 and 9-16; and source depths of 3100, 3575 and 4150 feet.

marginally with depth.

Given the complexity of propagation through a multi-layered structure, with sharp variations in incidence angles, it would be difficult to interpret the above measurements as indicative of a particular fracture orientation or fracture density with any degree of certainty. The approach I now follow is to apply forward modelling to attempt to find a suitable match to the observed shear-wave anisotropy measurements In the next section, I examine the effect of introducing distributions of micro-cracks or fractures, with varying orientations and crack densities, into a layered model.

3.6 Modelling

Synthetic seismograms are generated by forward modelling, firstly assuming isotropy, then incorporating anisotropic layers, for comparison with the observations. Velocities for a layered model are estimated using an iterative, layer stripping algorithm, i.e. minimizing the difference between observed and calculated traveltimes until a suitable match in arrival times is achieved. Anisotropy is included in the model by inserting distributions of micro-cracks, with a variety of crack parameters into the isotropic matrix. I use the Hudson method, to calculate the elastic constants of the resulting cracked, effectively anisotropic solid. The goodness of fit of the resulting anisotropic layered models is defined by three criteria:

(1) a suitable match between observed and synthetic seismograms, in terms of amplitudes and traveltimes.

(2) conformity with the physical parameters of the known geology, ie number of layers and positions of interfaces.

(3) the best agreement between observed polarization and time delay measurements and those calculated for the anisotropic models.

Models are restricted to horizontal plane layers, with no lateral variation in properties. Also, models are limited to hexagonal anisotropic symmetry with a horizontal axis of

symmetry, so the effect of dipping cracks is not considered.

3.6.1 Velocity analysis

Before any forward modelling can be undertaken, I first need to determine a velocity-depth relationship which can be input into a layered model. Direct P- and S-wave arrival times are measured firstly using an interactive trace picking routine, then by cross correlating windowed shear-wave arrivals. The application of the cross-correlation is intended to improve the accuracy of the arrival time picks to within ±0.5ms. This error represents the limitation imposed by the sampling interval. I then apply a layer stripping algorithm (Pujol *et al.* 1988) to determine interval velocities between each geophone and to model the traveltimes. The velocity in each successive layer is adjusted until the misfit between the observed and modelled traveltimes is minimized. Model arrival times are calculated by an iterative ray tracing procedure. This is repeated for each source depth. Calculated isotropic P- and S-wave velocities are shown in Figure 3.18 (a)-(i). Each diagram shows the velocities obtained for both P- and S-waves propagating from a common source position to geophones in each of the 3 wells. For example, the velocities obtained for P- and S-waves propagating from the 3100 foot source to geophones at each of the three azimuths are shown for: (a) well 13-01; (b) well 9-45; and (c) well 9-16. This was expected to highlight any azimuthal variation in velocity. In general, the velocities obtained for each layer are reasonably stable, suggesting that the inversion has given reliable results. Given the depth of each interface between the 4 major geological boundaries, I average the interval velocities within each layer to obtain an estimate of formation velocity. Average P- and S-wave velocities are summarised in Table 3.1 for the three source positions. Velocity certainly varies with both source position and azimuth; however, these differences are small. For example, the shear-wave velocities obtained for the Viola limestone, show standard deviations from the mean of 226, 189 and 357 feet/s, for source positions of 3100, 3575 and 4150 feet. Taken as a percentage of the mean, this amounts to azimuthal perturbations in the velocities measured for the Viola
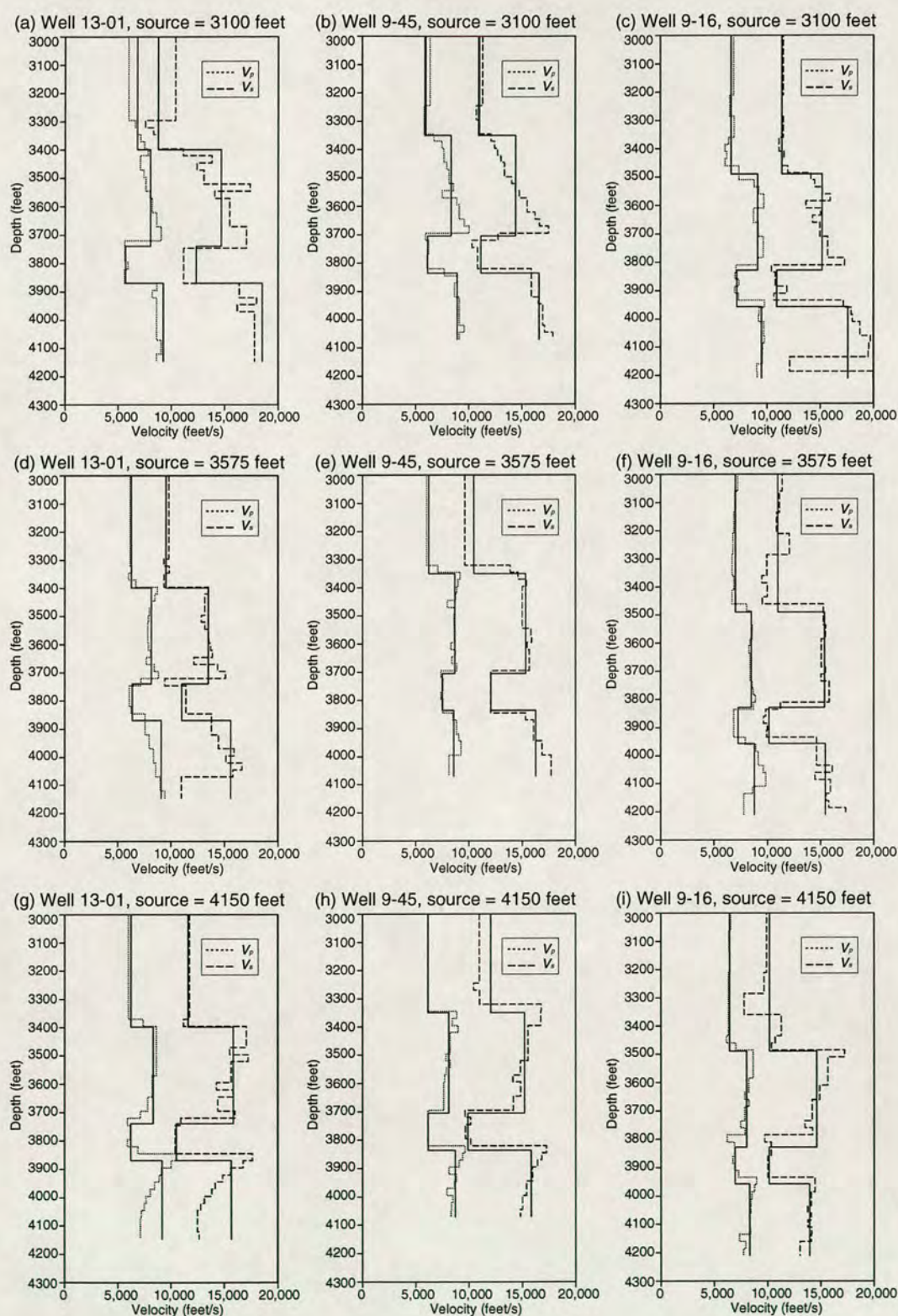
Figure 3.18. Results of traveltime inversion of *P*-wave arrivals (dashed line) and *S*-wave arrivals (dotted line) at each well azimuth, 13-01, 9-45 and 9-16, for source depths of: 3100 feet, (a), (b) and (c); 3575 feet, (d), (e), (f); and 4150 feet, (g), (h) and (i). Formation velocities for the principal geologic divisions, obtained by averaging over a depth range are marked by the solid lines.

Table 3.1. Velocities calculated by inversion of cross-hole traveltimes.

		Source depth (feet)	Formation Velocity (feet/s)			
			Woodford	Hunton	Sylvan	Viola
9-16	V_p	3100	11,407	15,159	10,902	17,598
		3575	10,998	15,372	10,142	15,430
		4150	10,221	14,608	10,159	13,941
	V_s	3100	6,643	9,128	7,157	9,476
		3575	7,026	8,501	7,226	8,772
		4150	6,433	8,059	6,955	8,314
9-45	V_p	3100	10,961	14,398	11,127	16,601
		3575	10,488	15,318	12,058	16,262
		4150	12,054	15,225	9,889	15,825
	V_s	3100	5,933	8,337	6,111	8,924
		3575	6,262	8,665	7,492	8,592
		4150	6,149	8,106	6,176	8,692
13-1	V_p	3100	8,774	14,682	12,341	18,491
		3575	9,524	13,483	10,998	15,571
		4150	11,664	15,831	10,504	15,634
	V_s	3100	6,827	8,044	5,698	9,244
		3575	6,279	8,129	6,352	9,052
		4150	6,274	8,318	6,228	9,186

limestone of 2.4%, 2.1% and 4.1%. Perturbations are of similar magnitudes for the other velocities.

These velocity perturbations may have a number of causes:

(1) inconsistency in traveltime picks, where *P*- or *S*-wave energy is low.

(2) inherent instability of the inversion procedure.

(3) anisotropic effects, velocity variation with angle of propagation through a particular layer.

However, it would be inconclusive, given the limited aperture of coverage, and also incorrect, given the limitations of the inversion procedure to interpret the above velocity variations as evidence of seismic anisotropy. The ray tracing used for the inversion is only valid for isotropic wave propagation. The presence of any seismic anisotropy will introduce systematic errors in the velocities obtained. This being the case, the velocity analysis is only intended as an intermediate step to the more rigorous forward modelling.

It is interesting to compare these velocity measurements with the compressional velocities from the sonic log in Figure 3.7. Although the shale velocities are well matched, the traveltime inversion is unable to image the thinner subdivisions in both the Hunton and Viola limestones. Instead we see a smearing out of the velocities over these intervals.

3.6.2 Isotropic modelling

I apply the ANISEIS modelling package to generate synthetic seismograms by the reflectivity method for a given source wavelet shape. Isotropic media are parameterized by a density and the compressional and shear-wave velocities derived above. Densities are calculated using an empirical relationship between compressional velocity and density derived by Gardner *et al.* (1974). As previously stated, there are imposed limitations of horizontal plane layers and lateral homogeneity.

The preliminary isotropic structure used for forward modelling of the observed cross-hole wavefield is shown in Figure 3.19. This consists of 7 layers, whose interface depths match those of the principal formations making up the local geology. The principal hydrocarbon reservoirs are indicated by shading. In order to model the reflected wavefield, the Viola sub-zone 3 is assigned a significantly lower S-wave velocity than the surrounding layers, giving a sharp contrast in the V_P / V_S ratio (and hence Poisson's ratio). Since the amplitude of reflected energy is dependent on the Poisson's ratio of the two materials, this was expected to increase the amplitude of the energy reflected from Viola sub-zone 3.

Model pulse shape is based on the far field air gun signature. The wavelet is an anti-symmetric, two and a half cycle pulse, with a peak frequency of 100 hz. In isotropic media, the pulse shape observed at each geophone is dependent on the source polarization. The vertical airgun source, as demonstrated in section 3.4, generates both radially polarized P-waves and SV-polarized shear waves. Shear waves propagating through anisotropic media will split into two discrete wavelets with distinct polarizations. In general the two polarizations are independent of the source polarization. The resultant wavelet observed on each geophone component is a vector sum of the two.

Synthetic seismograms generated for the 7 layer, isotropic model are shown in Figures 3.20, 3.21 and 3.22 for source positions of 3100, 3575 and 4150 feet, respectively. Visual examination shows that the direct P-wave arrivals from the shallow source position, Figure 3.20, provide a good match to the observations in terms of both the traveltimes and the amplitudes at all three azimuths. The arrival times of the direct shear-waves also show reasonable agreement with the observations, but considerable differences in amplitude are apparent. The observed amplitude variation between geophone levels from the actual data is primarily due to the source radiation pattern, section 3.4. As previously discussed, the modelling package cannot recreate exactly this radiation pattern, consequently, differences between modelled and observed shear-wave amplitudes occur. Also the model seismograms fail match the observed wavefield in terms of amplitude distribution between geophone components.
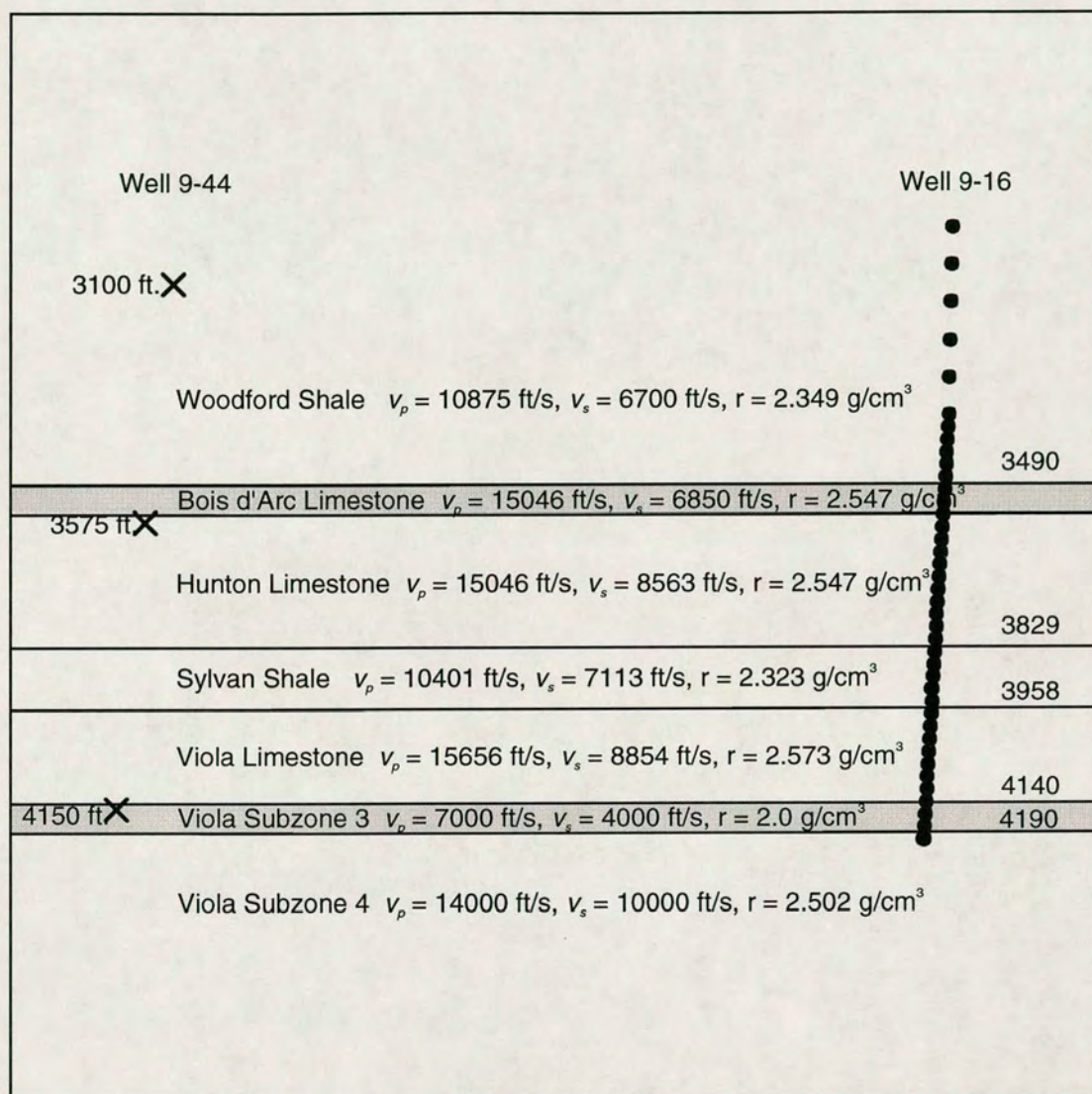
Figure 3.19. Preliminary isotropic velocities and interface depths used for forward modelling of observed wavefield. Synthetics are generated for all three source positions.
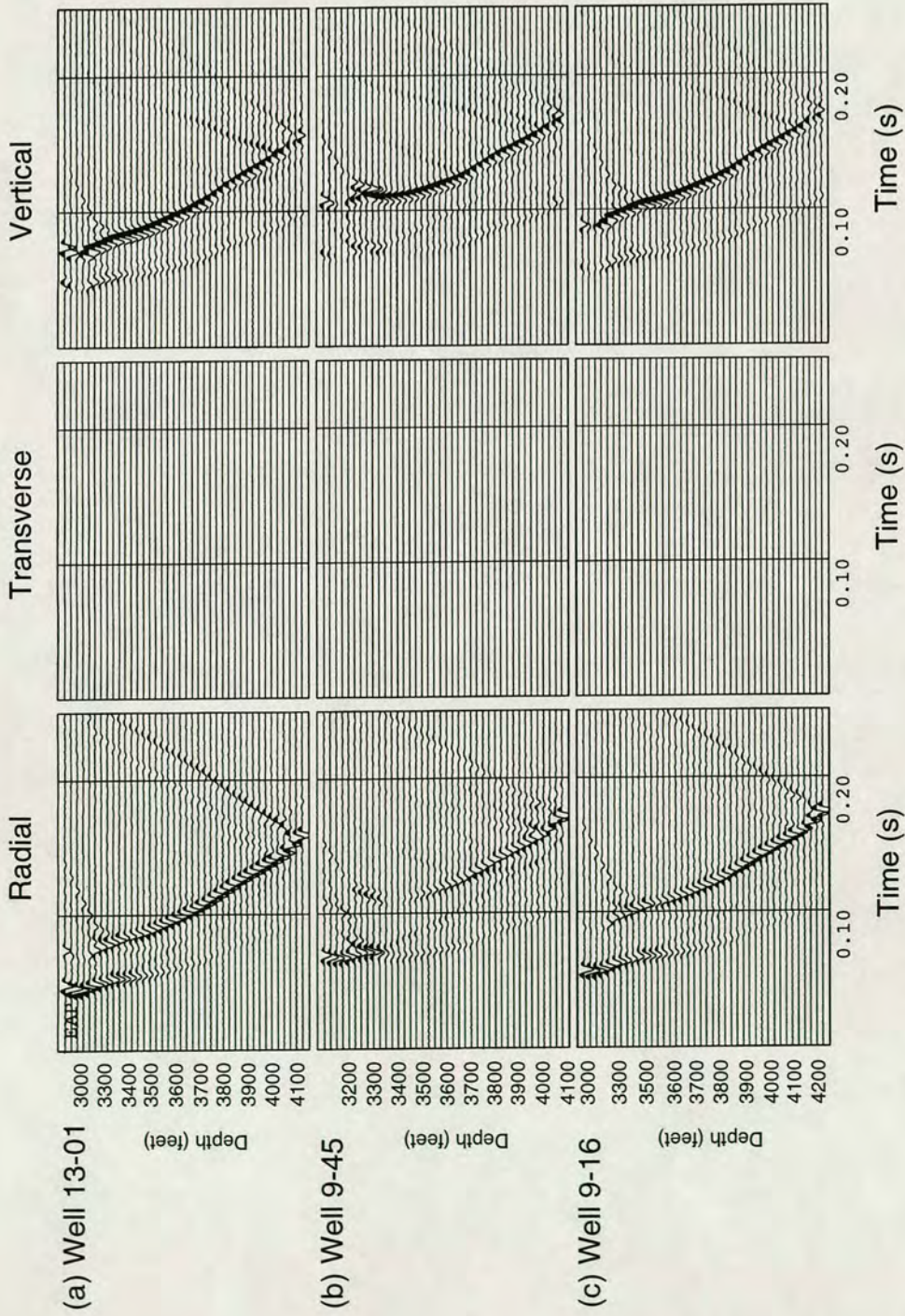
Figure 3.20. Multicomponent common sources gathers for the isotropic model.
Source depth of 3100 feet, from: (a) well 13-01; (b) well 9-45; (c) well 9-16.
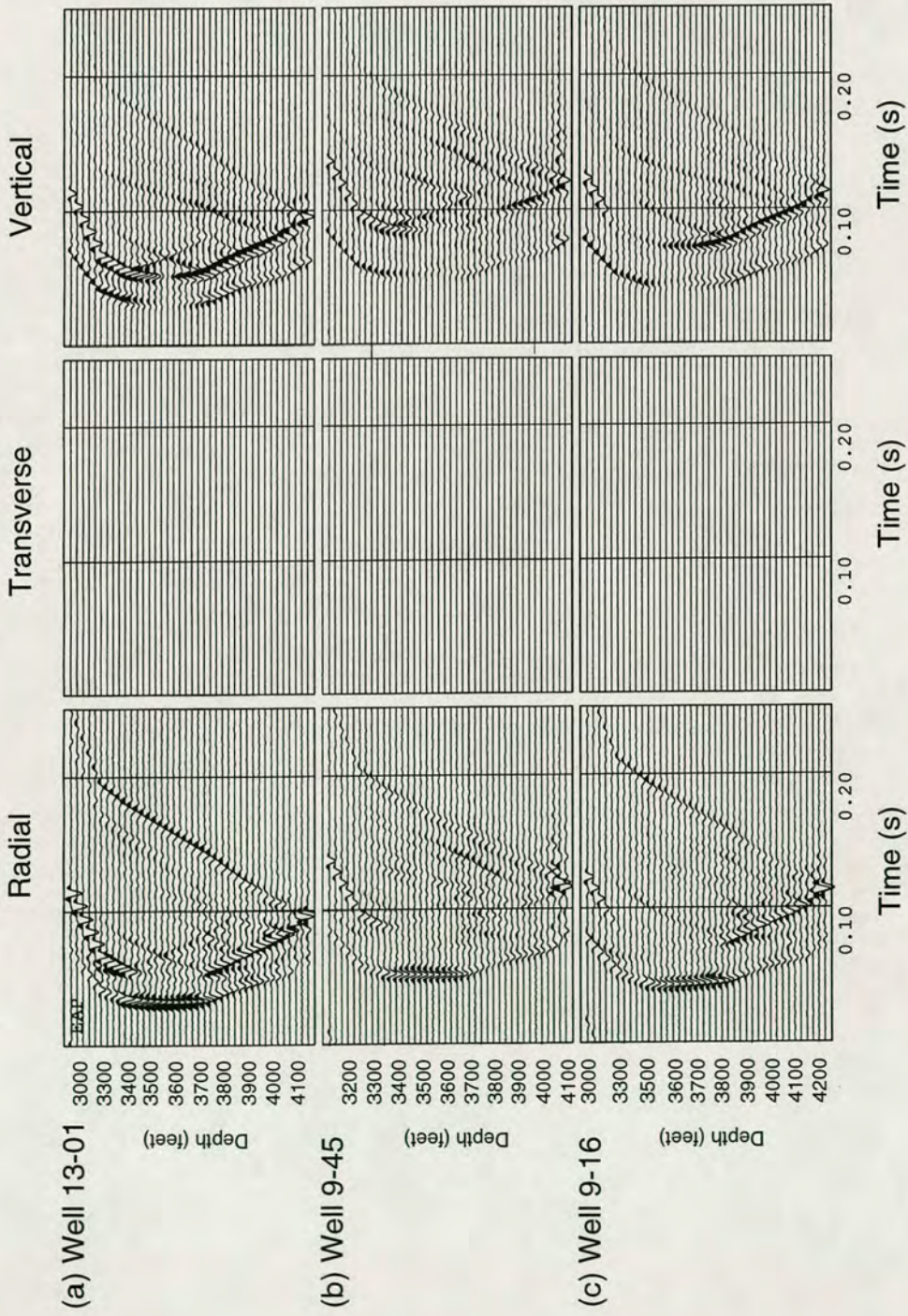
Figure 3.21. Multicomponent common sources gathers for the isotropic model. Source depth of 3575 feet, from: (a) well 13-01; (b) well 9-45; (c) well 9-16.
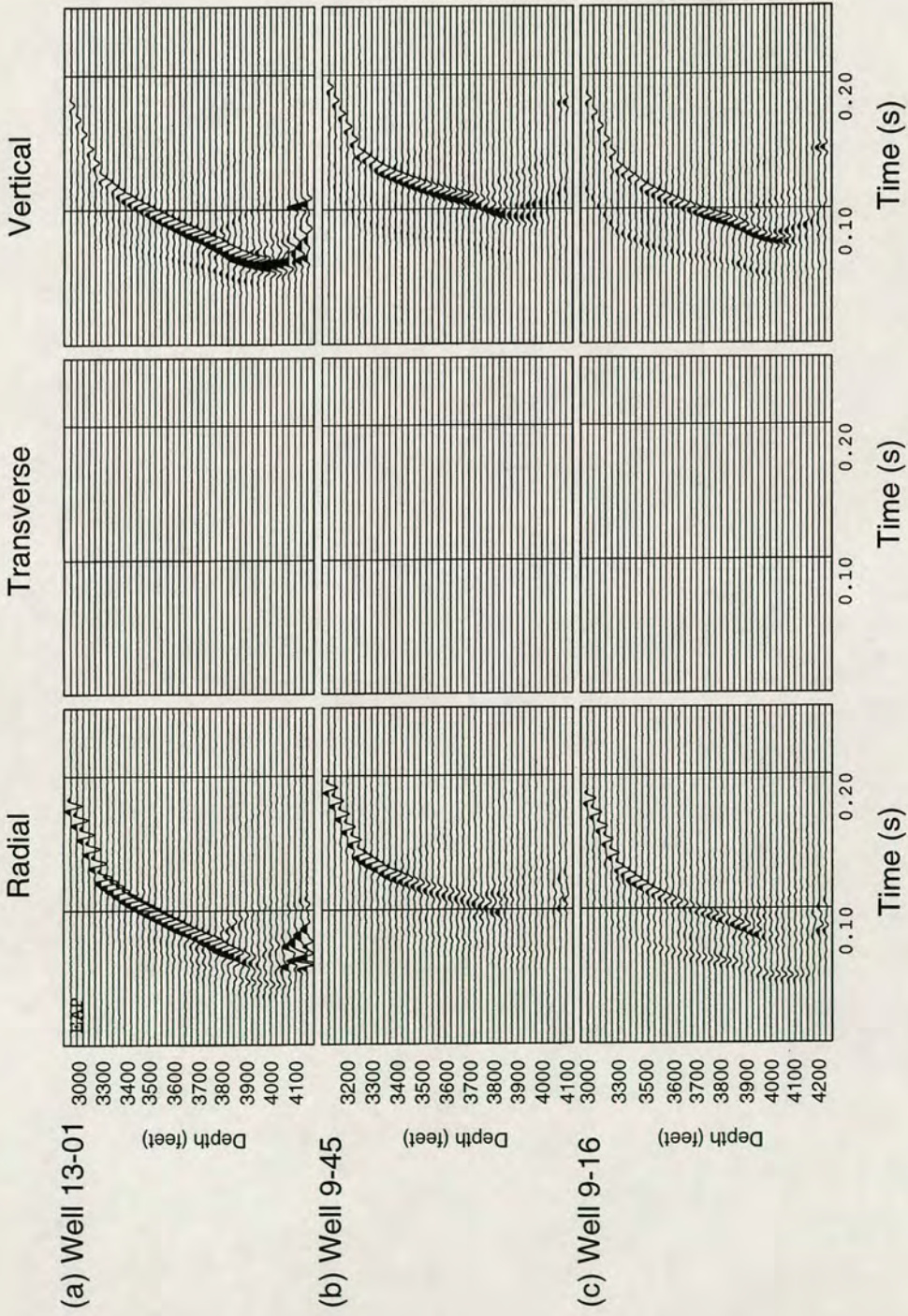
Figure 3.22. Multicomponent common sources gathers for the isotropic model. Source depth of 4150 feet, from: (a) well 13-01; (b) well 9-45; (c) well 9-16.

As expected for an isotropic plane-layered model, shear waves are restricted to radial and vertical components of motion.

P-wave amplitudes and traveltimes from the source position at 3575 feet, Figure 3.21, again show a reasonable agreement with observations. Direct shear-wave amplitudes are considerably stronger than those observed. Again, this is possibly a result of source radiation. Reflected *SP* and *SS* arrivals have much lower amplitudes. The observed reflected transverse component of shear-wave motion is clearly absent from this model. Synthetic seismograms for the 4150 foot source position are displayed in Figure 3.22. Amplitudes and traveltimes of both *P*- and *S*-waves are well matched on radial and vertical components, for all three azimuths. As before, there is no transverse component of shear-wave motion.

The isotropic modelling clearly suggests that wave propagation in isotropic media cannot produce a transverse component of shear-wave motion without violating at least one of the assumptions of horizontal plane layers, lateral homogeneity, or a purely *SV* source. Allowing that these assumptions are valid, I now introduce anisotropy into the model, in the form of thin reservoir layers containing distributions of micro-cracks or fractures.

3.6.3 The inclusion of anisotropy

Anisotropy is introduced by placing distributions of micro-cracks into a particular layer. Using Hudson's parameterization, crack distributions are specified by the 4 parameters: cracks radius, crack aspect ratio, crack density and crack content. In section 2.6, I discussed the sensitivity of the parameters of shear-wave splitting to variations in crack parameters. Shear waves were found to be sensitive only to comparatively large changes in aspect ratio and only minor changes in properties were observed. In view of this I do not attempt to model variation in aspect ratio. Also, I consider only a fixed crack radius, given that Hudson's formulations require only that crack dimensions are smaller than the seismic wavelength. Therefore, we might expect the models to be correct for any crack dimensions smaller than this. As the cracked

media are expected to contain hydrocarbons I also assume that the cracks are liquid filled or saturated. Holding these three properties constant I now examine the effect of varying crack orientation and crack density on expected polarizations and delays.

The following possibilities are examined.

1. Only reservoir layers contain distributions of micro-cracks. Four crack orientations are examined, distributed around the regional stress direction of NE-SW, at N15°E, N35°E, N55°E and N75°E. Crack densities of 0.05, 0.1 and 0.2 are considered.

2. Weak background anisotropy, given by distributions of cracks with a low crack density (ε=0.01) in all layers, with stronger anisotropy in the reservoir layers. The crack densities in the reservoir layers are ε=0.02, 0.05, 0.1 and 0.2. Crack orientations as for previous model.

3. Distributions of micro-cracks in all layers with the same crack density and orientation. Crack densities of ε=0.01, 0.02, 0.03, 0.04, 0.05 and 0.1 are considered. Crack orientations as for previous model.

Models are limited to the case where crack strike is constant with depth.

Given any particular model the problem is now how to decide quantatively which of the models best fits the observations. To do this the model response must be parameterized in terms of a polarization and time delay at each geophone so that each model response can then be compared with the corresponding observations of polarization and time delay to assess the goodness of fit.

Model responses are derived in two ways. For shear waves transmitted through the reservoir layers from the sources at 3100 and 4150 feet, model responses are calculated using an anisotropic ray-tracing algorithm (Horne, 1995). Vertical slowness is calculated analytically for a given horizontal slowness, thus specifying the propagation direction within any given layer. This allows the calculation of a raypath

through a sequence of horizontal layers for the given horizontal slowness. The algorithm performs a search over horizontal slowness to find a ray which connects source and geophone. The $qS1$ polarization is given by the solution of the Christoffel equation for the particular direction of propagation. This method is limited to monoclinic symmetry with a horizontal plane of symmetry. Also, the ray-tracing assumes plane wavefronts so the calculations are for phase rather than group velocity.

For the reflected shear waves from the 3575 foot source, the model responses are measured from synthetic seismograms generated for each model. The advantage of this is that the synthetic data are treated in the same way as the observed data. However this process is much more time consuming as the full-waveform anisotropic modelling is computer intensive. The DTS measurement technique is applied to windowed shear-wave arrivals from each common source gather giving the dependence of polarization and time delay on geophone depth.

Calculated model polarizations and time delays for each source and azimuth are shown in Figures 3.23 and 3.24, for distributions of cracks in the reservoir layers only with a fixed crack density of $\varepsilon = 0.2$ and the four crack orientations, N15°E, N35°E, N55°E and N75°E. Similarly, Figures 3.25 and 3.26 show the calculated polarizations and time delays for models with the same four crack strikes as above, but with cracks in all layers with a constant crack density of $\varepsilon = 0.03$.

Direct shear waves from the 3100 foot source show comparable behaviour for both types of model, except that those geophones above the Bois d'Arc reservoir layer show the effects of propagation in anisotropic media for the models with anisotropy in all layers.

Model responses are also comparable for the reflected shear waves from the 3575 foot source. In general polarizations and time delays calculated by applying DTS to windowed synthetic seismograms show a less smooth variation than those calculated using the anisotropic ray-tracing.

For direct shear waves from the 4150 foot source, both types of model show similar polarization behaviour at geophones furthest from the source positions. However, for geophones close to the source position polarizations clearly deviate. The

Figure 3.23. Modelled polarizations at each azimuth and source depth, for models with anisotropy in the reservoir zones only, with a crack density of 0.2 and crack strikes of N15E, N35E, N55E and N75E.

84

Figure 3.24. Modelled time delays at each azimuth and source depth, for models with anisotropy in the reservoir zones only, with a crack density of 0.2 and crack strikes of N15E, N35E, N55E and N75E.
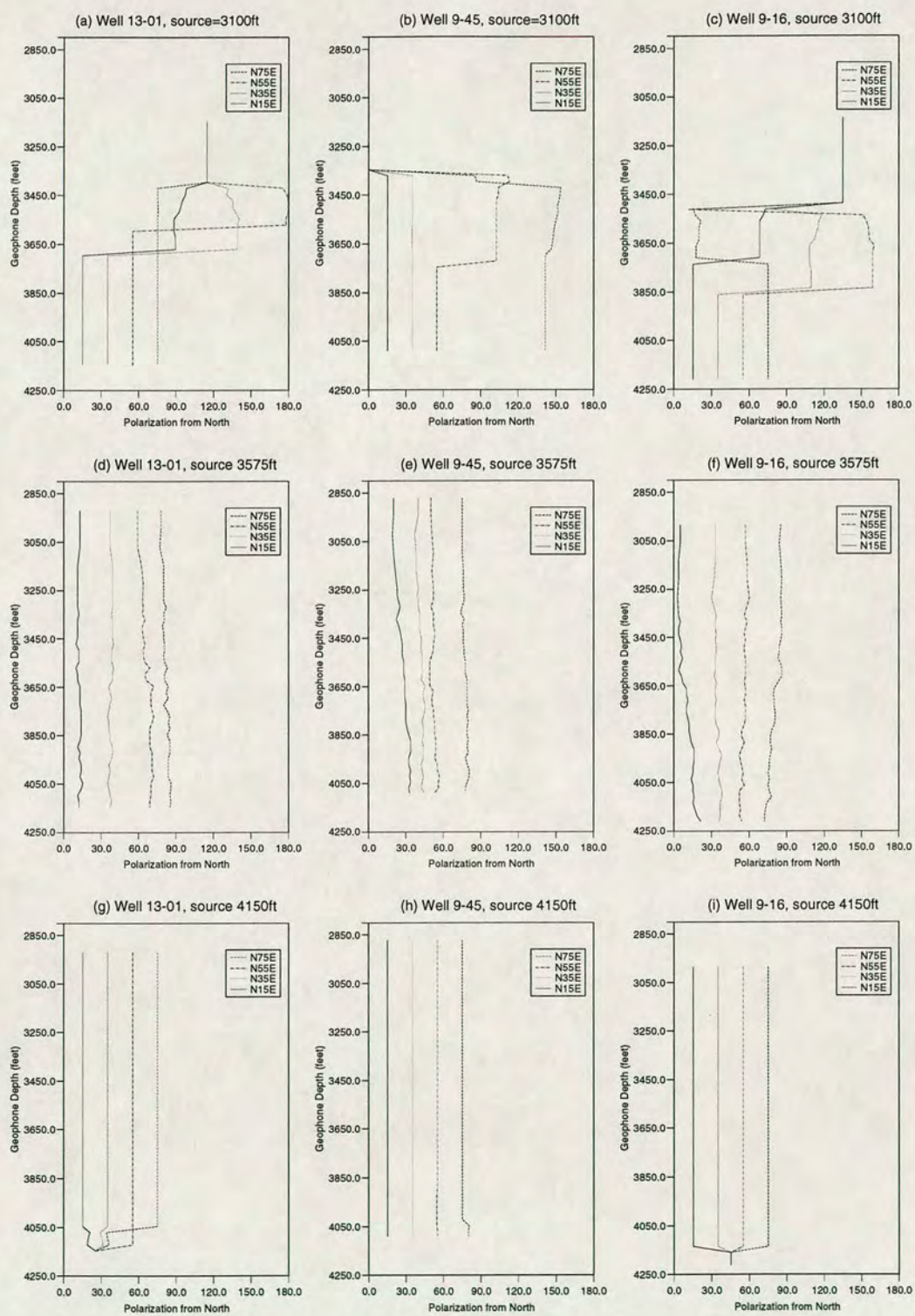
Figure 3.25. Modelled polarizations at each azimuth and source depth, for models with anisotropy in all layers, with a constant crack density of 0.03 and crack strikes of N15E, N35E, N55E and N75E.
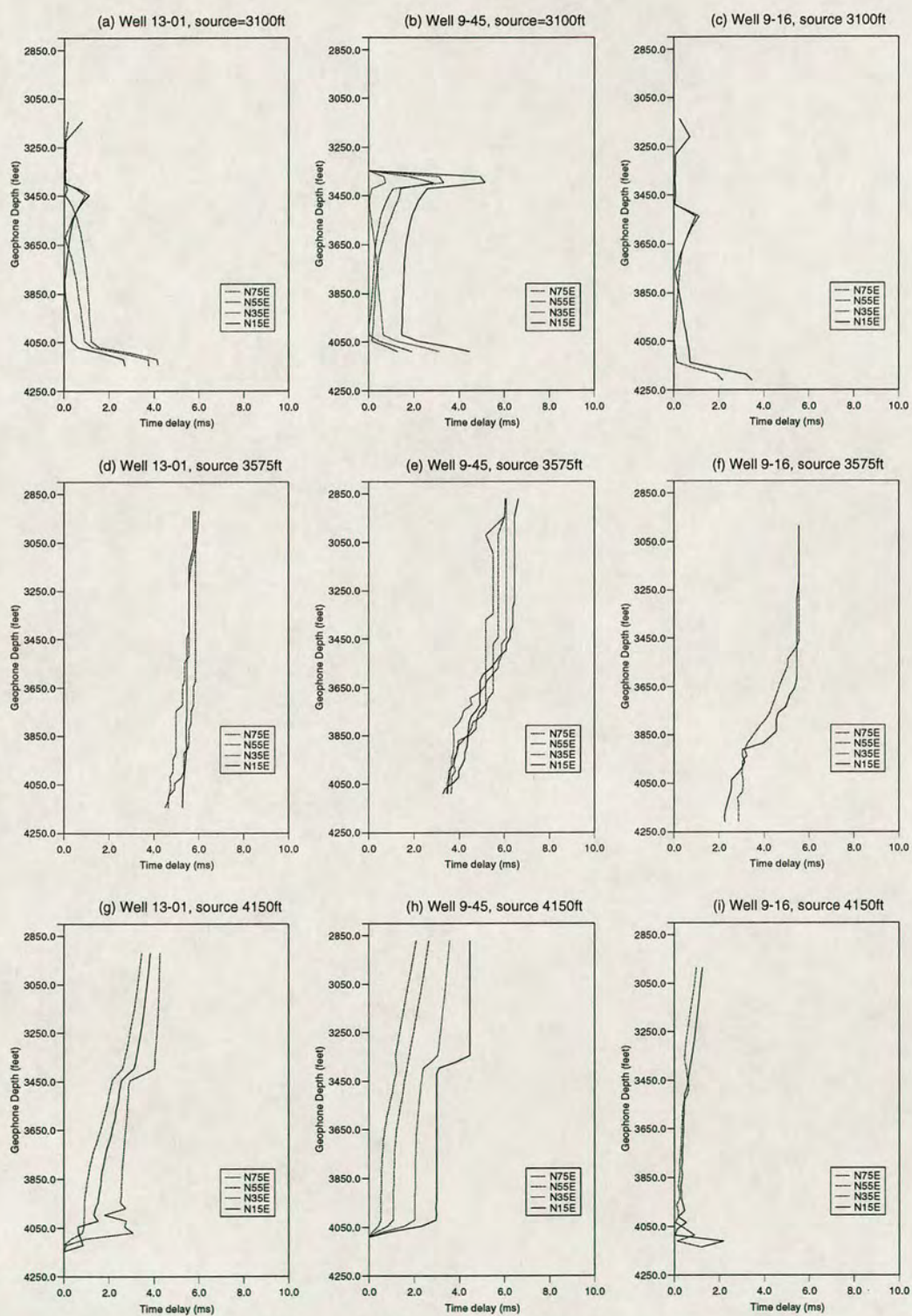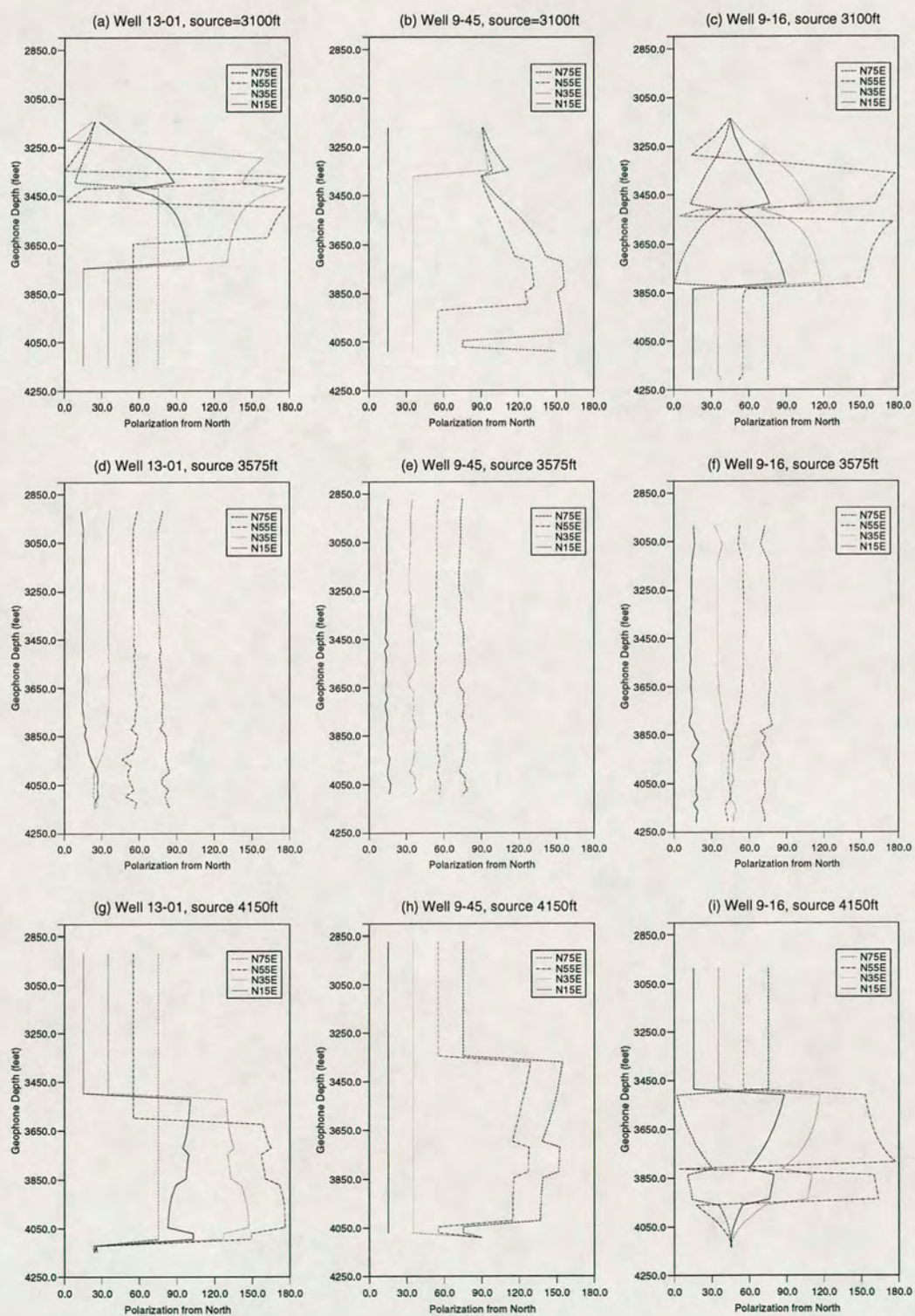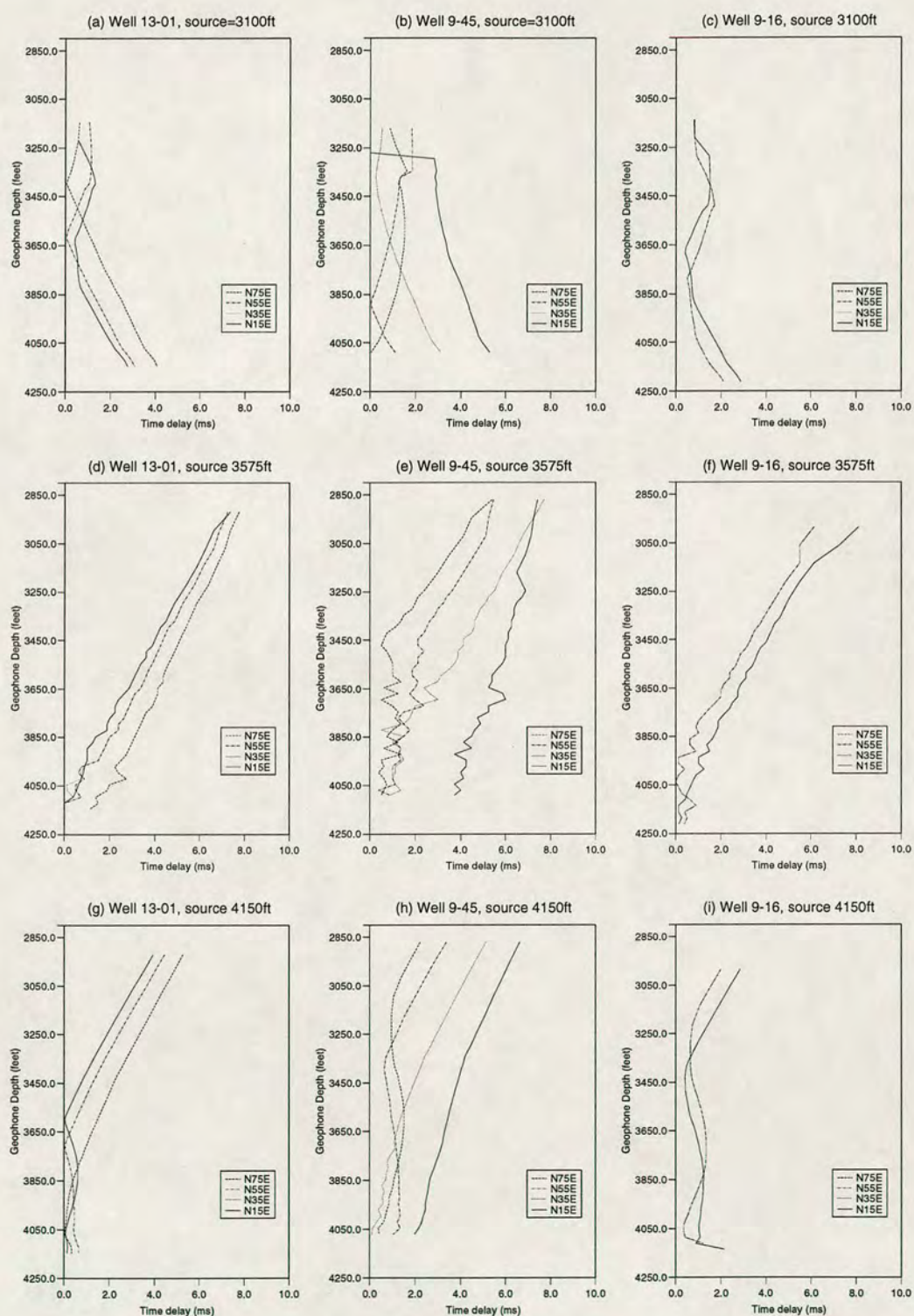
Figure 3.26. Modelled time delays at each azimuth and source depth, for models with anisotropy in all layers, with a constant crack density of 0.03 and crack strikes of N15E, N35E, N55E and N75E.

differing *qS1* polarizations can be explained by the velocity contrast between the reservoir layer and the surrounding layers. Shear waves propagate at near-vertical incidence through the anisotropic reservoir layers, but propagate at higher incidence through the surrounding layers. This results in a change in *qS1* polarization angle with depth for models with anisotropy in all layers. Whereas polarization remains constant with depth for models with anisotropy in the reservoir layers only.

3.7 Model misfit and resolution

Given the observed series of polarizations and time delays for different source depths and geophone azimuths and the expected responses for the models described above, I measure the agreement between the data and the models using a merit function to determine the best-fit parameters.

3.7.1 The merit function.

A least-squares or *l2-norm* merit function can be used to calculate the misfit for each model.

$$f(x^o) = \frac{1}{N} \sum_{i=1}^{N} \left(\frac{x_i^o - x_i^m}{\delta x_i}\right)^2 \tag{3.5}$$

where x is the time delay and polarization projected in the H-plane. The subscript i denotes the observation number and the superscripts o and m denote observed response and modelled response respectively. δx are the errors in the observed time delay or *qS1* polarization. However, outliers in the data were found to have a disproportionate influence on the solution.

Alternatively a merit function which uses the *l1-norm* or least absolute value can be used to calculate model fitness. This type of function is known to be less sensitive to the presence of outliers, ie 'robust', (Claerbout and Muir, 1973).

$$f(x^o) = \frac{1}{N} \sum_{i=1}^{N} \left| \frac{x_i^o - x_i^m}{\delta x_i} \right|$$ (3.6)

3.7.2. Weighting

The standard *l2-norm* can be made less sensitive to outliers by assigning weights to these points. Individual weights are calculated from the residuals, therefore those points with large residuals will have smaller weights. To introduce some estimate of scale, ie whether the residual is large or not, the scaled residual u is used,

$$u_i = \frac{x_i^o - x_i^m}{\sigma_r}$$ (3.7)

where u_i is the residual between the ith observed and modelled values and σ_r is some robust measure of scale. The most commonly used σ_r is the standard deviation σ. However, a more robust measure in the presence of outliers is the sample *interquartile range*. The fourths are the values halfway between the media and the extrema. The interquartile range σ_f is then the difference between the two fourths. For a Gaussian distribution, $\sigma_f = 1.349\sigma_r$. Therefore a robust standard deviation σ_r, assuming a Gaussian distribution holds for the majority of the data is given by

$$\sigma_r = \frac{\sigma_f}{1.349}$$ (3.8)

The weighting function can be defined in a number of ways, see Hoaglin *et al.* (1983) for a summary. Here, I follow the method of Huber (1964). The weights are defined by,

$$w(x_i) = \begin{cases} 1 & |u_i| \leq k \\ \dfrac{k}{u_i} & |u_i| > k \end{cases}$$ (3.9)

where k determines the transition point. Although outliers still have some bearing on

the model fit, their influence is reduced.

3.7.3 The choice of parameter k

The parameter k determines the degree of weighting. If the residual is greater than k times σ then the point is downweighted. For a normal distribution, one standard deviation on either side of the mean includes 68% of the samples. A second standard deviation includes 95%, while a third increases this to over 99%. Therefor a choice of $k=2$ will weight the outside 5%. The value of k will increase with the sample size N, because of the increased probability of outliers in large datasets. Here, I choose $k=1.5$.

3.7.4 The robust misfit function

The misfit function is now modified by including the weights calculated for both polarizations and time delays.

$$f(x^o) = \frac{1}{N} \sum_{i=1}^{N} w(x_i)(\frac{x_i^o - x_i^m}{\delta x_i})^2 \qquad (3.10)$$

Equation 3.10 is applied to observations of $qS1$ polarization and time delay between $qS1$ and $qS2$ arrivals for all models. Misfit values are calculated for polarization and time delay separately to allow the relative contribution of each parameter to be assessed. A summed misfit value can be calculated by taking the average of the misfits in the polarization and the time delay.

As an aid to displaying model resolution, I define a likelihood function, after Tarantola (1987) as

$$L = e^{-\frac{1}{2}f} \qquad (3.11)$$

where f is the misfit function value.

To resolve the best fitting model for all azimuths, values of f and L are

calculated for observations of polarization and time delay at all three azimuths together. The resulting values of L are plotted against model crack strike for fixed crack densities in Figures 3.27, 3.28 and 3.29.

Figure 3.27 shows how model fitness for the observed polarizations, as given by the likelihood function L varies with both source position for all three classes of model. Figures 3.27(a), (b) and (c) show values of L at each of the three source levels for models with reservoir anisotropy only. Similarly, Figures 3.27(d), (e) and (f) show the variation in L for models with weak background anisotropy and variable reservoir anisotropy, where the orientation of the anisotropy is constant with depth. Figures 3.27(g), (h) and (i) show values of L at each of the three source levels for models with anisotropy in all layers, with a constant crack density and crack orientation.

The best-fit to observed polarizations from the 4150 foot source is given by models with reservoir anisotropy only and a crack strike of N35°E. A similar best fit crack strike is obtained for the 3575 foot source. In this case there is greater similarity between the misfit values for each class of model, however, models with reservoir anisotropy only still give the best fit. Models for the upper source position, in general, a relatively poorer fit than those for the lower two source positions.

Similarly, Figure 3.28 shows model fitness values for the observed time delays. These show some interesting differences from the misfit values obtained for the observed polarizations above. Values of L for the deepest source are seen to be relatively lower than those from the 3100 foot and 3575 foot source positions. The best fit is given by a model with a low crack density anisotropic background and a reservoir crack density of $\varepsilon=0.2$. Model fitness values for the 3575 foot source are greatest for models with cracks in the reservoir only with a crack density of $\varepsilon=0.2$. The best fit to the observations at the shallowest source position is given by models with anisotropy in all layers with a constant crack density of $\varepsilon=0.05$.

In all cases the calculated fitness values for time delays are comparable for all classes of model. This suggests that the model space is poorly resolved and that the observed time delays can be approximated by a variety of crack distributions: high crack densities in the reservoir layers only, with an isotropic or weakly anisotropic

Figure 3.27. Values of the likelihood parameter calculated for polarizations from all considered cross-hole models. Each graph shows the variation of fitness with crack azimuth and crack density for each source for the three different types of model.

Figure 3.28. Values of the likelihood parameter calculated for time delays from all considered cross-hole models. Each graph shows the variation of fitness with crack azimuth and crack density for each source for the three different types of model.
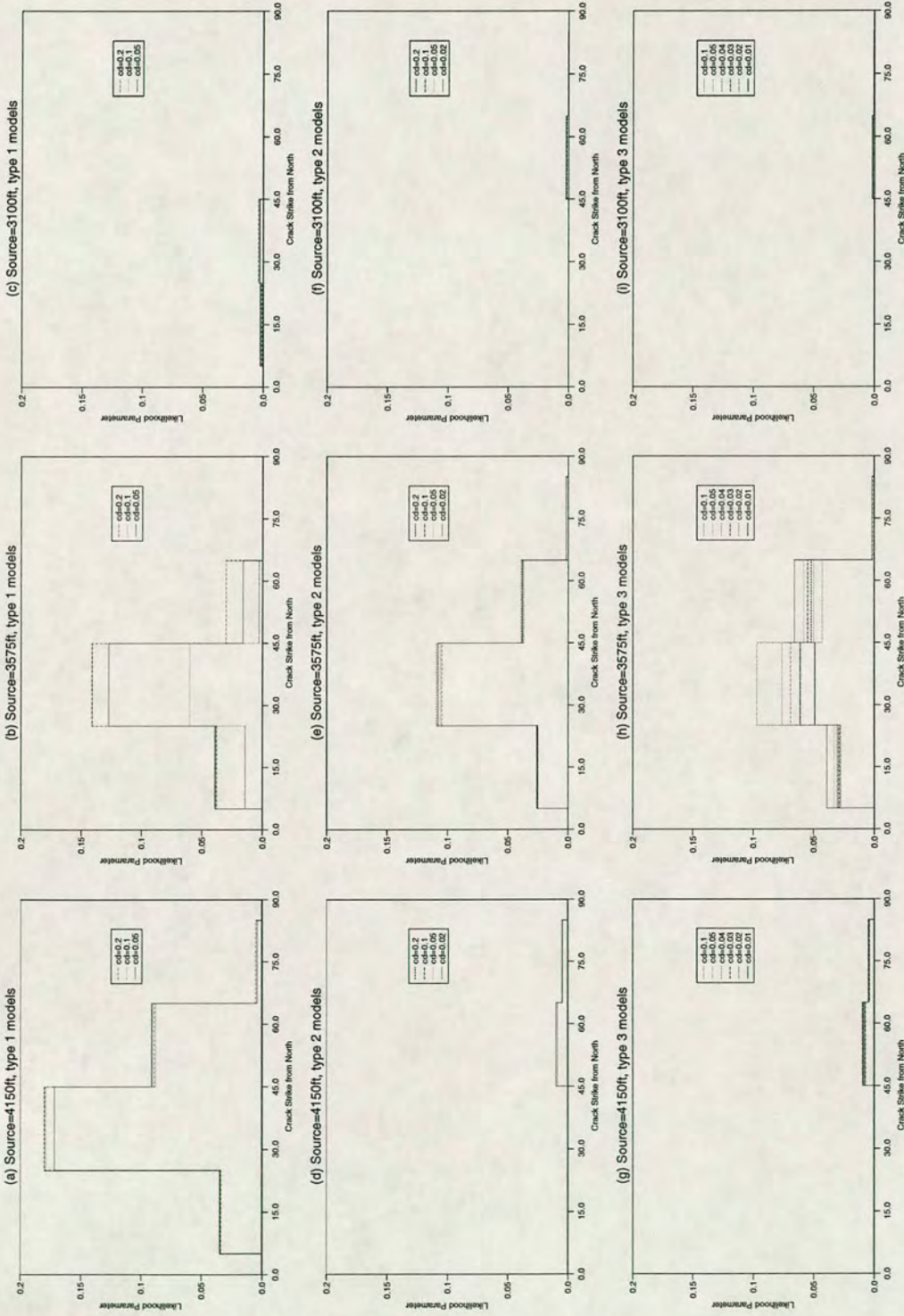
Figure 3.29. Values of the likelihood parameter calculated for both polarizations and time delays from all considered cross-hole models. Each graph shows the variation of fitness with crack azimuth and crack density for each source for the three different types of model.
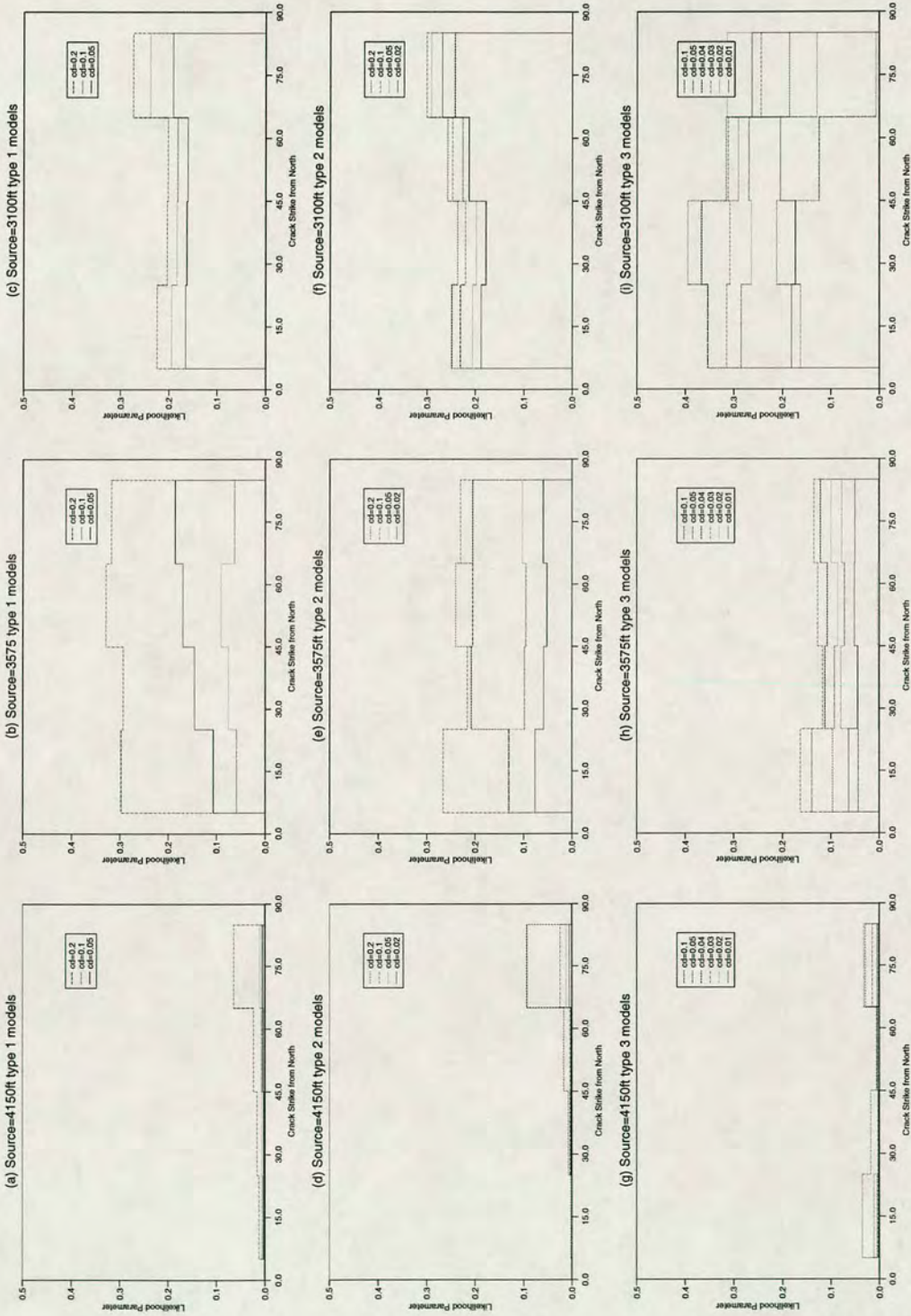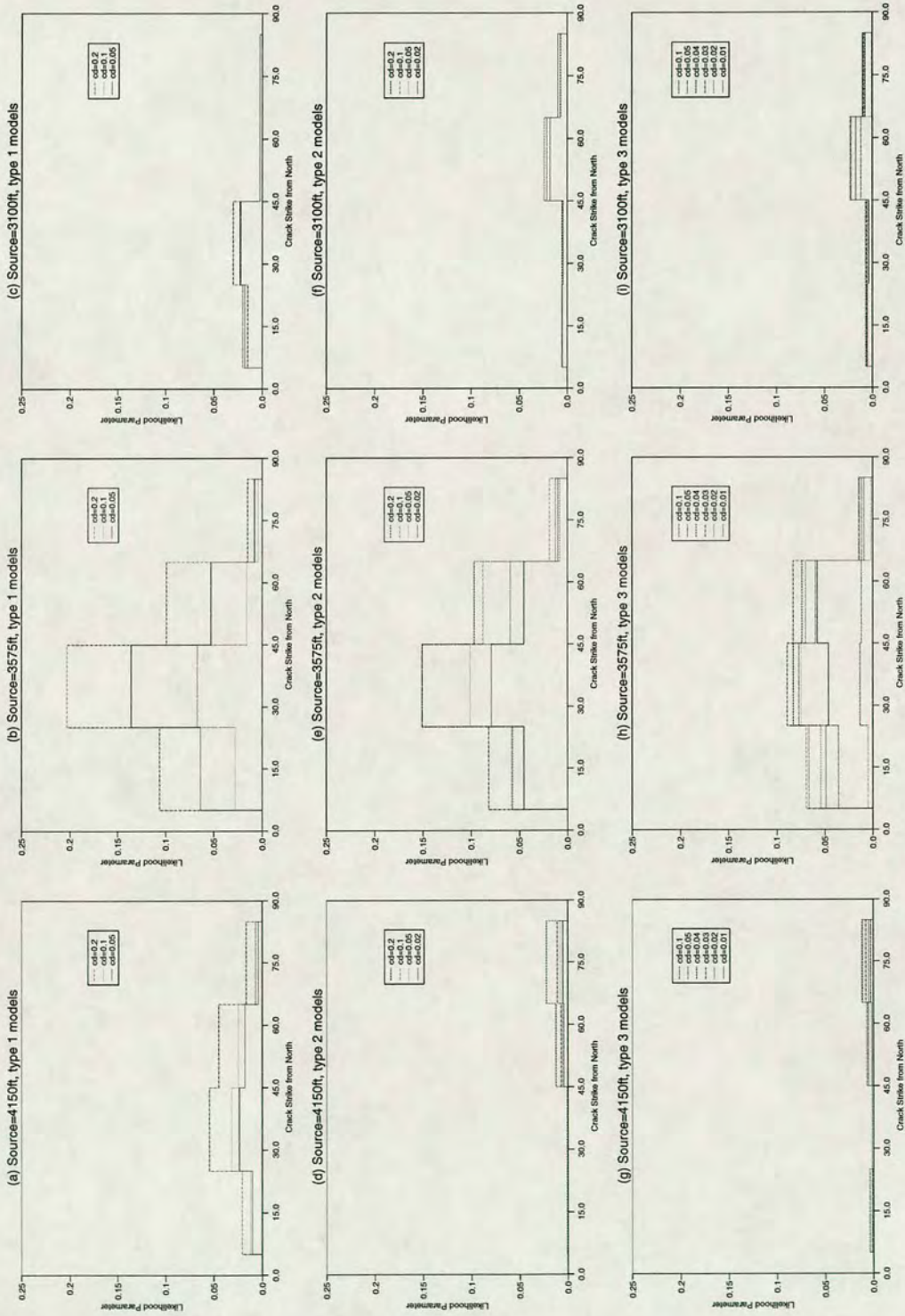
background; or by lower crack densities in all layers of the model. In addition, model fitness for delays is relatively insensitive to the crack orientation.

Figure 3.29 shows how model fitness, calculated for observed polarization and time delay together, varies with source position for all three classes of model. Comparing this with the previous two figures shows that the crack orientation has the dominant effect in defining the best fit model. A general best-fit is given by a model with reservoir anisotropy only with a crack orientation of N35°E and a crack density of $\varepsilon=0.2$.

Given a best-fit crack strike of N35°E and crack density of $\varepsilon=0.2$, I generate synthetic seismograms for the best-fit anisotropic model. These are displayed in Figures 3.30, 3.31 and 3.32 for each source position. Synthetic seismograms for the 3100 foot source position, Figure 3.30, now contain a significant transverse component of shear-wave motion for wells 13-01 and 9-45. A smaller component of transverse motion can also be seen on the synthetics for well 9-16. Similarly, there is now a reflected transverse component of shear-wave motion on the synthetic seismograms for the 3575 foot source in Figure 3.31. Although amplitudes of the reflected shear waves on the synthetics are considerably less than those on the observed seismograms, this must still represent a significant improvement over the isotropic model. The other inconsistency between model and observations is that the dip of the reflected wavefronts from the model is less than that observed. The synthetic seismograms for the 4150 foot source position are shown in Figure 3.32. Seismograms for all three azimuths now contain a transverse component of motion due to shear-wave splitting within the Viola 3 reservoir zone. Transverse amplitudes for well 9-16 are less than those observed, suggesting that the best-fit model crack strike may be a little too near the radial direction for this azimuth. Again, the anisotropic models represent a significant improvement over the isotropic models.

95

Figure 3.30. Multicomponent common sources gathers from a source depth of 3100 feet for the best-fit anisotropic cross-hole model. The Bois d'Arc reservoir zone contains distributions of micro-cracks striking N35E, with a crack density of 0.2.

Figure 3.31. Multicomponent common sources gathers from a source depth of 3575 feet for the best-fit anisotropic cross-hole model. The Viola limestone reservoir zone contains distributions of micro-cracks striking N35E, with a crack density of 0.2.

96

97

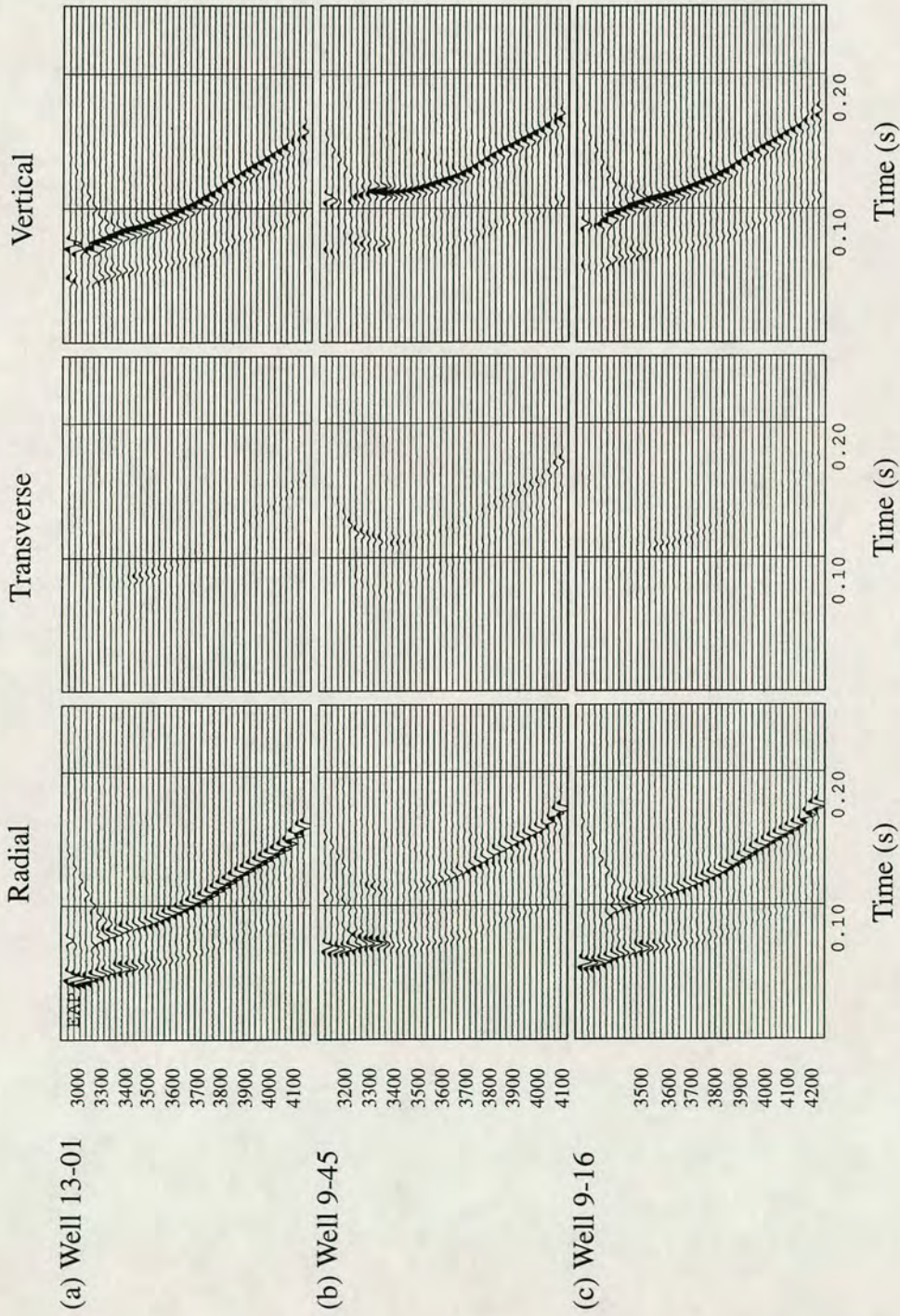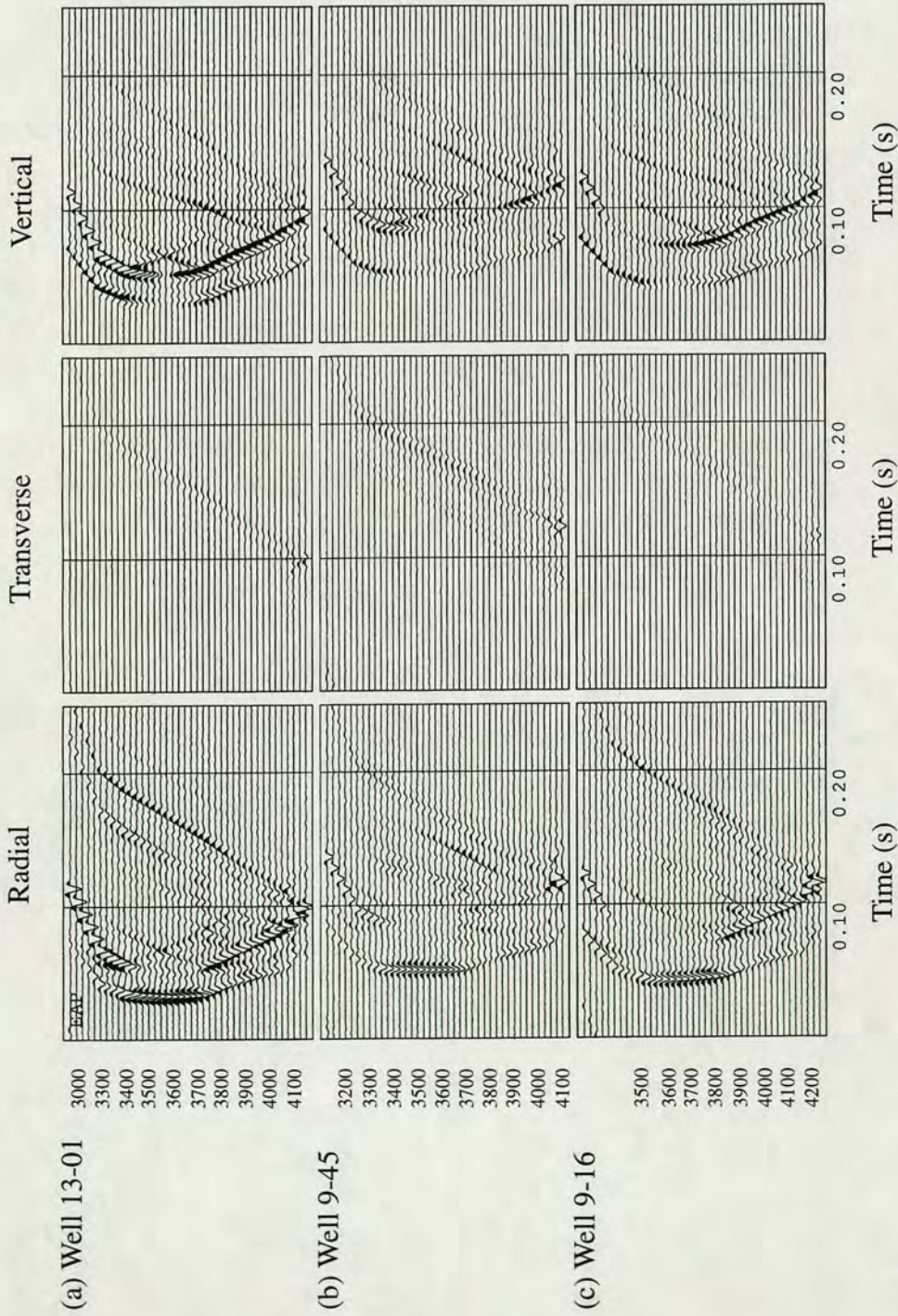Figure 3.32. Multicomponent common sources gathers from a source depth of 4150 feet for the best-fit anisotropic cross-hole model. The Viola limestone reservoir zone contains distributions of micro-cracks striking N35E, with a crack density of 0.2.
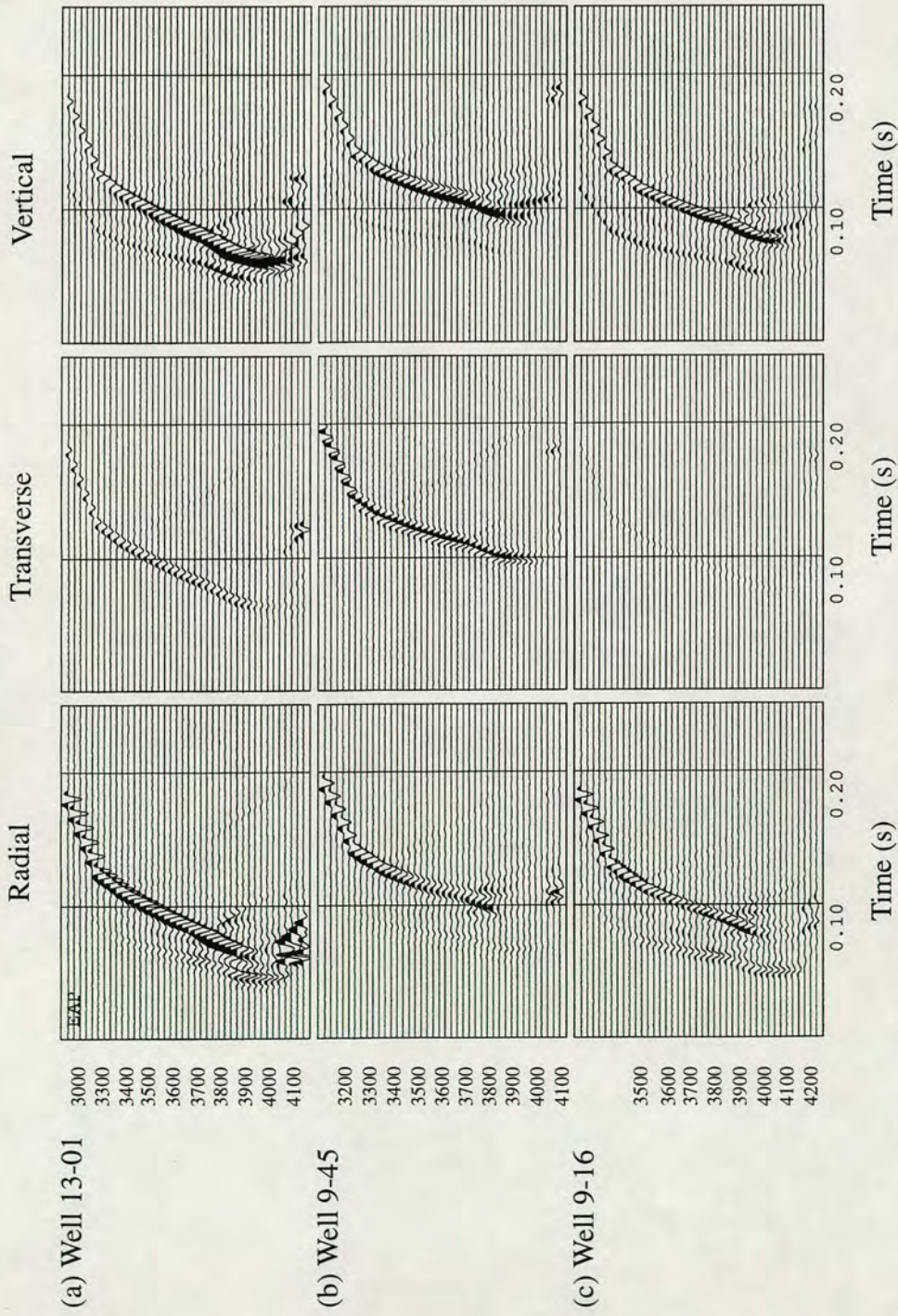
3.7 Discussion

Two reservoir rocks have been imaged using seismic waves propagating through and reflecting from the pay zone. Characteristics of the seismograms are indicative of shear-wave propagation in anisotropic media. This seismic wave behaviour can be effectively modelled by the inclusion of vertical fractures into the isotropic layered model. The elastic response of each layer can then be described by 5 (or possibly more) elastic constants.

Three classes of anisotropic model were considered. Model responses for varying crack strikes and crack densities were compared with the observed measurements of polarization and time delay. A weighted least-squares misfit function was used to determine those model responses which gave the best fit to the observations.

The best match to the observed polarizations was given by models in which only the low velocity reservoir layers contain cracks. However, observed time delays can also be modelled by lower crack densities distributed throughout all the model layers. This suggests that model crack orientation is the dominant influence on model fitness, whereas model crack density is poorly constrained.

Model crack strike directions from the three cross-hole azimuths can be compared with local stress directions in the Arkoma basin. Given the EDA hypothesis, fracture orientation is expected to comply with these directions. Results suggest that the best-fit crack strike of N35°E is sufficiently close to the expected direction of NE-SW, that the link between the two can be reinforced.

Reservoir anisotropy is found to be considerably stronger than expected. Crack densities of $\varepsilon=0.2$ for the best-fit model are significantly higher than many previous observations of anisotropy, where crack densities were commonly found to be less than 0.05. This may suggest that limestone reservoirs, such as those imaged here, may have higher crack densities than other types of reservoir rock, perhaps as a consequence of fractures being the only form of reservoir permeability.

Two methods have been used to calculate model responses. Firstly, by using

anisotropic ray-tracing to calculate $qS1$ polarization angles and time delays for particular azimuths and incidence angles. Secondly, by directly measuring polarizations and time delays from synthetic seismograms generated for the anisotropic models. Of the two methods, I would suggest that the former is to be preferred because it avoids the lengthy calculations and considerable expense of the latter. However, the latter has the advantage of applying the same treatment to the synthetics as to the observations.

Because of the constraints of the forward modelling approach, the considered solutions are limited to a subset of the possible model solutions. It is possible that better fits to the observed parameters may be achieved by considering other models. This problem is much more difficult to resolve and would almost certainly require the use of some form of optimized inversion procedure, as opposed to the trial and error approach utilised here.

Finally, it is possible that some of observed features of the cross-hole wavefield, such as the high amplitude reflected shear-waves from the 3575 foot source, may be explained by structural inhomogeneities rather than effective anisotropy of the reservoir formation. For example, dipping interfaces could give rise to out of plane reflections. Well deviations may exaggerate this. However, the calculated dip of the layers is small, ~6°, so this effect is likely to be minimal. This may be an area for future work.

CHAPTER 4. THE IATAN EAST HOWARD FIELD; A COMPARISON OF VSP AND CROSSHOLE SEISMIC DATA

4.1 Introduction

In this chapter, I compare the shear-wave splitting parameters measured in multicomponent vertical seismic profile and multicomponent cross-hole data. Both data sets were recorded from boreholes in the same hydrocarbon reservoir, at the Iatan East Howard field in Texas. The reservoir in question is known to contain distributions of vertical fractures with a strong alignment pattern in accordance with the regional trend (Wilkinson 1953).

My objectives were to investigate the seismic anisotropy of the reservoir by measuring the observed shear-wave splitting. I examine differences in the anisotropy of the rockmass imaged by the cross-hole and the VSP data. I also look at how the measurements of fracture direction, given by the $qS1$ polarizations, compare with the fracture orientation measured in core samples and by injection water breakthrough.

Shear-wave splitting is observed on all the VSP's, indicative of some form of seismic anisotropy. The two anisotropic parameters, $qS1$ polarization, and the time delay between the $qS1$ and $qS2$ arrivals are measured using two anisotropic estimation techniques. Polarization of the leading split shear-wave from the near offset VSP's is used to infer fracture orientation. Data modelling of the vertical seismic profiles, uses full waveform synthetic seismograms for propagation through both isotropic and effectively anisotropic media. A plane layered anisotropic earth model significantly improves the model's fit with the observations.

$QS1$ polarization directions and time delays are estimated for two cross-hole azimuths, using a numerical search technique. Both geophones and sources are positioned within the reservoir zone. The methods discussed in Chapter 2 are used to generate models of $qS1$ polarization direction and time delays within a fractured, anisotropic reservoir.

4.2 Geological background

The Iatan East Howard Field is situated in Mitchell County, Texas, on the Western edge of the Midland valley graben (Figure 4.1). In their evaluation of waterflood operations, Smith and Mitchell (1988) propose that oil production in this field is from laterally discontinuous, high porosity zones in Permian age Clearfork dolomites at between 2300 and 3200 feet. Pay zone reservoir parameters such as porosity and permeability vary from 4-17% and 0.1-120md, respectively.

Core samples indicate the presence of vertical fractures with an orientation of N65°E to N85°E (Mitchell 1985). The fractures also cause early breakthrough of injection water in producing wells during waterflood operations, when injector and producer wells are aligned with fracture direction. This fracture direction agrees with the regional fracture pattern which is NE-SW.

Permian stratigraphy in this area is summarised in Figure 4.2. and can be divided into four principal series. The Clearfork group directly overlies the Spraberry formation and has similar fracture distributions as the Spraeberry (Wilkinson 1953). Above the Clearfork dolomites are the Guadalupe series, consisting of interbedded dolomites and clastic beds, and the Ochoan series of redbeds, halites and anhydrites.

4.3 Data Acquisition

In September 1989 two multicomponent VSP's were recorded in the Iatan East Howard Field, Mitchell County, Texas. Acquisition geometry is described in Figure 4.3. The data were recorded simultaneously at two wells, I-130 and I-227, from both near offset and far offset source positions. The near offset source was positioned 336 feet. from I-130 with an azimuth of N85°E from the wellhead, and at 530 feet. from I-227, with an azimuth of N347°E from the wellhead. The far offset source was positioned 2753 feet from I-130 with an azimuth of N85°E from the wellhead, and at 2456 feet from I-227, with an azimuth of N73°E from the wellhead.

Omnipulse (Tinkle *et al.* 1989) was used as a source of *P*, *SH* and *SV* energy.
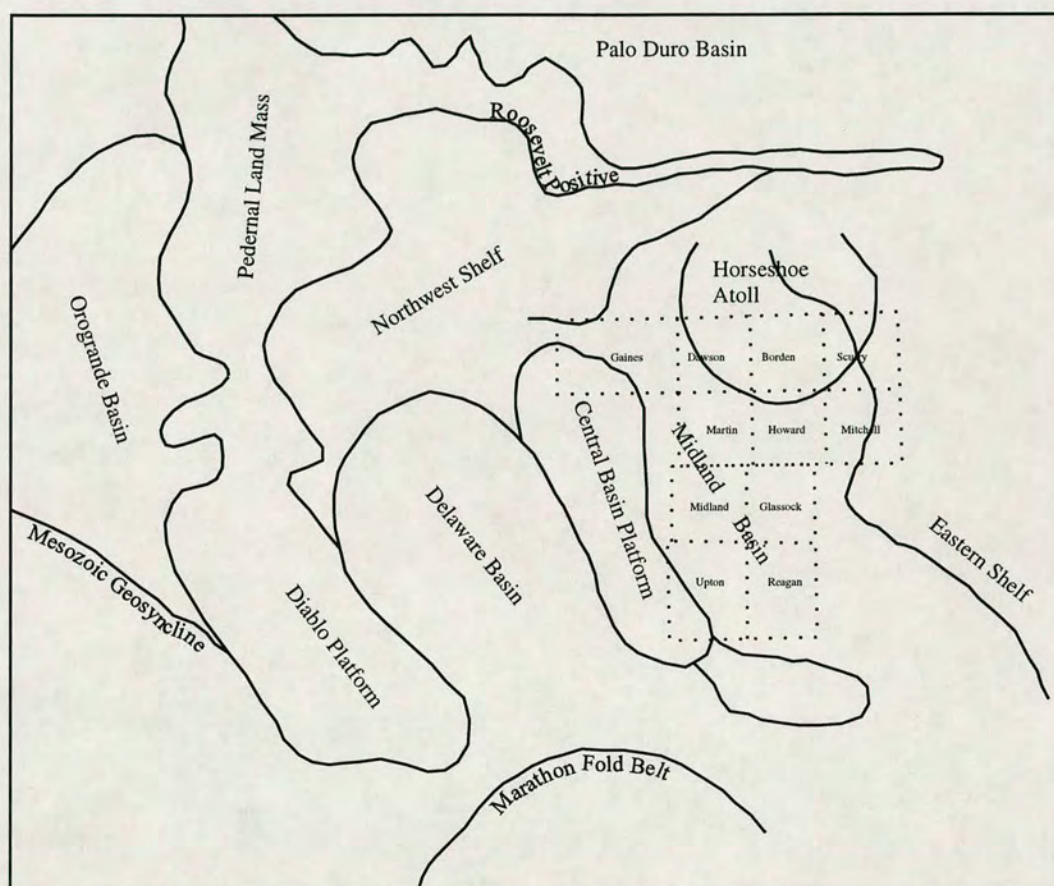
Figure 4.1. Major structural features of West Texas (after Owen 1975), showing Midland Valley. The Iatan East Howard field is located in Mitchell County, on the Eastern flank of the Midland Basin.

SYSTEM	SERIES	FORMATION	GROUP
PERMIAN	OCHOAN	DEWEY LAKE RUSTLER SALADO CASTILE	QUARTERMASTER
	GUADALUPIAN	TANSILL YATES SEVEN RIVERS QUEEN GRAYBURG	WHITEHORSE
		SAN ANDRES SAN ANGELO GLORIETA	PEASE RIVER
	LEONARDIAN		CLEARFORK
		SPRABERRY	WICHITA
	WOLFCAMPIAN	DEAN	

Figure 4.2 Permian stratigraphy of the Midland Valley.

I-152

I-130

Near offset
source

Far offset
source

I-227

N

1000 ft.

Figure 4.3. Acquisition geometry for Iatan VSP and crosshole experiment. The VSP's were recorded in wells I-130 and I-227from both near and far offset source positions. The crosshole data were recorded in wells I-152 and I-227, with sources in well I-130.
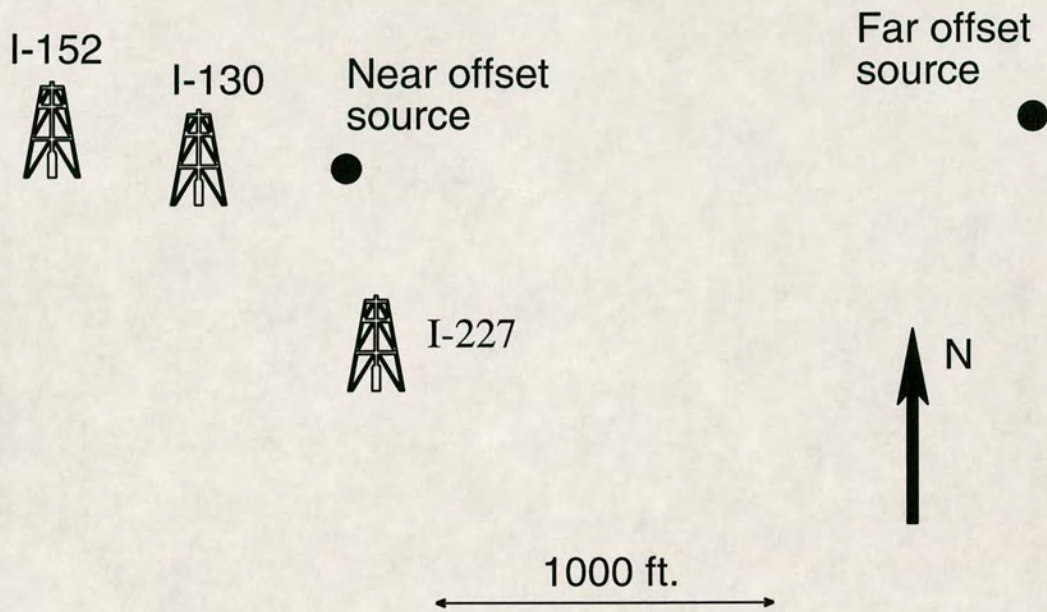
This source is a modified land airgun attached by a pivot to a baseplate which couples to the ground. The airgun can be tilted at an angle of up to 45° to the vertical to the left and right of the truck to generate shear waveforms with opposite polarities. Subtracting traces from left and right shots maximizes shear-wave energy while minimizing P-wave energy, which has a constant polarity. Similarly, addition of left and right shots will maximize P-wave and minimize shear wave energy. Generated SH and SV shear waveforms have been shown to be highly repeatable. For this survey, sources were oriented in both inline and crossline directions with both positive and negative polarities.

A variable receiver spacing and two separate geophone tools were used, resulting in three discrete sections for the I-130 VSP. Between 2500 and 3200 feet, the Bolt Wellseis multilevel 3 component tool was used, giving a 20 ft. receiver spacing in the zone of interest. Above this, a single SIE 3-component tool was used, at intervals of 300ft. between 300-1500ft. and 100ft. intervals between 1500-2500ft. Shooting was carried out from the bottom of the well upwards. A total of 50 levels were recorded in well I-130 for the near offset source. The far offset source was only recorded between 2500-3200ft. giving 36 levels.

For well I-227, a single SIE 3-component tool was used at depths of between 2767-3267ft, with a variable spacing, giving 10 near offset levels and 11 far offset levels. The geophone convention is right handed with Z positive downwards for all data.

The cross-hole data were recorded to carry out porosity mapping of the Upper Clearfork formation by waterflood EOR. Wells I-152 and I-227 were used as receiver wells A and B respectively. Forty-five geophone levels were used in each well, at depths between 2300 and 3265 feet, with a variable spacing of 10-35 feet. Sources were located in well I-130, also between depths of 2300 and 3265 feet, with forty-five separate positions similar to those in the receiver wells. Each shot was recorded for all receiver positions giving 2025 raypaths for each well

A downhole airgun was used as an impulsive source of both P- and S-wave energy, with shear waves generated by conversion at the fluid-casing interface around

the borehole. The source hung freely within the fluid column.

All data were recorded with a sample interval of 500 microseconds.

4.4 Multicomponent VSP

Shear wave splitting is observed on all the VSP's, indicative of some form of seismic anisotropy. Polarization of the leading split shear-wave is used to infer fracture orientation. The two anisotropic parameters, *qS1* polarization, and the time delay between the *qS1* and *qS2* arrivals are measured using two anisotropic estimation techniques. These measurements were confirmed by visual examination of seismograms and particle motions and then interpreted in terms of an effective seismic anisotropic reservoir, which contains distributions of parallel micro-cracks, striking in the *qS1* polarization direction and whose density is related to the observed time delays. Full waveform modelling is used to generate synthetic seismograms in vertically inhomogeneous anisotropic models, which are compared with the observed data.

4.4.1 Pre-processing

Processing flow is shown in Figure 4.4. Stacked data are sorted into a sequential order. Shots of opposite polarity are added and subtracted to give *P*- and *S*-wave sources respectively (see section 4.3).

Amplitude spectra of windowed *P*- and *S*-wave arrivals are used to design band pass filters which optimise noise reduction, leaving the desired part of the direct signal unaffected. Data were badly contaminated by high-frequency noise, particularly on the horizontal geophone components. Zero phase filters are used, to avoid any possible phase alteration to the shear waveforms. *P*-wave data are filtered using a 5-70 Hz bandpass. Shear wave data are filtered using a 5-30 Hz bandpass.

In the absence of gyrodata, *P*-wave arrivals from the far offset source position are used to align the geophones in the horizontal plane and correct for systematic twisting of the sonde as the tool was pulled up the hole. Polarization angles are
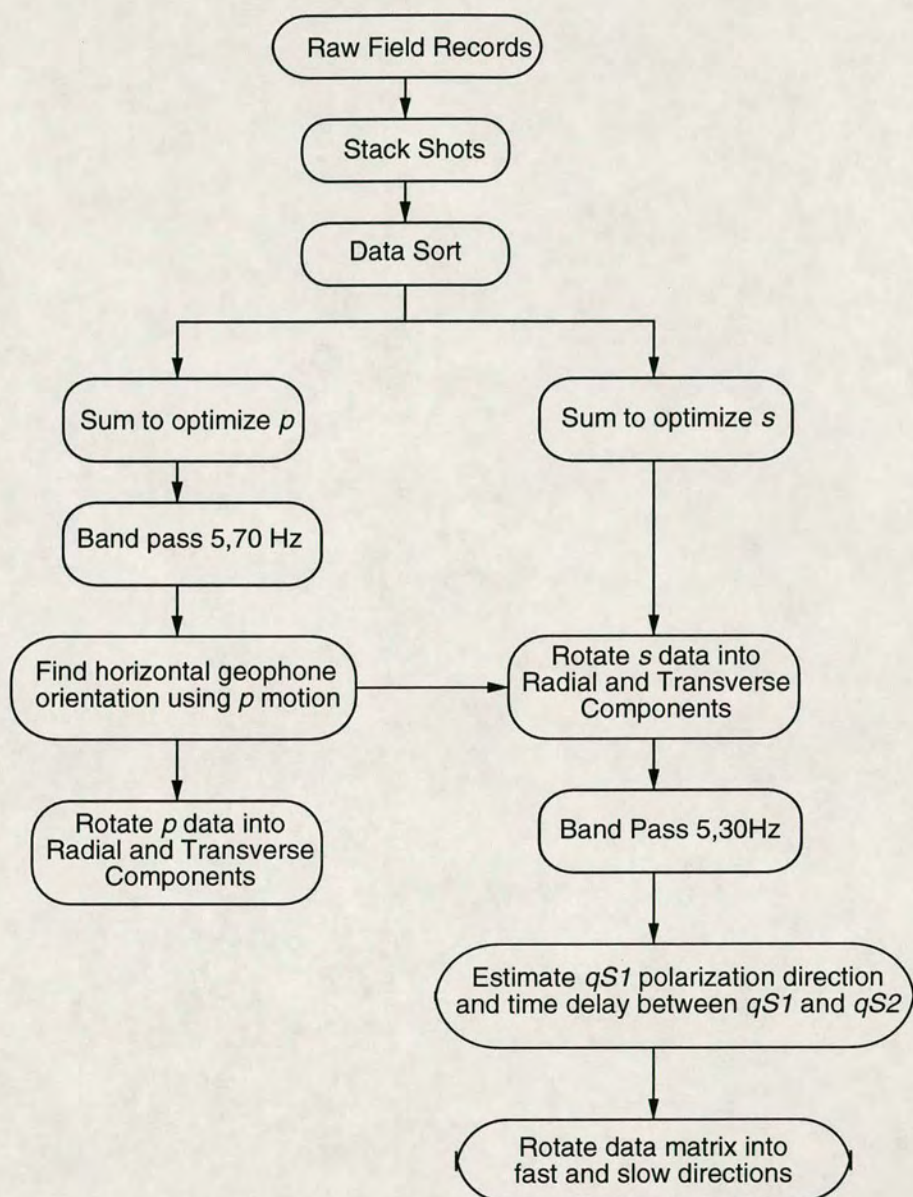
Figure 4.4. Processing sequence for Iatan VSP data

calculated by eigen analysis of the covariance matrix using a 0.025s window about the initial *P*-wave arrival. First breaks are picked from the vertical component. Data from near and far offset sources in well I-227 are rotated in the same way. These rotation angles for each geophone are then applied to the shear wave sources.

Four component near offset and nine component far offset data from well I-130 are displayed in Figures 4.5 and 4.6 as examples of data quality. Data from well I-227 are of a similar quality. The multicomponent data are represented as matrices, with columns corresponding to the source orientation and rows corresponding to the geophone component the data was recorded on (Tatham and McCormack 1991). Four and nine component data are represented by 2×2 and 3×3 matrices respectively. This facilitates the application of matrix algebra for processing and interpreting the shear waves.

Examination of Figure 4.5 shows that the primary shear-wave arrival has two cycles followed by lower amplitude arrivals. Most of the shear-wave energy appears on the components parallel to the source orientation, for example the energy imparted into the ground by the inline source appears mainly on the inline (radial) horizontal geophone component. Visual comparison of the near offset arrival times in Figure 4.5, indicates a noticeable time shift between arrivals on the radial and transverse components. Shear waves on transverse component are clearly in advance of those on the radial components.

The pulse shape is consistent between all levels for the I-130 inline source, Figure 4.5, with a peak frequency of around 17hz, although the period appears to lengthen with depth. Below 3050 feet, the I-130 near offset crossline source shows a noticeable change in wavelet shape. This wavelet instability is also observed on the I-227 near offset inline source component. Given that both are generated by the same source truck, one possible explanation for such instability could be poor coupling between the source baseplate and the ground.
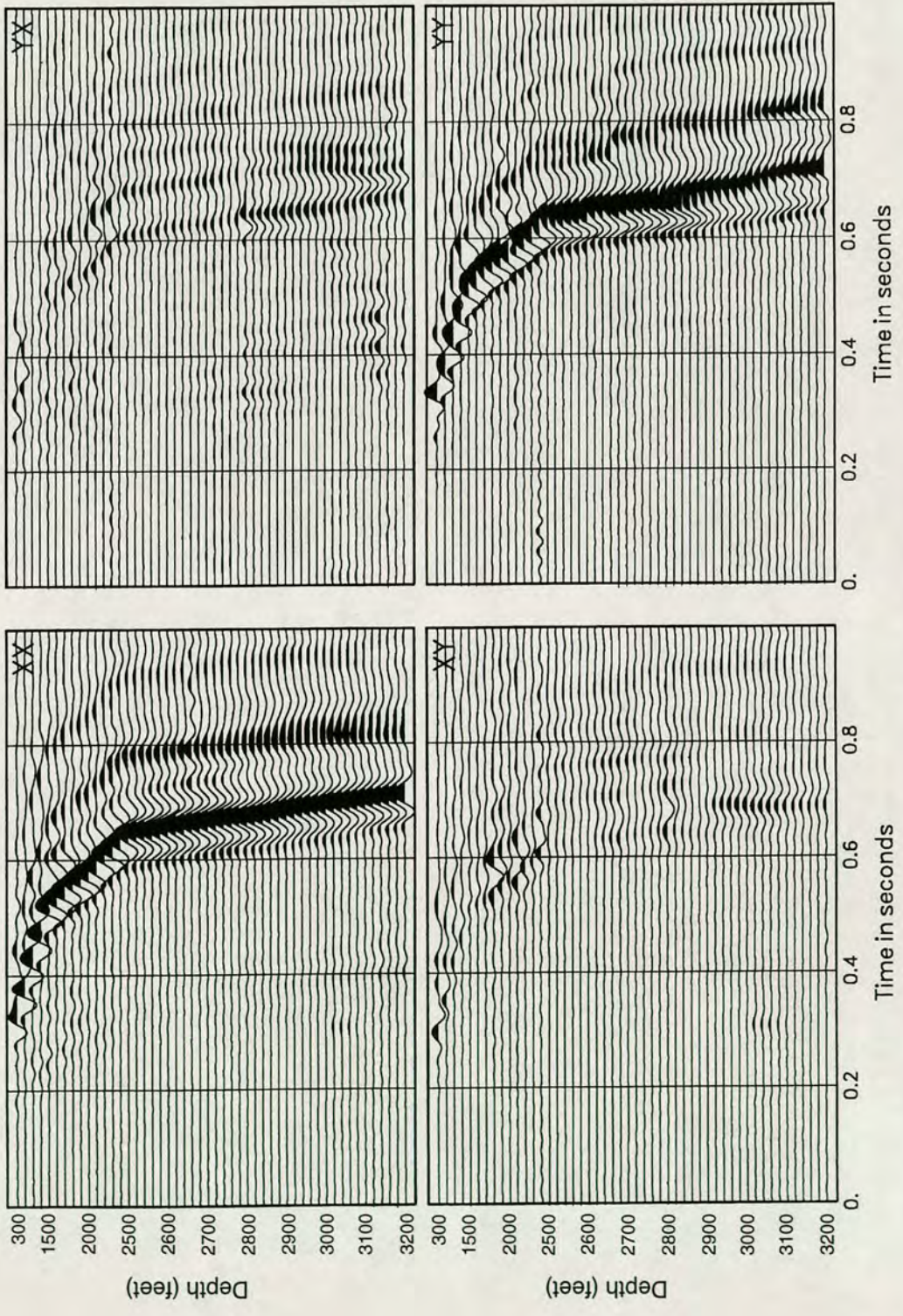
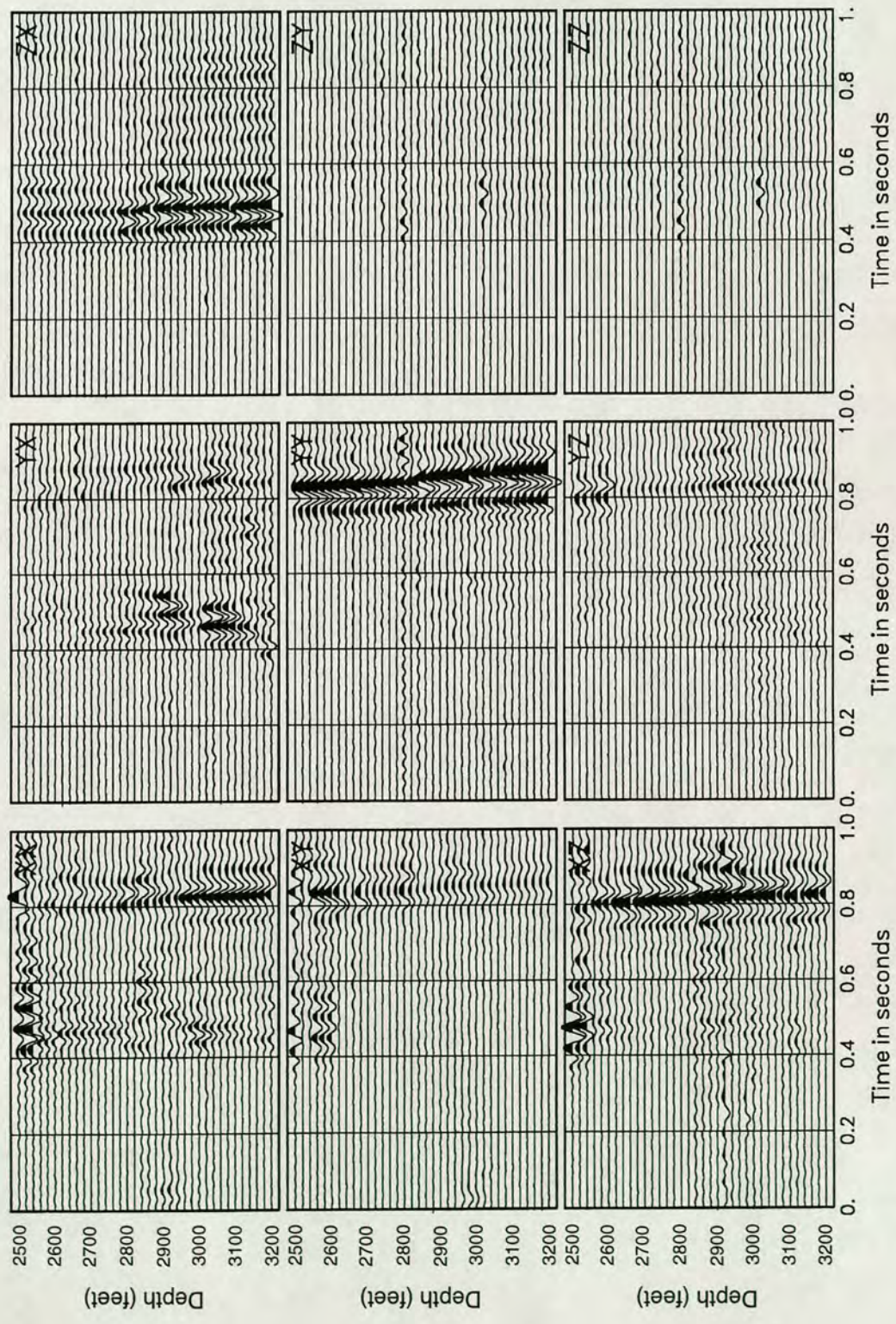Figure 4.5. Four component data matrix for well I-130, near offset source.

Figure 4.6. Nine component data matrix for well I-130, far offset source.

4.4.2 Shear-wave splitting measurement

Examination of shear-wave particle motion in the plane perpendicular to the raypath is used, firstly as a visual quality control measure, and secondly to ensure that measurement of the parameters of shear-wave splitting gives reasonable results. Horizontal plane particle motion diagrams for selected geophone levels from I-130 and I-227 near offsets are shown in Figure 4.7 for both inline and crossline sources. Particle motion is sub-linear, suggesting that the anisotropic response is close to azimuthal isotropy, so shear-wave splitting is minimal. However, given that the acquisition direction is sub-parallel to the regional fracture trend, we would expect any observed shear-wave splitting to be low. The natural polarization direction being approximately parallel to acquisition for I-130 near and far offset and I-227 far offset, and perpendicular to acquisition in I-227 near offset.

Polarizations of the leading split shear-wave and time delays between the *qS1* and *qS2* arrivals are measured using two algebraic techniques which are based on a convolutional model for wave propagation through a uniformly anisotropic solid. Both methods find an algebraic solution to the recorded shear wave data matrix, or medium response. A full explanation of the two methods, the *dual cumulative technique*, *DCT*, and the *dual independent technique*, *DIT*, may be found in the publication by Zeng and Macbeth (1993a). *DCT* employs synchronous rotations of both source and geophone, similar to an Alford type rotation (Alford 1986), to minimize the off-diagonal elements of the data matrix by direct eigen-analysis. This gives a single angle θ for the directional medium response. In *DIT*, sources and geophone are rotated separately and minimization of the off-diagonal elements is achieved by singular value decomposition of the data matrix, giving two estimates of polarization angle: θ_g the angle from the radial geophone component and θ_s, the angle from the inline source direction. In both cases, the time delay, $\Delta\tau$, is calculated by cross-correlation of the diagonal elements after minimization.

Both these estimation techniques can give accurate results for synthetic seismograms generated for propagation through anisotropic media, where the data
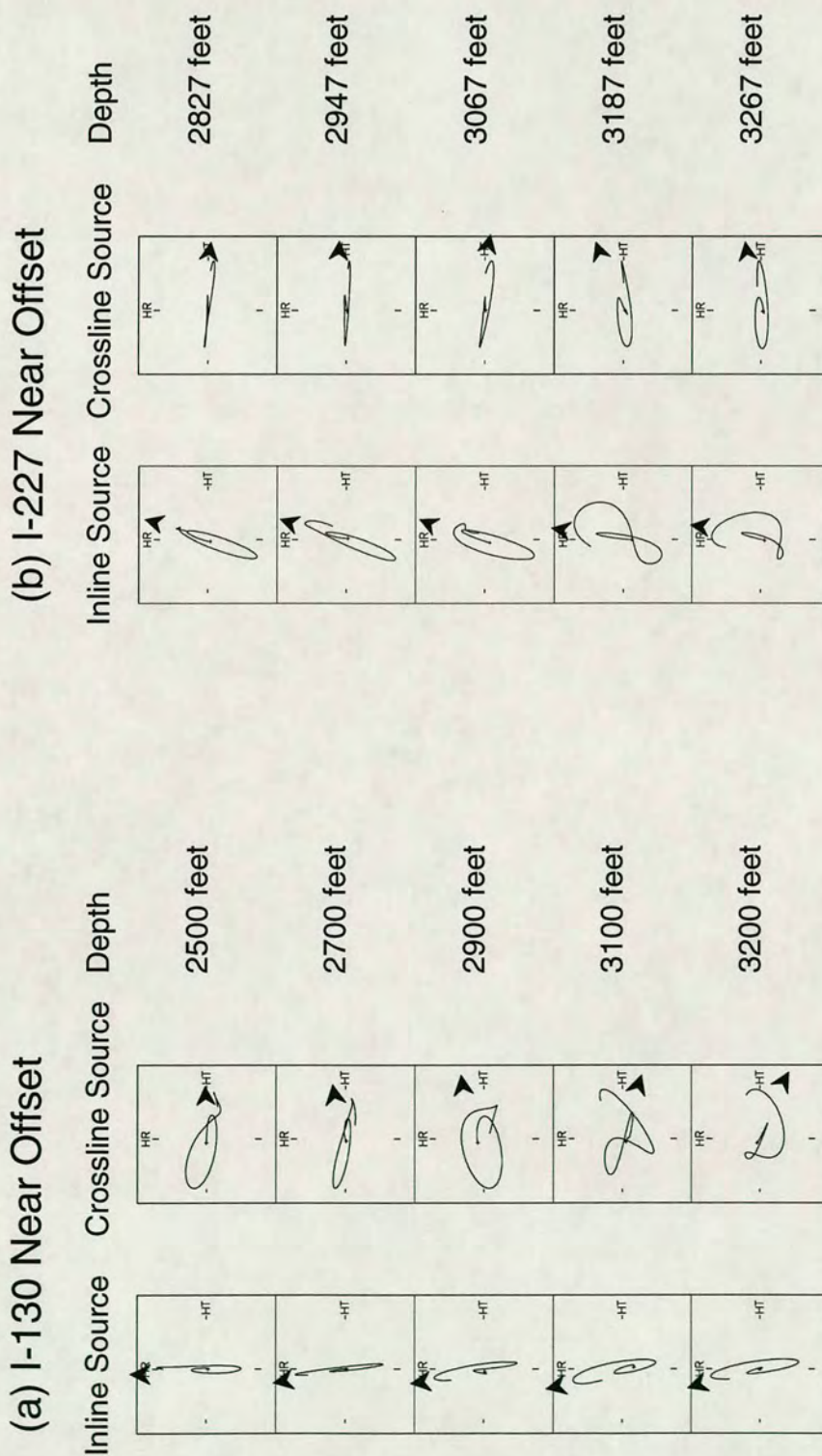
Figure 4.7. Horizontal plane particle motions of windowed shear-wave arrivals from (a) I-130 near offset VSP and (b) I-227 near offset VSP.

matrix is symmetric. Zeng and MacBeth (1993b) have investigated how small degrees of data matrix asymmetry can effect the results. Asymmetry may be due to common acquisition errors such as source and geophone misalignment and source energy imbalance effect results. In general, both methods were found to be tolerant of small experimental errors introduced in modelled seismograms, and still provide well resolved solutions.

The main requirement for successful application is that fast and slow shear waves are orthogonal. MacBeth and Yardley (1992) show how these techniques can give erroneous results where crack strike changes with depth, resulting in multiple shear-wave splitting and subsequent data matrix asymmetry.

Figure 4.8 shows the results of *DCT* and *DIT* for near offset data from wells I-130 and I-227. Measurements are made using a variable length time window (start and end times picked interactively) encompassing the first cycle of the shear wavelet. Tests using various windows suggest that the techniques show some instability to variation in window size, caused by the change in wavelet shape on the crossline source. Both methods give a *qS1* polarization direction of approximately N170°E below a depth of around 1700 feet. Above this, coverage is poor and polarizations are scattered.

In well I-130 time delays are close to zero in the near surface and increase sharply to around 10ms, between 1700 and 2300 feet. Between 2300-2700 feet delays increase only slightly. Below this, the delay continues to increase slowly to a maximum of around 15ms. Time delay estimates from well I-227 also show time delays gradually increasing between 2700-3300 feet, within the reservoir zone.

Results of *DCT* and *DIT* for the far offset data are shown in Figure 4.9. The *qS1* polarization estimates for I-130 show considerable scatter around N70°E to N80°E. Well I-227 shows convergence of *DIT* source and geophone angles to N60°E. Time delays in I-130 show a linear increase from close to 0ms at 2700 feet to approximately 8ms at 3250 feet. I-227 shows a very similar pattern of time delays to I-130, increasing to around 10ms at 3300 feet.

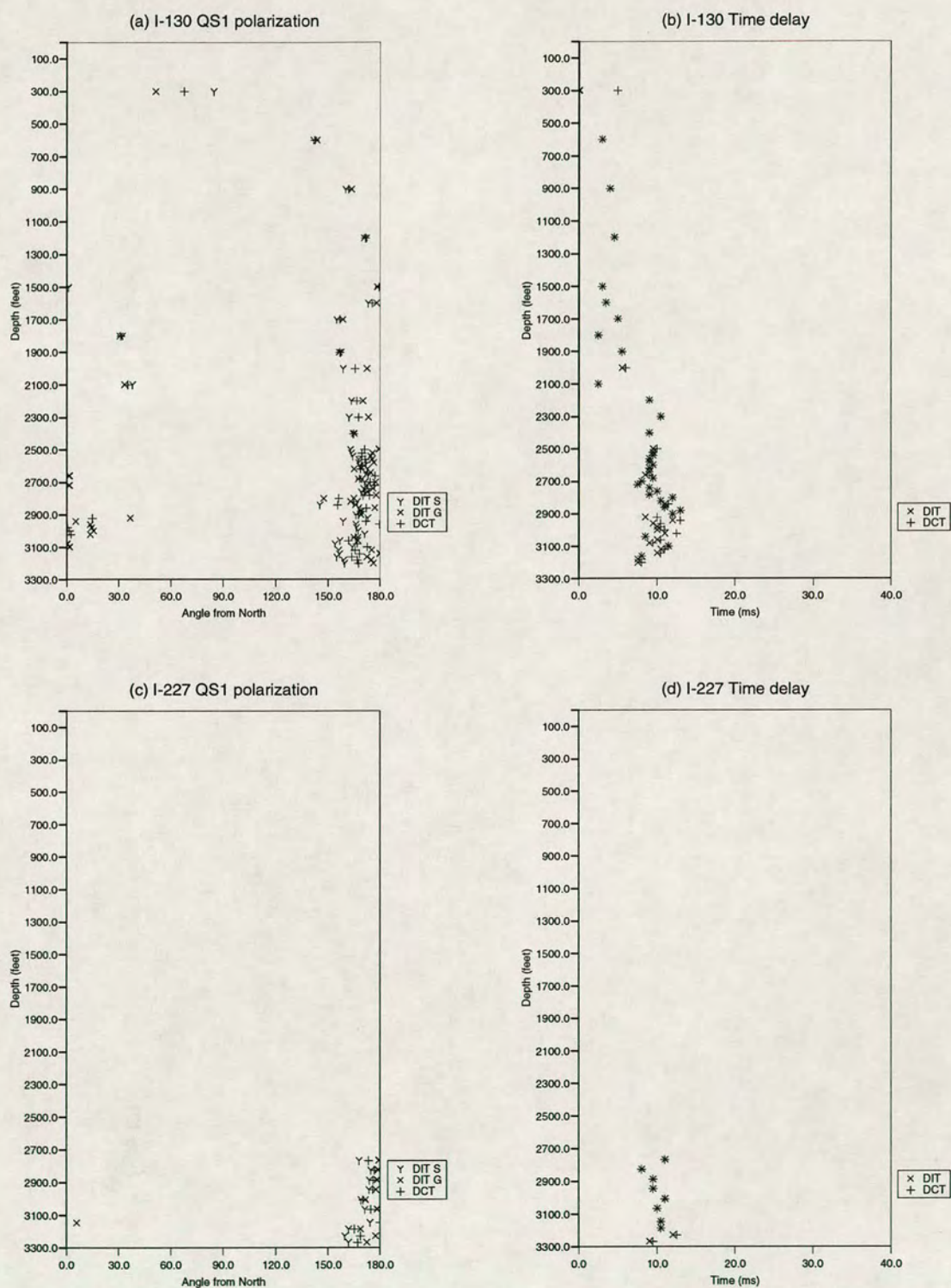Figure 4.10 (a) shows the measured *qS1* polarizations, estimated by *DCT*,

Figure 4.8. Estimation results using DCT and DIT for near offset data.
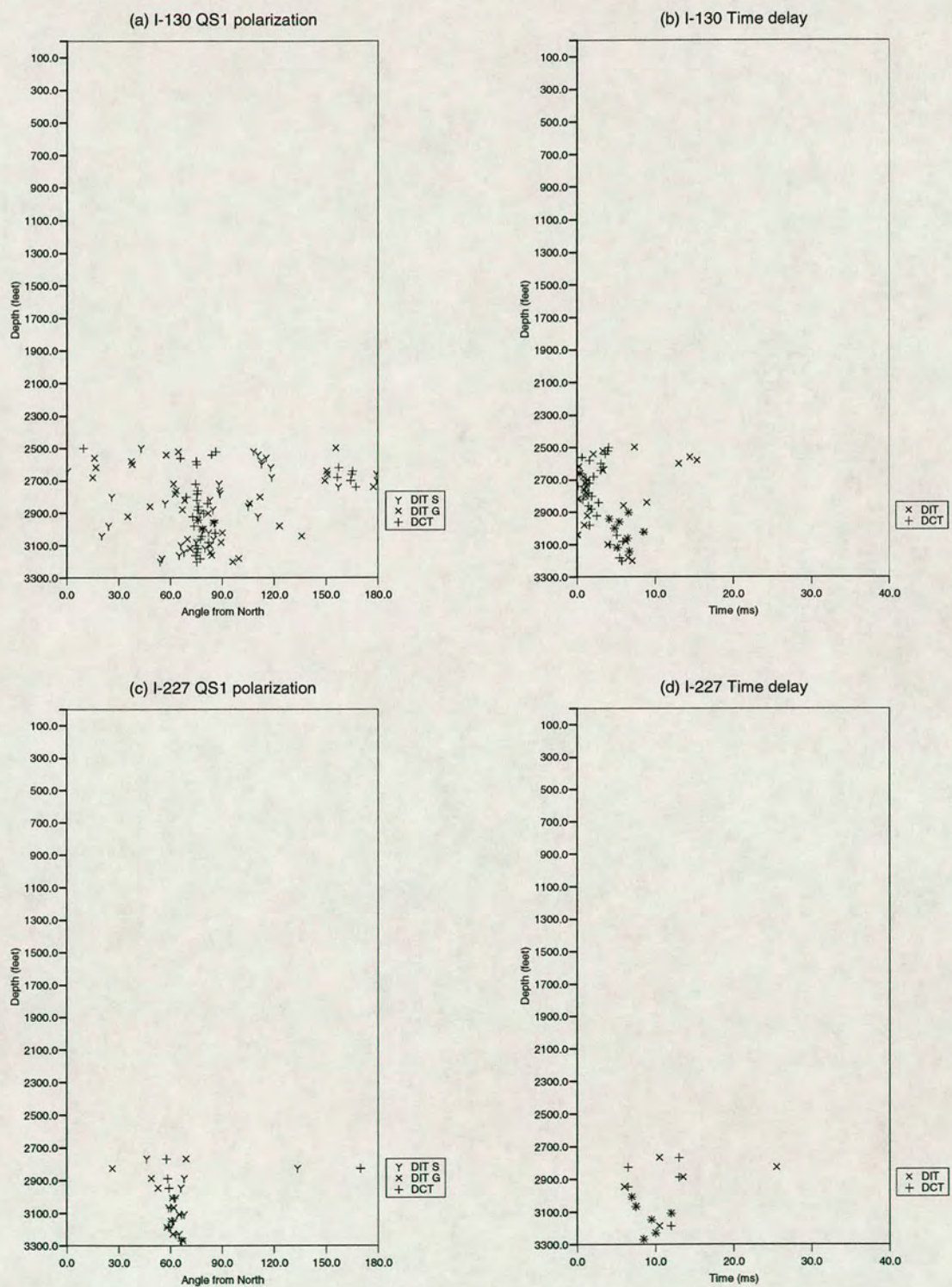
Figure 4.9. Far offset estimation results from wells I-130 and I-227.
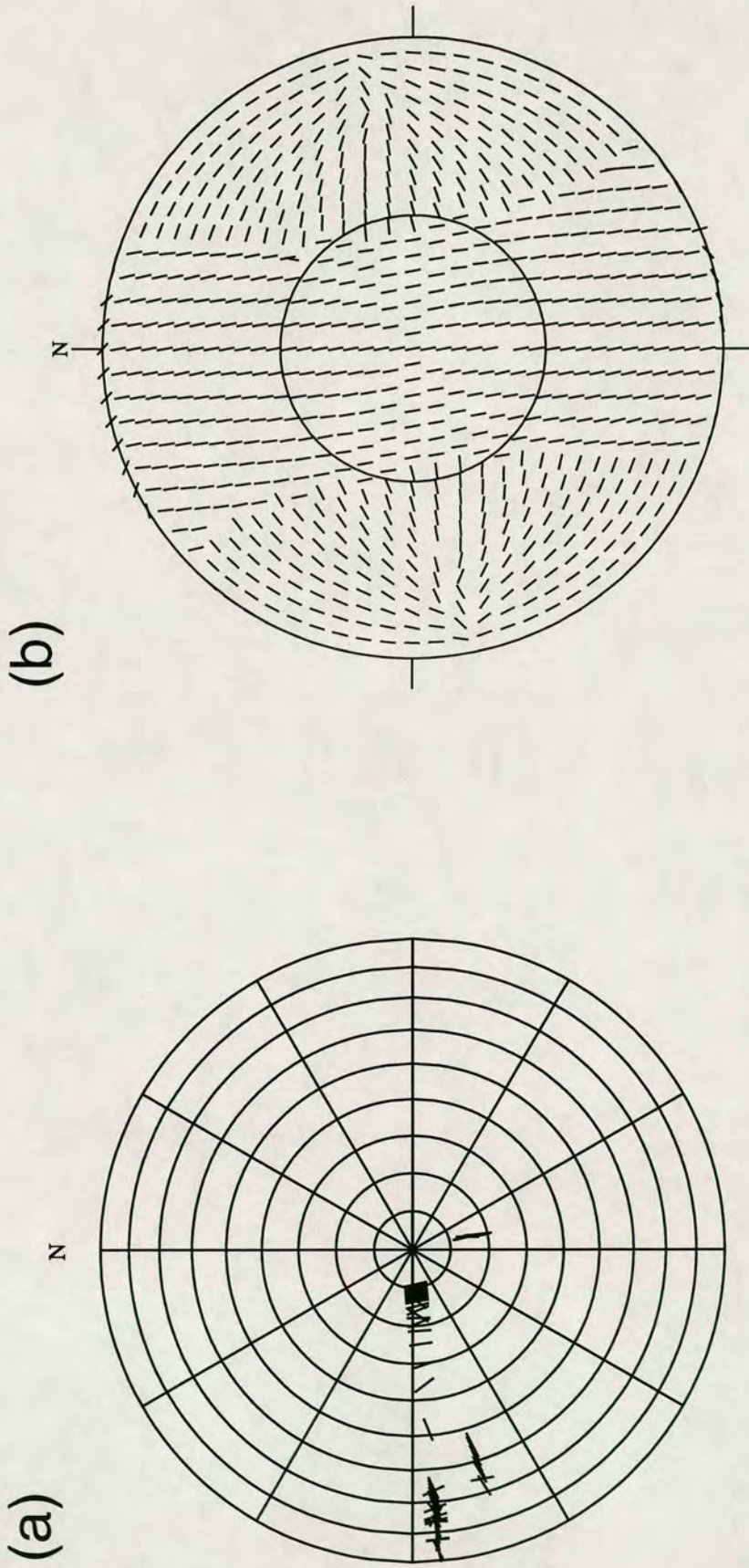
Figure 4.10. Observed horizontal plane *qS1* polarizations, (a), measured from Iatan VSP data in wells I-130 and I-227, plotted on equal area projection. Polarizations shown are calculated using the DCT method. The horizontal plane qS1 polarizations for rays propagating at group velocity, shown in (b), calculated for an anisotropic halfspace, containing distributions of vertical microcracks, with crack density 0.05 and aspect ratio of 0.001, striking 170° from North, are shown for comparison

plotted on an equal area projection. The polarizations for near-vertical propagation can be used to infer the direction of crack strike, given as N170°E. For comparison, Figure 4.10 (b) shows the horizontal plane $qS1$ polarizations calculated for an anisotropic half-space containing distributions of vertical micro-cracks, modelled using the formulations of Hudson, 1986. The micro-cracks have a crack density of $\varepsilon=0.05$ and aspect ratio $\gamma=0.001$, and strike N170°E. On visual examination the half-space model provides a good fit for the near-offset observations, but differences are apparent for the far-offset measurements.

4.4.3 Deriving a velocity structure

Direct P-wave arrival times from the Iatan VSP's are timed to within ±0.5ms, using an interactive picking routine. The error given above is that due to uncertainty in the first break pick, which may be obscured by noise. I use the layer stripping algorithm developed by Pujol, Burridge and Smithson (1985), to invert the traveltimes to each geophone and obtain interval velocities between the geophone levels for each source location. This method is a simple iterative procedure whereby the velocity of each layer is calculated in turn. For a given layer, the take-off angle for the ray arriving at the bottom of the layer is varied until the difference between the velocity computed from the traveltime and that obtained from Snell's law is minimized. The method requires as many layers as geophone levels.

Interval velocities derived from this procedure are plotted against depth and displayed in Figure 4.11(a). Breaks in this curve are considered as layer boundaries, allowing the derivation of a coarser velocity structure, where layers include more than one geophone. The near surface structure is poorly resolved, as the geophones are spaced at intervals of 300 feet, the top three geophones are considered to be contained in separate layers.

Similarly, S-wave arrival times are picked for both the fast and slow shear-wave components. The results of inversion of these traveltimes are shown graphically in Figures 4.11 (b) and (c). Layer boundaries may be inferred at the same depths as
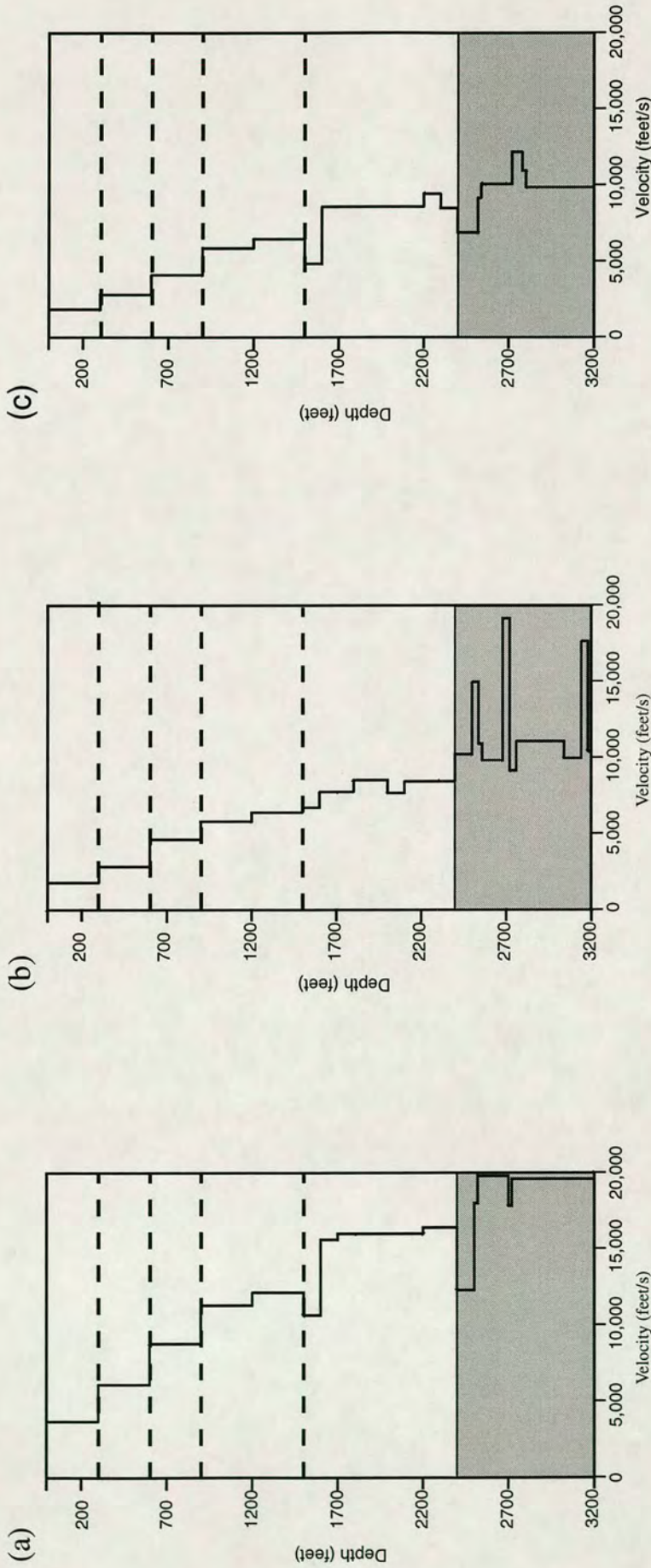
Figure 4.11. Results of traveltime inversion for: (a) direct *p* arrivals; (b) *qS1* arrivals; and (c) *qS2* arrivals. The velocity structure is divided into a four layer model on the basis of these results.

118

Table 4.1. *P*- and *S*-wave velocities from inversion of traveltimes from I-130 near offset VSP.

Thickness	v_p	v_{s1}	v_{s2}	ρ	% difference
300	3692	1795	1846	1.79	2.75
300	6113	2845	2800	2.03	1.58
300	8798	4611	4125	2.23	10.54
600	11735	6087	6143	2.39	0.91
900	15439	8040	8260	2.56	2.66
800	18575	10456	9458	2.68	9.54

those given from the *P*-wave analysis. This gives a six layer velocity structure, based on the traveltime information, the deepest layer corresponding to the high velocity dolomites of the Clearfork formation. The velocities and densities for this model are shown in Table 4.1. Densities are calculated from the *P*-wave velocities, using the empirical relationship given in the paper by Gardner, Gardner and Gregory (1974).

Far offset traveltimes from well I-130 were also inverted to give a comparison of horizontal and vertical *S*-wave velocities within the reservoir zone below 2400 feet. Since far offset geophone levels were only recorded between 2400-3200 feet, the velocities of the first five layers given by inversion of the near offset times, were input into the inversion scheme for the far offset traveltimes. The results of the inversion procedure for the far offset traveltimes are shown graphically in Figure 4.12 and also in tabular form in Table 4.2.

The difference between horizontal and vertical *S*-wave velocities, can be interpreted as evidence of transverse isotropy with a vertical axis of symmetry and around 10% differential *S*-wave velocity anisotropy. Alternatively, the discrepancy between horizontal and vertical velocities may be caused by structural inhomogeneity or steeply dipping layers. However, the horizontal *P*-wave velocities calculated from the far offset arrival times do not show much variation from the vertical. Steeply dipping layers are unlikely given the gentle dip of sediments in this area of the basin.

4.4.4 Anisotropic modelling

My next step was to interpret the above anisotropic estimates and velocity results, in terms of an anisotropic model containing cracked, effectively anisotropic layers, which could be input to the Aniseis full-wave modelling package. The *qS1* polarization direction in I-130 near offset is consistent below 1500 feet, at N170°E. This is taken as the fracture direction to be input into Aniseis as an initial starting point.

Crack densities may be evaluated approximately by the time delay curves. Time delay increases from 0 to 10ms between 1500 and 2400 feet. Given a *qS1*
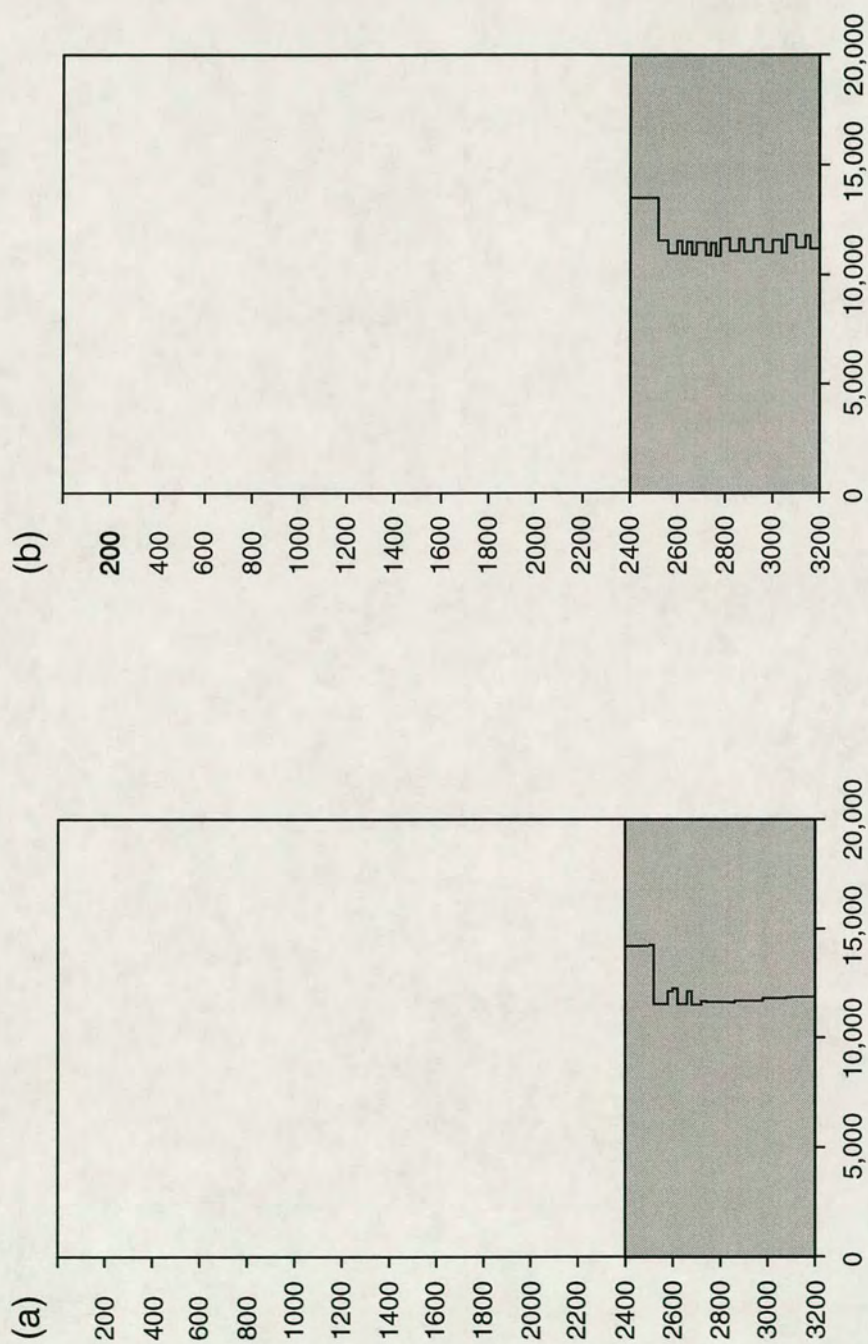
Figure 4.12. Traveltime inversion of I-130 far offset *s* arrivals. (a) *qS1*, (b) *qS2*. Data were only recorded between 2400 and 3200 feet. Above this I assume the same velocity structure as that derived for the near offset data.

Table 4.2. *S*-wave velocities from inversion of traveltimes to geophones within the Clearfork reservoir formation, for well I-130, near and far offset source positions.

I-130 Near offset		I-130 Far offset	
V_{S1} (ft/s)	V_{S2} (ft/s)	V_{S1} (ft/s)	V_{S2} (ft/s)
10456	9458	11722	11280

velocity of 8040ft/s, and assuming vertical incidence, the fast shear-wave will travel this distance in Δt_{s1}=112ms. Thus the slower shear-wave will take Δt_{s2}=122ms, giving a *qS2* velocity of 7371ft/s. The percentage difference velocity anisotropy of 8% can be equated to a crack density of about ε=0.08. Similarly, between 2400 and 3200 feet, the time delay increases from 10 to 14.5ms. Given a *qS1 velocity* of 10456ft/s, the *qS1* traveltime will be approximately 76.5ms and the *qS2* traveltime, 81ms. This gives a *qS2* velocity of 9876ft/s. Here, the percentage difference in the two velocities is 5.5% and can be represented by a crack density ε = 0.05. Above 1500 feet, time delays are very small, so the structure is assumed to be isotropic. Figure 4.13 shows a schematic representation of the anisotropic structure derived for the Iatan VSP model. The properties of the model are summarized in Table 4.3.

Given these parameters as an initial starting point I then generated synthetic seismograms for a range of anisotropic models. For each models, I measured the shear-wave splitting parameters, *qS1* polarization and time delay between *qS1* and *qS2* arrivals, using *DCT*. A qualitative comparison of the observed and modelled splitting parameters was used to determine the best-fit model.

Firstly, I considered models with crack anisotropy in the Clearfork reservoir formation only. Three crack orientations, N5°E, N95°E and N165°E and crack densities of ε=0.05 and 0.1 were examined. Models with a crack strike of N95°E proved to be a good match to the far offset observations. However, these models were discounted on the basis that they were unable to explain the build up in time delays above the reservoir zone from the near offset observations.

Secondly, I considered models with an anisotropic layer immediately above the reservoir and an isotropic reservoir layer. The same crack orientations and crack densities as above were examined. Modelled delays within the reservoir layer were found to be too low to match the observations at both near and far offsets.

I then generated synthetic seismograms for models with anisotropy in both layers. I examined crack orientations of N145°E, N155°E, N160°E, N165°E, N170°E, N5°E. An orientation of N170°E was found to give the best fit to the observed *qS1* polarizations. Crack densities of ε=0.05, ε=0.08 and ε=0.1 were examined. But a
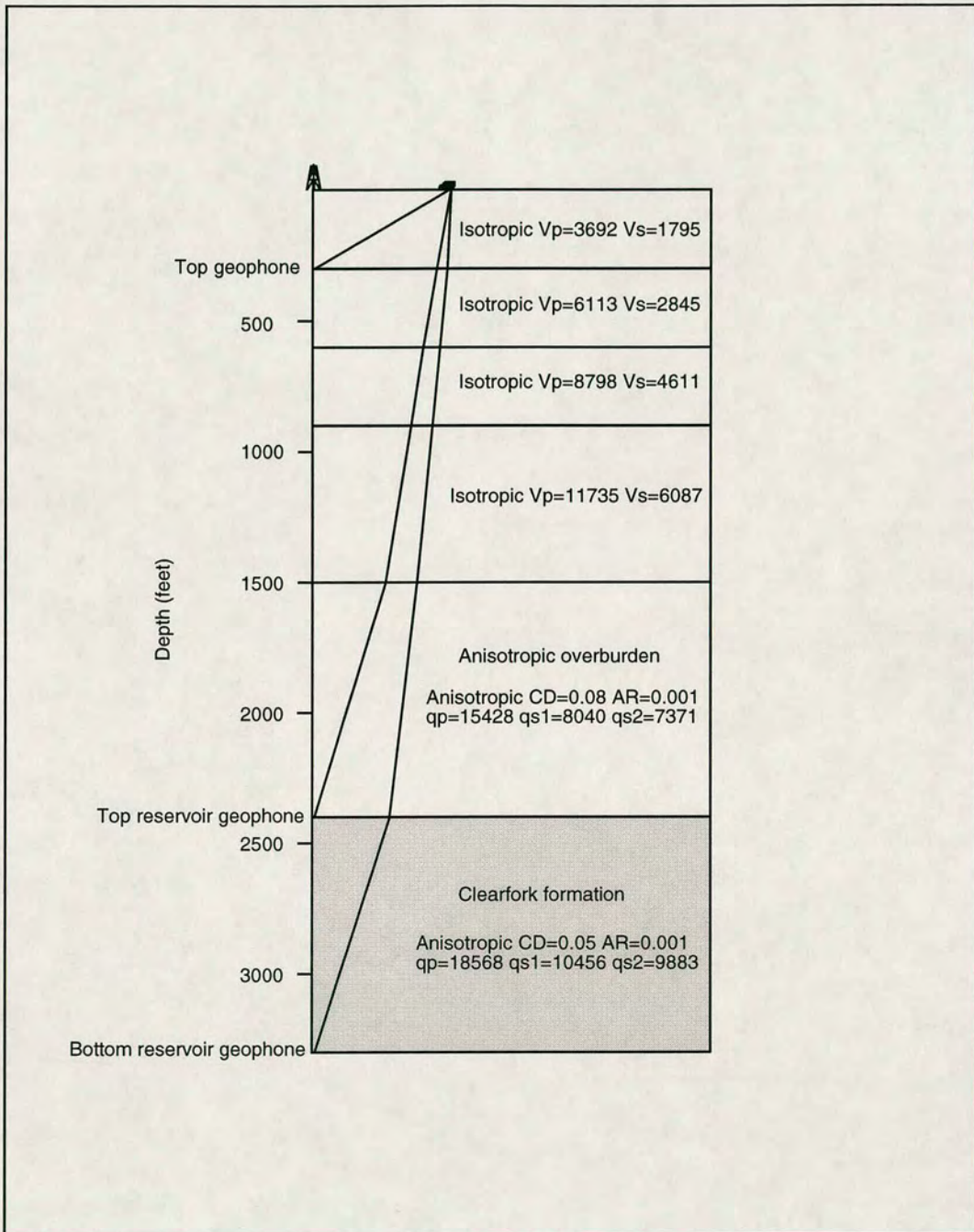
Figure 4.13. Anisotropic structure for initial Iatan VSP models.

Table 4.3. Parameters for the Iatan VSP model used for generating synthetic seismograms.

Thickness (feet)	Isotropic v_p (ft/s)	Isotropic v_s (ft/s)	Crack density	Crack radius (m)	Aspect ratio	Crack content	Crack strike
300	3692	1795	-	-	-	-	-
300	6113	2845	-	-	-	-	-
300	8798	4611	-	-	-	-	-
600	11735	6087	-	-	-	-	-
900	15428	8040	0.08	0.001	0.001	wet	N170°E
800	18568	10456	0.05	0.001	0.001	wet	N170°E

combination of ε=0.08 in the upper layer and ε=0.05 in the reservoir layer was found to give the best match to the observations of time delay.

Full-wave synthetic seismograms generated for the above model are shown in Figures 4.14 and 4.15, for near and far offset source positions, well I-130. A comparison of the modelled seismograms with the observed data shows that the model provides a good fit in terms of traveltimes and the character of the waveforms. The pulse shape used in the models was extracted from an averaged pulse shape from I-130 near offset data.

The DCT results for the model are displayed alongside those for the observed data in Figures 4.16 and 4.17. Figure 4.16 shows the DCT polarization measurements for each of the four VSP's displayed on equal-area polar projections for (a) observed; and (b) modelled seismograms. These diagrams show that a good fit has been achieved for the near offset observations within 20° of vertical propagation and for the I-130 far offset VSP. Measurements from the I-227 far offset VSP models show some differences in the polarization azimuth of around 15°-20° to those from the actual data.

Figure 4.17 shows the time delays measured by DCT for the modelled seismograms, marked by a solid line for each VSP, with the observed time delays at each geophone level, marked by a cross. Again it is apparent that the best fit is for the near offset data, but a large discrepancy clearly exists for the far offset time delays.

I have shown above that the Iatan VSP data can be reasonably modelled by propagation through effectively anisotropic media, however, two main points are worthy of closer attention. Firstly, the crack strike in the reservoir zone is approximately 90° different to that measured from core samples and injection water breakthrough. Secondly, the model does not provide an adequate fit for the far offset arrival times. I will show in the next section that the inclusion of transverse isotropy, modelled by horizontal micro-cracks, can provide a better fit for the far offset observations.
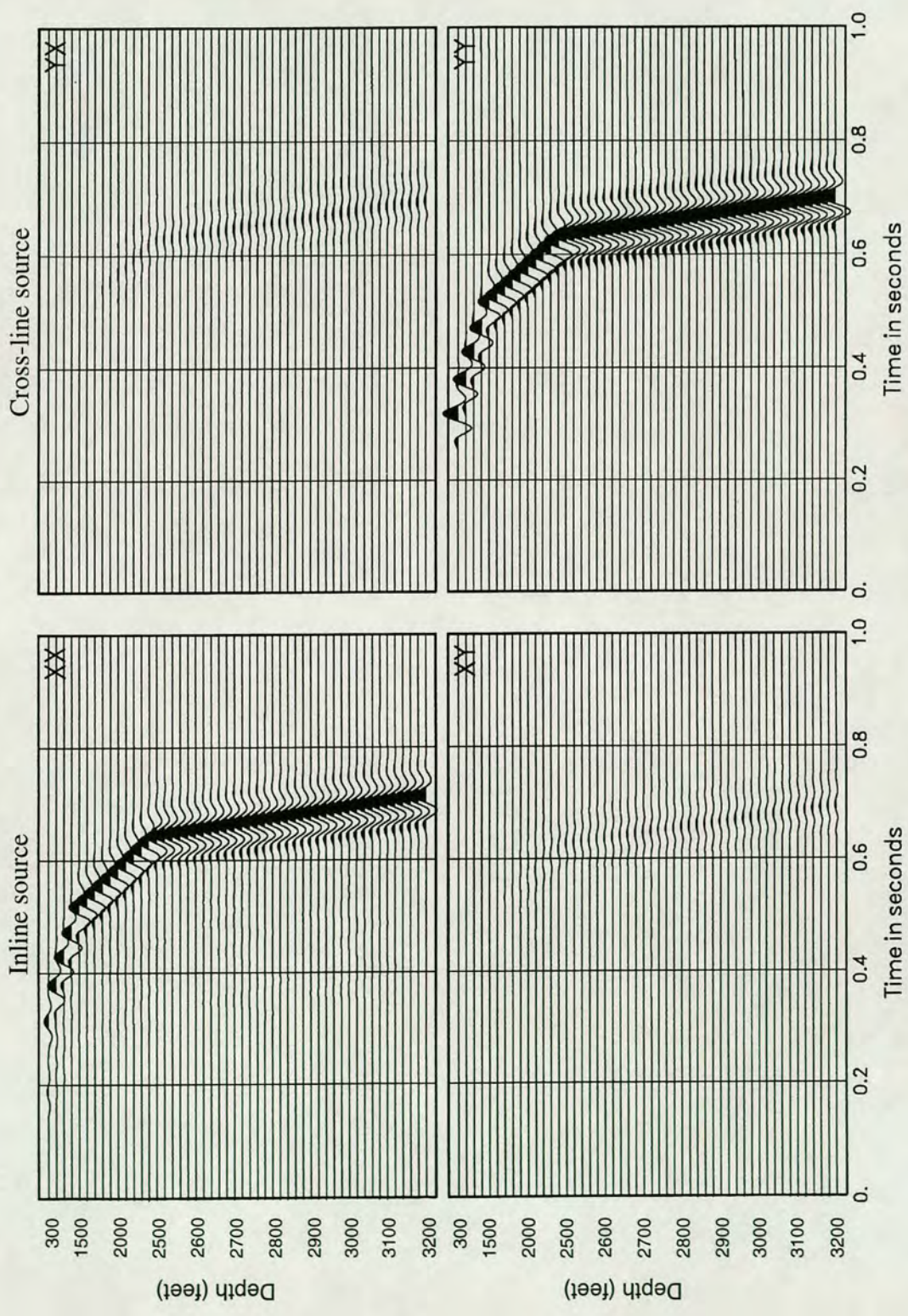
127

Figure 4.14. Four component data matrix for anisotropic model well I-130, near offset source.

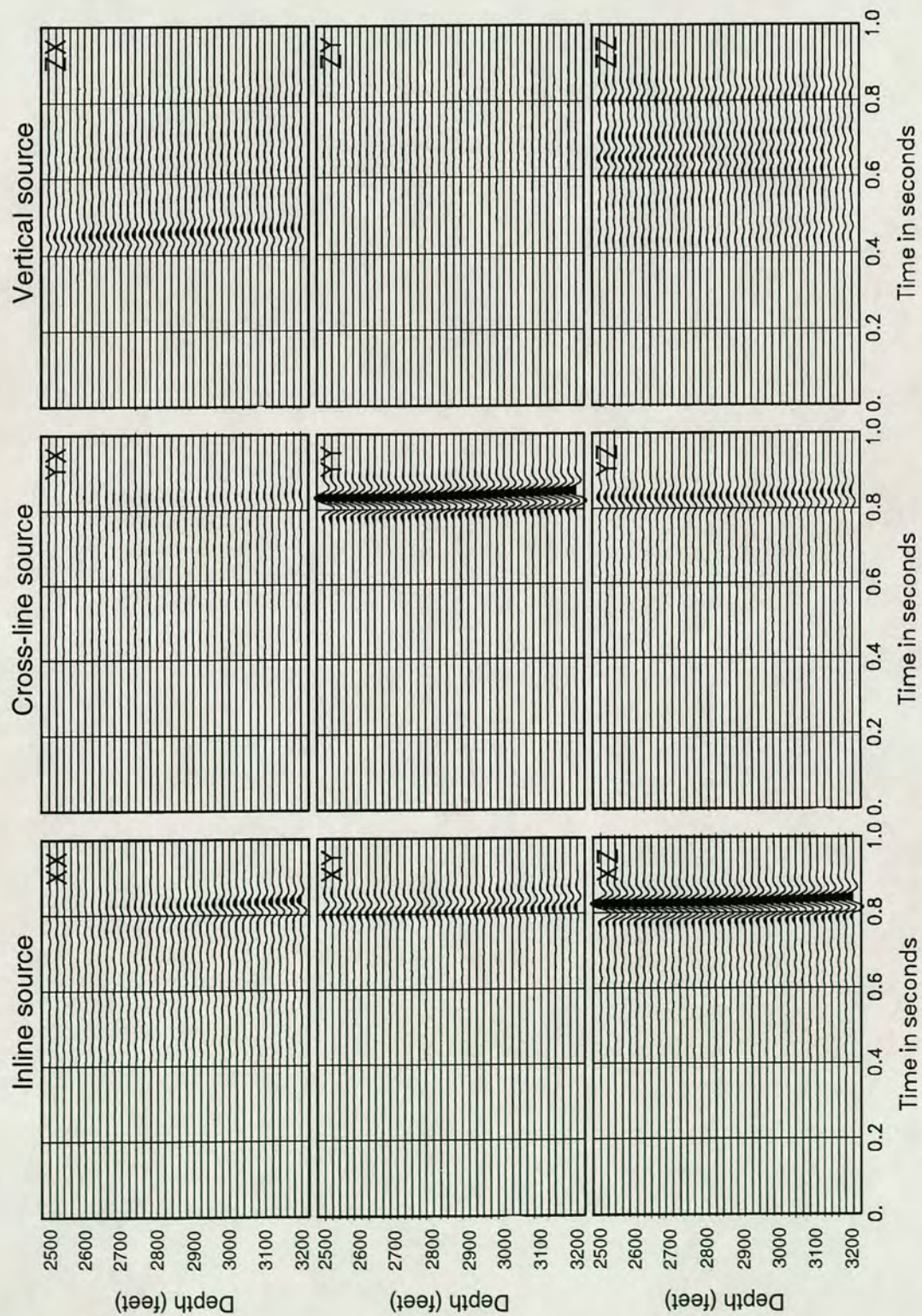Figure 4.15. Nine component data matrix for anisotropic model well I-130, far offset source.
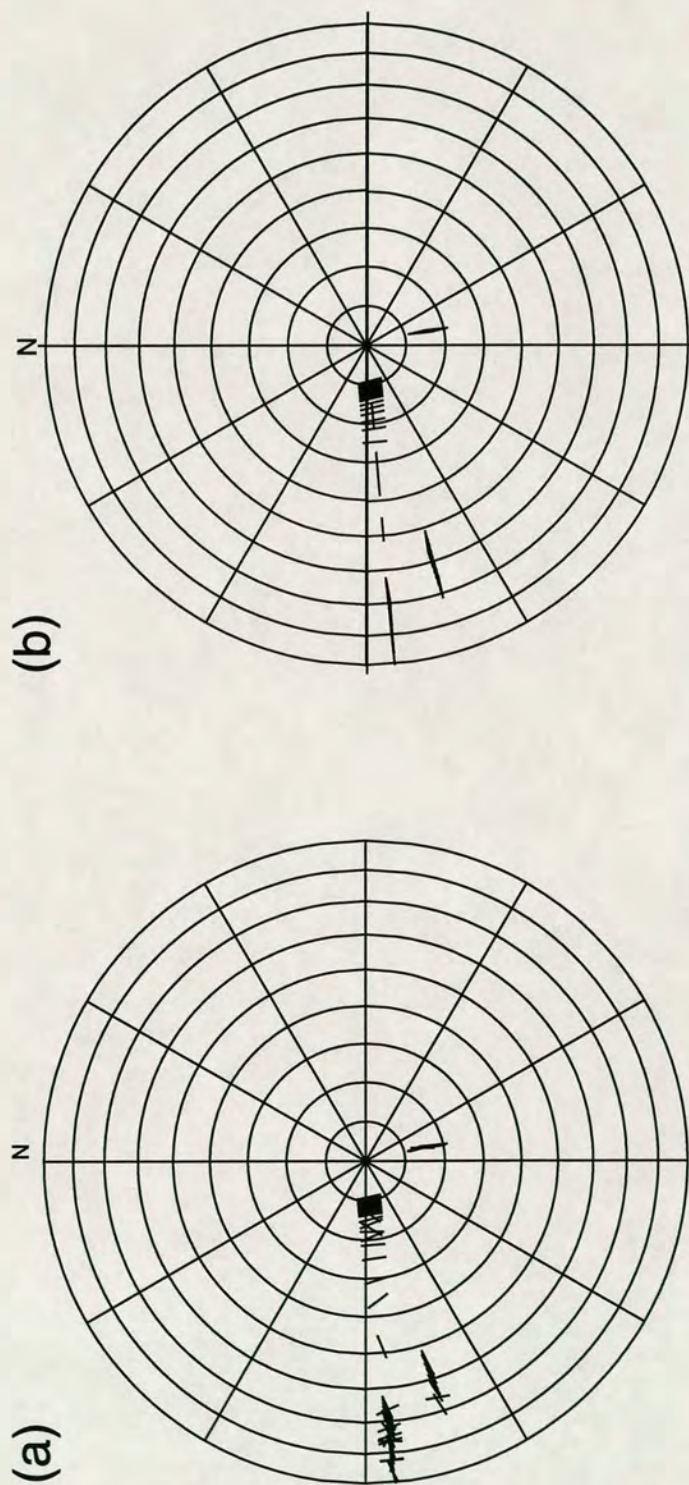
Figure 4.16. Observed horizontal plane *qS1* polarizations, (a), measured from Iatan VSP data in wells I-130 and I-227, plotted on an equal area projection. Polarizations shown are calculated using DCT. Polarizations shown in (b), are those measured by DCT for the first anisotropic model, with a crack strike of N170°E.

Figure 4.17. Observed (crosses) and modelled (solid line) time delays for Iatan VSP's, measured using the DCT method. The model has two anisotropic layers with parallel crack strikes of N170E. Layer 5 has a crack density of 0.08 and layer 6 has a crack density of 0.05.

4.4.5 The inclusion of transverse isotropy

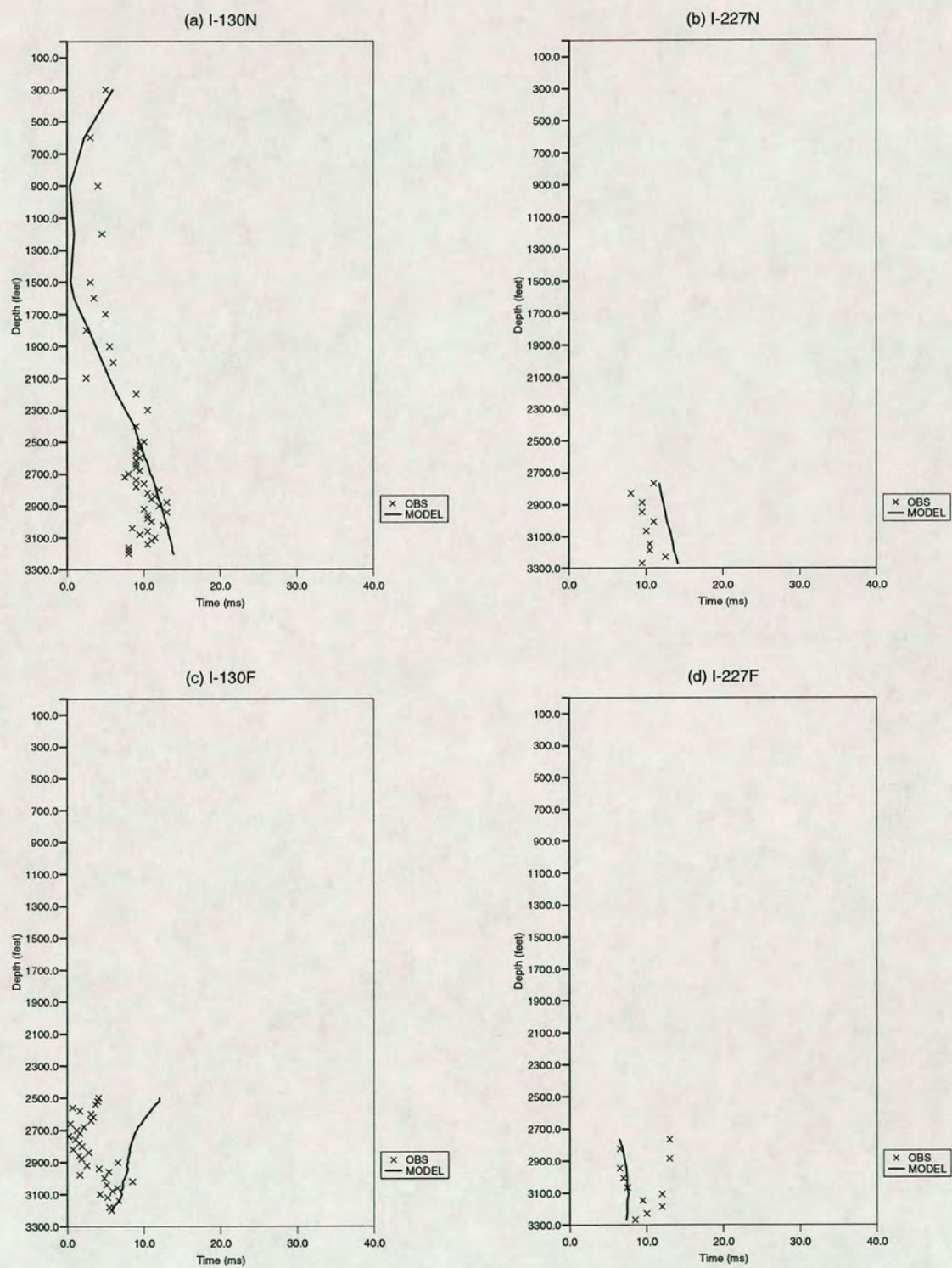The inversion of the far-offset arrival times, Table 4.2, shows that horizontal velocities are 5-10% faster than vertical velocities. I interpret this as evidence of substantial transverse isotropy in the reservoir. In such a limestone reservoir, this could be due to horizontal bedding planes or horizontal jointing, rather than an oriented mineral grain effect such as that observed in clays and shales. As discussed in Chapter 2, combinations of transverse isotropy and azimuthal anisotropy due to vertical fractures will give rise to orthorhombic anisotropic symmetry.

To include these properties within the model, I redefine the reservoir layer with an isotropic velocity comparable to that observed from observations at far offsets. The inclusion of a horizontal crack set reduces the vertical velocity to match that observed at near offsets, giving a material which is effectively transversely isotropic. Hudson's formulations (1986), for the scattering of seismic energy caused by distributions of cracks in weakly anisotropic materials, are used to define a vertical crack set, giving effective azimuthal anisotropy. Figure 4.18 shows Plate Carée projections of the horizontal plane $qS1$ polarizations of shear waves propagating at group velocity through distributions of vertical cracks striking N170°E in a TIV matrix with: (a) 5%; and (b) 10% shear wave velocity anisotropy. The vertical crack sets are defined by a crack density, $\varepsilon = 0.05$, and aspect ratio, $\gamma = 0.001$. The TIV is defined by a horizontal crack set with aspect ratio, $\gamma = 0.001$, and crack densities: (a) $\varepsilon = 0.05$; and (b) $\varepsilon = 0.1$. Directions of point singularities are marked by open circles. Areas with the same range of azimuth and incidence angles as the four Iatan VSP's are indicated by the shaded boxes. The three dimensional patterns of polarizations for both 5% and 10% TIV are very similar, with only minor differences at near horizontal incidence in directions close to the crack strike, and small changes in the directions of the point singularities.

The polarizations of shear-waves , propagating at near vertical incidence from the near-offset sources are unaltered by the inclusion of TIV. However, shear waves propagating from the far offset source position travel through the reservoir at much
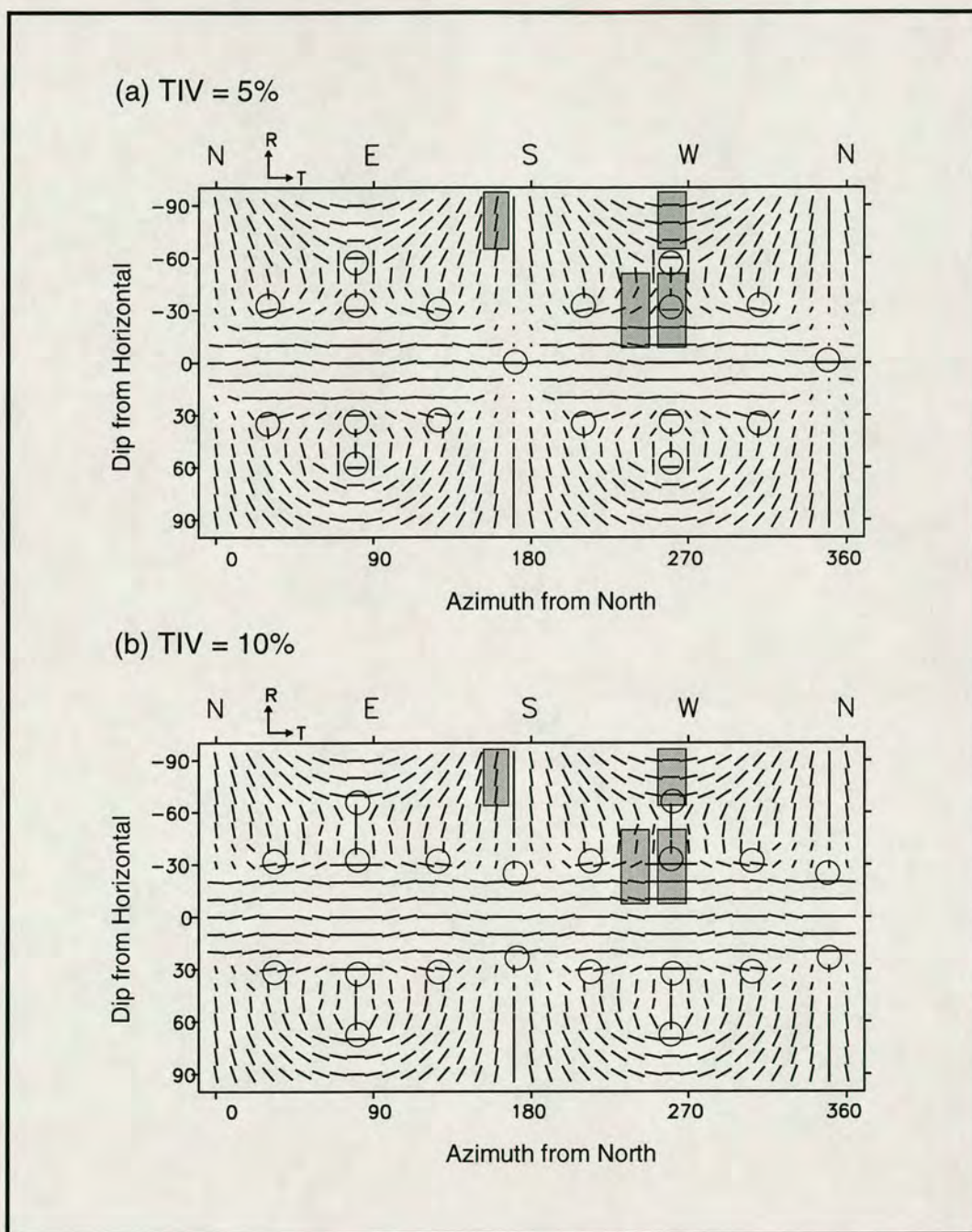
Figure 4.18. Plate Caree projections of theoretical, horizontal plane polarization directions for shear wave propagating through distributions of vertical micro-cracks striking N170E, with a crack density of 0.05 and aspect ratio of 0.001, in a transversely isotropic matrix defined by horizontal crack sets with: (a) crack density $\varepsilon=0.05$ and aspect ratio $\gamma=0.001$; and (b) crack density $\varepsilon=0.1$ and aspect ratio $\gamma=0.001$ Directions of point singularities are marked by open circles. Shaded areas indicate those angles covered by the four Iatan VSP's.

nearer horizontal incidence. We can see from Figure 4.18, that angles of propagation for I-130 far offset are close to a singularity direction. Therefore, we might expect to observe irregularities in shear-wave polarizations and amplitudes, characteristic of a singularity direction.

I generate synthetic seismograms for the reservoir material shown in Figure 4.18. To asses the effect on the measured shear-wave splitting parameters, I apply the DCT and DIT methods to calculate $qS1$ polarizations and time delays for windowed shear-wave arrivals. The measured polarizations and time delays for an orthorhombic reservoir model, where the TIV is defined by a horizontal crack set with $\varepsilon=0.05$, are displayed in Figures 4.19 and 4.20. We can see that both the $qS1$ polarizations and the time delays are relatively unchanged by the inclusion of transverse isotropy in this case.
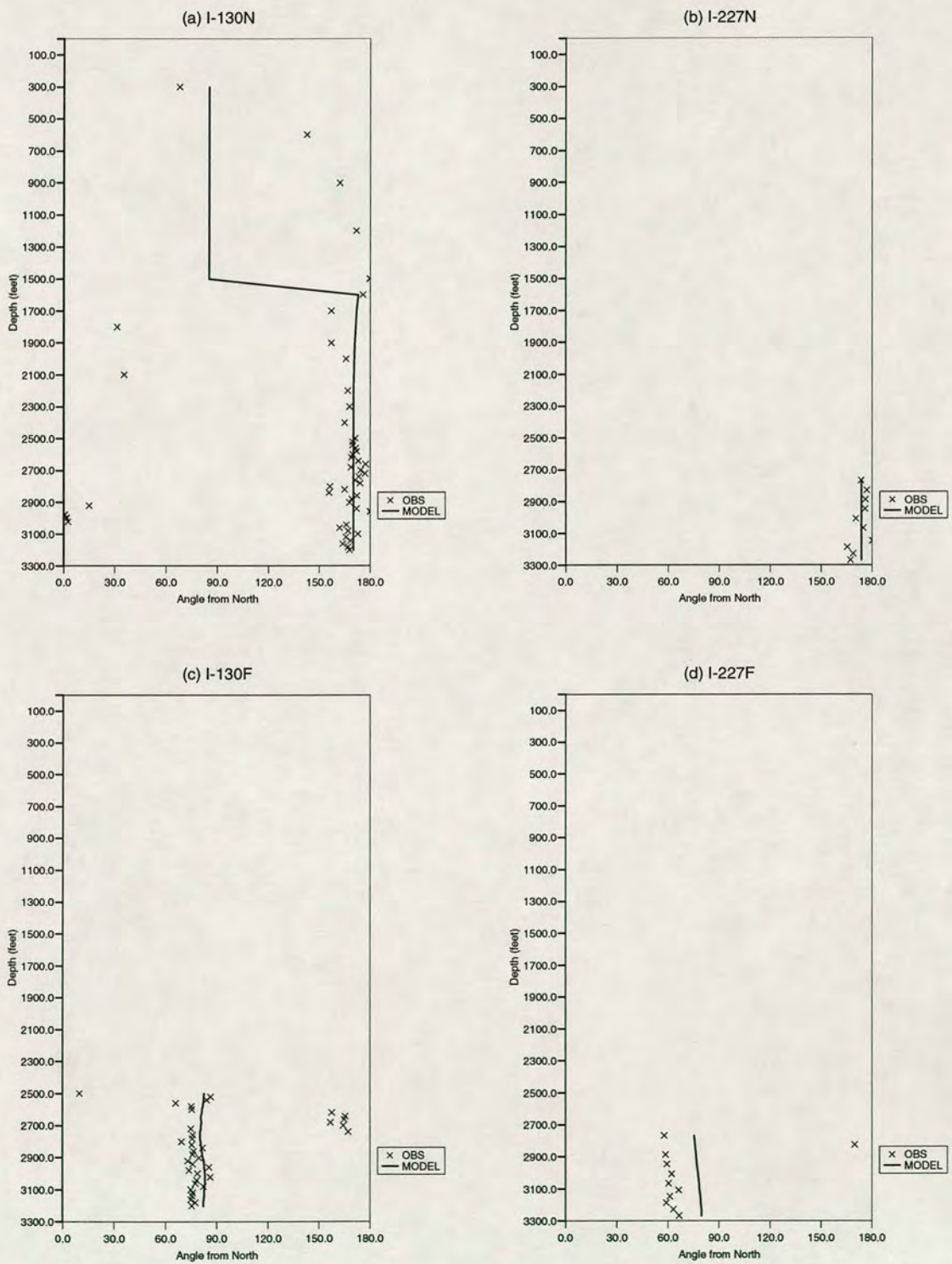
Figure 4.19. Observed and modelled polarizations for Iatan VSP's, measured using the DCT method. The model has two anisotropic layers with parallel crack strikes: layer 5 has a crack density of 0.08 and crack strike of N170°E; layer 6 contains distributions of microcracks with a crack density of 0.05 and a crack strike of N170°E, set in a T.I.V. matrix defined by a horizontal crack set with crack density $\varepsilon=0.05$ and aspect ratio $\gamma=0.001$.

Figure 4.20. Observed (crosses) and modelled (solid line) time delays measured using DCT method. The model has two anisotropic layers with parallel crack strikes: layer 5 has a crack denstiy of 0.08 and crack strike of N170E; layer 6 contains distributions of microcracks with a crack density of 0.05 and crack strike of N170E set in a T.I.V. matrix defined by a horizontal crack set with a crack density ε=0.05 and aspect ratio γ=0.001.
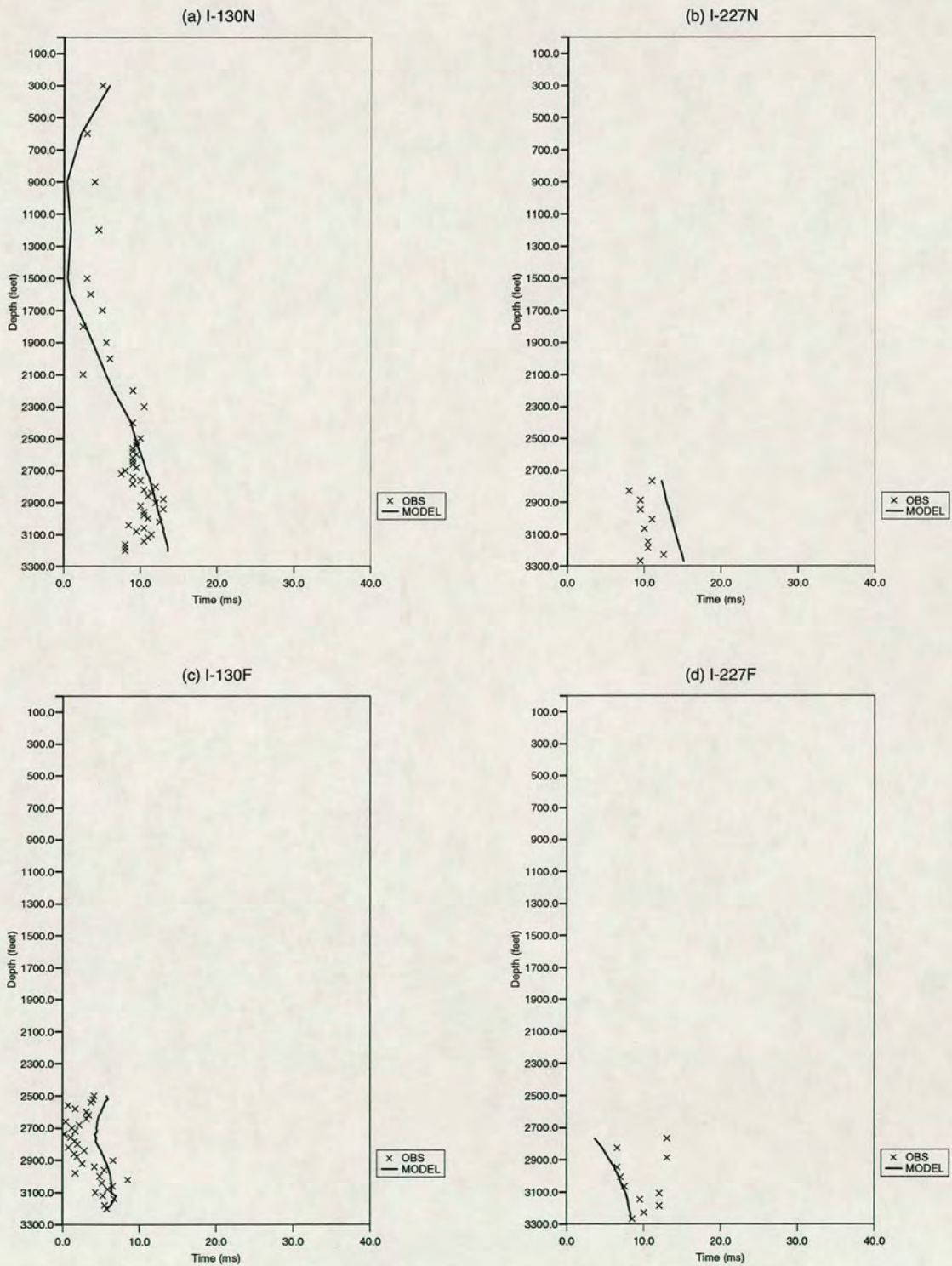
4.5 Crosshole seismic data

The crosshole data offers the possibility of examining the shear waves within the Clearfork reservoir zone, without the distortion commonly associated with propagation through the near surface. The wavefield properties can then be compared with those obtained from the multicomponent VSP experiment. However, as seen in the Chapter 3, the crosshole recording environment can show greater instability than VSP's, as the generation of shear waves is dependent on conversion at the fluid rock interface around the borehole. Also, other wave modes may obscure or distort the shear wave signal, making correct recognition of seismic anisotropy difficult. Figure 4.21 shows a schematic representation of the two crosshole azimuths. The shaded area delineates the Clearfork reservoir formation, which is known to be fractured. Oil production within this formation is from discontinuous high porosity zones.

4.5.1 Data processing

The large quantity of Iatan crosshole data (2025 raypaths) enabled a selective approach to data analysis, based on the dual criteria of signal stability and signal to noise ratio. Data were supplied in common geophone gathers of 45 traces, giving 45 gathers for each of the crosshole azimuths. In general, common receiver gathers show more regular variation in polarizations between different paths than common source gathers. This is because the observed shear wave polarizations are dominated by the near geophone anisotropic structure, so each trace in a common receiver gather has been filtered by the same near geophone anisotropy. Common source gathers tend to show more variation from path to path because of different near geophone effects. Visual examination of the seismograms determined the gathers with the cleanest shear wave data for analysis of shear wave splitting. Figures 4.22 and 4.23 show straight line raypath diagrams for some of the geophones used from surveys A and B. These show the amount of angular coverage of each of the surveys, because of the smaller offset, survey A provides much greater angular coverage than survey B.
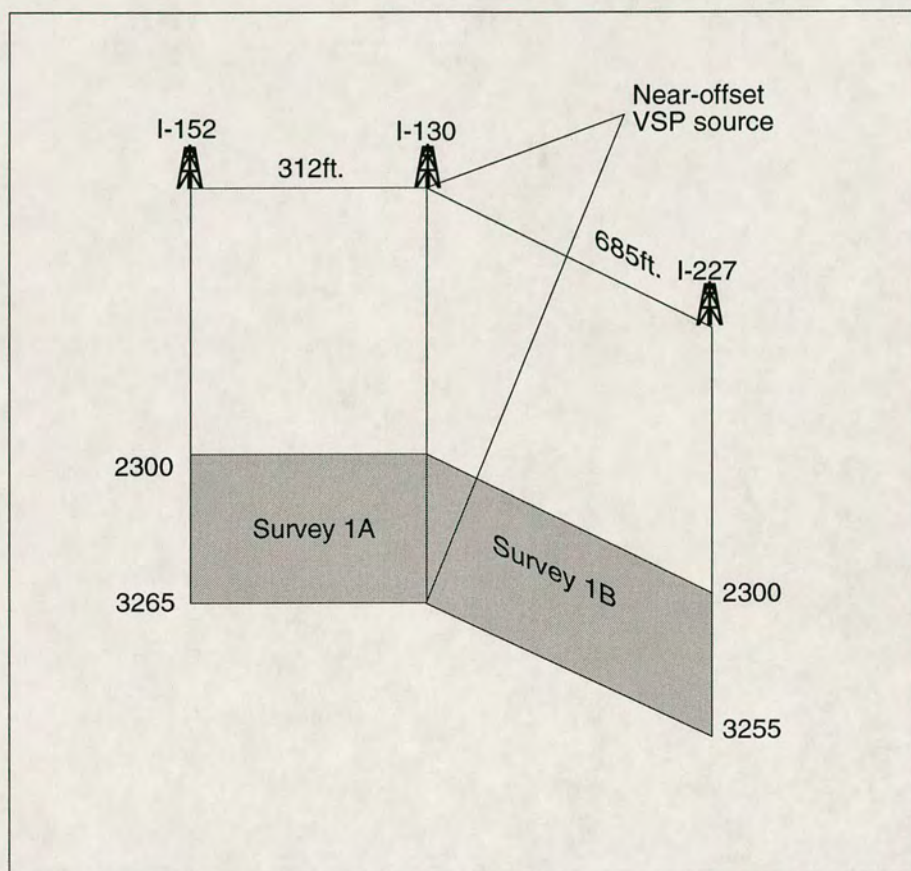
Figure 4.21. Schematic representation of the Iatan crosshole geometry. Crosshole data are recorded in wells I-152 and I-227, from sources in well I-130, to carry out waterflood evaluation of the Upper Clearfork reservoir zone. There are 45 geophones and 45 sources, giving a total of 2025 raypaths through the reservoir zone for each azimuth.
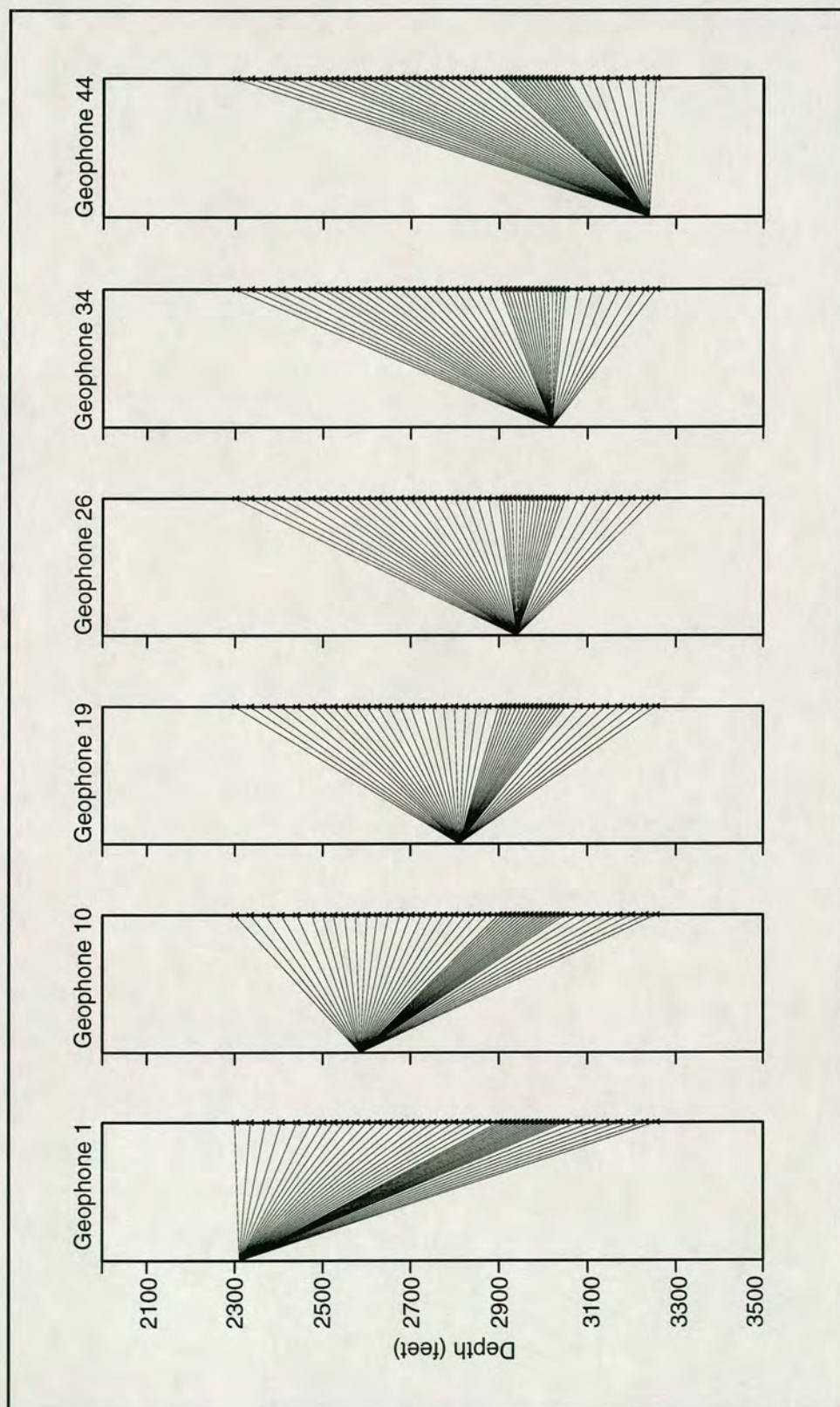
Figure 4.22. Straight line raypaths for selected geophones in well I-152 (crosshole survey A), showing the angular coverage of the crosshole experiment.
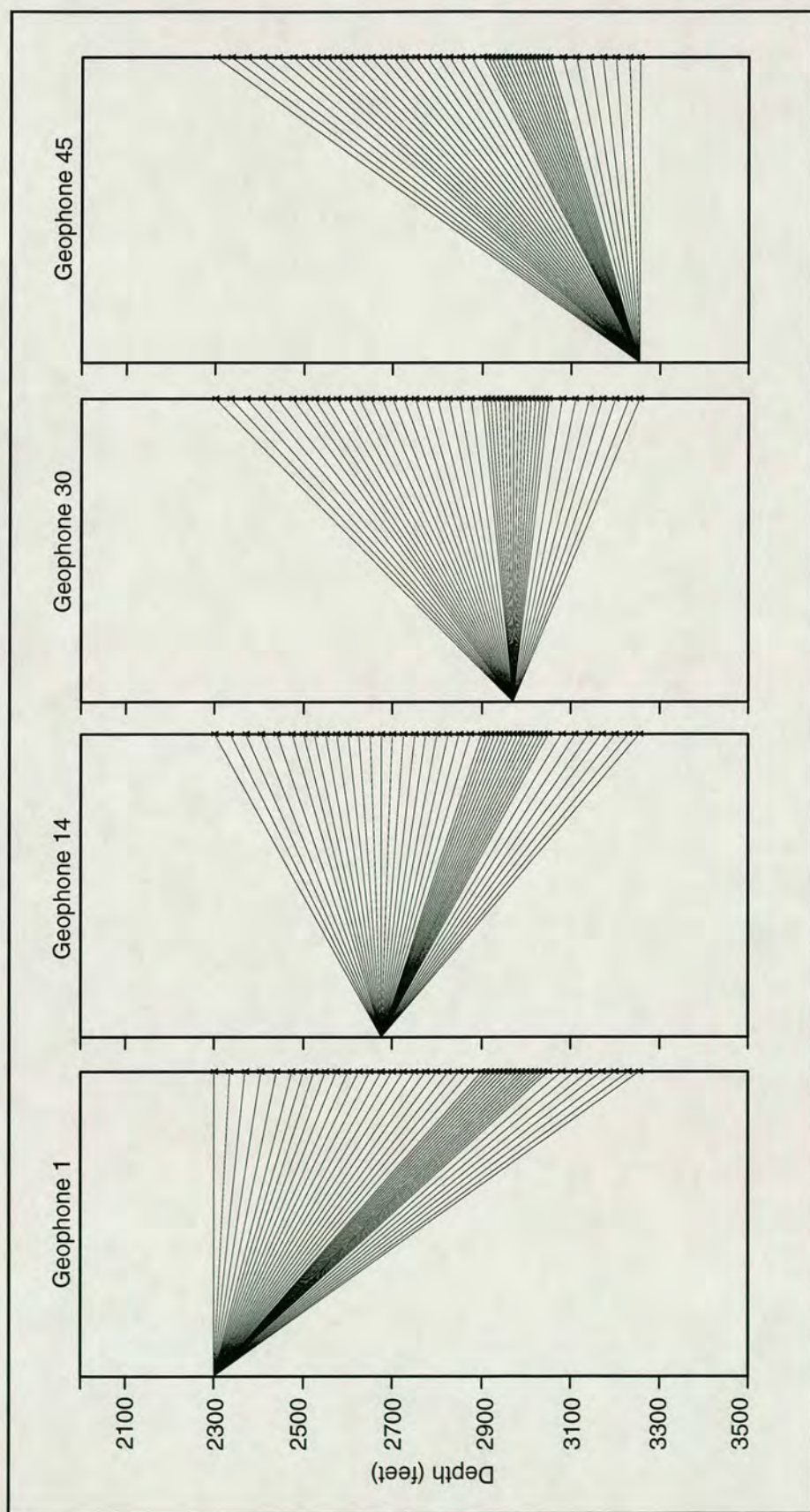
Figure 4.23. Straight line raypaths for selected geophones in well I-227 (crosshole survey B), showing the angular coverage of the crosshole experiment.

Table 4.4.

Iatan crosshole survey A.			
Geophone information from well 152.			
Geophone number	Geophone depth in feet	Mean orientation from radial	Mean deviation in orientation
1	2310	59.9	3.1
5	2450	14.7	4.4
10	2585	31.32	3.1
15	2710	51.1	4.0
19	2810	11.3	2.9
26	2940	27.4	3.8
30	2980	103.9	4.6
34	3020	119.4	4.0
38	3060	58.7	1.6
44	3240	100.1	8.8

Table 4.5.

Iatan Crosshole Survey B. Geophone information from well I-227.			
Geophone number	Geophone depth in feet	Mean orientation from radial	Mean deviation in orientation
1	2300	167.0	6.5
4	2405	216.8	12.2
14	2675	104.9	2.4
22	2875	8.4	1.4
30	2970	159.8	5.6
33	3000	281.8	5.6
41	3140	62.9	4.4
45	3255	336.8	4.6

Geophone orientation in the horizontal plane is calculated from the windowed *P* arrivals in the same manner as for offset VSP data. Assuming there is no movement of the geophone tool between shots, a mean orientation angle can be calculated along with the deviation from the mean for each geophone gather. The geophones are rotated into the radial and transverse directions using these mean orientation angles.

After rotation the seismograms are filtered using a zero-phase band pass filter, between 10-250 Hz. Filter design was tested on geophone 1 of survey A, based on amplitude spectra and seismogram character before and after application.

A summary of the geophones used, together with geophone rotation angles, is shown in Tables 4.4 and 4.5 for surveys A and B respectively.

4.5.2 Initial analysis of seismograms

Three-component receiver gathers for selected geophones, from datasets A and B are shown in Figures 4.24 and 4.25, respectively. Geophone rotation has been successfully applied in each instance, so that *P*-wave energy is minimized on the transverse component. Amplitude scaling is relative between individual geophone components (R,T and V), but not between different geophones or source levels at the same geophone. This means of display was found to give the most consistent picture of a coherent shear wavefront, preventing domination of the gathers by high amplitude noisy wave-trains.

The wavelet appears to be stable between different source levels and different geophones for both *P*- and *S*-waves. Each arrival consists of 1-2 cycles. The frequency content of the two body waves is similar at around 250 Hz, although shear-wave amplitudes are noticeably larger, again confirming the down-hole airgun to be a powerful source of shear-wave energy.

A comparison of the relative amplitudes of *P*- and *S*-waves, reveals that *P*-wave amplitudes are greatest in horizontal directions while shear wave amplitudes increase moving towards vertical. This is primarily a consequence of source radiation effects. The amplitude distribution complies with expected *P*- and *S*-wave radiation
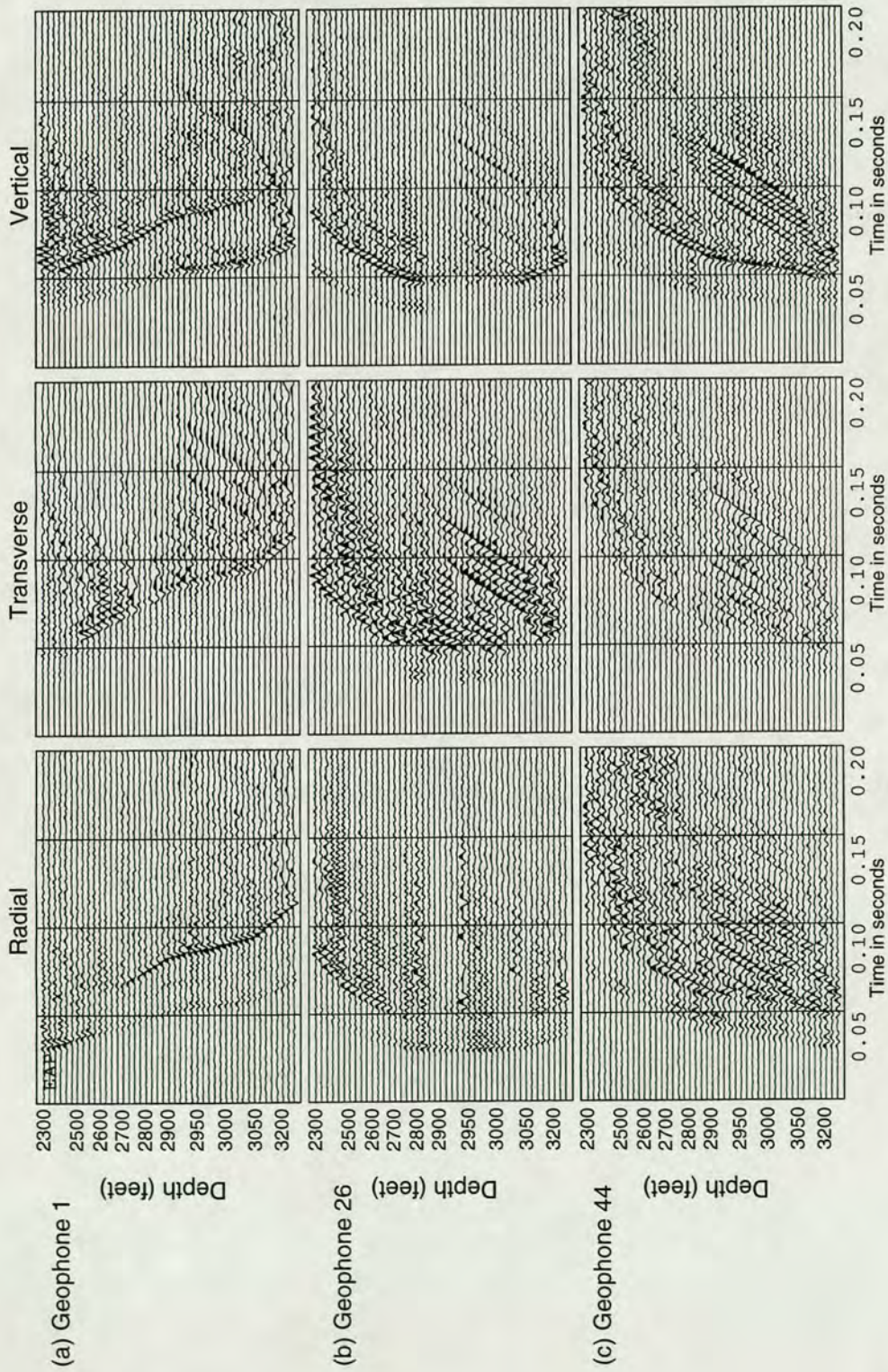
Figure 4.24. Three component common geophone gathers, from geophones 1, (a), 26, (b) and 44, (c), well I-152, cross-hole survey A.
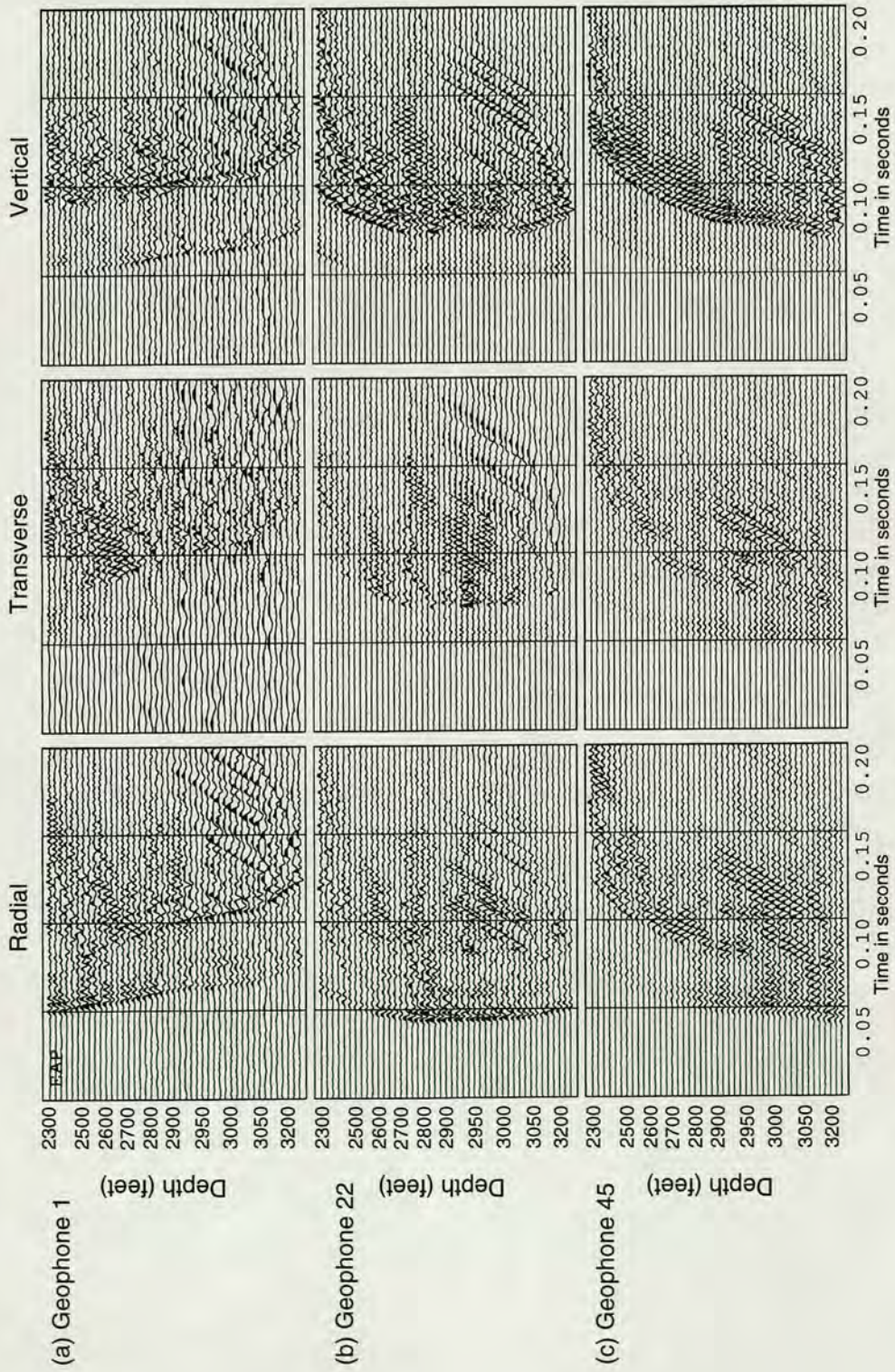
Figure 4.25. Three component common geophone gathers, from geophones 1, (a), 22, (b) and 45, (c), well I-227, cross-hole survey B.

patterns for an airgun situated in a borehole. Shear-wave energy is generated by *P-SV* conversion at the liquid-solid interface around the borehole. The resulting shear waves should be polarized in the vertical-radial plane. However, lower amplitude, but coherent shear-wave arrivals also exist on the transverse geophone component. For example, see geophone 1 of survey A, Figure 4.24(a). This feature may be attributed to scattering by near vertical fractures within the reservoir, as the initially, purely *SV*, shear waves travel obliquely across the fractures.

4.5.3 Borehole and guided wave modes

Arrivals with significantly larger moveouts are also present on the common geophone gathers, arriving after the two direct body wave arrivals. These are thought to be borehole wave modes, tube waves, propagating along the borehole fluid solid interface. These waves seem to propagate predominantly in downwards direction and are most prominent on geophone 44 of survey A, Figure 4.24 (c) and geophone 45 of survey B, Figure 4.25 (c). The tube waves also display distinctive polarization behaviour and in most cases appear to contain a strongly transversely polarized element. Barton and Zoback (1988) link the polarization of borehole guided waves to *in situ* stress orientation and fracture directions.

It is difficult to ascribe to any of the arrivals on the seismograms, the characteristics of guided waves travelling parallel to a horizontal interface. Such waves are typically produced by low or high velocity channels, given appropriate velocity contrasts and frequencies, and have been commonly observed in crosshole surveys. Channel waves display distinctive dispersive behaviour which can be related to the physical properties of the waveguide. These waves are also sensitive to propagation in anisotropic media. At any rate, the apparent absence of such wave modes is certainly unexpected and may, perhaps, be due to a lack of high velocity contrasts within the reservoir layer, or the near monotonic nature of the seismic source.

4.5.4 Differences between datasets A and B.

Differences in the character of the seismograms between datasets A and B are clear. Dataset A shows good quality coherent shear arrivals, with a reasonable signal to noise ratio, on all three components. In comparison, dataset B arrivals are ringy in nature, with a lower signal to noise ratio. Shear energy has a lower amplitude and is primarily in the sagittal plane. I offer the following arguments to explain these differences. Dataset A has near vertical raypaths and shorter pathlengths, whereas for dataset B, raypaths are closer to horizontal and pathlengths are approximately twice as long. The longer pathlengths may give rise to greater attenuation of the relatively high frequency shear waves. Also, as a consequence of the source radiation pattern, shear waves display smaller amplitudes in horizontal directions.

In addition, dataset A is acquired at an acute angle to the natural fracture azimuth, whereas B is close to perpendicular. Amplitude attenuation will be more severe for propagation perpendicular to the fracture planes due to increased scatter of energy. In theory, *SV* modes propagating perpendicular to distributions of natural fractures should show no splitting, which could explain the lack of energy on the transverse geophone component.

4.5.5 Hodogram analysis.

Figure 4.26 (a) and (b) show hodograms of the shear-wave particle motion in the two orthogonal planes, horizontal, normal. Particle motion for individual source-geophone pairs is displayed in a data matrix of source depth against geophone depth. Common sources lie in columns and common geophones in rows. This allows both examination of shear wave behaviour as a function of source depth at each geophone, but also comparison of shear-wave variation with geophone depth within the reservoir.

Horizontal raypaths lie nearest to the main diagonal of the grid. Near vertical raypaths lie in the two off-diagonal areas. Shear waves travelling in near-vertical directions, up or down, show remarkable consistency in both horizontal and normal
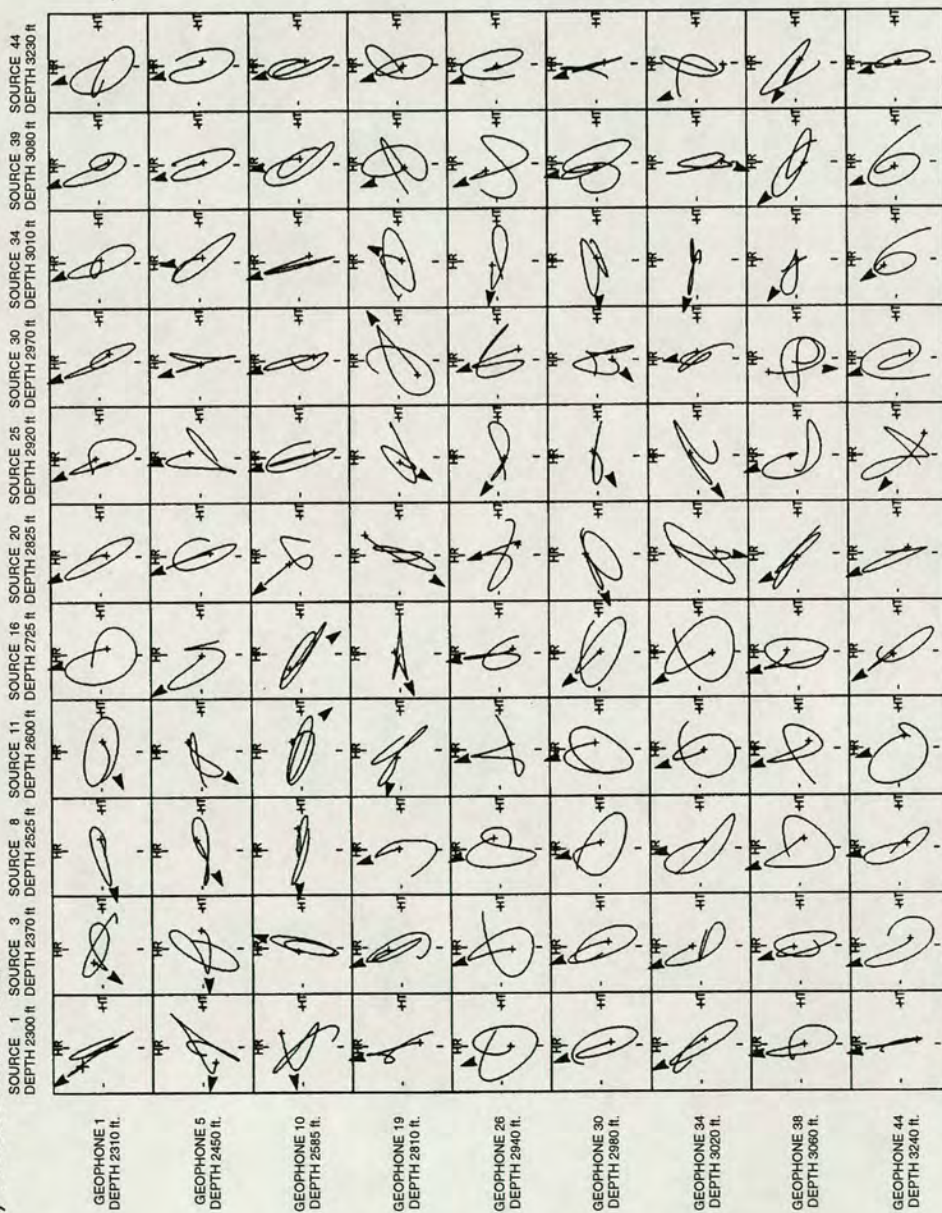
147

(a) Horizontal Plane

Figure 4.26. Windowed shear-wave particle motion for selected source-geophone pairs from cross-hole survey A.
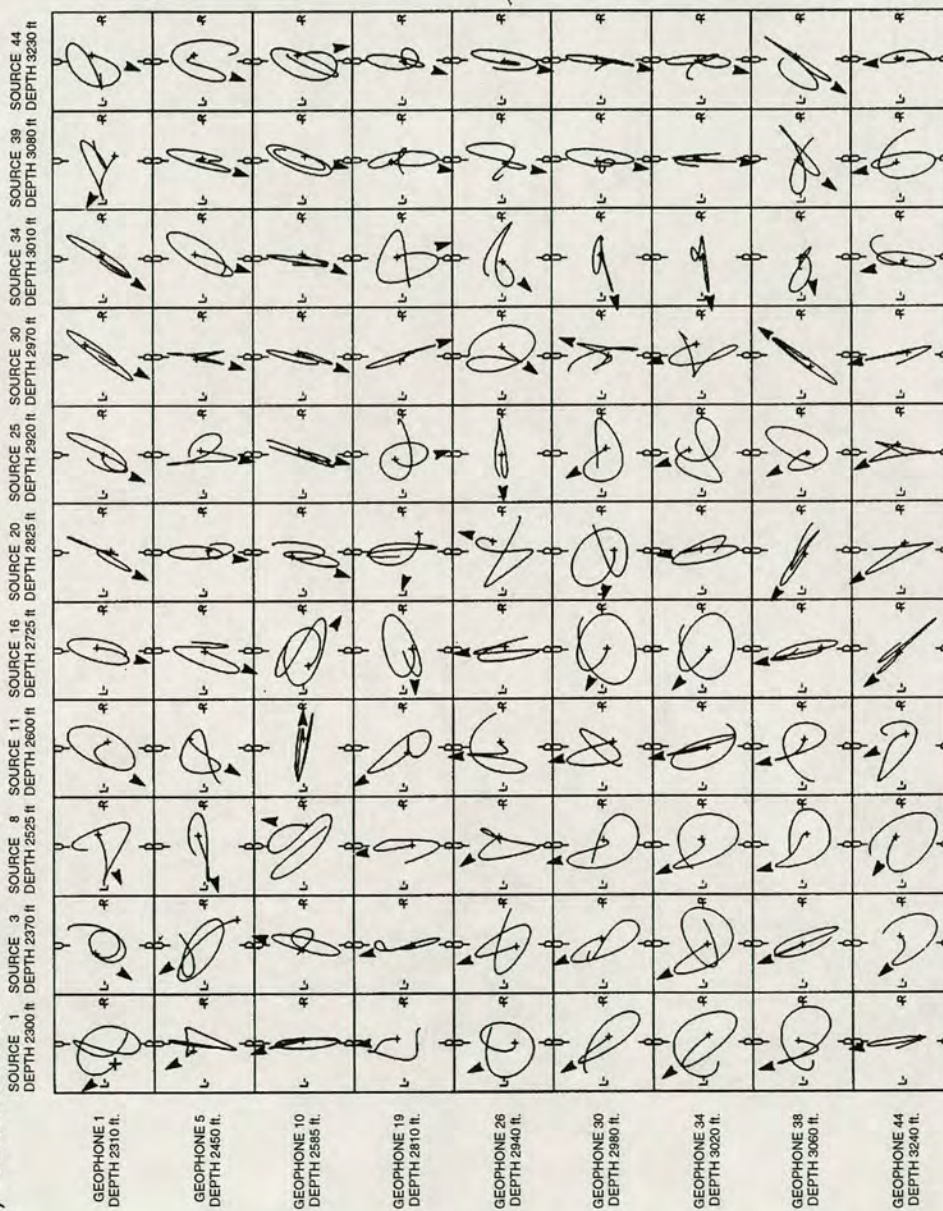
(b) Normal Plane

Figure 4.26. Windowed shear-wave particle motion for selected source-geophone pairs from cross-hole survey A.

plane which appears to be independent of geophone depth. An estimate of the initial direction of shear-wave motion is indicated by an arrowhead. In horizontal directions, coherent behaviour is less obvious due to the low amplitudes of shear waves in these directions.

Some of the hodograms display features similar to those of classic shear-wave splitting behaviour. Particle motion is cruciform, caused by the arrival of a second, slower, arrival with an orthogonal polarization to the initial linear arrival. However, many of the hodograms display greater complexity, with numerous phase shifts and subtle amplitude variations, which cannot easily be explained by a simple EDA model.

To assist the hodogram analysis, I estimate the polarization of the initial shear-wave motion by constructing a covariance matrix for th first few samples of each shear-wave arrival. The polarization direction within this time window is given by the principal eigen vector of the covariance matrix. I refer to this measurement as the instantaneous polarization. The accuracy of this method depends on the picking of the shear-wave first break and an impulsive shear-wave arrival. Measured polarization angles are displayed as a function of angle of emergence at the geophone. The emergence angle is calculated from the sagittal plane motion of windowed shear arrivals. Assuming that shear-wave behaviour does not vary greatly with geophone depth in the reservoir, which appears to be the case, this allows the results to be plotted together, giving an averaged picture of the shear wave dependence on propagation angle through the reservoir.

Figures 4.27 and 4.28 show the results of measurement of initial polarization as a function of angle from horizontal, for datasets A and B, in both horizontal and normal planes. The horizontal plane polarizations for A lie between 140°-170° from radial, while normal plane polarizations lie between 0°-30° for upgoing shear waves and 140°-180° for downgoing. For crosshole dataset B, polarizations are more scattered and the greatest concentration of measurements lie in near horizontal directions. Horizontal plane measurements show a great deal of scatter, with the bulk of polarizations lying around 30°. The normal plane measurements indicate that the shear waves are polarized almost entirely in the vertical direction.
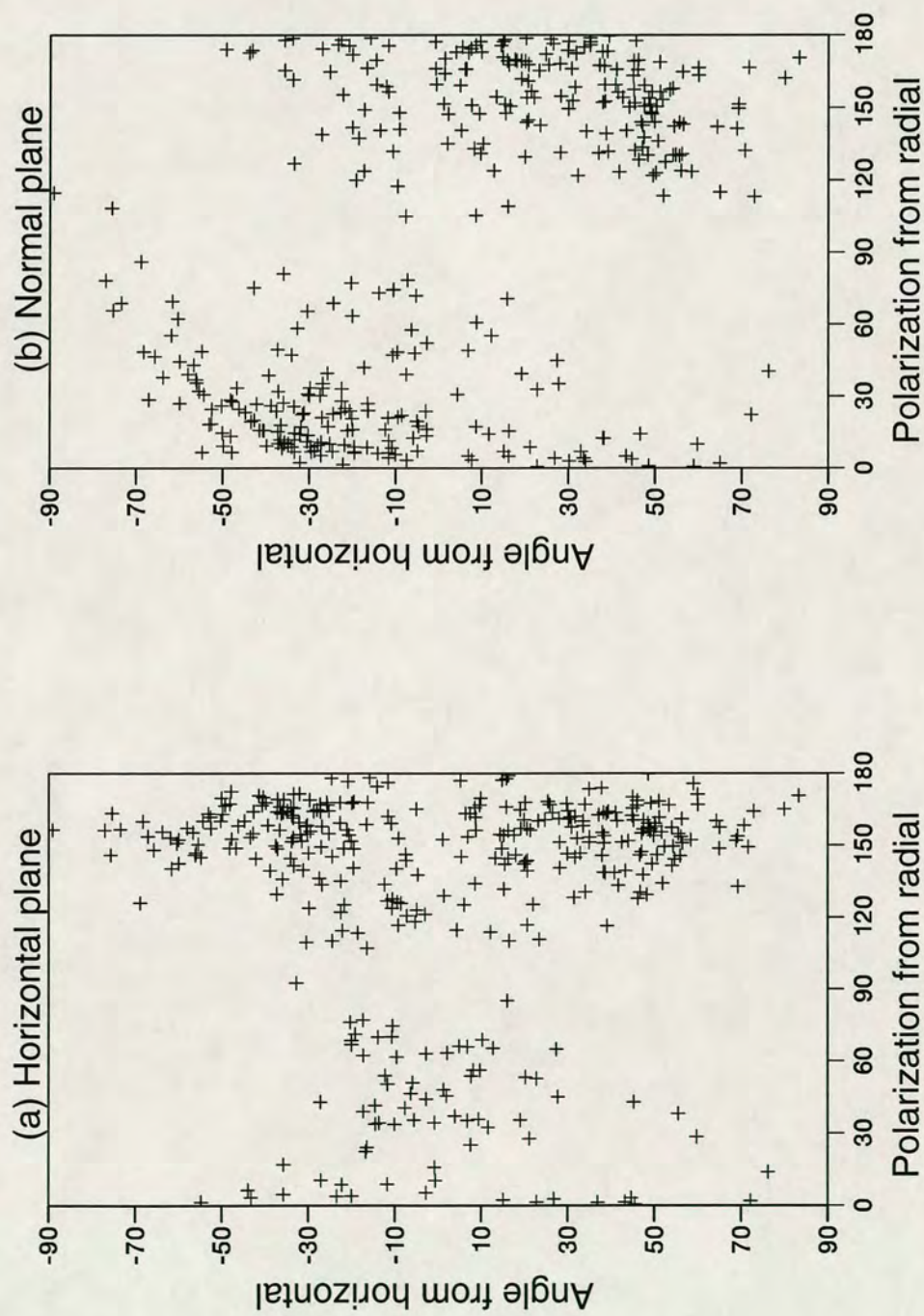
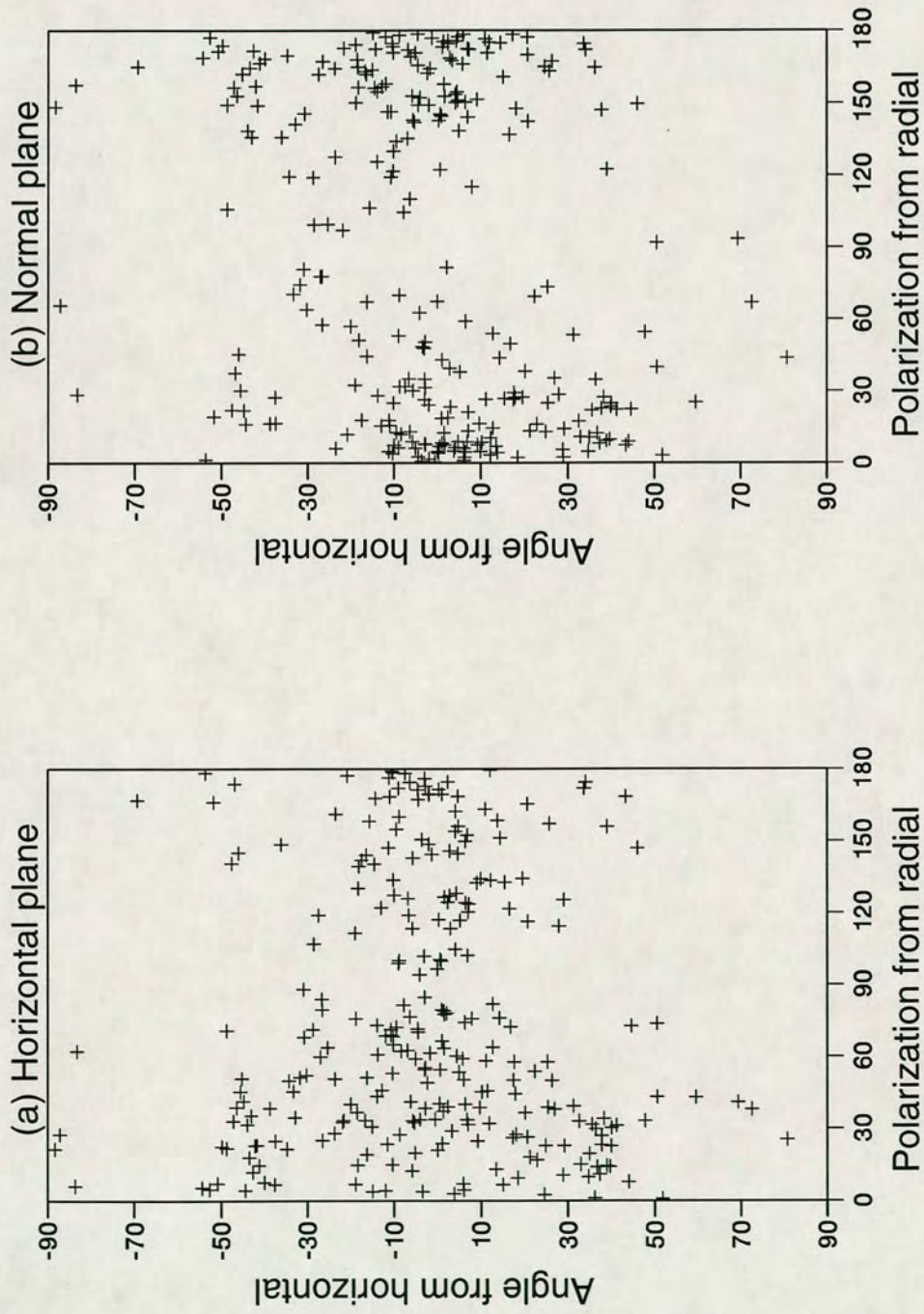Figure 4.27. Instantaneous polarizations of windowed shear-wave arrivals from crosshole dataset A.

151

Figure 4.28. Instantaneous polarizations of windowed shear-wave arrivals from cross-hole dataset B.

4.5.6 Numerical measurement of polarization and time delay.

I use the numerical estimation method *DTS* (Campden 1990) to calculate the *qS1*-wave polarization angles and time delays between *qS1* and *qS2* waves, for different geophones within the reservoir zone for both crosshole datasets A and B. *DTS* is applied to windowed shear-wave arrivals in both the horizontal and normal planes. The measured polarization and time delays are again displayed as a function of angle from horizontal. Results are shown in Figures 4.29 and 4.30 for A and B respectively.

Horizontal plane polarization angles for dataset A give results consistent with those from the hodogram analysis, with an estimated *qS1* direction of between 140°-170° from radial, except for near horizontal raypaths. Normal plane measurements, Figure 4.29(b), also comply with the instantaneous polarization estimates. Time delays are normalized over 100m raypaths, based on the straight line source receiver distances for each measurement. For survey A, delays increase from approximately 1ms/100m for directions close to vertical to around 3-4ms/100m in horizontal directions. Crosshole dataset B, (Figure 4.30), gives a horizontal *qS1* angle of around 50° within ±10° of the horizontal and which move towards the radial direction as propagation moves towards vertical. However, coverage is limited beyond ±45° of the horizontal. Normal plane polarization estimates display a similar trend although the degree of scatter makes interpretation of these results difficult. Normalized time delays are smaller than those from A, most delays being under 2ms/100m.

It should be noted that measurements along horizontal raypaths are likely to have greater uncertainties, given the low amplitude of shear waves propagating in these directions.

4.6 Modelling the cross-hole observations

Assuming a homogeneous reservoir, raypaths within this layer may be approximated by straight lines between sources and geophones. This assumption may

153

(a) Horizontal plane measurements.
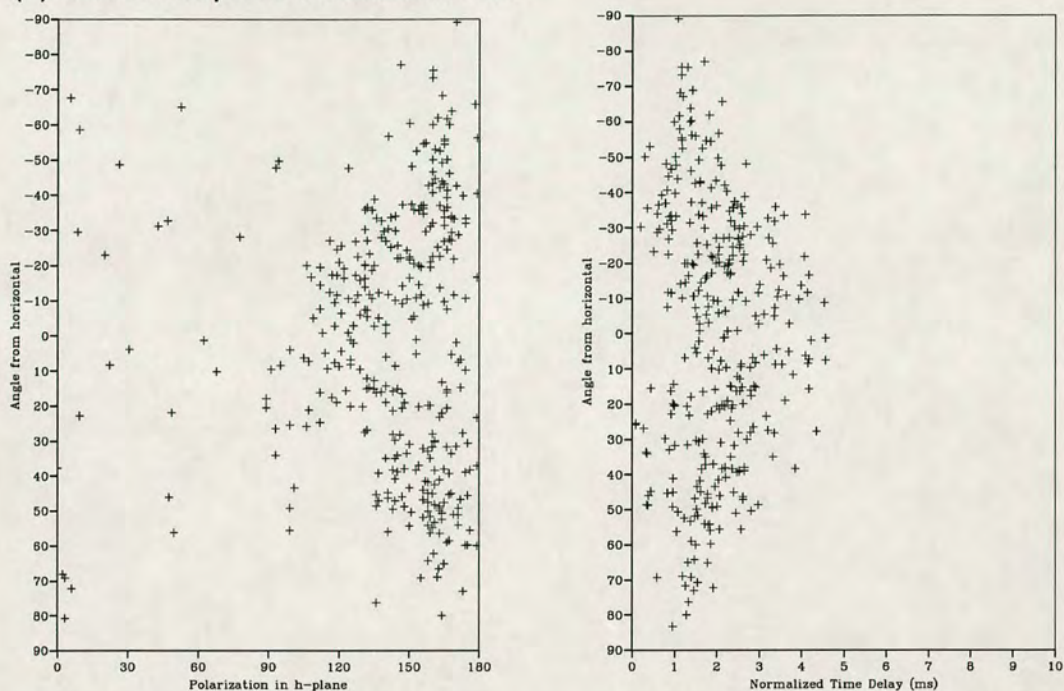
(b) Normal plane measurements.

Figure 4.29. DTS measurements in horizontal (a) and normal (b) planes for Iatan crosshole survey A. Time delays are normalized over 100m.

154

(a) Horizontal plane.

(b) Normal plane
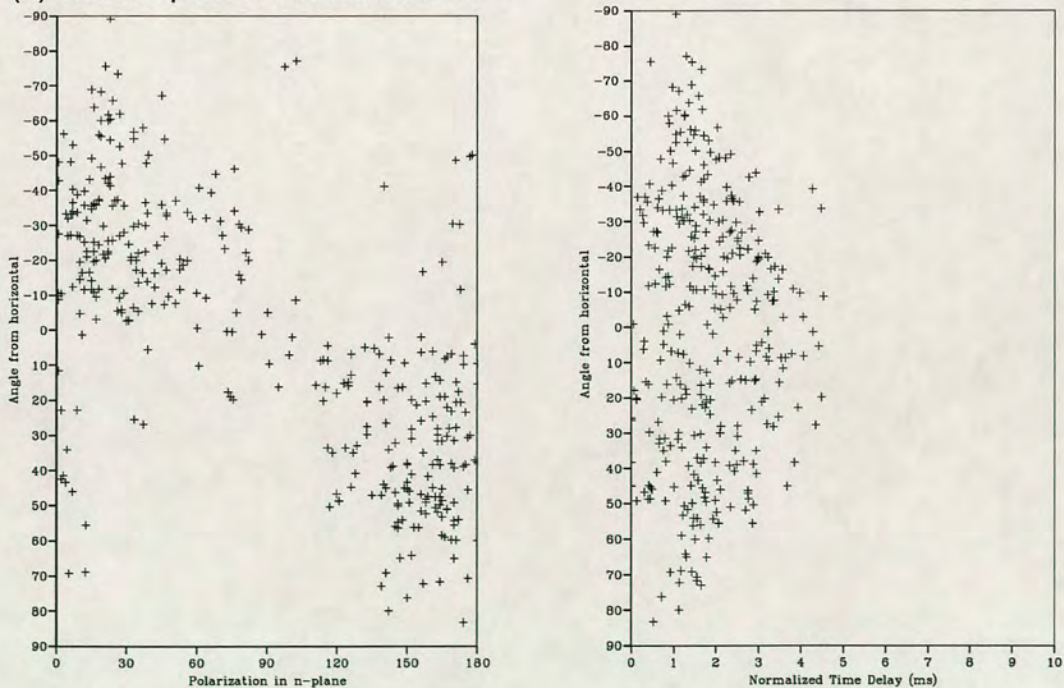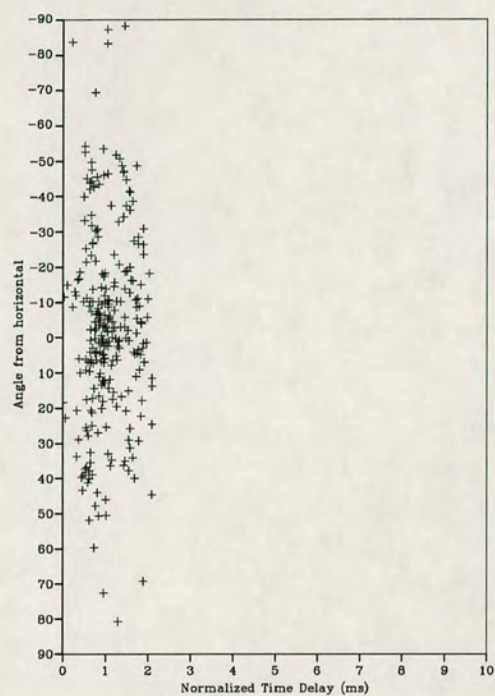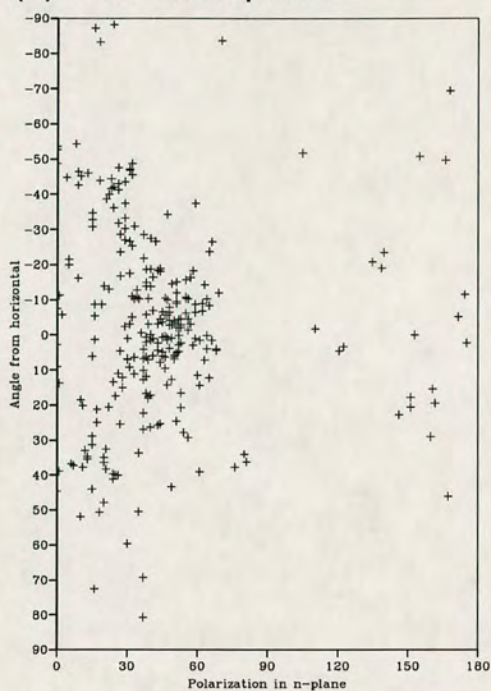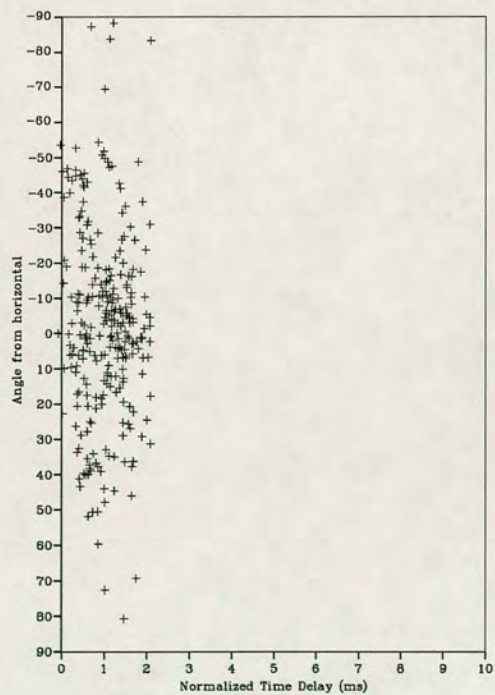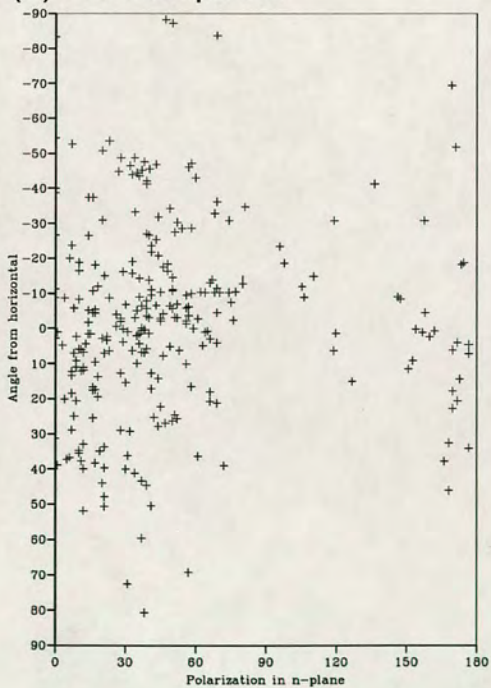

Figure 4.30. DTS measurements in horizontal (a) and normal (b) planes, for Iatan crosshole survey B. Time delays are normalized over 100m.

be considered valid for small acoustic impedance contrasts within this region. This enables the examination of polarization variation with angle of propagation rather than depth. Polarization estimates can then be readily compared with theoretical shear-wave behaviour for various anisotropic media. Polarizations and time delays can be calculated from the elastic constants of anisotropic materials using the Christoffel equation (1.8), to determine polarization and velocity variation with angle of propagation.

4.6.1 Comparison of crosshole results and VSP model

Figure 4.31 shows the zones of expected behaviour of polarization and time delay for distributions of micro-cracks striking between ±12.5° of N170°E, as a function of angle from horizontal. Each plot may be considered as a vertical cross section of a Plate Carée projection whose azimuth corresponds to the radial direction of the crosshole survey. Polarizations and time delays are calculated using radial directions of N279°E for survey A and N137°E for survey B. Time delays are normalized over 100m. A comparison of this model with the observations from survey A in Figure 4.29, shows that although the observed horizontal plane polarizations do lie within the zone of expected behaviour for some directions, in general, the agreement is poor.

In contrast, observed horizontal plane *qS1* polarizations from survey B, Figure 4.30, show a good agreement with this model. Therefore, the possibility of lateral variability in the anisotropic response of the reservoir cannot be ruled out.

4.6.2 Comparison of crosshole results with regional fracture trend.

Core sample measurements and directions of injection water breakthrough indicate that fracture orientation in the Clearfork dolomites may lie between N60°E-N85°E. I calculate expected behaviour of polarizations and time delays for shear waves propagating through a reservoir with such a fracture orientation. Using the same

(a) Cross-hole survey A
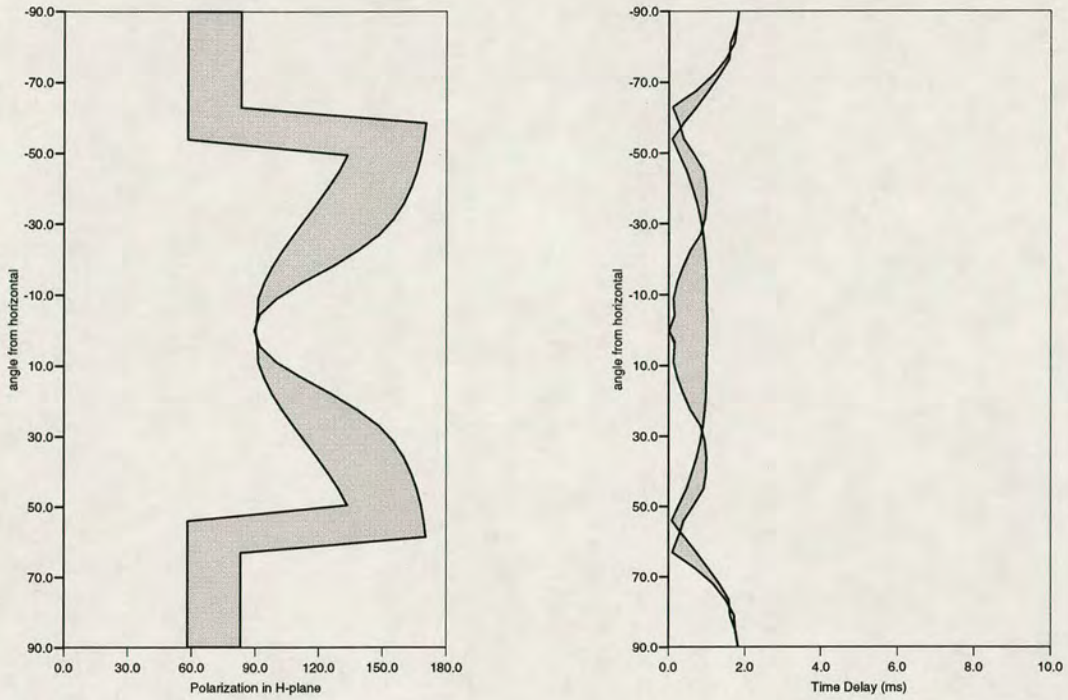
(b) Cross-hole survey B

Figure 4.31.Expected *qS1* polarizations and time delays between *qS1* and *qS2* arrivals plotted as functions of angle from horizontal for distributions of parallel Hudson cracks with crack density ε=0.05, striking ±12.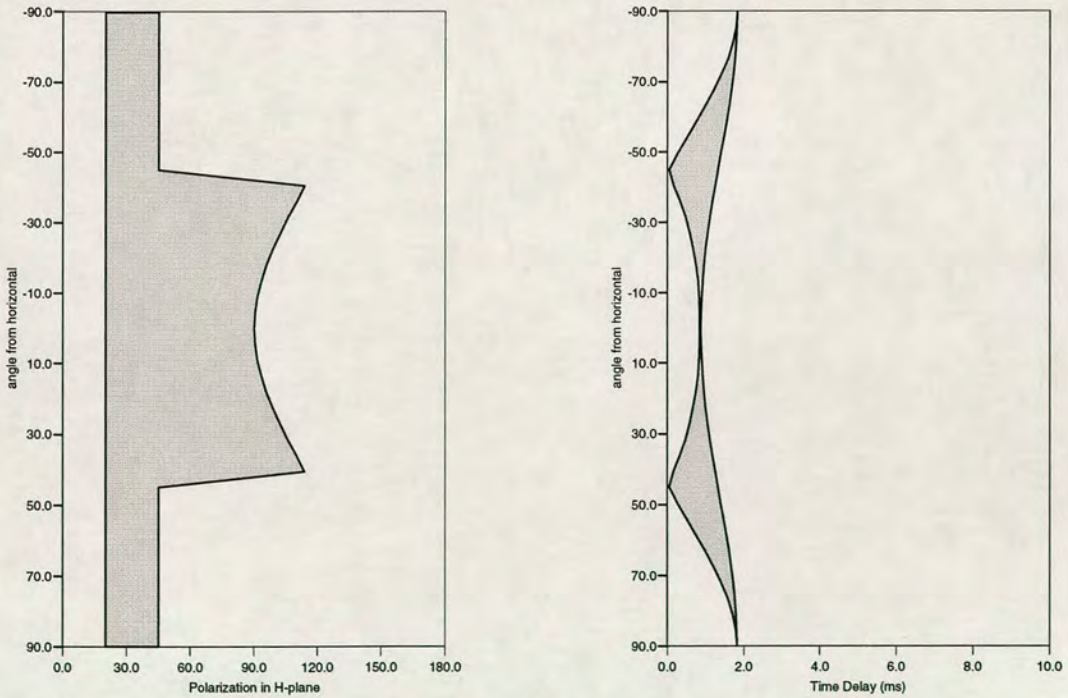5° from N170°E in an isotropic matrix. For: (a) cross-hole survey A, given a radial direction of N279°E and; (b) cross-hole survey B, given a radial direction of N137°E. Delays are normalized over 100m.

model for the Clearfork formation as above, I rotate the elastic constants so that the fracture alignment is in accordance with the above directions.

Figure 4.32 shows a Plate Carée projection of the variation of $qS1$ polarization with direction of propagation through a Clearfork reservoir model containing distributions of vertical micro-cracks striking N75°E, with a crack density, $\varepsilon=0.05$ and aspect ratio, $\gamma=0.001$. The shaded areas delineate the expected range of polarizations at the two crosshole azimuths, given a variation in crack strike of ±10° about N75°E. Vertical cross sections across these two areas yield plots of polarization and time delays against angle from horizontal shown in Figure 4.33 for each azimuth. The shaded areas indicate expected polarizations and time delays for crack strikes between N60°E and N85°E.

For crosshole survey A, Figure 4.33(a), cracks striking N85°E have a constant polarization angle of 166° from radial for all incidence angles. Cracks at N60°E have a polarization angle of 141° from radial for angles between 40° and 90° from horizontal. For angles closer to horizontal we cross the shear-wave line singularity, where the $qS1$ and $qS2$ velocity sheets intersect and cross, resulting in approximately orthogonal polarizations. The calculated polarizations for survey B, Figure 4.33(b), show the effects of this line singularity for both crack strike directions.

Comparing the observed polarizations in Figures 4.27 to 4.30, with this model, we can see that cracks striking in directions between N60°E and N85°E provide a much better fit to the measurements from survey A. However, this is at the cost of a reduction in the goodness of fit for survey B. An azimuthally anisotropic model, with a particular crack orientation can be used to model either of the cross-hole azimuths. However, the crack strike direction is not consistent between the two azimuths.

4.6.3 The introduction of TIV to the cross-hole models.

I now consider the effect of the introduction of TIV on the $qS1$ polarizations and time delays between $qS1$ and $qS2$ arrivals, for shear waves propagating at angles of incidence equivalent to those in the cross-hole data. Figures 4.34 and 4.35 show the
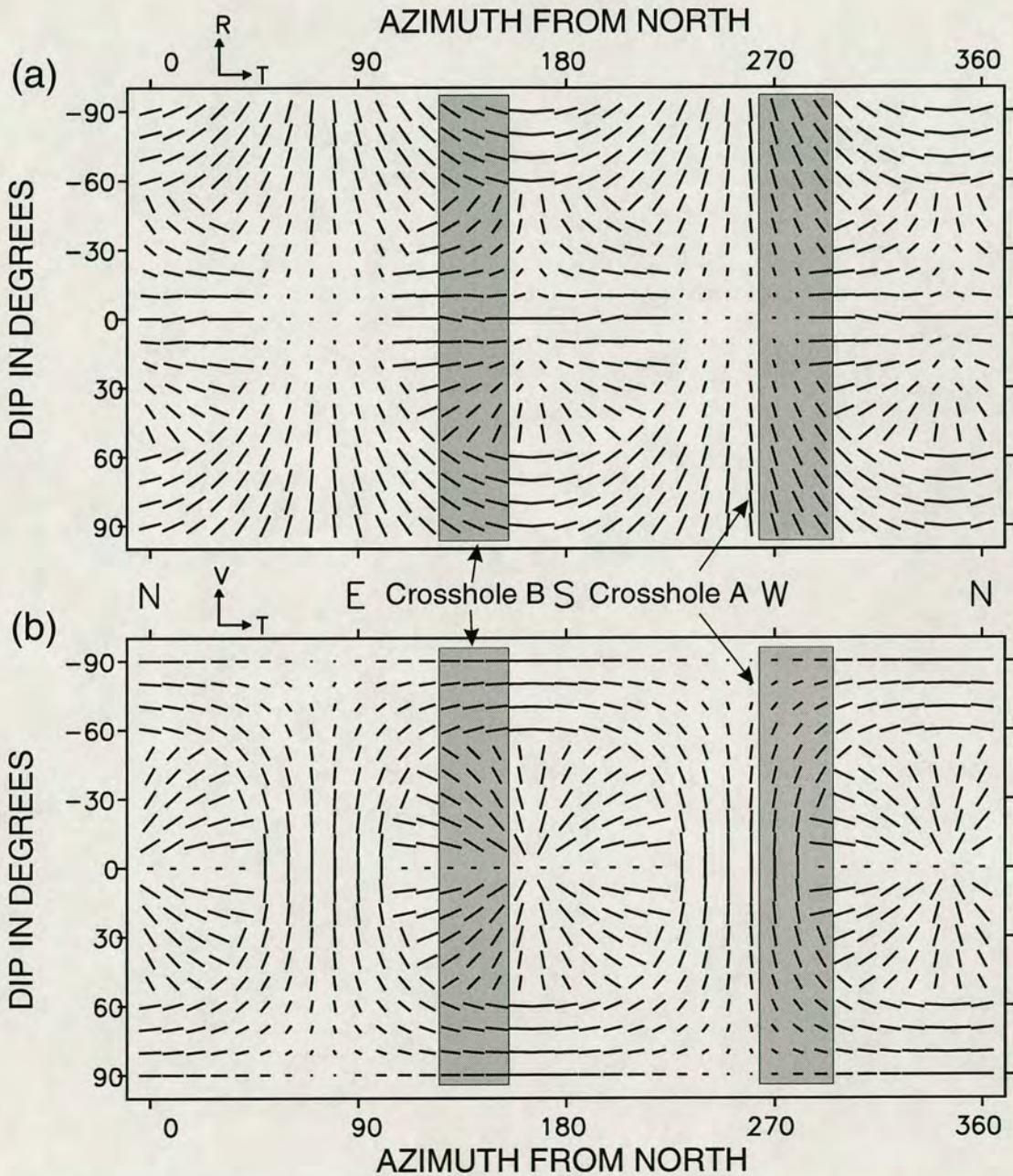
Figure 4.32. Plate Carée projection of theoretical polarizations in the (a)horizontal and (b) normal planes, given by distributions of parallel microcracks striking at an angle of N75°E, with a crack density of 0.05 and aspect ratio of 0.001. Shaded areas delineate the approximate expected polarization observed at Iatan crosshole azimuths A and B, for cracks striking in accordance of the regional trend of N60°E-N85°E.

(a) Cross-hole survey A
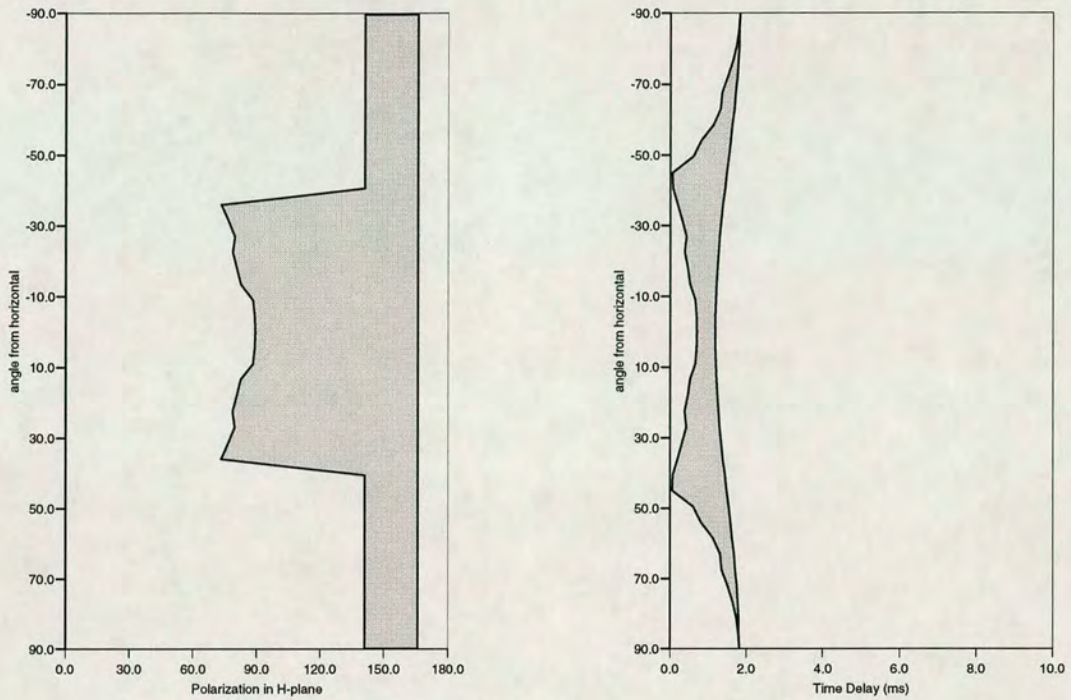
(b) Cross-hole survey B
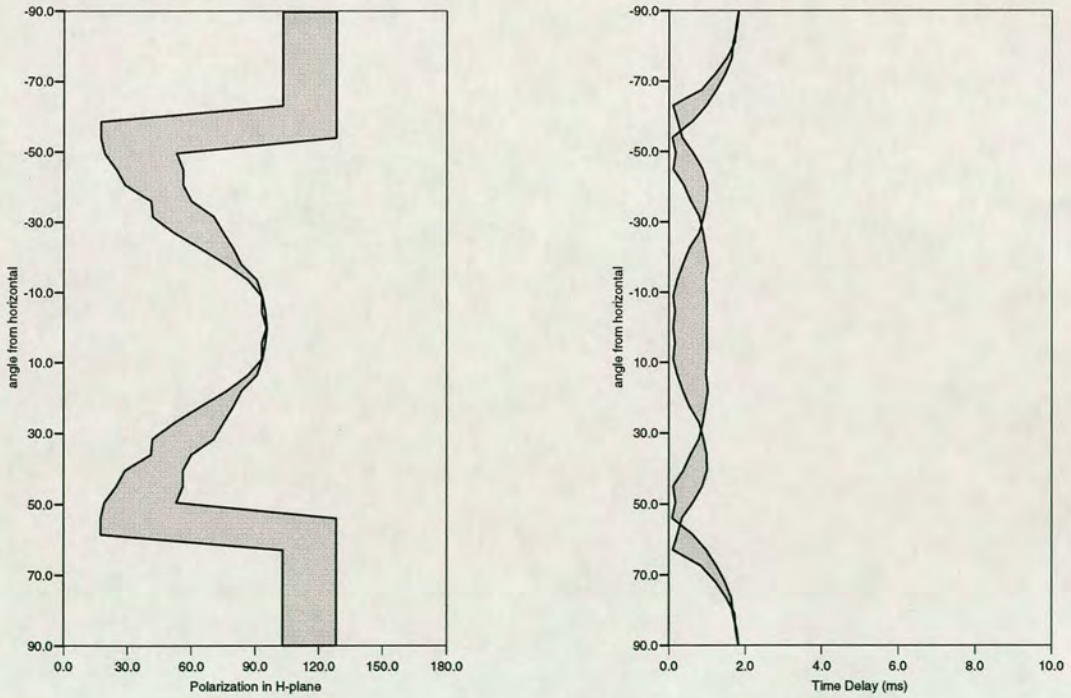
Figure 4.33.Expected *qS1* polarizations and time delays between *qS1* and *qS2* arrivals plotted as functions of angle from horizontal for distributions of parallel Hudson cracks with crack density ε=0.05, striking N60°E–N85°E in an isotropic matrix. For: (a) cross-hole survey A, given a radial direction of N279°E and; (b) cross-hole survey B, given a radial direction of N137°E. Delays are normalized over 100m.

expected zones of behaviour of *qS1* polarizations and time delays between *qS1* and *qS2* arrivals for vertical cracks striking ±12.5° of N170°E in a TIV matrix. The TIV is specified by using horizontal crack sets with crack densities of ε=0.05 and ε=0.1 in Figures 4.34 and 4.35 respectively. Distributions of vertical cracks are incorporated into the resulting anisotropic media using Hudson's formulations to give orthorhombic anisotropic symmetry.

The models retain some of features of the single crack set models in Figure 4.31, for example, the near-vertical polarizations remain the same at both cross-hole azimuths. However, at near-horizontal propagation, the *qS1* arrival is polarized in a transverse direction, regardless of crack strike, for all directions of interest. Time delays are significantly increased for near horizontal directions. There is no improvement in the goodness-of-fit for survey A over the single crack set model.

Similarly, Figures 4.36 and 4.37 show the effect of combining transverse isotropy with a vertical axis of symmetry and vertical cracks striking between N60°E-N85°E. The same patterns of behaviour as described above are observed at both azimuths.

The results for the orthorhombic models shown above, demonstrate that the inclusion of a horizontal crack set reduces the width of the bands of expected *qS1* polarizations which results from a single vertical crack set. As a result, there is no improvement in the fitness of either model to the observed polarizations. Similar behaviour is expected for other forms of TIV, such as that produced by sequences horizontal layers. The modelled time delays for the orthorhombic models are not affected in the same way and the increase in model time delays along near-horizontal raypaths may even improve the fitness of the model to the observations. However, these results cannot rule out the presence of TIV without information from another source such as analysis os shear-wave travel-times.

(a) Cross-hole survey A

(b) Cross-hole survey B
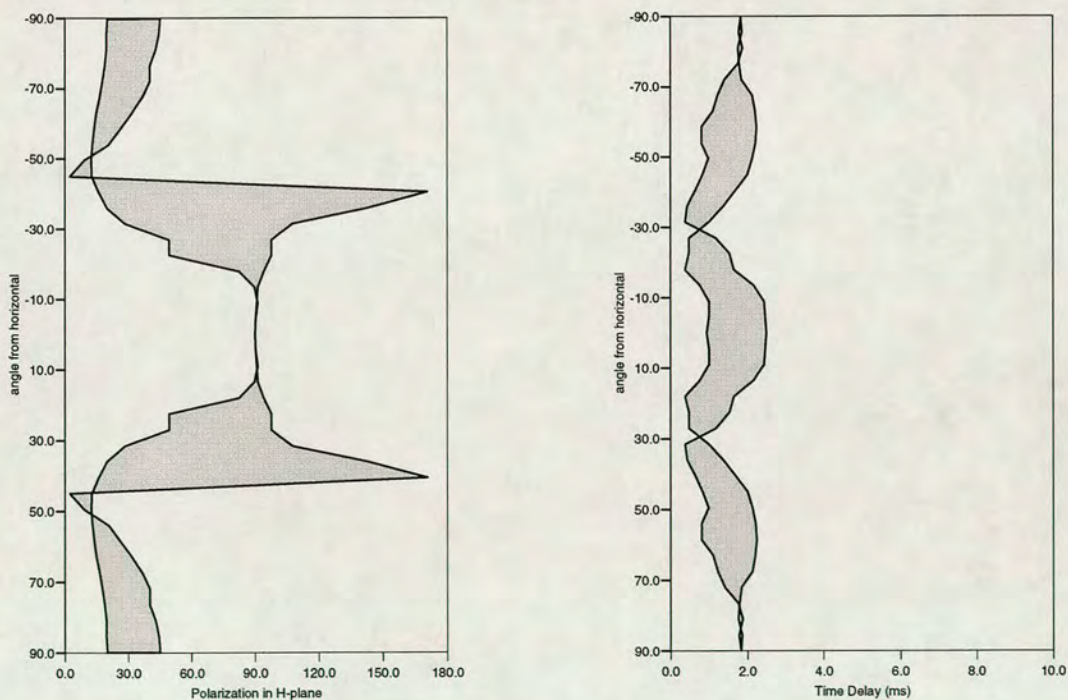
Figure 4.34.Expected zones of behaviour of *qS1* polarizations and time delays between *qS1* and *qS2* arrivals plotted as functions of angle from horizontal for parallel Hudson cracks with crack density ε=0.05, striking ±12.5 of N170°E in a TIV matrix. TIV is specified by horizontal cracks with a crack density ε=0.05. For: (a) cross-hole survey A, given a radial direction of N279°E and; (b) cross-hole survey B, given a radial direction of N137°E. Delays are normalized over 100m.

(a) Cross-hole survey A
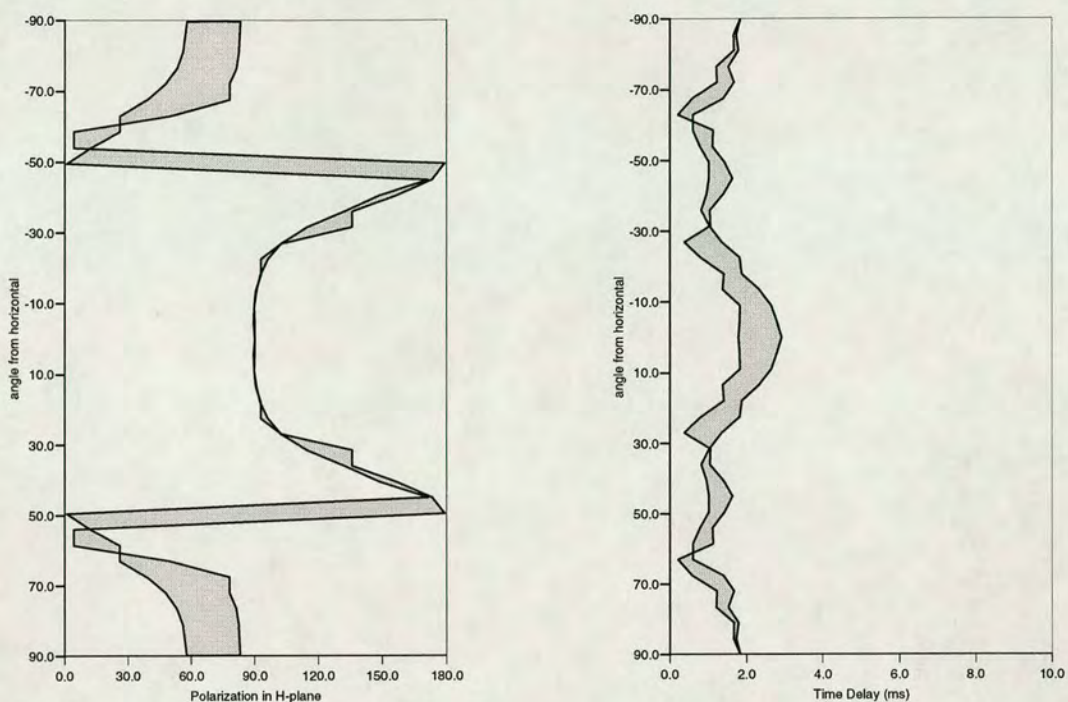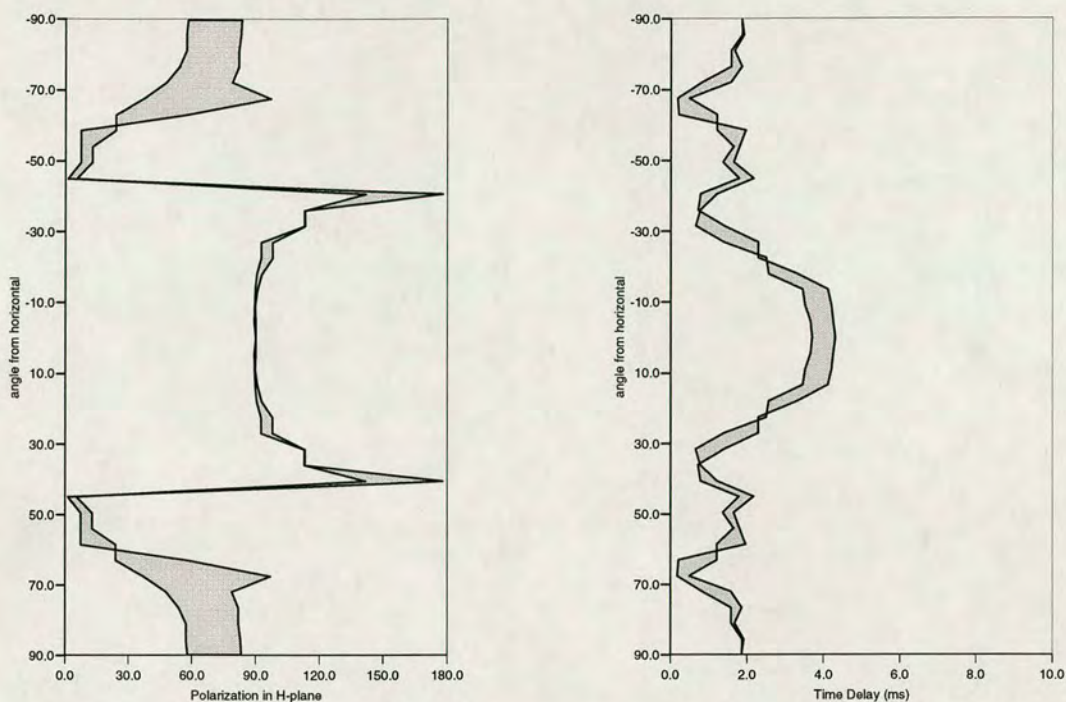

(b) Cross-hole survey B
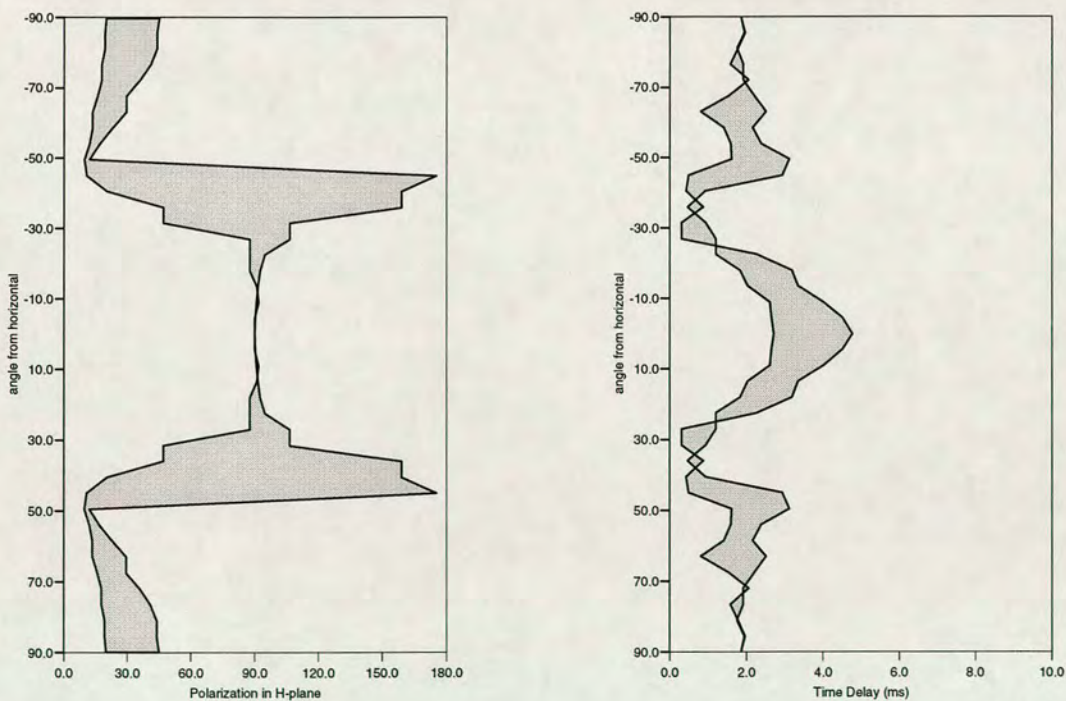
Figure 4.35.Expected zones of behaviour of *qS1* polarizations and time delays between *qS1* and *qS2* arrivals plotted as functions of angle from horizontal for parallel Hudson cracks with crack density ε=0.05, striking ±12.5 of N170°E in a TIV matrix. TIV is specified by horizontal cracks with a crack density ε=0.1. For: (a) cross-hole survey A, given a radial direction of N279°E and; (b) cross-hole survey B, given a radial direction of N137°E. Delays are normalized over 100m.

(a) Cross-hole survey A
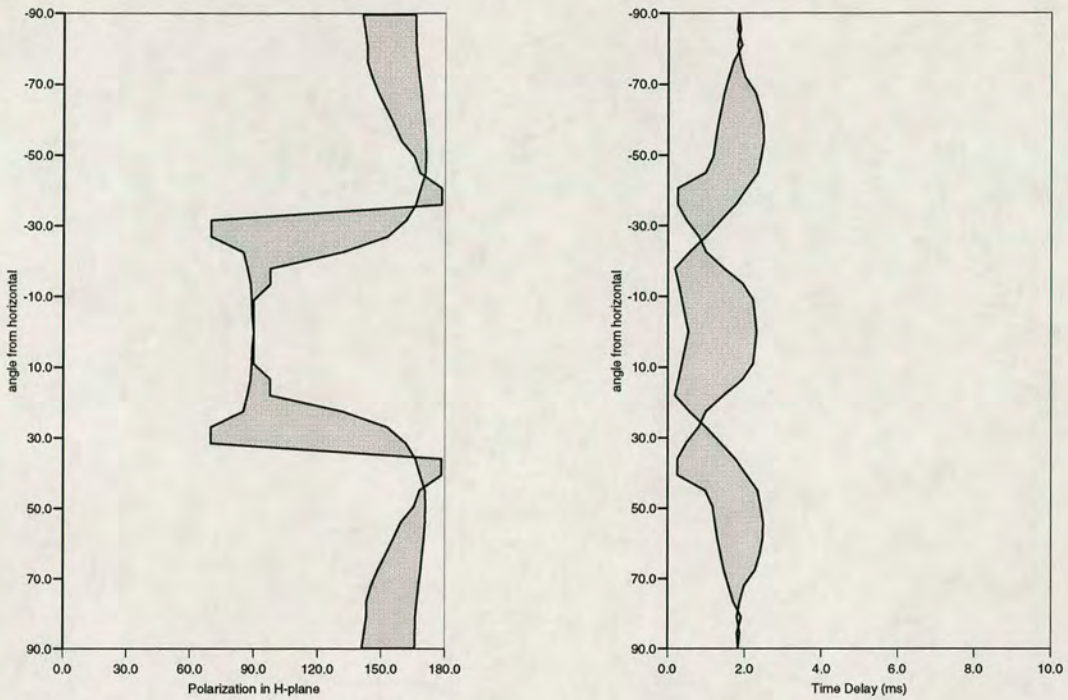
(b) Cross-hole survey B
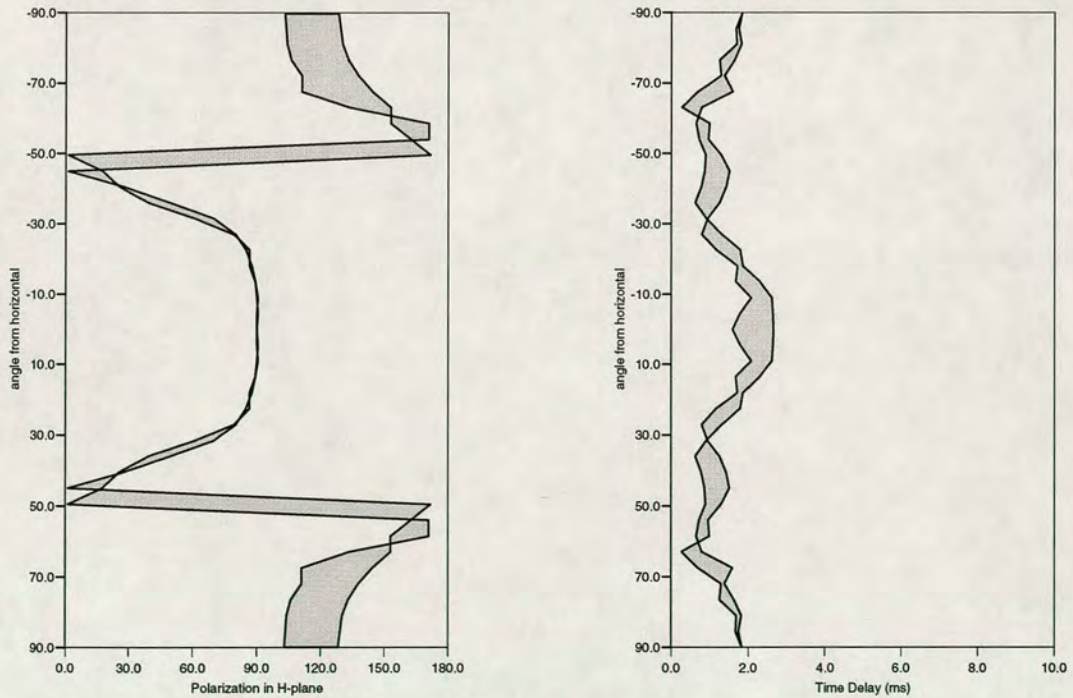
Figure 4.36.Expected *qS1* polarizations and time delays between *qS1* and *qS2* arrivals plotted as functions of angle from horizontal for distributions of parallel Hudson cracks with crack density ε=0.05, striking N60°E–N85°E in a T.I.V. matrix, specified by horizontal cracks with a crack density ε=0.05. For: (a) cross-hole survey A, given a radial direction of N279°E and; (b) cross-hole survey B, given a radial direction of N137°E. Delays are normalized over 100m.

(a) Cross-hole survey A
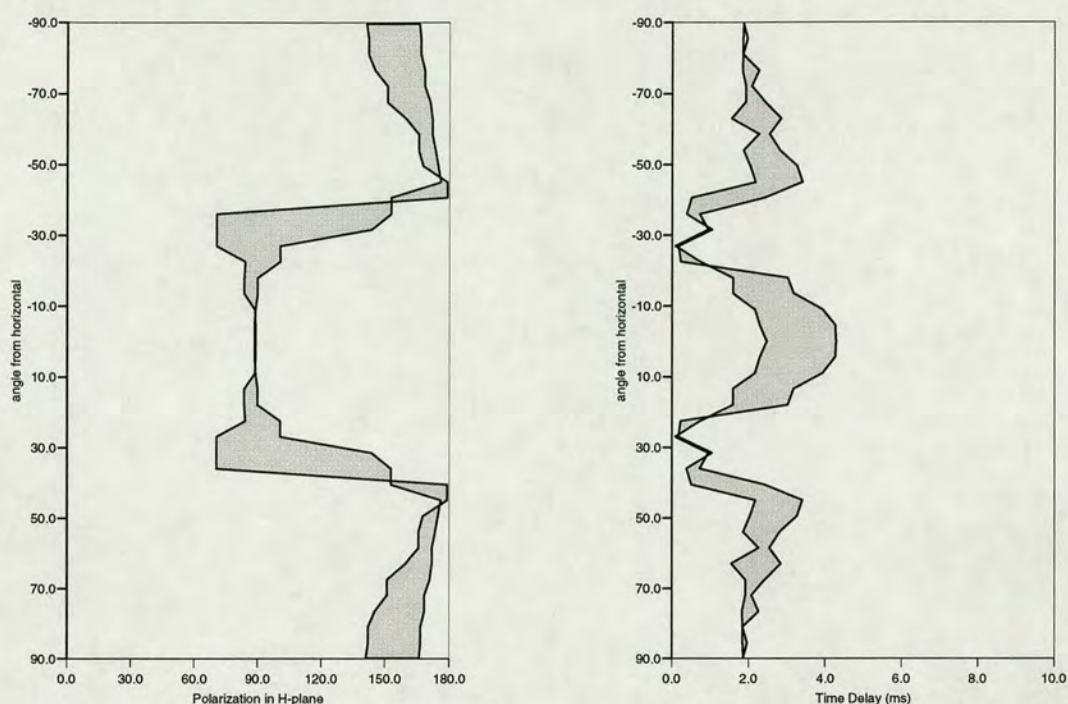
(b) Cross-hole survey B
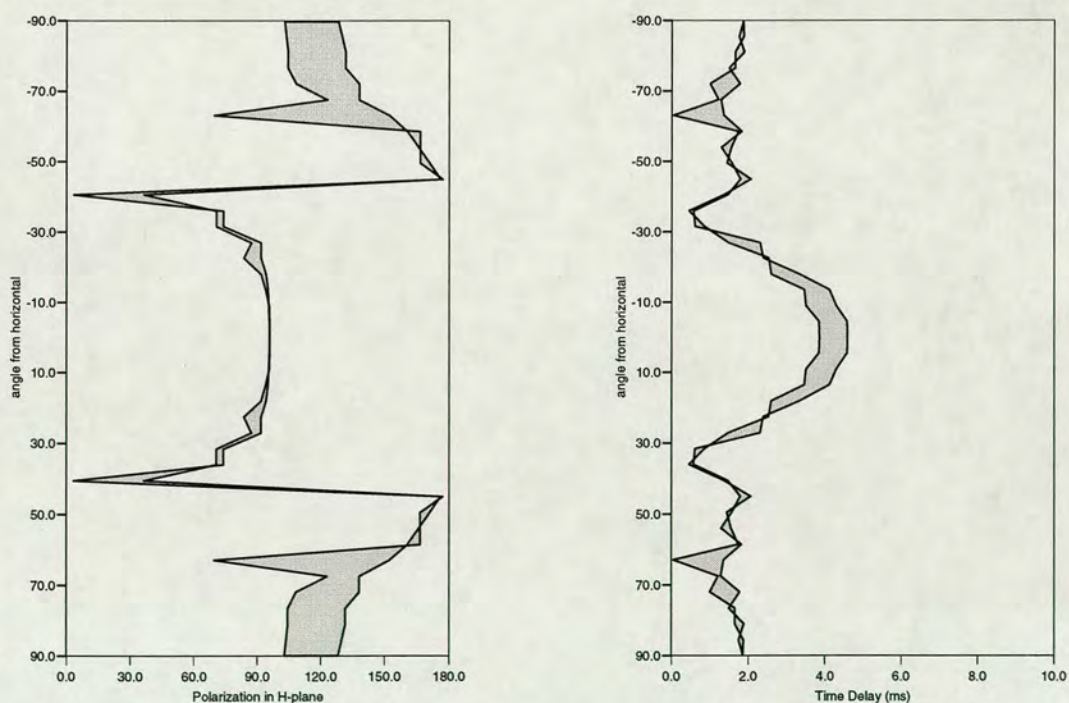
Figure 4.37.Expected *qS1* polarizations and time delays between *qS1* and *qS2* arrivals plotted as functions of angle from horizontal for distributions of parallel Hudson cracks with crack density ε=0.05, striking N60°E–N85°E in a T.I.V. matrix, specified by horizontal cracks with a crack density ε=0.1. For: (a) cross-hole survey A, given a radial direction of N279°E and; (b) cross-hole survey B, given a radial direction of N137°E. Delays are normalized over 100m.

4.7 Implications for the VSP models

How does the anisotropy measured from the crosshole experiment relate to that observed from the VSP data? It is possible that the crosshole and VSP experiments may image a different type of anisotropic scattering, related to small and large scale rock properties. For the two sets of results to be compatible would require a near orthogonal change in crack strike with depth.

I now consider the implications of the $qS1$ polarization directions measured at the two cross-hole azimuths, for the VSP results and modelling. The $qS1$ polarization measurements from cross-hole survey B are consistent with the crack strike obtained from the VSP model of N170°E. However, the results from cross-hole survey A appear to suggest an approximately orthogonal crack strike. For the VSP and cross-hole azimuth A results to be compatible would require an abrupt change in crack strike at depth. In this section I examine how a changing crack orientation within the reservoir layer affects the shear-wave splitting parameters for the VSP models. A model misfit parameter, χ, is then calculated for each model to quantify the goodness of fit.

4.7.1 Does crack strike change with depth?

Cracks at depth are generally expected to be approximately perpendicular to the minimum horizontal compressive stress. However, in near surface areas this may vary depending on local geological conditions (Crampin 1990), giving rise to changing crack strike with depth. Such transitions can give rise to misleading estimates of $qS1$ polarization direction from analysis of shear wave seismic data. Winterstein and Meadows (1991a, 1991b) suggest that decreasing time delays observed from VSP data at three different sites, the Lost Hills field in California, and the Railroad Gap and Cymric fields in the San Joaquim Basin, may infer changing crack strike with depth. Application of a layer stripping algorithm at these sites also supported this assumption.

In general, a change in crack strike will lead to multiple shear-wave splitting

and subsequent distortion of the wavelet shape. Macbeth and Yardley (1992) show that in the case of an abrupt change in crack strike between an upper and lower layer the *qS1* polarization angle given by both *DCT* and *DIT* does not agree with the crack strike in the lower layer. The two angular parameters θ_G and θ_S from *DIT* diverge near the point where the change take place, with θ_G tending towards the new crack strike and θ_S tending towards a constant value. *DCT* gives an incorrect value between these two angles.

For an orthogonal change in crack strike the polarization directions of the fast and slow shear-waves are exchanged for near-vertical propagation. However, the slower shear-wave, *qS2*, will remain the first arrival until the propagation distance increases to a point where the fast shear-wave overtakes it. As a consequence of this measured time delays will decrease to zero, then increase. So the diagnostic feature of a near-orthogonal change in crack strike will be a decrease in time delay.

Figure 4.38 shows the measured polarizations for a models where the crack strike in layer 5 is N170°E, but that in layer 6 is N80°E. Comparing this plot with the polarization behaviour of models where crack strike is constant with depth, Figures 4.16 and 4.19, it is clear that the polarization measurements from both the near and far offset models are insensitive to this change.

However, an examination of the time delay behaviour in Figures 4.39, shows that time delays for the near offset model begin to decrease, as expected, below 2400 feet, where the change in orientation occurs. At far offsets the magnitudes of the model time delays show small variations from the constant crack strike with depth model, but a distinctive change in behaviour does not occur.

4.7.2 Model fitness

Given the possibility that crack strike could change with depth, I examine models in which the crack strike in the upper layer is constant at N170°E. The crack strike in the lower layer is rotated in increments of 10° from North to East. The crack density in the reservoir layer is varied for each rotation angle from ε=0.01 to 0.05 in
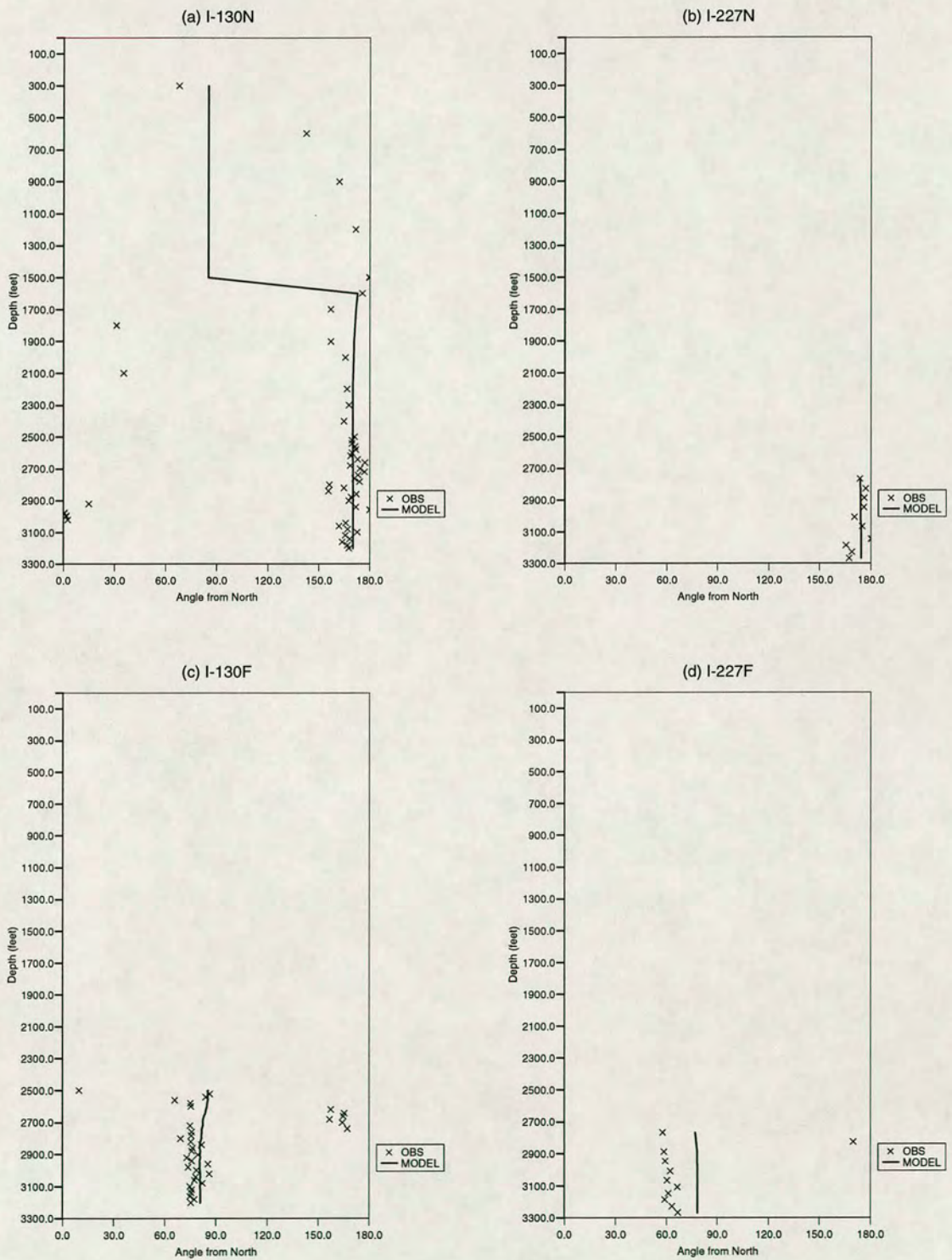
Figure 4.38. Observed and modelled polarizations for Iatan VSP's, measured using the DCT method. The model has two anisotropic layers with orthogonal crack strikes: Layer 5 has a crack density of 0.08 and crack strike of N170°E and layer 6 has a crack density of 0.05 and a crack strike of N80°E.
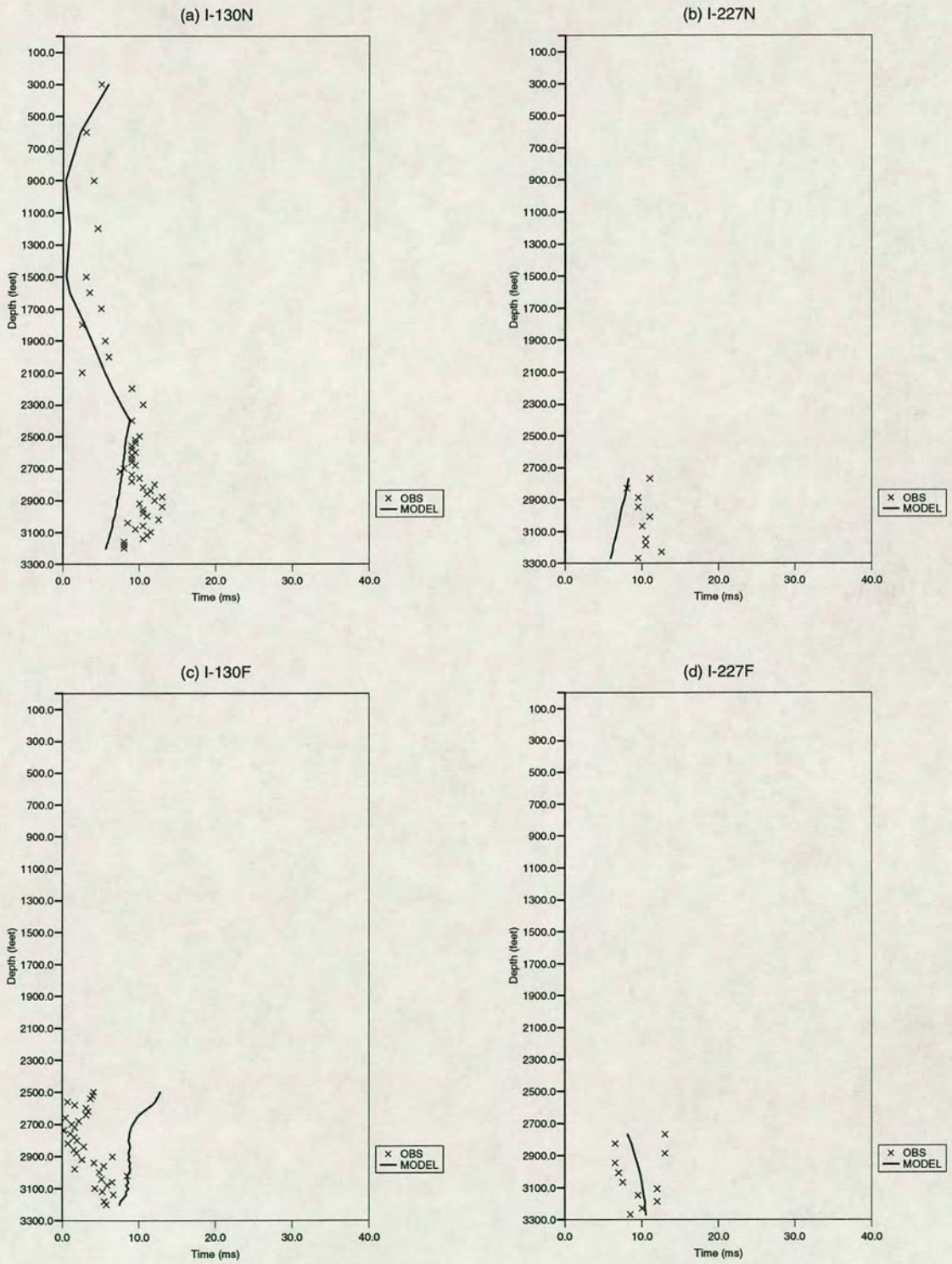
Figure 4.39. Observed (crosses) and modelled (solid line) time delays measured using the DCT method. The model has two anisotropic layers with orthogonal crack strikes: layer 5 has a crack density of 0.08 with cracks striking N170E; layer 6 has a crack density of 0.05 with cracks striking N80E

increments of 0.005. Synthetic seismograms are generated using forward modelling for each model and *DCT* is used to measure the model shear-wave splitting parameters.

A model fitness parameter, χ, is determined for each VSP model using the merit function defined by equation 3.10. Errors in each polarization measurement of ±10°, and in each delay measurement of ±1ms, are used in the calculation. Misfit in polarization and time delay are determined separately.

Figure 4.40 shows contoured misfit function values for polarizations and time delays plotted against crack orientation and crack density. Data were interpolated into a more finely sampled grid of 36 cells in the *X*-direction and 20 cells in the *Y*-direction., before contouring.

Figures 4.40(a) and (b) show the misfit in polarization and time delay for the I-130 near offset measurements. The misfit values for polarization show the relatively poor resolution of the minima. The region below 1.2 covers a wide range of orientations and crack densities. An orientation of N160°E-N170°E lies within the minimum region for all crack densities sampled. However, orientations of N70°E-N80°E also lie within this region for lower crack densities. This demonstrates the insensitivity of the near offset polarizations to changes in crack strike at depth.

Examination of the misfit function for delay measurements, Figure 4.40(b) shows that two minima exist, N0°E-N50°E and N120°E-N180°E. The range of crack densities has been significantly reduced. Combining misfit information for polarizations and time delays suggests that the best-fit solutions for the I-130 near offset measurements lie in the range of crack strikes from N120°E-N180°E and crack densities from ε=0.01-0.02.

Figures 4.40(c) and (d) show similar plots for the I-227 near offset polarizations and time delays. The minima in the polarization misfit (below the 0.8 contour) lies between crack orientations of N90°E-N155°E and crack densities of ε=0.01-0.03. The minima for the delays (below the 1.1 contour) again lie in two areas, N0°E-N20°E and N135°E-N155°E. Combining information for polarizations and delays gives a best fitting solutions of crack strikes between N135°E-N155°E and
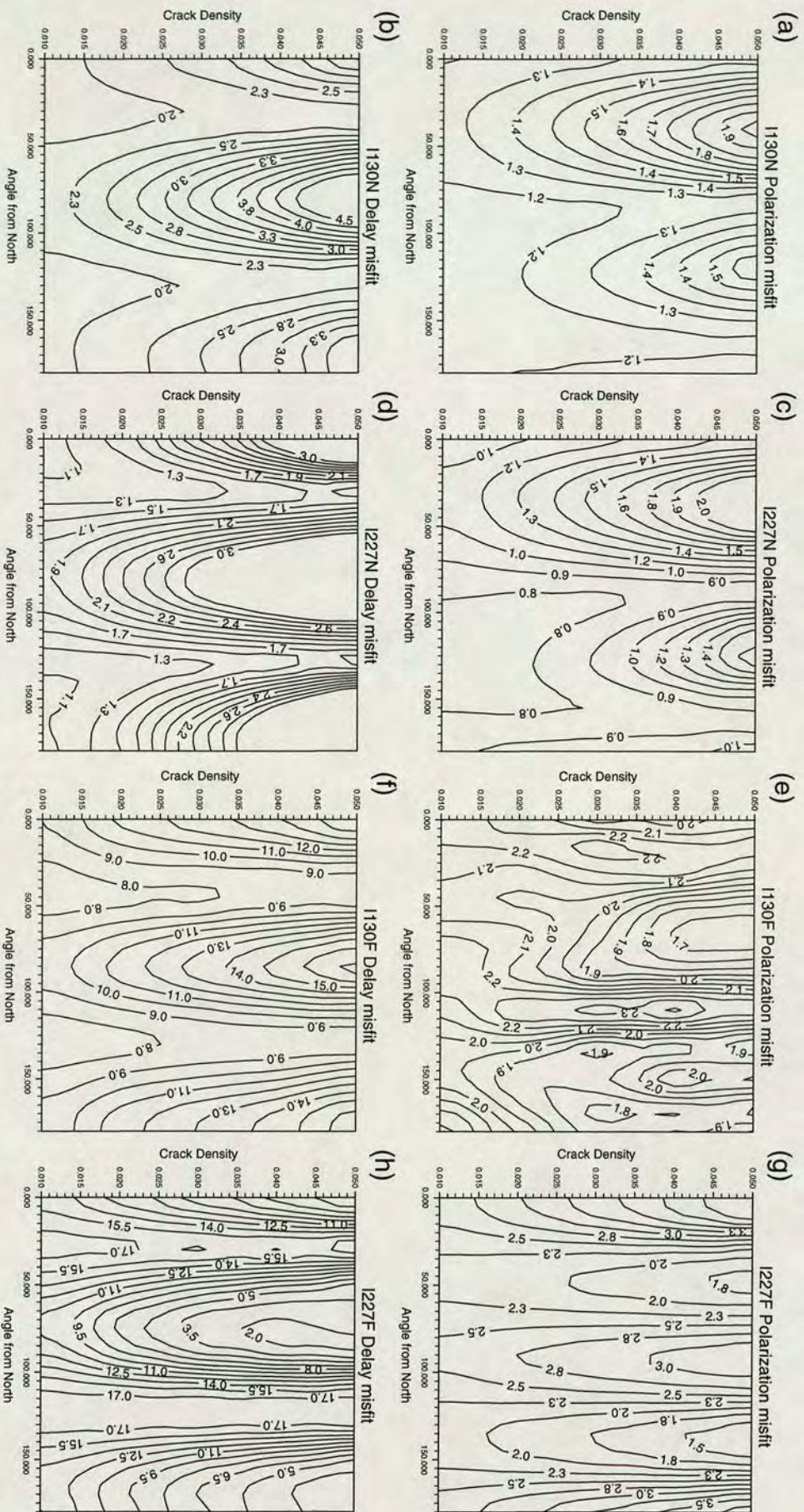
Figure 4.40. Contoured misfit function values for Iatan VSP models calculated for $qS1$ polarization and time delay between $qS1$ and $qS2$ arrivals, plotted for a range of crack orientations and crack densities. Lower values indicate a better fit to the observations.

crack densities below ε=0.015.

The behaviour of the misfit function for the I-130 far offset polarizations, Figure 4.40(e) shows more complexity. Minima exist in several directions between N140°E-N180°E for a range of crack densities. An additional minima occurs between N55°E-N75°E for crack densities above ε=0.04. Two minima occur for time delay misfits, Figure 4.40(f): N25°E-N55°E for crack densities of ε≤0.035; and N110°E-N145°E for crack densities of ε≤0.025. Delay misfits are significantly higher indicating a relatively poor fit to the observed time delays. In this case the minima for polarization and time delay do not overlap.

The misfit function values for I-227 far offset display similar behaviour, Figure 4.40(g) and 4.40(h), with the minima for polarizations failing to agree with those for delays. In this case the delay misfit is least for higher crack densities than calculated for the other VSP's.

Overall, the misfit analysis suggests that the best-fit reservoir crack density is likely to be somewhat less than previously used, ε=0.02 or less. The best-fit reservoir crack strike lies between N140°E and N170°E, suggesting that crack strike is approximately constant with depth. As expected, time delays show more sensitivity between models with constant crack strikes and those with an orthogonal change in crack strike at depth.

4.8 Discussion

Wave propagation through the Clearfork reservoir formation exhibits many of the characteristics of wave propagation in an effectively anisotropic medium. I have obtained four independent measures of *qS1* polarization direction: from near offset VSP's; from far offset VSP's; crosshole dataset A; and crosshole dataset B. Consideration of the near offset VSP data alone, suggests a fracture strike of N170°E, which is constant with depth. Both far offset VSP's give *qS1* directions which are approximately orthogonal. This appears to be consistent with a simple vertical crack model. The time delay build up above the reservoir formation is indicative of an

anisotropic near-surface, which could be obscuring the reservoir anisotropy. Inversion of fast and slow arrival times from the I-130 near offset VSP yields a multi-layered velocity structure, which, in conjunction with the measured anisotropic parameters, allows generation of synthetic seismograms by forward modelling. Measured model parameters provide a good fit for near offset observations, in terms of both traveltimes and anisotropic parameters. However, there is a considerable misfit in both far offset traveltimes and polarizations; the observed and modelled $qS1$ directions deviating by up to 20°. The inclusion of transverse isotropy into the reservoir model, resulting in orthorhombic anisotropic symmetry, significantly improves model fitness for far offset arrival times, without degradation in fit for the near offset observations.

The spatial resolution of anisotropy obtained from the VSP's is relatively poor, despite geophone spacing in the reservoir of 20 feet. The structure can only resolved in terms of massive layers, whose crack properties are uniform with depth. It is known that actual oil production is from high porosity zones, stringers, within the Clearfork formation.

Interpretation of near offset $qS1$ polarizations as a fracture strike of N170°E disagrees with independent measurements of fractures within the reservoir. Measurements from core samples and injection water breakthrough directions indicate a fracture direction of between N60°E and N85°E. A well established regional fracture trend also runs in this direction. In view of this, I examined the effect of a change in crack orientation at depth. Models with an abrupt change in crack strike also the fit the observed $qS1$ polarizations. However, an orthogonal or near-orthogonal change introduces a decrease in modelled near offset time delays which is not seen in the observations. Calculated misfit function values, in general, support the conclusion that the best-fit model has constant crack strike with depth.

The cross-hole seismic data allows examination of anisotropy in the reservoir zone at higher frequencies and along shorter raypaths, without the distortion associated with propagation through the near-surface. Anisotropic parameters are measured at individual geophones as a function of incidence angle. Numerical measurements of the shear-wave splitting parameters, when applied to windowed shear-wave arrivals, are

consistent with particle motion hodograms and instantaneous polarizations calculated from the covariance matrix. Anisotropic behaviour within the Clearfork formation appears to be relatively depth invariant. This allows observations for all geophone depths to be viewed together, giving an averaged picture of the dependence of polarization and time delay.

Horizontal plane polarization angles from crosshole survey A lie in a distinct zone between 140° and 170° from the radial direction. Modelling shows that these measurements fall within the range of behaviour expected for distributions of cracks striking between N60°E and N85°E. This is in agreement with the *a priori* results from core samples and injection water breakthrough directions. Measured time delays between *qS1* and *qS2* arrivals increase from around 1ms/100m for near-vertical propagation to below 4ms/100m for near-horizontal propagation. These time delays are larger than expected for a vertical crack model with a crack density of ε=0.05 or less, however, the inclusion of TIV can provide a better fit to the observed time delays in near-horizontal directions.

Polarization measurements from crosshole survey B are distributed between 20°-60° from radial, with most of the measurements being within ±20° of horizontal propagation. Modelling shows that these measurements fall within the zone of expected behaviour for distributions of cracks striking between ±12.5° of N170°E, which is in agreement with the crack strike obtained from the VSP measurements. Measured time delays between *qS1* and *qS2* arrivals lie between 1-2ms/100m for all directions of propagation, around half of that for survey A. This also agrees with the expected behaviour shown for such crack distributions.

Taken together, the crosshole results may suggest an apparent lateral variation in crack properties between wells I-227 and I-152. However, I believe this is unlikely because of the small distances between the wells and the uniformity of the geology.

Overall, the different estimates of *qS1* polarization, from VSP and cross-hole data are all consistent with a model crack strike of around N170°E, except for cross-hole azimuth A. This conflict of information cannot be easily explained. Especially since measurements of from the latter were thought to be more reliable than those

from survey B because of the shorter path-lengths and shorter more near vertical coverage. As a result, I was unable to find a model which was compatible with all observations without extending the model space beyond that for two crack sets, one horizontal and one vertical.

CHAPTER 5: CONCLUSIONS

5.1 Introduction

The aim of this study was to apply the cross-hole method to examine the behaviour of shear-waves propagating through known fractured reservoirs and to resolve the seismic anisotropy within the reservoir zone. Observations of shear-wave splitting have been analyzed in three separate reservoir formations and the seismic anisotropy has been related to the fracture systems. The advantage of cross-hole observations is that the seismic anisotropy measured at depth does not suffer degradation in data quality due to the severe scattering at the near surface. In addition, the use of cross-hole data ensured that the anisotropic parameters measured cannot be related to a near-surface effect or an anisotropic overburden, which has inhibited many previous studies of reservoir anisotropy in VSP data (Yardley 1993). The main findings are summarized in the following sections.

5.2 Theoretical study of shear-wave polarizations and time delays

Polarizations and time delays of split shear-waves have been calculated from the elastic constants of materials with varying combinations of two anisotropic symmetries. These parameters were displayed on Plate Carée projections for a full range of azimuths and incidence angles. The modelling showed the probable sensitivity of the parameters of shear-wave splitting to variations in the anisotropic rock properties. I conclude that changes in crack properties are likely to be difficult to detect as large changes in both aspect ratio and crack density resulted in comparatively minor variations to the three dimensional patterns of polarizations and time delays. However, the position of shear-wave singularities does appear to contain important information on the types and relative amounts of anisotropy. The implications for field data are that unique solutions may not exist for a particular set of observations. Many possible model solutions may exist for a set of results, which

cannot be easily resolved, particularly where experimental errors are large. Accurate resolution of the anisotropy will necessarily require both careful planning of acquisition parameters and sufficiently large angular coverage.

5.3 Observations of shear-wave anisotropy

Cross-hole data from the East Fitts field has been used to image two separate reservoir rocks using seismic waves propagating through and reflected from the pay zone. Shear-wave splitting has been measured numerically at three azimuths and three source positions. A best-fit model in which the reservoirs contain distributions of vertical fractures has been determined by forward modelling. The important conclusion in this case is that the observed anisotropy has been related to an actual reservoir fracture system. Fracture orientation for the best-fit model compares favourably with local stress directions in the area of the survey, providing corroborating evidence of the relationship between fracture orientation and the local stress field (Crampin 1993). Two methods were used to determine model parameters. Firstly, by using anisotropic ray-tracing to calculate $qS1$ polarization angles and time delays for particular azimuths and incidence angles. Secondly, by directly measuring polarizations and time delays from synthetic seismograms generated for the anisotropic models. As the generation of synthetic seismograms and the numerical measurement of parameters is both time consuming and costly in terms of computer processing, I suggest that the former method should be used whenever possible. However, the latter has the advantage of applying the same treatment to the synthetics as to the observations.

In the second case study I examined measurements of seismic anisotropy for shear waves propagating through the fractured Clearfork reservoir formation, from both VSP and cross-hole seismic data. The reservoir is known to contain vertical fractures aligned in accordance with a well-known regional trend. Four independent measures of $qS1$ polarization direction have been obtained: from near offset VSP's; from far offset VSP's; from cross-hole dataset A; and from cross-hole dataset B. The near and far offset VSP $qS1$ polarization directions are consistent with a reservoir

fracture orientation of N170°E. However this direction is incompatible with independent measurements of fracture orientation from core samples and injection water break-through directions.

Measurements of the *qS1* polarization direction from cross-hole dataset A, did fall into the areas expected for cracks striking between N60°E and N85°E. But measurements of *qS1* polarization direction from the second cross-hole dataset, B, are consistent with a reservoir crack strike of ±12.5° from N170°E. The scatter in measured *qS1* directions measured from the cross-hole data fell within a relatively wide range of crack strikes suggesting that either experimental errors are large or that crack strike within the reservoir formation is variable. The cross-hole data is unable to resolve areas of high or low fracturing within the Clearfork reservoir formation, which appears as a homogeneous fractured unit even at high frequencies of 250Hz. This may suggest that observed *qS1* polarization directions may represent the spatial average of the fracture orientations within the whole formation.

The difference in polarization directions given by the VSP's and the cross-hole data cannot be easily explained. I investigated the possibility of an abrupt change in crack strike at depth by forward modelling. However, calculation of model fitness for various orientations suggested that a near-orthogonal change in crack strike does not improve model fitness. Lateral variability in fracture direction is another possibility, but I believe this is unlikely due to the small distance involved.

Finally, I conclude that anisotropy introduces a non-uniqueness of solution which presents a formidable hurdle for forward modelling. The considered solutions represent only a small, albeit interesting, corner of possible model solutions and other much better fitting solutions to the observed parameters may exist within the full parameter space. Because of the great extent of the possible solutions the drawbacks of the forward modelling approach are only too obvious and in future such a trial and error method should not constitute an effective means of finding appropriate solutions.

5.4 The cross-hole method

The cross-hole method has been shown to be reasonably successful in resolving reservoir anisotropy in the above cases. I conclude that from the evidence here that the cross-hole method is likely to give a more reliable picture of anisotropy at depth than surface studies, which can suffer degradation by propagation through the near-surface. However, drawbacks do exist which may inhibit usage for this purpose in future. Firstly, the angles of propagation in cross-hole geometries are such that solid cones of directions in which the $qS1$ polarization directions are aligned parallel to the cracks do not exist, so less diagnostic information on the anisotropy present is available. Accurate resolution of anisotropic properties is likely to require some form of modelling. Secondly, although the down-hole airgun is, in general, a good source of both P- and S-wave energy, there is insufficient horizontally propagating shear-wave energy to allow accurate measurement of anisotropy in these directions.

Finally, and perhaps most importantly, the cross-hole method is expensive, given that two boreholes, as opposed to one for a VSP, are required. Increased azimuthal coverage cannot be obtained without the drilling of additional wells. This being the case, cross-hole studies are generally restricted to monitoring changes in existing oil-fields, rather than as an exploration tool. I suggest that a possible application for shear-wave studies could lie in this area. In particular, the study of shear-wave data acquired both before and after an improved oil recovery operation may be of great interest.

5.5 Shear-wave anisotropy

Although theoretical studies into the possible effects of seismic anisotropy are abundant, to a large extent the relationship between apparent shear-wave splitting and actual fracturing at depth remains poorly resolved. In general, there is a lack of published material with data examples. However, even if reservoir fracturing is not the direct cause of the observed shear-wave anisotropy, the two are likely to be related in

some way, given the similarity between observed polarizations and the fracture alignment. This study has provided further evidence of a positive relationship between azimuthal anisotropy and the presence of distributions of fracture systems. However, more work is undoubtedly required before this relationship can be adequately resolved.

Both the East Fitts and Iatan East Howard fields are ideal for the study of seismic anisotropy, given the geological simplicity of each area. Structural complexity, such as steeply dipping layers or lateral inhomogeneity are likely to present considerable difficulties in the interpretation of multicomponent data. Given that many reservoirs display complex structure and stratigraphy, we must develop tools to assist the processing and modelling of anisotropy in these contexts. Until such tools are developed and successfully implemented, I suspect that shear-wave splitting studies are likely to remain a topic for research rather than an established method for the identification and characterization of fracture systems. However, shear waves are much more sensitive to the details of fluid-fluid and fluid-rock interactions than P-waves. Therefore, shear-wave splitting may have more applications in reservoir engineering and monitoring fluid-fluid production fronts using time lapse analyses.

5.6 Suggestions for future directions of work

My primary suggestion for any future work undertaken in this field would be for the application of an optimized global inversion scheme such as simulated annealing or a genetic algorithm (Horne 1995) to the data studied here. This may provide more accurate resolution of reservoir crack parameters and prevent selection of local maxima as the global solution. As a corollary to this I would also suggest that future acquisition geometries should be considered carefully and that pre-survey modelling should be carried out to help the optimization procedure.

Developments in technology should bring about improved down-hole sources, which can generate shear waves with more than one polarization. This should allow the application of dual source measurement techniques. Additional processing algorithms should also be developed more suitable for measurement of shear-wave

splitting parameters in cross-hole studies, for example the method of Cho and Spencer (1992) could be applied to estimate polarization and slowness from the multicomponent cross-hole wavefield.

Finally, with regard to the modelling of shear-wave behaviour, it is important that any method of generating synthetic seismograms should allow the source to be embedded in an anisotropic medium. Although the methods has been developed by several authors, *e.g.* Tsvankin and Chesnokov (1990) the complexity of calculation is significantly increased. Continued improvements in the field of computing should make this problem computationally realistic.

REFERENCES

Arbenz, J.Z., 1956. Tectonic map of Oklahoma, *Oklahoma Geol. Survey,* OM-3.

Alford, R.M., 1986. Shear data on presence of azimuthal anisoptropy: Dilley, Texas, *56th Ann. Internat. Mtg., S.E.G., Houston, Expanded Abstracts,* 476-479.

Backus, G.E., 1962. Long-wave anistropy produced by horizontal layering, *J. Geophys. Res.,* **66,** 4427-4440.

Baptie, B.J., Crampin, S. and Liu, E., 1993. Displaying shear-wave splitting in cross-hole surveys for materials with combinations of EDA and PTL anisotropy, *Can. J. Expl. Geophys.,* **29,** 227-235.

Baptie, B.J. and Crampin, S., 1994. Shear-wave anisotropy from multicomponent VSP data, Iatan East Howard field, Mitchell County, Texas, *56th Ann. Internat. Mtg., E.A.E.G., Vienna, Expanded Abstracts.*

Barton, C.A. and Zoback, M.D., 1988. Determination of in situ stress orientation from borehole guided waves, *J. Geophys. Res.* **93,** 7834-7844.

Booth, D.C. and Crampin, S., 1983. The anisotropic reflectivity technique: theory, *Geophys. J. Roy. astr. Soc.,* **72,** 755-766.

Booth, D.C. and Crampin, S., 1985. Shear wave polarizations on a curved wavefront at an anisotropic free-surface, *Geophys.J. Roy. astr. Soc.,* **83,** 31-45.

Booth, D.C., Crampin, S., Evans, R. and Roberts, G., 1985. Shear wave polarizations near the North Anatolian fault - I. Evidence for anisotropy induced shear-wave splitting, *Geophys. J. Roy. astr. Soc.* **83,** 61-73.

Bush, I., 1990. *Modelling shear-wave anisotropy in the Paris Basin,* Ph.D. thesis, University of Edinburgh.

Bush, I. and Crampin, S., 1987. Observations of EDA and PTL anisotropy in shear-wave VSP's, *57th Ann. Internat. Mtg., Soc. Expl. Geophys., New Orleans, Expanded abstracts,* 646-649.

Campden, D.A., 1990. *Analysis of multi-component VSP data for shear-wave anisotropy,* Ph.D. Thesis, University of Edinburgh.

Červený, V. and Firbas. P., 1984. Numerical modelling and inversion of traveltimes of seismic body waves in inhomogeneous anisotropic media, *Geophys. J. R. astr. Soc.,* **76,** 46-51.

Chapman, C.H. and Shearer, P.M., 1984. Ray tracing in azimuthally anisotropic media, *Geophys. J.*, **96**, 65-83.

Cho, W.H. and Spencer, T.W., 1992. Estimation of polarization and slowness in mixed wavefields, *Geophysics,* **57**, 805-814.

Claerbout, J.F. and Muir, F., 1973. Robust modelling with erratic data, *Geophysics,* **38**, 826-844.

Cliet, C., Brodov, L., Tikonov, A., Marin, D. and Michon, D., 1991. Anisotropy for reservoir delineation, *Geophys. J. Internat.*, **107**, 417-428.

Crampin, S., 1981. A review of wave motion in in anisotropic and cracked elastic media, *Wave Motion*, **3**, 343-391.

Crampin, S., 1984a. An introduction to wave propagation in anisotropic media, *Geophys. J. R. astr. Soc.*, **76**, 17-28.

Crampin, S., 1984b. Effective anisotropic elastic constants for wave propagation through cracked solids, *Geophys. J. Roy. astr. Soc.,* **76**, 135-145.

Crampin, S., 1989. Suggestions for a consistent terminology for seismic anisotropy, *Geophys. Prosp.,* **37**, 753-770.

Crampin, S., 1990. Alignment of near-surface inclusions and appropriate geometries for geothermal hot-dry-rock experiments, *Geophys. Prosp.,* **38**, 621-631.

Crampin, S., 1991. Effects of point singularities on shear-wave propagation in sedimentary basins, *Geophys. J. Internat.,* **107**, 531-543.

Crampin, S., 1993. Arguments for EDA, *Can J. Expl. Geophys.*, **29**, 18-30.

Crampin, S., Evans, R. and Atkinson, B.K., 1984. Earthquake prediction: a new physical basis, *Geophys. J. R. astr. Soc.*, **76**, 147-156.

Crampin, S. and Kirkwood, S.C., 1981. Velocity variation in systems of anisotropic symmetry, *J. Geophys.*, **49**, 35-42.

Crampin, S. and Yedlin, M., 1981. Shear-wave singularities of wave propagation in anisotropic media, *J. Geophys.*, **49**, 43-46.

Dart, R.L., 1987. Horizontal stress orientations from well-bore breakouts in the south-central United States, *40th Ann. Mtg. Am. Geol. Soc. Abstracts*, p269.

Davis, T.L. and Lewis, C., 1990. Reservoir characterization by 3D, 3C seismic imaging, Silo Field, Wyoming, *The Leading Edge* **9**, 11, 22-25.

Douma, J., 1988. The effect of aspect ratio on crack-induced anisotropy. *Geophys. Prosp.*, **36**, 614-632.

Douma, J. and Crampin, S., 1990. The effect of a changing aspect ratio of aligned cracks on shear-wave vertical seismic profiles: a theoretical study, *J. Geophys. Res.*, **95**, 11,293-11,300.

Eshelby, J.D., 1957. The determination of the elastic field of an ellipsoidal inclusion and related problems, *Proc. Roy. Soc., London, Series A*, **241**, 376-396.

Fuchs, K. and Müller, G., 1971. Computation of synthetic seismograms with the reflectivity method and comparison with observations, *Geophys. J. R. astr. Soc.*, **23**, 417-433.

Garbin, H.D. and Knopoff, L., 1975. Elastic moduli of a medium with liquid-filled cracks, *Quar. J. Appl. Maths.*, **30**, 453-464.

Gardner, G.H.F., Gardner, L.W. and Gregory, A.R., 1974. Formation velocity and density - the diagnostic basis of stratigraphic traps, *Geophysics*, **39**, 770-780.

Helbig, K., 1984. Transverse isotropy in exploration seismics, *Geophys. J. R. astr. Soc.*, **76**, 79-88.

Hoaglin, D.C., Mosteller, F. and Tukey, J.W. 1983. *Undestanding robust and exploratory data analysis.* John Wiley and Sons, New York.

Holmes, G.M., Crampin, S. and Young, R.P., 1993. Preliminary analysis of shear-wave splitting in granite at the Underground Research Laboratory, Manitoba, *Can. J. Expl. Geophys.*, **29**, 140-152.

Horne, S.A., 1995. *Applications of genetic algorithms to problems in seismic anisotropy*, Ph.D. Thesis. University of Edinburgh.

Huber, P.J., 1964. Robust estimation of a location parameter, *Ann. Math. Stat.*, **35**, 73-101.

Hudson, J.A., 1980. Overall properties of a cracked solid, *Math. Proc. Cam. Phil. Soc.*, **88**, 371-384.

Hudson, J.A., 1981. Wave speeds and attenuation of elastic waves in material containing cracks, *Geophys. J. R. astr. Soc.*, **64**, 133-150.

Hudson, J.A., 1986. A higher order approximation to the wave propagation constants for a cracked solid, *Geophys. J. Roy. astr. Soc.,* **87,** 265-274.

Hyatt, D.L., 1936. Preliminary report on the Fitts Pool, Pontotoc County, Oklahoma, *Bull. Am. Assoc. Pet. Geol.,* **20,** 951-974.

Keith, C.M. and Crampin, S., 1977. Seismic body waves in anisotropic media: propagation through a layer, *Geophys. J. R. astr. Soc.,* **49,** 209-223.

Kramer, D., 1991. Multicomponent multioffset VSP processing, *61st Ann. Internat. Mtg., Soc. Expl. Geophys., Houston, Expanded abstracts,* 38-42.

Krey, Th. and Helbig, K., 1956. A theorem concerning anisotropy of stratified media and it's significance for reflection seismics, *Geophys. Prosp.,* **4,** 294-301.

Lee, M.W. and Balch, A.H., 1982. Theoretical seismic wave radiation from a fluid-filled borehole, *Geophysics,* **47,** 1308-1314.

Levin, F.K., 1979. Seismic velocities in transversely isotropic media, *Geophysics,* **44,** 918-936.

Li, X.Y., Mueller, M.C. and Crampin, S., 1993. Case studies of shear-wave splitting in reflection surveys in South Texas, *Can. J. Expl. Geophys.,* **29,** 189-215.

Liu, E., 1989. *Shear-wave splitting in cross-hole seismology and channel waves in anisotropic waveguides,* Ph.D. thesis, University of Edinburgh.

Liu, E. Crampin, S. and Booth, D.C., 1989. Shear-wave splitting in cross-hole surveys: modelling, *Geophysics* **54,** 57-65.

Liu, E. Crampin, S. and Queen, J.H., 1991. Fracture detection using cross-hole surveys and reverse seismic profiles at the Conoco Borehole Test Facility, Oklahoma, *Geophys. J. Internat.,* **107,** 449-4643.

Love, A.E.H., 1944. *A treatise on the mathematical theory of elasticity,* Dover, New York.

Macbeth, C. and Yardley, G.S., 1992. Optimal estimation of crack strike, *Geophys. Prosp.,* **40,** 849-872.

McGonigle, R. and Crampin, S., 1982. A Fortran program to evaluate the phase and group velocity surface in an anisotropic solid, *Computers and Geoscience,* **8,** 221-226.

Mairs, T., 1966. A subsurface study of the Fernvale and Viola formations in the Oklahoma portion of the Arkoma basin, *Tulsa Geol. Soc. Dig.,* **34,** 60-81.

Martin, M.A. and Davis, T.L., 1987. Shear-wave birefringence: a new tool for evaluating fractured reservoirs, *The Leading Edge,* **6,** 10, 22-28.

Mitchell, S.M., 1985. Reservoir description applied to Iatan East Howard field, Mitchell County, Texas, *A.A.P.G. Bull.,* **69,** 288-289.

Mueller, M.C., 1991. Prediction of lateral variability in fracture intensity using multi-component shear-wave surface seismic as a precursor to horizontal drilling in the Austin Chalk, *Geophys. J. Internat.,* **107,** 409-415.

Musgrave, M.J.P., 1970. *Crystal Acoustics,* Holden Day, San Francisco, California.

Nishizawa, O., 1982. Sesimic velocity anisotropy in a medium containing oriented cracks- transversely isotropic case, *J. Phys. Earth,* **30,** 331-347.

Pujol, J., Burridge, R. and Smithson, S.B., 1985. Velocity Determination from offset VSP data, *J. Geophys. Res.,* **90,** 1871-1880.

Postma, G.W., 1955. Wave propagation in stratified media, *Geophysics,* **20,** 780-806.

Smith, D.P. and Mitchell, S.M., 1988. Evaluation of waterflood operations at Iatan East Howard field, Mitchell County, Texas, *A.A.P.G. Bull.,* **72,** 249.

Sutherland, P.K., 1988. Late Mississippian and Pennsylvanian depositional history of the Arkoma basin area, *Geol. Soc. Am. Bull.,* **100,** 1787-1802.

Tarantola, A., 1987. *Inverse problem theory: methods for data fitting and model parameter estimation.* Elsevier, Amsterdam.

Tatham, R.B. and McCormack, M.D., 1991. *Multicomponent seismology in petroleum exploration,* Investigations in Geophysics **6,** SEG.

Taylor, D.B., 1990. *ANISEIS Manual, Version 4.5,* Applied Geophysical Software, Houston.

Tinkle, A.R., Watts, D.E., Beitel, J.E. and Cook, G.R., 1989. Analysis of *P-* and *S-* wave signatures from the Bolt Omnipulse, *SEG Workshop: Recording and processing vector wavefield data, Snowbird, Abstract,* 48.

Thomsen, L., 1986. Weak elastic anisotropy. *Geophysics,* **51,** 10, 1954-1966.

Tsvankin, I.D. and Chesnokov, E.M., 1990. Synthesis of body wave seismograms from point sources in anisotropic media, *J. Geophys. Res.*, **95**, 11,317-11,331.

Wild, P. and Crampin, S., 1991. The range of effects of azimuthal isotropy and EDA anisotropy in sedimentary basins, *Geophys. J. Internat.*, **107**, 513-529.

Wilkinson, W.M., 1953. Fracturing in Spraberry reservoir, West Texas, *Am. Assoc. Pet. Geo. Bull.*, **37**, 250-265.

Winterstein, D.F. and Meadows, M.A., 1991a. Shear wave polarizations and subsurface stress directions at Lost Hills field, *Geophysics*, **56**, 1331-1348.

Winterstein, D.F. and Meadows, M.A., 1991b. Changes in shear wave polarization azimuth with depth in Cymric and Railroad Gap oil fields, *Geophysics*, **56**, 1349-1364.

Yardley, G.S., 1994. *Identification and characterization of fractured reservoirs by analysis of shear-wave anisotropy*, Ph.D. Thesis, University of Edinburgh.

Zeng, X. and MaCBeth, C., 1993a. Algebraic processing techniques for estimating shear-wave splitting in near-offset VSP data: theory, *Geophys. Prosp.*, **41**, 1033-1066.

Zeng, X. and MaCBeth, C., 1993b. Accuracy of shear-wave polarization estimates from near-offset VSP data, *Can. Jou. Expl. Geophys.*, **29**, 246-265.

Zoback, M.L. and Zoback, M., 1980. State of stress in the conterminous United States, *J. Geophys. Res.*, **85**, 6113-6156.

Zatsepin, S.V. and Crampin, S., 1995. The metastable poro-reactive and interactive rockmass: stress-sensitive anisotropic poro-elasticity, *65st Ann. Internat. Mtg., Soc. Expl. Geophys., Houston, Expanded abstracts*, 918-921.

FAX

**GLOBAL SEISMOLOGY RESEARCH GROUP
BRITISH GEOLOGICAL SURVEY
MURCHISON HOUSE
WEST MAINS ROAD
EDINBURGH EH9 3LA**
+44 (0)131 667 1000 [Switchboard]
+44 (0)131 667 1877 [Fax]
http://ul.nmh.ac.uk [INTERNET]

FROM: Brian Baptie

TO: C.J.E.G. Editor
ORG: Canadian Socitey of Exploration Geophysicists
FAX: 001 403 262 7383
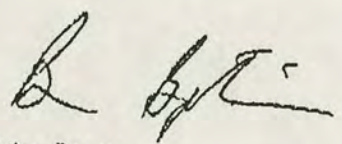
DATE: 11 December, 1995
TIME: 16:20
PAGES: 1 [TOTAL]

Dear Editor,

Permission to reproduce a paper

Please could you grant me permission to reproduce a paper published in the special issue of C.J.E.G. for the 5IWSA. I would like to attach this paper to my Ph.D. thesis for the University of Edinburgh, U.K.

The paper is Baptie, B., Crampin, S., and Liu, E., 1993, Displaying shear-wave splitting in cross-hole surveys for materials with combinations of EDA and PTL anisotropies: Can. J. Expl. Geophys. 29, 227-235.

Yours Sincerely

Brian Baptie

11/12/95

Permission Granted with
Pleasure.

Good luck.

J.H. Payne
CSEG Office Manager.

DISPLAYING SHEAR-WAVE SPLITTING IN CROSS-HOLE SURVEYS FOR MATERIALS WITH COMBINATIONS OF EDA AND PTL ANISOTROPIES

Brian Baptie[1], Stuart Crampin[1] and Enru Liu[2]

Abstract

This paper addresses two current developments: the increasing number of cross-hole surveys and horizontal wells and the recognition of combinations of matrix anisotropy and the anisotropy due to vertical fractures in sedimentary basins. The dip of raypaths in cross-hole surveys and other subsurface surveys is significantly different from the near-vertical raypaths in reflection surveys and vertical seismic profiles. Consequently, polar projections are no longer appropriate for displaying the parameters of shear-wave splitting in cross-hole surveys. Here we present shear-wave polarizations and time delays between faster and slower split shear-wave arrivals in more convenient Plate Carée (equal-area cylindrical) projections for a range of combinations of EDA and PTL anisotropy (crack anisotropy and matrix anisotropy, respectively) common in sedimentary basins. The combination of these two types of hexagonal anisotropic symmetry, with perpendicular axes, leads to orthorhombic symmetry with three mutually perpendicular symmetry planes. In such orthorhombic systems, shear waves display anomalous behaviour in directions of propagation near point singularities, where the polarizations and amplitudes of rays of shear waves may fluctuate rapidly for small changes in direction. The three-dimensional variations in polarizations, time delays and positions of point singularities can be used for the interpretation of multicomponent shear-wave data sets in cross-hole and other subsurface surveys.

Introduction

Shear-wave splitting is commonly observed in sedimentary basins in three-component shear-wave reflection surveys, vertical seismic profiles (VSPs) and cross-hole surveys (CHSs) [see recent review by Crampin and Lovell (1991)]. Such behaviour is characteristic of shear-wave propagation in at least the upper half of the crust and is diagnostic of some form of seismic anisotropy along the raypath (Crampin, 1985a). Typically, the polarization of the shear waves for nearly vertical propagation is scattered about the direction of maximum horizontal stress (Crampin, 1987; Crampin and Lovell, 1991). The polarization of the shear-wave splitting along nearly vertical raypaths has been used to obtain the

orientation of subsurface fractures (Mueller, 1991, 1992) and the delay between the split shear waves has been correlated with the rate of hydrocarbon production (Cliet et al., 1991; Lewis et al., 1991; Li et al., 1993). As a result, monitoring the distinctive behaviour of shear waves appears to have direct applications to reservoir characterization and optimization of production.

Bush and Crampin (1987, 1991) in the Paris Basin, Yardley and Crampin (1993) in Texas, Slater et al. (1993) in the Caucasus and others, have shown that the anisotropy of sedimentary basins may be the result of combinations of azimuthal *anisotropy* and transverse isotropy with a vertical axis of symmetry [azimuthal *isotropy*, in the terminology of Crampin (1989)]. The azimuthal anisotropy appears to be caused by cracks, microcracks and preferentially oriented pore space known as *extensive-dilatancy anisotropy* or EDA (Crampin, 1987, 1993a; Crampin and Lovell, 1991). Azimuthal isotropy is a matrix anisotropy, characterized by *P*- and *S*-waves travelling faster in horizontal than in vertical directions. It can be caused either by aligned grains such as shales (Kaarsberg, 1968; Robertson and Corrigan, 1983) or by finely layered horizontal bedding (Krey and Helbig, 1956; Levin, 1979, 1980) which can be conveniently modelled by repeated (P)eriodic sequences of (T)hin (L)ayers (Postma, 1955), which we shall call *PTL anisotropy* (Crampin, 1989). Since aligned grains and bedding have similar seismic properties, we shall use the term PTL anisotropy to refer to both types of matrix anisotropy.

Typically, PTL anisotropy and EDA anisotropy have orthogonal symmetry axes (vertical for PTL and horizontal for EDA). The combination of PTL and EDA anisotropy leads to orthorhombic symmetry (Wild and Crampin, 1991), which we shall call (C)racked (L)ayer (A)nisotropy or *CLA anisotropy*. The polar projections of, for example, Wild and Crampin (1991) and many others are appropriate for the nearly vertical raypaths in reflection surveys and VSPs. However, with the increasing use of more horizontal raypaths in

CHSs and between horizontal wells, polar plots are no longer adequate. (Equatorial regions are heavily distorted in polar plots centred on the North Pole.)

This paper demonstrates the behaviour of shear-wave splitting for a range of combinations of EDA and PTL anisotropies in Plate Carée (equal-area cylindrical) projections (following Liu et al., 1989) to aid the interpretation of shear waves from CHSs. Holmes et al. (1993), in this issue, has used such projections to display the polarizations of microcracks in a controlled-source shear-wave survey over a wide range of azimuths and angles of incidence in the Underground Research Laboratory at Pinawa, Manitoba, of the Atomic Energy of Canada Ltd.

SHEAR-WAVE PROPAGATION IN ANISOTROPIC SOLIDS

The behaviour of shear waves in anisotropic solids is fundamentally different from their behaviour in isotropic media, although the differences may be subtle and easily overlooked. Two shear waves propagate in every direction of phase velocity with the faster, $qS1$-, and slower, $qS2$-waves, having mutually orthogonal polarizations. The differences in velocity and polarization between the two waves leads to the phenomena of shear-wave splitting (Crampin, 1978, 1981) which introduces phase and amplitude differences into the different components of motion. The polarizations and delays measured from split shear waves may be used to estimate orientations and percentages of anisotropy and hence, the orientations and densities of subsurface cracks and fractures.

A further complication is that traveltimes estimated from field observations are measured along seismic rays propagating at the group velocity and seldom allow phase velocity to be estimated directly. In anisotropic solids, where the group velocity diverges from the phase velocity both in magnitude and direction, the polarizations of the two shear waves are no longer mutually orthogonal for propagation along seismic rays at the group velocity except in certain symmetry directions (Crampin, 1981, 1989).

Consequently, the variation of shear-wave velocities in anisotropic solids can be described by two surfaces referring to phase and group velocity. The phase-velocity surfaces are analytically continuous and must touch in at least two directions (usually many more) called shear-wave singularities (Crampin and Yedlin, 1981). There are three distinct types of singularity: line, kiss and point singularities. Sections of phase-velocity surfaces near point singularities, the commonest type of singularity, usually display high curvature, so that shear-wave polarizations may vary rapidly for small differences in raypath direction. This causes shear waves, propagating at group velocity, to show anomalies in polarizations and amplitudes as well as various cuspoidal features (Crampin, 1991). It was the behaviour of shear-wave polarizations in multioffset VSPs in the Paris Basin that allowed Bush and Crampin (1987, 1991) to recognize for the first time the presence of combinations of EDA and PTL anisotropy in sedimentary basins.

Wild and Crampin (1991) show that combinations of EDA and PTL anisotropies have, necessarily, many directions of point singularities, where rays of shear waves have anomalous particle motion. The directions of these singularities are dependent on the types and relative proportions of EDA and PTL anisotropy in the rock mass. Since the faster split shear wave may not be polarized parallel to the crack strike for near vertical raypaths, it is necessary to understand the behaviour of combinations of EDA and PTL anisotropy in order to identify the orientations of subsurface fracturing.

FORMULATIONS FOR EDA AND PTL

The five independent elastic constants of a PTL solid may be derived from the elastic properties and the ratio of thicknesses of repeated sequences of isotropic layers, by the formulations of Postma (1955). These are valid for layer thicknesses of less than about half a seismic wavelength. The resultant structure has hexagonal anisotropic symmetry, with the axis of symmetry normal to the layering assumed to be vertical. In this paper, varying amounts of PTL anisotropy are expressed as the percentage of differential shear-wave velocity anisotropy (Crampin, 1989). The elastic constants for the PTL materials used in this paper are given in Table 1. These are derived from layer velocities typical of those observed in sedimentary basins.

Table 1. Elastic constants of PTL anisotropy, in 10^9Pa. Density = 2.6 g/cm^3.

	% aniso-tropy	c_{1111} $= c_{2222}$	c_{3333}	c_{1122}	c_{3311} $= c_{2233}$	c_{2323} $= c_{1313}$
PTL1	2%	41.378	39.690	15.808	15.186	12.418
PTL2	12%	32.272	24.835	11.907	9.509	7.949
PTL3	22%	28.576	17.369	10.156	6.644	5.631

The other principal form of seismic anisotropy, recognized by azimuthal variations in shear-wave behaviour, can be modelled by distributions of stress-aligned, fluid-filled microcracks and orientated pore space (Crampin, 1984, 1985b), known as extensive-dilatancy anisotropy or EDA. Such EDA cracks are aligned normal to the minimum compressional stress and, since this direction is usually horizontal below near-surface stress anomalies (Crampin, 1990), the cracks are typically aligned vertical, striking parallel to the maximum horizontal compressional stress.

EDA cracks are calculated with the formulations of Hudson (1980, 1981) and incorporated into PTL anisotropy using the formulations of Hudson (1986) for the scattering of seismic waves by distributions of aligned cracks in anisotropic solids. Crack density, ε, and aspect ratio, γ, are defined as $\varepsilon = Na^3/v$ and $\gamma = d/a$, respectively, where N is the number of cracks of radius a and half thickness d in volume v. Crack dimensions are assumed to be small with respect to seismic wavelength (Crampin, 1993b) and the approximations are thought to be valid for $\varepsilon < 0.1$ (Crampin 1984) and $\gamma < 0.3$ (Douma and Crampin, 1990). In this paper, we use

crack densities of $\varepsilon = 0.01$ and $\varepsilon = 0.05$ and aspect ratios of $\gamma = 0.001$ and $\gamma = 0.05$. EDA cracks also have hexagonal symmetry with, typically, a horizontal axis of symmetry.

The elastic constants for each combination are used to calculate polarizations and delays using the Kelvin-Christoffel equations, which give the components of the elastic tensor matrix in terms of the elastic constants and the phase velocity direction cosines. The eigenvalues and eigenvectors of the matrix give velocities and polarizations, respectively, of the three body waves. Group velocities are calculated and plotted for a grid of phase-velocity directions. As phase and group velocities are not coincident in anisotropic solids, this procedure leads to some distortion. This distortion is negligible for PTL of 2% but will be more significant for PTL anisotropies of 12% and 22%, although the general patterns of behaviour are preserved.

SHEAR-WAVE SPLITTING IN PLATE CARÉE PROJECTIONS

The behaviour of shear-wave splitting in Plate Carée projections is demonstrated in Figure 1 for (a) PTL, (b) EDA and (c) CLA anisotropy, following Liu et al. (1989). The polarizations of the leading split shear wave, projected onto the horizontal radial/transverse (R-T) plane and the vertical/transverse (V-T) plane, are shown for a full range of raypaths, covering 360° of azimuth, and dips from +90° for downward propagation to -90° for upwards propagation. This represents the polarizations of shear waves radiating from a point source, as measured by horizontal instruments (R-T plane) and vertical-transverse instruments (V-T plane), on the walls of a cylinder enclosing the source. The cylinder has then been opened out (mapped) to give a conventional Cartesian (Plate Carée) map projection. Contoured normalized time delays between the fast and slow split shear waves are shown and north-south sections of the contours at five specified azimuths.

Figure 1a shows the behaviour of shear waves in a purely PTL material, PTL2, having 12% differential shear-wave velocity anisotropy (constants listed in Table 1). Figure 1b shows the pattern of polarizations and delays for shear waves propagating through parallel vertical water-filled EDA cracks, striking east-west, with a crack density of $\varepsilon = 0.05$ and $\gamma = 0.05$, representing 5% differential shear-wave anisotropy, in an isotropic matrix ($\alpha = 3.5$, $\beta = 2.02$ km/s, $\rho = 2.2$ g/cm^3). The effect of inserting the EDA cracks of Figure 1b into the matrix with PTL anisotropy of Figure 1a leading to CLA anisotropy is shown in Figure 1c.

The purely PTL anisotropy in Figure 1a shows a distinctive band of transverse polarizations of the leading split shear wave, for directions of propagation between about ±30° of the horizontal, representing *SH*-wave motion. Outside this band, shear waves are polarized in the sagittal plane, representing *SV*-motion. The 90° change in polarizations marks the direction of a line singularity (indicated by arrowheads), characteristic of hexagonal symmetry (Crampin, 1989). There are also kiss singularities, indicated by dots, in the directions of the symmetry axes – the North and South poles of Figure 1a. Time delays are largest for horizontal directions.

The projection of purely EDA anisotropy in Figure 1b also shows distinctive patterns of behaviour. There is a band of nearly parallel polarizations for azimuths close to the crack strike in both R-T and V-T projections, where the time delays have their largest values. Line singularities (indicated by arrowheads), where polarizations of the leading shear wave change by an average of 90°, are also present, but with an orthogonal orientation to those for PTL anisotropy. Two kiss-singularities are marked with dots. The patterns of polarizations and delays, produced by EDA anisotropy in Plate Carée projections, lack any strongly diagnostic features such as seen in polar projections, where the polarization of shear waves along one near-vertical raypath can demonstrate the strike of the EDA cracks. This means that observations from a large number of directions of dip and azimuth are required to identify the characteristics of EDA anisotropy in CHSs (Liu et al., 1989).

The combined PTL and EDA anisotropies in Figure 1c yield CLA anisotropy with patterns of polarizations and delays displaying orthorhombic symmetry. The line singularities of Figures 1a and 1b have pulled apart and point singularities have appeared on the traces of these pull-apart remnants of line singularities (Crampin, 1989). These point singularities, in directions approximately indicated by circles, are places where the phase velocity surfaces touch at the vertices of convex and concave cones. The polarizations and time delays along seismic rays propagating at the group velocity may be much more complicated, with complex cuspoidal lids, fins and ridges on the surface of the group velocity surfaces (Crampin, 1991). These features are irregular in outline and frequently do not have clearly defined centres. Consequently, the positions of the circles merely indicates the approximate centre of the anomaly. In particular, polarizations and time delays may vary rapidly near point singularities and may lead to anomalous shear-wave amplitudes, polarizations and time delays, such as those observed by Bush and Crampin (1991).

COMBINATIONS OF EDA AND PTL ANISOTROPY IN PLATE CARÉE PROJECTIONS

The pattern of shear-wave behaviour for a range of directions in rocks with CLA anisotropy varies significantly with the relative amounts of PTL anisotropy and the relative crack densities and aspect ratios of the distribution of parallel vertical cracks. Figures 2, 3 and 4 show Plate Carée projections of delays and polarizations produced by EDA cracks introduced into three different PTL solids. The PTL materials: PTL1, PTL2 and PTL3, respectively, have anisotropies with differential shear-wave velocities of 2%, 12% and 22%. The EDA cracks are specified by crack densities of $\varepsilon = 0.01$ and 0.05 (giving differential shear-wave velocity anisotropies due to the aligned cracks of approximately 1% and 5%) and by aspect ratios of $\gamma = 0.001$ and 0.05. The figures are similar in format and notation to Figure 1. Note that there is inversion symmetry about a point source for all anisotropic variations in uniform homogeneous solids.
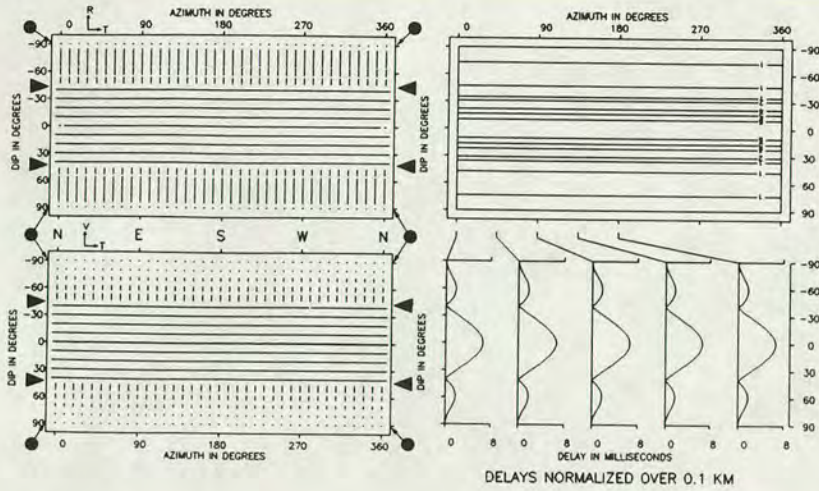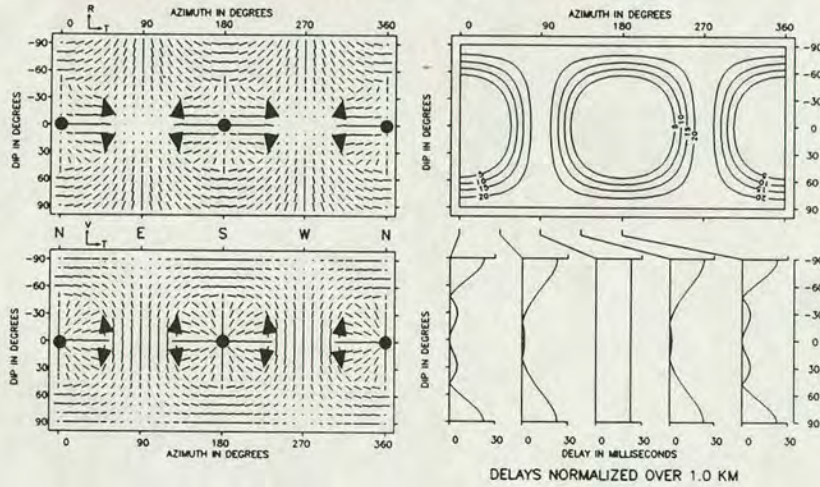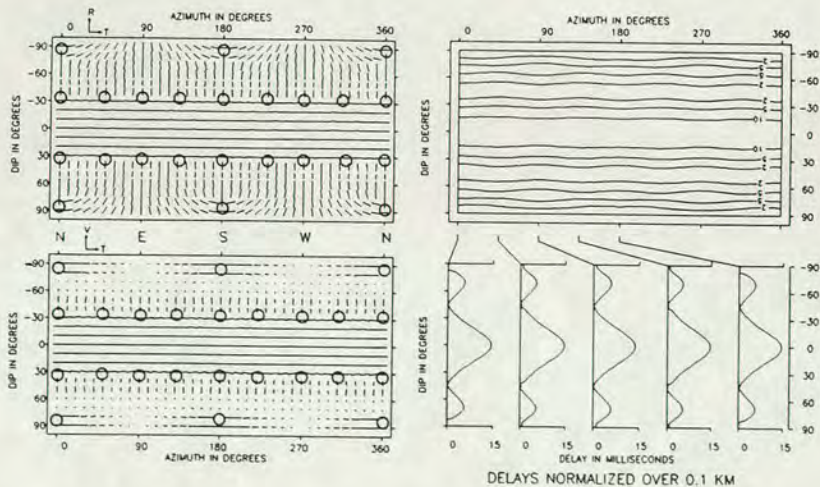
Fig. 1. Plate Carée equal-area cylindrical projections of the polarizations and time delays of split shear waves propagating along rays at the group velocity through: **(a)** PTL anisotropy with 12% differential shear-wave anisotropy; **(b)** EDA anisotropy of parallel vertical cracks striking east-west with crack density of $\varepsilon = 0.05$ and aspect ratio $\gamma = 0.05$; and **(c)** CLA anisotropy combining material in (a) with the cracks in (b). The four sections of each figure are: polarizations of leading split shear waves projected onto, top left, (R)adial/(T)ransverse (R-T) planes and, bottom left, (V)ertical/(T)ransverse (V-T) planes; and, top right, contours of the time delays in ms normalized over 100 m and, bottom right, north-south sections of contoured time delays at indicated azimuths. The polarizations show projections of a fixed-length vector on to the appropriate R-T and V-T planes. Arrows indicate directions of line singularities, solid circles indicate directions of kiss singularities and open circles indicate approximate directions of point singularities. Azimuths are measured from North through East.

The directions of point singularities in these orthorhombic symmetries are sensitive to changes in the relative parameters of the anisotropies making up the CLA anisotropy. Their directions may be used as a benchmark to describe the differences between each projection.

Variations in PTL anisotropy

Figure 2 shows the effects of variations in PTL anisotropy. Combinations of three PTL solids, PTL1, PTL2 and PTL3, with differential shear-wave anisotropies of 2%, 12% and 22%, respectively, are shown pervaded by thin cracks with crack density $\varepsilon = 0.01$ and aspect ratio $\gamma = 0.001$. For the strong PTL anisotropy of 22% for PTL3 in Figure 2c, the broad band of transverse polarizations of pure PTL (Figure 1a) is still present, but the line singularities at the edge of the broad band have each been replaced by eight nearly coplanar point singularities (Crampin, 1989). The kiss singularity, which exists for vertical directions of propagation in pure PTL anisotropy with hexagonal symmetry (Figure 1a), has divided into two point singularities which have moved towards the horizontal plane at azimuths of 0° and 180° (the 360° azimuth is a repeat of the 0° azimuth).

In contrast, in Figure 2a (PTL1), where the PTL anisotropy is comparable to the crack anisotropy, the singularities which in Figure 2c are close to the directions of line singularity of the pure PTL anisotropy (Figure 1a) have now moved closer to the line singularity in the pure EDA anisotropy in Figure 1b. Again, the line singularity has been replaced by eight point singularities. The three-dimensional distribution of the singularities corresponding to the projection shown in Figure 2a is approximately equivalent to the distribution shown in Figure 2c, rotated by 90° about a horizontal E-W axis (azimuth 90°).

For the intermediate PTL anisotropy of 12% for PTL2 in Figure 2b, the point singularities are dispersed in directions between the almost planar line singularities in PTL and the almost planar singularities of EDA anisotropy (which are perpendicular because of the orthogonal symmetry axes). As the ratio of relative PTL and EDA anisotropies changes, the point singularity derived from the kiss singularity moves towards the pull-apart remnant of the line singularity and displaces a point singularity which moves towards the centre of the orthogonal pull-apart remnant line singularity.

The other effect of decreasing the amount of PTL, for a fixed crack anisotropy, is to decrease the time delays between the first and second split shear waves. For PTL3 (22%) the maximum delay is around 15 ms (normalized over 0.1 km). For PTL2 (12%) the maximum delay is about half this value, while for PTL1 (2%) the maximum delay has decreased to about 10 ms. Note that in Figure 2a for convenience the delays have been normalized over 1 km, whereas in Figures 2b and 2c they are normalized over 100 m.

Variations in EDA crack density

Figures 2 and 3 show the same PTL anisotropies for two different crack densities, $\varepsilon = 0.01$ and 0.05, for a constant aspect ratio of $\gamma = 0.001$. It can be seen that increasing crack density produces similar effects as reducing the percentage of PTL anisotropy, since the directions of the singularities are dependent on the ratio of EDA to PTL anisotropies. The point singularities move away from directions centred around one symmetry axis to directions centred around the other symmetry axis. Examining Figures 2a and 3a we can see that as the crack anisotropy exceeds that due to the PTL this shift in the symmetry axes becomes more complete. With increasing crack density, the band of parallel polarizations parallel to the crack strike becomes much more pronounced. Delays increase with crack density increases in each of the three PTL anisotropies.

Variations in EDA crack aspect ratio

The effect of varying aspect ratio can be seen by comparing Figures 3 and 4 which have the same PTL anisotropies pervaded by cracks of the same crack density ($\varepsilon = 0.05$) with two different aspect ratios, $\gamma = 0.001$ and 0.05, respectively. Changing aspect ratio makes comparatively little difference to the directions of the singularities for PTL anisotropies of 12% and 22%. However, the point singularities away from the equator tend to cluster together with increasing aspect ratio at about 45° from the horizontal direction, which is most marked for PTL of 2%.

DISCUSSION

Observations in CHSs are usually strictly confined to raypaths in a few vertical sections within about 45° of the horizontal. It is clear from examining any of Figures 1-4 that such raypaths in a limited number of vertical sections will probably not yield enough diagnostic information to identify PTL and EDA anisotropies and orientations. This is a different situation from polar projections of vertical motion, when a few nearly vertical rays of shear waves can lead to estimates of crack strike and stress orientation (Crampin and Lovell, 1991).

However, cross-hole surveys do present the opportunity to examine shear waves at higher resolution, with the advantages of higher frequencies and raypaths where most of the path is in the zone of interest, as well as avoiding the sometimes severe interactions of the shear waves with the free surface (Evans, 1984; Booth and Crampin, 1985). The greater resolution offered by CHSs should allow a more detailed evaluation of the anisotropy present in a rock mass by analyzing shear-wave splitting.

Difficulties arise if the cross-hole surveys include boundaries with significant impedance contrasts. The polarizations of shear waves crossing such boundaries at oblique angles suffer from the effects of the internal shear-wave window (Liu and Crampin, 1990). In addition, various interface waves may be guided or trapped by the boundary, so that in some cases the dominant energy of the CHS seismograms will be in guided waves not body waves (Liu et al., 1991).

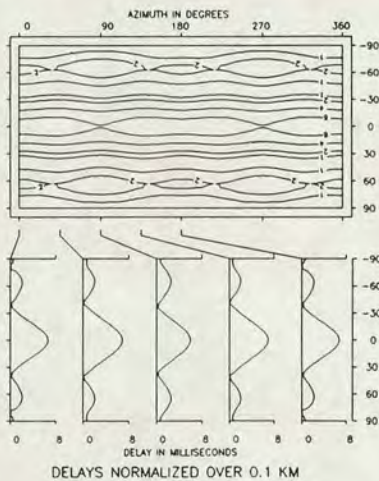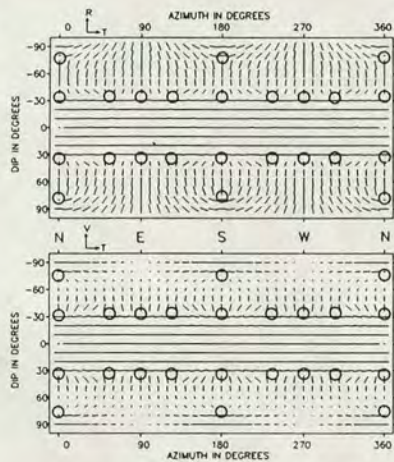Changes in the properties of shear-wave splitting for the varying amounts of EDA and PTL anisotropy demonstrates
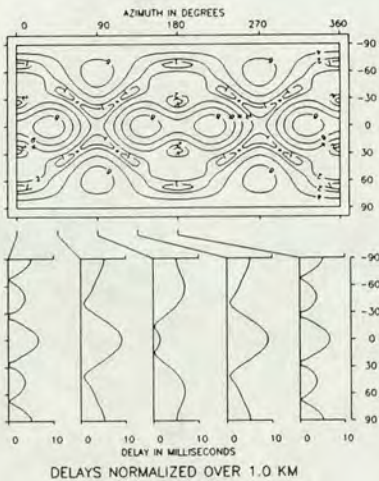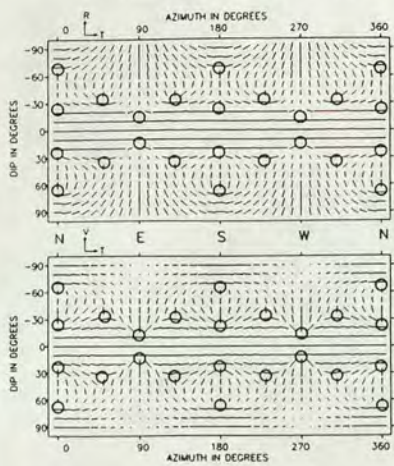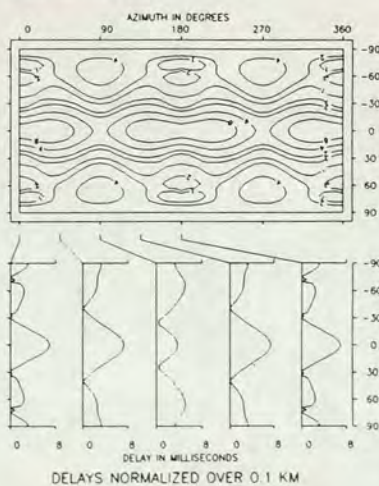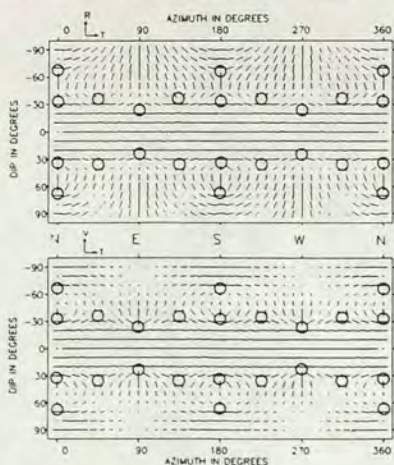
Fig. 2. Plate Carée projections of the polarizations and time delays of split shear waves propagating through CLA anisotropy, for an EDA crack distribution with crack density $\varepsilon = 0.01$ and aspect ratio $\gamma = 0.001$ in uncracked matrices with PTL anisotropy: **(a)** PTL1 – 2% differential shear-wave anisotropy; **(b)** PTL2 – 12%; and **(c)** PTL3 – 22%. Note different normalizations of the contour plots. Format and notation as in Figure 1.

(a)

ASPECT RATIO=0.001   CRACK DENSITY=0.05

PTL=2%

Fig. 3. Similar projections to Figure 2 for EDA crack distributions with crack density ε = 0.05 and aspect ratio γ = 0.001 in the same three PTL anisotropies. Format and notation as in Figure 1.

DELAYS NORMALIZED OVER 1.0 KM

(b)

PTL=12%

DELAYS NORMALIZED OVER 0.1 KM

(c)

PTL=22%

DELAYS NORMALIZED OVER 0.1 KM

how shear-wave behaviour may be further used to measure types and relative amounts of anisotropy present in a rock mass. However, observations are needed from a number of

azimuths and dips to interpret the polarizations and delays in terms of rock structure. Plate Carée projections may be particularly useful for the interpretation of data sets where the
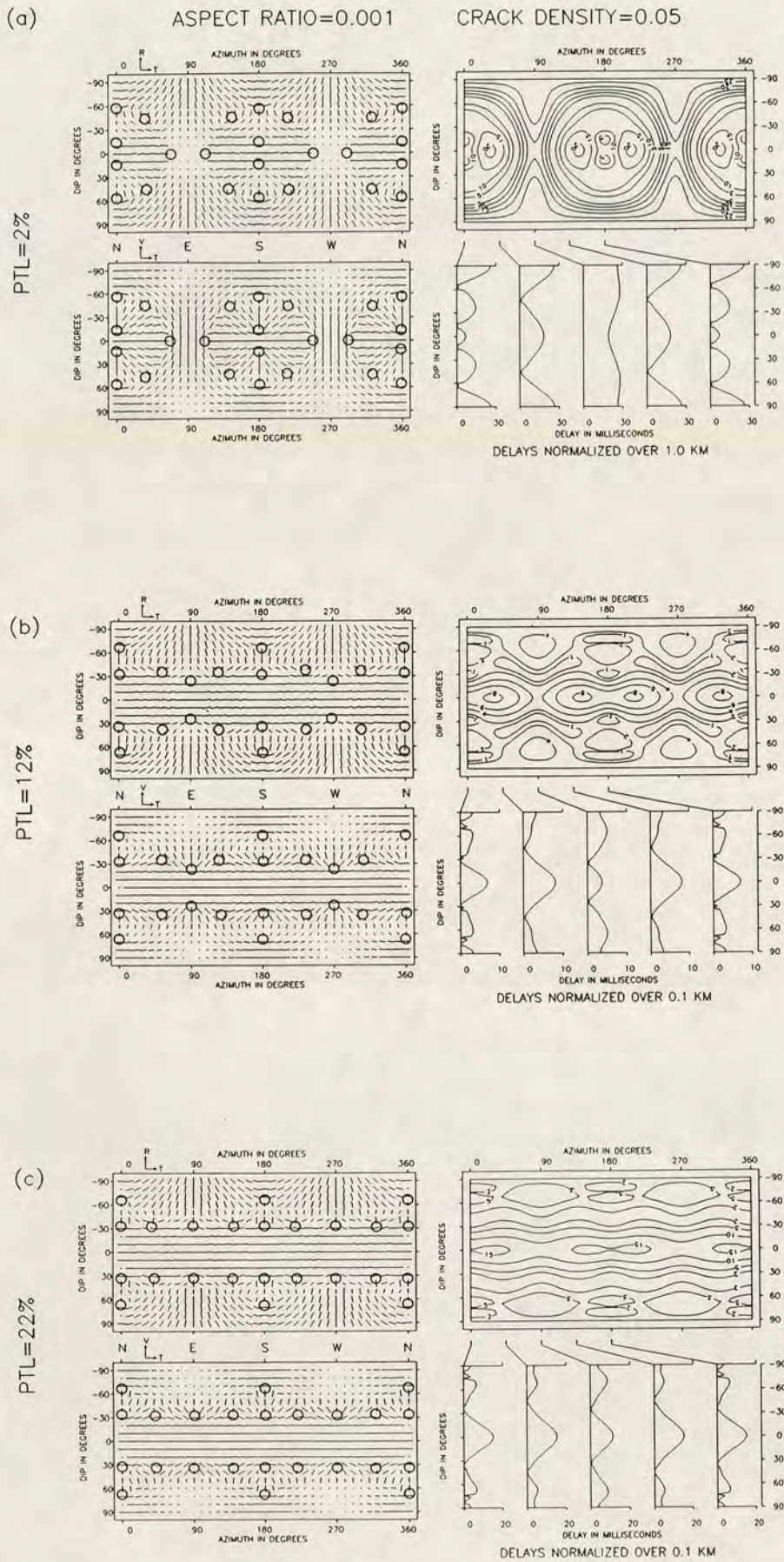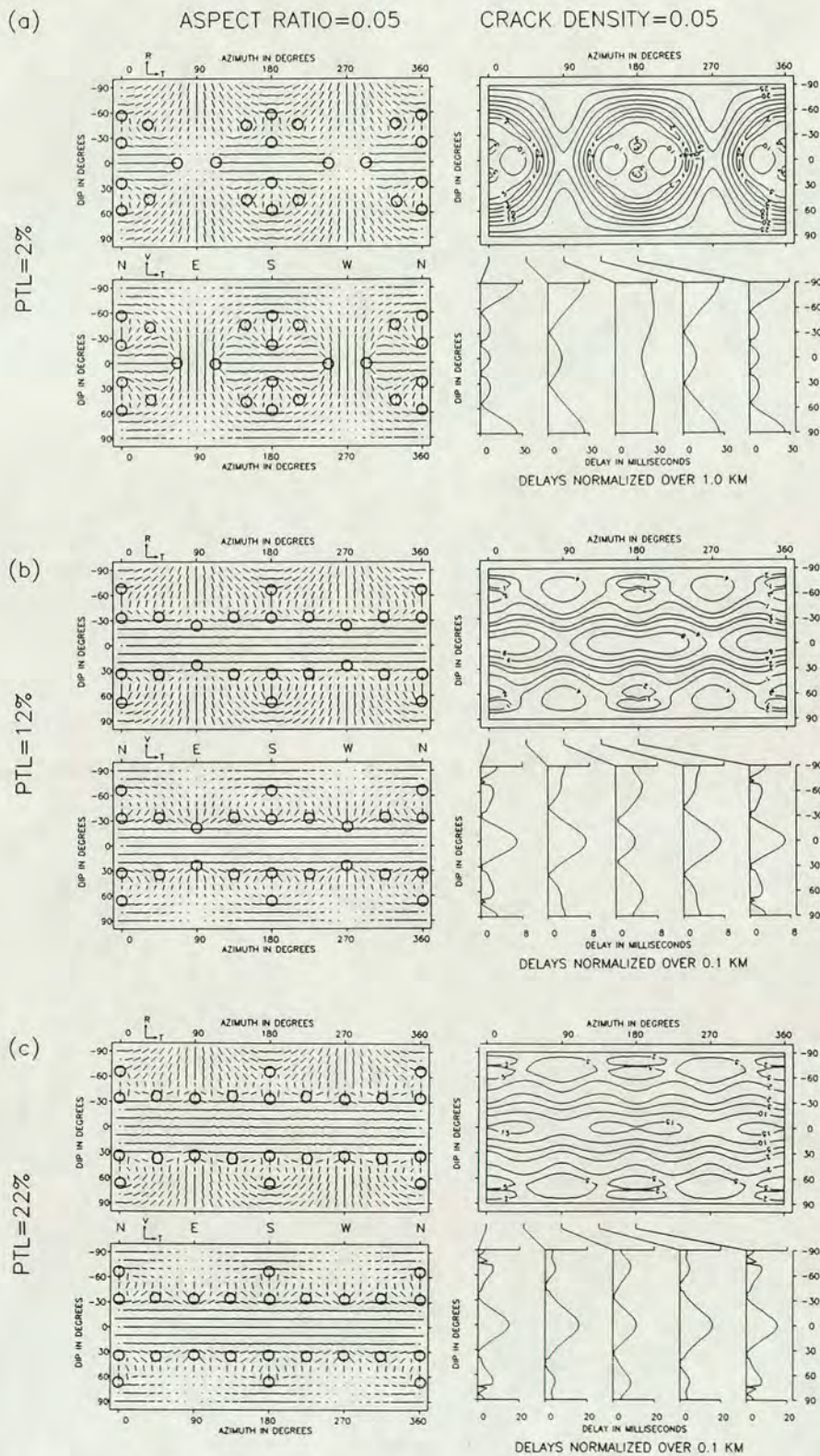

Fig. 4. Similar projections to Figure 2 for EDA crack distributions with crack density ε = 0.05 and aspect ratio γ = 0.05 in the same three PTL anisotropies. Format and notation as in Figure 1.

angular coverage is large, as in the experiment described by Holmes et al. (1993) where the results have been plotted in cylindrical projection and interpreted using models similar to the ones used here.

The following conclusions can be drawn from the behaviour of the shear waves for the modelled structures. The polarizations of shear waves at the wide angles typical of CHSs through vertical or near-vertical cracks are no longer parallel to the crack strike in media with orthorhombic symmetry. The point singularities which occur in considerable numbers in combinations of PTL and EDA anisotropies can have a significant effect on shear-wave propagation. The shear-wave polarizations change by 90° near point-singularities and have anomalous time delays between the split shear waves and anomalous amplitudes. These are similar to the findings of Wild and Crampin (1991).

Furthermore, the directions of the point singularities for the models shown are widely distributed over the range of azimuths and dips. In a CHS it is likely that the directions of propagation would be such that the behaviour of the shear waves would show the effects of propagation near such point-singularities. The accurate positioning of singularities from real data sets and comparison with models are important as the directions (azimuths and angles of incidence) of singularities are critically dependent on the relationships of PTL and EDA anisotropy. These positions may provide a valuable directional correlation with the estimates of PTL and EDA anisotropy which are usually derived from velocity information. This may enable complex field measurements of polarizations and delays to be interpreted in terms of a uniform anisotropic structure, rather than mistaking such features for geological discontinuities.

REFERENCES

Booth, D.C. and Crampin, S., 1985, Shear-wave polarizations on a curved wavefront at an isotropic free-surface: Geophys. J. Roy. Astr. Soc. **83**, 31-45.

Bush, I. and Crampin, S., 1987, Observations of EDA and PTL anisotropy in shear-wave VSPs: 57th Ann. Internat. Mtg., Soc. Expl. Geophys., Exp. Abstr., 646-649.

_____ and _____, 1991, Paris Basin VSPs: case history establishing combinations of fine-layer (or lithologic) anisotropy and crack anisotropy from modelling shear wavefields near point singularities: Geophys. J. Internat. **107**, 433-447.

Cliet, C., Brodov, L., Tikonov, A., Marin, D. and Michon, D., 1991, Anisotropy survey for reservoir delineation: Geophys. J. Internat. **107**, 417-428.

Crampin, S., 1978, Seismic wave propagation through a cracked solid: polarization as a possible dilatancy diagnostic: Geophys. J. Roy. Astr. Soc. **53**, 467-496.

_____, 1981, A review of wave motion in anisotropic and cracked elastic-media: Wave Motion **3**, 343-391.

_____, 1984, Effective anisotropic elastic constants for wave propagation through cracked solids: Geophys. J. Roy. Astr. Soc. **76**, 135-145.

_____, 1985a, Evaluation of anisotropy by shear-wave splitting: Geophysics **50**, 142-152.

_____, 1985b, Evidence of aligned cracks in the Earth's crust: First Break **3**, 3, 12-15.

_____, 1987, Geological and industrial implications of extensive-dilatancy anisotropy: Nature **328**, 491-496.

_____, 1989, Suggestions for a consistent terminology for seismic anisotropy: Geophys. Prosp. **37**, 753-770.

_____, 1991, Effects of point singularities on shear-wave propagation in sedimentary basins: Geophys. J. Internat. **107**, 531-543.

_____, 1993a, Arguments for EDA: Can. J. Expl. Geophys. **29**, 18-30.

_____, 1993b, A review of the effects of crack geometry on wave propagation through aligned cracks: Can. J. Expl. Geophys. **29**, 3-17.

_____ and Lovell, J.H., 1991, A decade of shear-wave splitting in the Earth's crust: what does it mean? what use can we make of it? and what should we do next?: Geophys. J. Internat. **107**, 387-407.

_____ and Yedlin, M., 1981, Shear wave singularities of wave propagation in anisotropic media: Geophys. J. Roy. Astr. Soc. **49**, 43-46.

Douma, J. and Crampin, S., 1990, The effect of a changing aspect ratio of aligned cracks on shear-wave vertical seismic profiles: a theoretical study: J. Geophys. Res. **95**, 11, 293-11, 300.

Evans, J.R., 1984, Effects of the free surface on shear wavetrains: Geophys. J. Roy. Astr. Soc. **76**, 165-172.

Holmes, G.M., Crampin, S. and Young, R.P., 1993, Preliminary analysis of shear-wave splitting in granite at the Underground Research Laboratory, Manitoba: Can. J. Expl. Geophys. **29**, 140-152.

Hudson, J.A., 1980, Overall properties of a cracked solid: Math. Proc. Cambr. Phil. Soc. **88**, 371-384.

_____, 1981, Wave speeds and attenuation of elastic waves in material containing cracks: Geophys. J. Roy. Astr. Soc. **64**, 133-150.

_____, 1986, A higher order approximation to the wave propagation constants for a cracked solid: Geophys. J. Roy. Astr. Soc. **87**, 265-274.

Kaarsberg, E.A., 1968, Elasticity studies of isotropic and anisotropic rock samples: Trans. Soc. Min. Eng. **241**, 470-475.

Krey, T. and Helbig, K., 1956, A theorem concerning anisotropy of stratified media, and its significance for reflection seismics: Geophys. Prosp. **4**, 295-302.

Levin, F.K., 1979, Seismic velocities in transversely isotropic media: Geophysics **44**, 918-936.

_____, 1980, Seismic velocities in transversely isotropic media II: Geophysics **45**, 3-17.

Lewis, C., Davis, T.L. and Vuillermoz, C., 1991, Three-dimensional multi-component imaging of reservoir heterogeneity, Silo Field, Wyoming: Geophysics **56**, 2048-2956.

Li, X.-Y., Mueller, M.C. and Crampin, S., 1993, Case studies of shear-wave splitting in reflection surveys in South Texas: Can. J. Expl. Geophys. **29**, 189-215.

Liu, E. and Crampin, S., 1990, Effects of the internal shear-wave window: comparison with anisotropy induced splitting: J. Geophys. Res. **95**, 11, 275-11, 281.

_____, _____ and Booth, D.C., 1989, Shear-wave splitting in cross-hole surveys: modeling: Geophysics **54**, 57-65.

_____, _____ and Queen, J.H., 1991, Fracture detection using cross-hole surveys and reverse vertical seismic profiles at the Conoco Borehole Test Facility, Oklahoma: Geophys. J. Internat. **107**, 449-463.

Mueller, M.C., 1991, Prediction of lateral variability in vertical fracture intensity using multicomponent shear-wave surface seismic as a precursor to horizontal drilling in the Austin Chalk: Geophys. J. Internat. **107**, 409-415.

_____, 1992, Using shear waves to predict lateral variability in vertical fracture intensity: The Leading Edge **11**, 2, 29-35.

Postma, G.W., 1955, Wave propagation in a stratified medium: Geophysics **20**, 780-806.

Robertson, J.D. and Corrigan, D., 1983, Radiation patterns of a shear-wave vibrator in near-surface shale: Geophysics **48**, 19-26.

Slater, C., Crampin, S., Brodov, L.Y. and Kuznetsov, V.M., 1993, Observations of anisotropic cusps in transversely isotropic clay: Can. J. Expl. Geophys. **29**, 216-226.

Wild, P. and Crampin, S., 1991, The range of effects of azimuthal isotropy and EDA anisotropy in sedimentary basins: Geophys. J. Internat. **107**, 513-529.

Yardley, G.S. and Crampin, S., 1993, Shear-wave anisotropy in the Austin Chalk, Texas, from multioffset VSP data: case studies: Can. J. Expl. Geophys. **29**, 163-176.